Strontium Aluminate Nanoparticles: Synthesis, Characterization, and Luminescence

Afshani Aghajari, Jafar

How to cite

AFSHANI AGHAJARI, Jafar. Strontium Aluminate Nanoparticles: Synthesis, Characterization, and Luminescence. Doctoral Thesis, 2021. doi: 10.13097/archive-ouverte/unige:158932

This publication URL: https://archive-ouverte.unige.ch/unige:158932
Publication DOI: 10.13097/archive-ouverte/unige:158932

UNIVERSITÉ DE GENÈVE FACULTÉ DES SCIENCES

Section de chimie et biochimie
Département de chimie physique

Professeur Thomas Bürgi
Professeur Hans Hagemann

Nanoparticules d'aluminate de strontium: synthèse, caractérisation et luminescence
Strontium Aluminate Nanoparticles: Synthesis, Characterization, and Luminescence

THÈSE

présentée à la Faculté des sciences de l'Université de Genève
pour obtenir le grade de Docteur ès sciences, mention chimie

par

Jafar AFSHANI

Thèse N^{o} 5624

GENÈVE

Atelier ReproMail 2021

Résumé de la thèse

L'introduction en 1993 de phosphores de $SrAl_2O_4$ co-dopés avec Eu^{2+} et Dy^{3+} comme matériaux phosphorescents de longue durée (« long persistent phosphor (LPP) ») nonradioactifs avec des durées d'émission d'une dizaine d'heures a stimulé la recherche dans ce domaine. Des études détaillées de ce composé ainsi que d'autres membres du système $SrO\text{-}Al_2O_3$ furent entreprises pour développer de nouveaux matériaux pour la luminescence persistante. Cependant, le potentiel des aluminates de strontium n'est pas limité aux applications de luminescence persistente. La grande fenêtre de transparence qui s'étend de l'ultraviolet lointain à l'infrarouge proche permet d'autres applications comme matériaux optoélectroniques, de senseurs et pour la catalyse. $SrAl_{12}O_{19}$ comme membre de cette famille de composés est un crystal pour laser lorsqu'il est dopé avec Pr^{3+} ou Nd^{3+}. Cependant, certaines applications restent limitées à cause de la grande taille des grains cristallins. Malgré beaucoup de tentatives dans les dernières décennies, les méthodes de synthèse actuelles ne permettent pas d'avoir un bon contrôle de la morphologie et la distribution de taille de leurs particules. Dans ce travail de thèse, nous présentons une nouvelle méthode de préparation de nanoparticules sphériques de 200-300 nm de précurseurs pour ces matériaux. Le traitement thermique à 1150 °C mène à la formation de plaquettes hexagonales de $SrAl_{12}O_{19}$ pur. Par cette méthode, des nano-cristaux de $CaAl_{12}O_{19}$ ont pu aussi être obtenus. En utilisant diverses techniques comme la microscopie électronique de transmission (TEM), la diffraction aux rayons X de poudres et la spectroscopie infrarouge, nous avons illustré le mécanisme de formation des nanoparticules de même que leur progrès de croissance lors du processus de synthèse solvothermal de coprécipitation. Nos études indiquent que cette méthode de synthèse peut non seulement être appliqué à d'autres membres du système $SrO\text{-}Al_2O_3$, mais aussi au système $CaO\text{-}Al_2O_3$. C'est aussi une méthode prometteuse pour la préparation d'autres nanoparticules bi- ou multi-métalliques, qui sont typiquement difficile à obtenir.

Les cristaux de $SrAl_{12}O_{19}$ et $CaAl_{12}O_{19}$ possèdent un « band gap » de > 7 eV, ce qui les rend d'excellents hôtes pour des activateurs luminescents comme les terres rares. Nous avons obtenu une émission rouge foncée pour Eu^{3+} dans ces nanoparticules cristallins. Cette émission correspond à la transition $^5D_0 \rightarrow {}^7F_4$, qui est plus intense que la transition $^5D_0 \rightarrow {}^7F_0$ qui est habituellement la plus intense. Cette émission proche de l'infrarouge, associée à la taille des nano-cristaux, rend ces composés prometteurs pour des applications biologiques comme le «bio-imaging». De façon inhabituelle pour l'émission de Eu^{3+}, ces cristaux présentent aussi des bandes d'émission à partir des niveaux $^5D_{1\text{-}3}$, ce qui indique de faibles pertes d'énergie vibroniques dans ces nano-particules. Avec l'aide de calculs du champ cristallin, la position des niveaux d'énergie a été estimé pour permettre l'attribution des bandes observées. De plus, l'analyse spetroscopique a permis d'identifier au moins 3 différents types de compensation de charge pour Eu^{3+} dans ces nano-particlues.

Dans cette thèse, nous présentons de plus l'étude de la luminescence de Eu^{3+} dans des composés amorphes $SrO\text{-}Al_2O_3$. Notre analyse a mis en évidence deux observations particulières pour Eu^{3+} dans cette phase amorphe. La bande de transfert de charge de cette émission particulière est observée à une énergie très basse de 29400 cm^{-1}. Cette bande de transfert de charge correspond à l'excitation d'une bande d'émission inhabituellement intense à 566 nm correspondant à la transition $^5D_0 \rightarrow {}^7F_0$. Ces observations peuvent être attribuées à un ion Eu^{3+} fortement lié à un atome d'oxygène, ce qui mène à un fort champ axial. Il est possible qu'une espèce similaire dans le phosphore persistent $SrAl_2O_4:Eu^{2+},Dy^{3+}$ est responsable pour le processus de luminescence optiquement stimulée qui contribue à dépeupler les pièges d'électrons responsables pour l'émission peristente sous illumination UV proche.

Summary of the thesis

The introduction of Eu^{2+} and Dy^{3+} co-doped $SrAl_2O_4$ phosphor in 1993, as a bright green-emitting non-radioactive long persistent phosphor (LPP) material, capable of glowing for over an entire night, boosted the research in the field of LPPs. Soon extensive research began on this host compound and on the other members of the SrO-Al_2O_3 family, as well, in order to develop new afterglow materials. It was discovered that $Sr_4Al_{14}O_{25}$:Eu^{3+},Dy^{3+} also shows persistent luminescence properties. However, the potential of strontium aluminate compounds was not limited to the LPPs. The wide transparency window of these materials extending from the vacuum UV to the near infra-red (NIR) region of the spectrum, as well as their remarkable high thermal and chemical stabilities, paved their ways into other application extending from optoelectronics to the sensors, anti-counterfeiting, and catalysis. $SrAl_{12}O_{19}$ as a member of this family is a laser material when doped with Pr^{3+} or Nd^{3+}. Nevertheless, application of these materials is still limited due to their large crystalline grain sizes. Despite many attempts for almost three decades, the currently available synthesis methods fail to offer control over the morphology and size distribution of their particles. In this thesis we will present a novel synthesis method for the preparation of spherical precursor nanoparticles (NPs) of these materials in the range of 200-300 nm. Upon annealing at 1150 °C, hexagonal platelets of pure-phase $SrAl_{12}O_{19}$ were obtained. It was shown that, this method could further be used to obtain $CaAl_{12}O_{19}$ compound as well. Using different techniques such as transmission electron microscopy (TEM), powder X-rad diffraction (XRD), and infrared spectroscopy, we illustrated the NP formation mechanism, as well as their growth process during a solvothermal-coprecipitation process. Our current investigation indicates that, this synthesis method can be applied for the preparation of not only other members of the SrO-Al_2O_3 system, but also for the CaO-Al_2O_3. It is also a promising method for the preparation of other bi- or multi-metal NPs, which are usually challenging to achieve.

$SrAl_{12}O_{19}$ and $CaAl_{12}O_{19}$ crystals both poses huge band gaps of >7 eV, making them great hosts for the luminescent activators such as rare-earth metal-ions. We obtained a deep-red luminescence from Eu^{3+} ion doped into these crystalline NPs. This deep red emission originates from the $^5D_0 \rightarrow {}^7F_4$ transition, which appeared more intense than the normally the most intense $^5D_0 \rightarrow {}^7F_4$ transition. This deep-red luminescence as well as the nano sizes of the particles, make this phosphor a promising tool for biological applications such as bio-imaging. Unaccustomed to Eu^{3+}, emission bands from the $^5D_{1\text{-}3}$ states were also observed for the Eu^{3+} ion in these two host materials, which indicates the low vibronic energy loss in these NPs. With the help of crystal field (CF) calculations, the energy levels were estimated, which helped with the assignment of the different observed transitions. Moreover, spectroscopically probing their structures, at least three different types of charge compensation (CC) processes were identified for the Eu^{3+} ion in these NPs.

In this thesis we further present investigation of Eu^{3+} luminescence in the amorphous SrO-Al_2O_3 compounds. Our analysis revealed two different peculiar observations for the Eu^{3+} ion in the amorphous phase. The charge transfer band in this peculiar emission was observed at very low energy of 29400 cm_{-1}. This CT band in the excitation spectrum corresponded to an unusual intense transition at 566 nm originating from the $^5D_0 \rightarrow {}^7F_0$ transition. This feature can be assigned to Eu^{3+} strongly bound to one oxygen atom, leading to a strong axial field. It is possible that a similar species in the persistent phosphor $SrAl_2O_4$:Eu^{2+},Dy^{3+} is responsible for the optically stimulated luminescence process, which contributes to deplete the electron traps responsible for the afterglow upon near UV irradiation.

Contents

General Introduction

Strontium aluminates have a very rich crystal chemistry and, when doped with rare earth ions, they find many applications ranging from laser crystals to persistent phosphor materials. The study of the persistent phosphor $SrAl_2O_4$ (which is currently one of the best persistent phosphors) has been a main research topic of our research group in the last years, with the aim to obtain new insights into the electron trapping processes leading to the persistent emission.

However, other strontium aluminates have also very interesting properties and can potentially be considered for biological applications, however in this case it is desirable to obtain in a controlled way monodisperse nano-particles with a good size control. This is the main topic of this thesis, which addresses the successful synthesis of 200 nm – sized particles of single phase $SrAl_{12}O_{19}$ and $CaAl_{12}O_{19}$. This investigation includes also the investigations of the growth process from the precursors to amorphous and finally crystalline material.

In the initial stages of the thesis, several contributions to publications concerning the persistent phosphor $SrAl_2O_4$ were done, as an introduction to the spectroscopic and X-ray techniques necessary for the principal topic of this thesis. The corresponding papers are assembled in the last part of the thesis.

Background

History of persistent emission

“Long persistent phosphors”, “long phosphorescent phosphors”, and “afterglow materials” are all terms used to address a class of materials that keep emitting light for minutes, hours, and even days after ceasing the excitation source [1]. This extraordinary long persistent luminescence (LPL) phenomenon, appears magical not only for ordinary people but for scientists, as well, since the mechanism behind it is not fully understood to date. Although organic materials can also show LPL [2], majority of the LPPs materials consist of an inorganic matrix (host) and an activator (guest) doped inside the host. The activator is generally a rare earth metal ion; however, some transition metals have been used to develop inorganic LPPs, as well [3].

The history of these materials dates back to as early as 1000 years ago. A Chinese text written by Ying Wen, which is published in Song dynasty (960-1279 A.D.) describes (Figure. 1a) a “night-vision” painting of a cow by Zhi-e Xu [4]. Probably, the particular “night-vision” ink used in this painting was imported from Japan, where raw materials such as calcium from pearl shells and sulfur from volcanic activities were readily available for the synthesis of sulfates. However, more scientific reports on LPPs (Bologna stone) occurred in two books named “De Illuminabili Lapide Bononiensi Epistola” (Figure 1b) written by O. Montalbani and “Litheosphorus Sive de Lapide Bononiensi” by F. Licetus in 1634 and 1640, respectively [5]. Bologna stone was synthesized by an Italian shoemaker and alchemist via calcining $BaSO_4$ (barite), a mineral found in Monte Paderno, close to Bolognia, Italy in 1602 [6]. The magical orange and reddish afterglow of the stone was not unveiled before four centuries later, when M. Lastusaari et al proved through modern spectroscopy that the afterglow originate from the $3d^9 4s^1 \rightarrow 3d^{10}$ transition of monovalent copper (Cu^+) impurities in BaS [7].

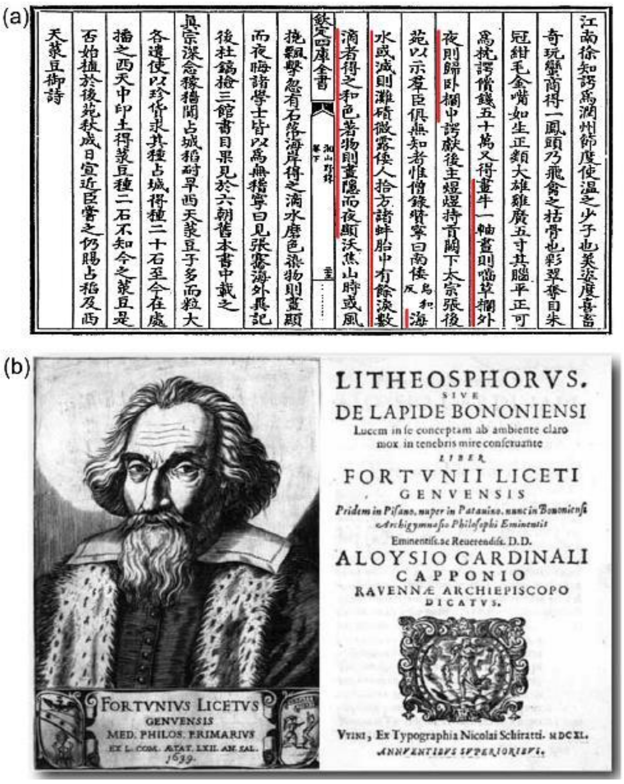

江南徐知諤爲潤州節度使温之少子也美姿度喜畜
奇玩蠻商得一鳳頭乃飛禽之枯骨也彩翠奪目朱
冠紺毛金嘴如生正類大雄雞廣五寸其腦平正可
爲枕諤償錢五十萬又得畫牛一軸晝則嚙草欄外
夜則歸卧欄中諤獻後主煜煜持貢闕下太宗張後
苑以示羣臣俱無知者惟僧錄贊寧曰南倭（烏和反）海
水或減則灘磧微露倭人拾方諸蚌胎中有餘淚數
滴者得之和色著物則晝隱而夜顯沃焦山時或風
欽定四庫全書（湘山野錄 卷下）
撓飄擊忽有石落海岸得之滴水磨色染物則晝顯
而夜晦諸學士皆以爲無稽寧曰見張騫海外異記
後杜鎬檢三館書目果見於六朝舊本書中載之
眞宗深念稼穡聞占城稻耐旱西天菉豆子多而粒大
各遣使以珍貨求其種占城得種二十石至今在處
播之西天中印土得菉豆種二石不知今之菉豆是
否始植於後苑秋成日宣近臣嘗之仍賜占稻及西
天菉豆御詩

FORTVNIVS LICETVS
GENVENSIS
MED. PHILOS. PRIMARIVS
EX L. COM. ÆTAT. LXII. AN. SAL.
1639.

LITHEOSPHORVS.
SIVE
DE LAPIDE BONONIENSI
Lucem in ſe conceptam ab ambiente claro
mox in tenebris mire conſeruante
LIBER
FORTVNII LICETI
GENVENSIS
Pridem in Piſano, nuper in Patauino, nunc in Bononienſi
Archigymnaſio Philoſophi Eminentis
Eminentiſs. ac Reuerendiſs. D.D.
ALOYSIO CARDINALI
CAPPONIO
RAVENNÆ ARCHIEPISCOPO
DICATVS.

VTINI, Ex Typographia Nicolai Schiratti. MDCXL.
ANNVENTIBVS SVPERIORIBVS.

Figure 1. a) Copy of the Chinese text describing the acquisition of “night-vision” cow paining (Figure reproduced from ref [6]). b) The book “Litheosphorus Sive de Lapide Bononiensi” about the afterglow phenomenon of the Bologna stone written by Fortunius Licetus in 1640 (Bologna, Italy) (Figure reproduced from ref [6]).

The so-called “night vision” materials did not attract a lot of attention in research until the end of the 20th century, even though some new materials including ZnS doped with Cu^+ as well as CaS and SrS doped with Eu^{2+}, Bi^{3+} and Ce^{3+} were introduced to this class of materials [4]. In 1866, a French chemist named T. Sidot serendipitily created a new night-vision material while trying to grow ZnS crystals. For over a century, ZnS doped with Cu^+ and later with Co^{2+} was the material of choice for afterglow application. This green emitting material was used during World War I&II as well as civil uses including luminous paints, watch dials, and glow-in-the-dark toys, etc [4, 8-10]. Nonetheless, the afterglow brightness of the ZnS phosphor was weak for practical purposes. Although introduction of radioactive elements such as Tritium (3H), Radium (Ra), and Promethium (Pm) to the structure of Zn crystals improved the brightness, the afterglow duration was far from the ultimate goal of lasting over an entire night.

By 1990s concerns were raised regarding the harmful impacts of the radioactive materials on people and environment. This began a decline in the sales of the watches made based on these materials. Meanwhile, the market faced increasing demand for the non-radioactive clocks despite their weak luminescence. As the demand increased and the big potential of the market for afterglow phosphors was exposed, Nemoto & Co., Ltd. started developing new non-radioactive afterglow materials with high efficiency in terms of brightness and duration. In 1993 Matsuzawa and his colleagues in Nemoto Company [11], successfully developed the extremely bright green LPP $SrAl_2O_4$:Eu^{2+},Dy^{3+}, capable of continuously emitting light for over 30 h after exposure to the illumination. Matsuzawa’s work started a new era in the field of LPPs and stimulated a remarkable research effort on these materials. Nonetheless, $SrAl_2O_4$ was not the only impressive member of the $SrO-Al_2O_3$ family and extensive research started on the other members such as $SrAl_{12}O_{19}$, $SrAl_4O_7$, $Sr_4Al_{14}O_{25}$, and $Sr_3Al_2O_6$.

Initially, applications of LPPs were limited to the safety signs and displays. Their extraordinary luminescence properties and their huge potential, gradually paved the way for their applications in different fields [1, 6, 12-14]. Bioimaging, in particular, is a prominent area, where LPPs have shown to be exceptionally promising [15-17]. During the bioimaging process, background emissions and the local heating caused by the excitation source are problematic to obtain high-contrast images. This can in principle be overcome by application of LPPs as they wouldn't require an excitation source during the imaging process. To fulfill this purpose, currently, extensive research is focused on the development of red and NIR-emitting LPPs with. In 2009 [18], $SrAl_2O_4:Eu^{2+},Dy^{3+}, Er^{3+}$ phosphor was reported to emit in the NIR region for ≈10 minutes. This emission resulted from an energy transfer process from Eu^{2+} to Er^{3+}.

Other than $SrAl_2O_4:Eu^{2+},Dy^{3+}$ with green afterglow, $Sr_4Al_{14}O_{25}:Eu^{2+},Dy^{3+}$ is another widely studied member of the $SrO-Al_2O_3$ system that exhibits LPL properties, as well [19]. This compound emits in the blue region of the spectrum. Combined with a pressure-sensitive luminophore it was used to develop a light charged pressure sensitive paint [20]. Recently, $Sr_4Al_{14}O_{25}:Eu^{2+}$ was used to smooth out the flicker of LEDs [21]. Photocatalysts [22-25], oxygen sensing [26], anti-counterfeiting [27], and solar cell performance improvement [28, 29] are a few of other currently emerging areas where LPPs have been utilized.

After almost three decades of extensive research, $SrAl_2O_4:Eu^{2+},Dy^{3+}$ remains still the best non-radioactive LPP know in terms of the emission intensity and duration. This compound is by far the most studied LPP [13]. Nevertheless, persistent luminescence is not the only fascinating aspect of the $SrO-Al_2O_3$ family and $SrAl_2O_4$ is not the only attractive member.

References

[1] Y. Li, M. Gecevicius, J. Qiu, Long persistent phosphors—from fundamentals to applications, Chem. Soc. Rev., 45 (2016) 2090-2136.

[2] S. Xu, R. Chen, C. Zheng, W. Huang, Excited state modulation for organic afterglow: materials and applications, Adv. Mater., 28 (2016) 9920-9940.

[3] Y. Zhuang, Y. Katayama, J. Ueda, S. Tanabe, A brief review on red to near-infrared persistent luminescence in transition-metal-activated phosphors, Opt. Mater., 36 (2014) 1907-1912.

[4] W.M. Yen, M.J. Weber, Inorganic phosphors: compositions, preparation and optical properties, CRC press, 2004.

[5] J. Hölsä, Persistent luminescence beats the afterglow: 400 years of persistent luminescence, The Electrochemical Society Interface, 18 (2009) 42.

[6 J. Xu, S. Tanabe, Persistent luminescence instead of phosphorescence: History, mechanism, and perspective, J. Lumin., 205 (2019) 581-620.

[7] M. Lastusaari, T. Laamanen, M. Malkamäki, K.O. Eskola, A. Kotlov, S. Carlson, E. Welter, H.F. Brito, M. Bettinelli, H. Jungner, The Bologna Stone: history's first persistent luminescent material, Europ. J. Mineral., 24 (2012) 885-890.

[8] S. Shionoya, W.M. Yen, H. Yamamoto, Phosphor handbook, CRC press, 2018.

[9] W. Hoogenstraaten, H. Klasens, Some properties of zinc sulfide activated with copper and cobalt, J. Electrochem. Soc., 100 (1953) 366.

[10] P.F. Smet, I. Moreels, Z. Hens, D. Poelman, Luminescence in sulfides: a rich history and a bright future, Materials, 3 (2010) 2834-2883.

[11] T. Matsuzawa, Y. Aoki, N. Takeuchi, Y. Murayama, A new long phosphorescent phosphor with high brightness, $SrAl_2O_4:Eu^{2+},Dy^{3+}$, J. Electrochem. Soc., 143 (1996) 2670.

[12] K. Van den Eeckhout, P.F. Smet, D. Poelman, Persistent luminescence in Eu^{2+}-doped compounds: a review, Materials, 3 (2010) 2536-2566.

[13] R.E. Rojas-Hernandez, F. Rubio-Marcos, M.Á. Rodriguez, J.F. Fernandez, Long lasting phosphors: $SrAl_2O_4$:Eu,Dy as the most studied material, Renew. Sustain. Energy Rev., 81 (2018) 2759-2770.

[14] V. Vitola, D. Millers, I. Bite, K. Smits, A. Spustaka, Recent progress in understanding the persistent luminescence in $SrAl_2O_4$:Eu,Dy, Mater. Sci. Technol., 35 (2019) 1661-1677.

[15] S. Singh, Red and near infrared persistent luminescence nano-probes for bioimaging and targeting applications, Rsc Advances, 4 (2014) 58674-58698.

[16] L. Liang, N. Chen, Y. Jia, Q. Ma, J. Wang, Q. Yuan, W. Tan, Recent progress in engineering near-infrared persistent luminescence nanoprobes for time-resolved biosensing/bioimaging, Nano Res., 12 (2019) 1279-1292.

[17] S. Wu, Y. Li, W. Ding, L. Xu, Y. Ma, L. Zhang, Recent advances of persistent luminescence nanoparticles in bioapplications, Nano-Micro Lett., 12 (2020) 1-26.

[18] N. Yu, F. Liu, X. Li, Z. Pan, Near infrared long-persistent phosphorescence in $SrAl_2O_4:Eu^{2+},Dy^{3+},Er^{3+}$ phosphors based on persistent energy transfer, Appl. Phys. Lett., 95 (2009) 231110.

[19] Y. Lin, Z. Tang, Z. Zhang, Preparation of long-afterglow $Sr_4Al_{14}O_{25}$-based luminescent material and its optical properties, Mater. Lett., 51 (2001) 14-18.

[20] D. Peng, Z. Zhong, T. Cai, S. Guo, X. Zhao, Y. Liu, Integration of pressure-sensitive paint with persistent phosphor: A light-charged pressure-sensing system, Rev. Sci. Instrum., 89 (2018) 085003.

[21] L. Wang, W. Wang, Z. Shang, P. Cao, M. Shi, B. Yang, J. Zou, Optical and reliability properties studies of $Sr_4Al_{14}O_{25}:Eu^{2+}$ film for high-CRI white LEDs, J. Mater. Sci.: Mater. Electron., 31 (2020) 13561-13569.

[22] S.G. Menon, A. Bedyal, T. Pathak, V. Kumar, H.C. Swart, $Sr_4Al_{14}O_{25}:Eu^{2+},Dy^{3+}$@ZnO nanocomposites as highly efficient visible light photocatalysts for the degradation of aqueous methyl orange, J. Alloys Compd., 860 (2021) 158370.

[23] F. Kang, G. Sun, P. Boutinaud, H. Wu, F.-X. Ma, J. Lu, J. Gan, H. Bian, F. Gao, S. Xiao, Recent advances and prospects of persistent luminescent materials as inner secondary self-luminous light source for photocatalytic applications, Chemical Engineering Journal, 403 (2021) 126099.

[24] X. Liu, X. Chen, Y. Li, B. Wu, X. Luo, S. Ouyang, S. Luo, A.A. Al Kheraif, J. Lin, A g-C_3N_4@Au@$SrAl_2O_4:Eu^{2+},Dy^{3+}$ composite as an efficient plasmonic photocatalyst for round-the-clock environmental purification and hydrogen evolution, J. Mater. Chem. A, 7 (2019) 19173-19186.

[25] S.-R. Eun, S. Mavengere, J.-S. Kim, Preparation of Ag-$TiO_2/Sr_4Al_{14}O_{25}:Eu^{2+},Dy^{3+}$ Photocatalyst on phosphor beads and its photoreaction characteristics, Catalysts, 11 (2021) 261.

[26] I. Aydin, K. Ertekin, S. Demirci, S. Gultekin, E. Celik, Sol-gel synthesized $Sr_4Al_{14}O_{25}:Eu^{2+}/Dy^{3+}$ blue–green phosphorous as oxygen sensing materials, Opt. Mater., 62 (2016) 285-296.

[27] X. Shen, S. Tang, Q. Hu, M. Ge, Doping $SrAl_2O_4:Eu^{2+},Dy^{3+}$ and thermochromic materials for the generation of anticounterfeiting membrane, ECS J. Solid State Sci. Technol., 9 (2020) 076001.

[28] H. Sun, L. Pan, X. Piao, Z. Sun, Enhanced performance of cadmium selenide quantum dot-sensitized solar cells by incorporating long afterglow europium, dysprosium co-doped strontium aluminate phosphors, J. Colloid Interface Sci., 416 (2014) 81-85.

[29] H. Sun, L. Pan, G. Zhu, X. Piao, L. Zhang, Z. Sun, Long afterglow $Sr_4Al_{14}O_{25}$:Eu,Dy phosphors as both scattering and down converting layer for CdS quantum dot-sensitized solar cells, Dalton Trans., 43 (2014) 14936-14941.

Crystal structures of strontium aluminates

Phase diagram

As shown in Figure 1, the phase diagram of SrO-Al_2O_3 system is complex. Strontium aluminate crystalizes in different phases, $SrAl_{12}O_{19}$ (SA_6), $SrAl_4O_7$ (SA_2), $Sr_4Al_{14}O_{25}$ (S_4A_7), $SrAl_2O_4$ (SA), and $Sr_3Al_2O_6$ (S_3A) being the most commonly encountered members. Capron and Douy [1] completed the initial diagram proposed by the studies of Massazza [2] and Ganits [3]. The notations used in this review follow as S for SrO and A_n for nAl_2O_3. For instance, $SrAl_{12}O_{19}$ (SrO-$6Al_2O_3$) is referred to as SA_6.

According to this phase diagram, it is possible to obtain different phases (or phase transition can easily occur) in the range of 1000-1500 °C. Therefore, to obtain a desired pure phase, it is crucial to control both kinetic and thermodynamic factors, precisely. Thermodynamic data of strontium aluminate compounds are rather scarce and a number of the synthesized phases are missing from the current phase diagram. For instance, $Sr_2Al_6O_{11}$ [4] and $Sr_7Al_{12}O_{25}$ [5] have successfully been prepared but they are absent in this diagram. More detailed description of the phase diagram is provided in section 3.4 [6].

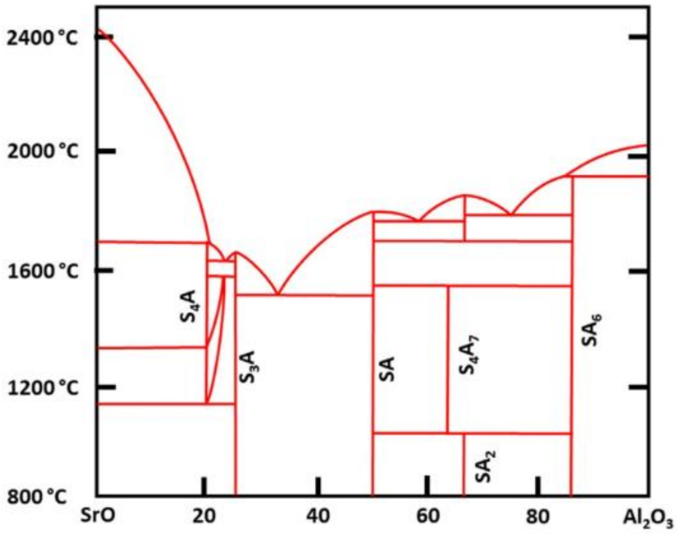

Figure 1. Phase diagram of the SrO-Al_2O_3 system [30, 31, 41, 42].

Optical properties of the dopants in strontium aluminates depend greatly on the local coordination and covalency of the host lattice [7]. As a general rule, increasing the SrO/Al_2O_3 ratio in the crystal structure leads to higher covalency and grater crystal field effect on the dopant. The crystal field experienced by the dopant can impact the energy levels and hence the emission energy. For trivalent rare earth ions, this effect is usually rather small, since the electrons in the 4f orbitals are screened by the outer 5d and 6S orbitals [8]. However, the f-d transitions of divalent rare earths alter dramatically due to the crystal field impression. Similarly, transition metals feel great influence, since their outer-most shells are exposed to the crystal field effect. It is possible for strontium to experience more than just one crystallographic site in a single pure-phase crystalline compound (Table 2, section 3.4). For instance, there exists only one crystallographic site for Sr^{2+} ion in $SrAl_{12}O_{19}$, whereas eleven different sites exist in $Sr_{10}Al_6O_{19}$. This means, eleven different emissions can in principle be observed for $Eu^{2+/3+}$ if doped in the latter structure. Therefore, the luminescence obtained from each member of the SrO-Al_2O_2 family can dramatically differ from one to another.

SrO-Al_2O_3 phases

1.1. $SrAl_{12}O_{19}$

Strontium hexaaluminate structure belongs to the magnetoplumbite family [9, 10]. It crystalizes in a hexagonal structure with space group P63/mmc (Figure 2). In this structure, O^{2-} anions form a closest packing arrangement together with Sr^{2+} cations. The stacking sequence repeats as ABABACBCBCABA along the c axis and the period completes after 10 layers. The third and eight layers contain the larger cation. There are 28 octahedral sites surrounded by anions in a unit cell, 18 of which are occupied by Al^{3+} ions.

In this structure, there exist two formula units per unit cell (Figure 2), which consists of five different crystallographic sites for Al^{3+} (three AlO_6 octahedra, one AlO_5 trigonal bipyramid, and one AlO_4 tetrahedra). Only one crystallographic site exists for the strontium ion in the structure, which coordinates to 12 oxygen atoms. The distance for the six in-plane oxygen atoms from the central strontium is 0.278 nm and the six out of plane oxygen atoms (three above and three under the plane) are located at 0.274 nm from the central atom. The average Sr-O distance is 0.276 nm. Figure 2 (right-hand side) shows the local coordination of the Sr^{2+} ion. Table 1 presents the Sr-O distances in the $SrAl_{12}O_{19}$ crystalline structure. More crystallographic information can be found in Table 1 in section 3.4, for $SrAl_{12}O_{19}$ as well as other crystal structures in the SrO-Al_2O_3 system. Tables 2 in the same section presents additional structural and thermodynamic information for the different phases discussed hereafter.

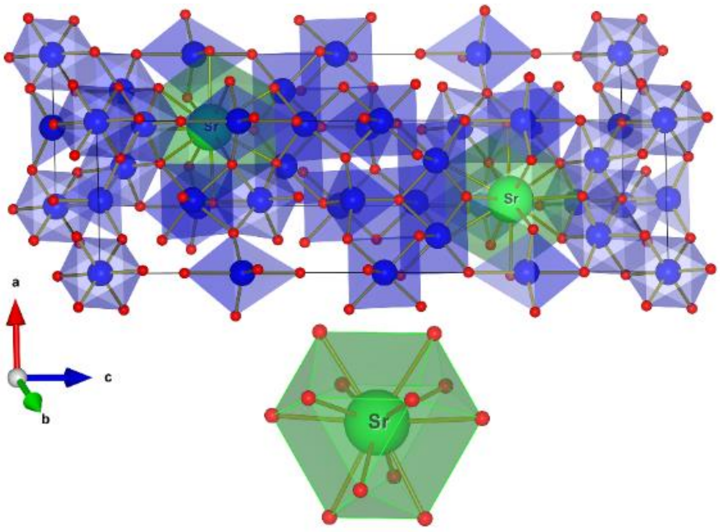

Figure 2. Crystal structure of SA_6 and local coordination geometry of Sr^{2+} ion.

Table 1. Sr-O distances in $SrAl_{12}O_{19}$.

Atoms	Distance (nm)
Sr-O5	0.274
Sr-O5	0.274
Sr-O5	0.274
Sr-O5	0.274
Sr-O5	0.274
Sr-O5	0.274
Sr-O3	0.278
Sr-O3	0.278
Sr-O3	0.278
Sr-O3	0.278
Sr-O3	0.278
Sr-O3	0.278

1.2. $SrAl_4O_7$

α-$SrAl_4O_7$ and β-$SrAl_4O_7$ are two polymorphs of $SrAl_4O_7$ structure. The α-$SrAl_4O_7$ crystalizes in a monoclinic structure with the space group C2/c (Figure 3) [11]. In this structure each unit cell accommodates four formula units. The lattice consists of corner sharing AlO_4 tetrahedral layers with the strontium ions embedded in between the layers. Aluminum occupies wo different tetrahedra sites, while there’s only one crystallographic site for strontium in this structure. The strontium ion is coordinated to seven oxygen atoms locate at different distances in the range of 0.250-0.286 nm from the central ion (Table 2). The average Sr-O distance in this structure is 0.261 nm.

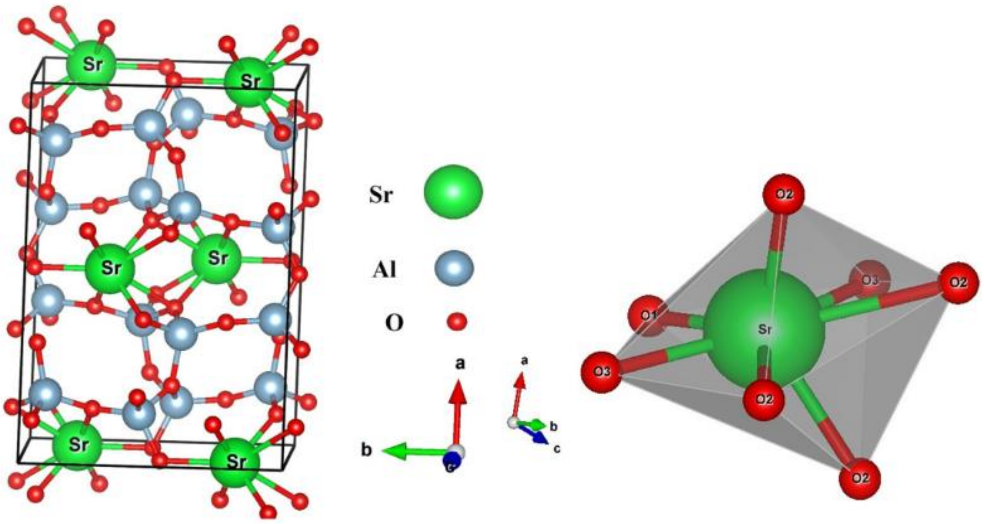

Figure 3. Unit cell of α-$SrAl_4O_7$ and the local coordination geometry of Sr^{2+} ions (Figure reproduced from ref. [12]).

Table 2. Sr-O distances in α-$SrAl_4O_7$.

Atoms	Distance (nm)
Sr-O1	0.256
Sr-O2	0.256
Sr-O2	0.256
Sr-O2	0.280
Sr-O2	0.280
Sr-O3	0.251
Sr-O3	0.251

β-$SrAl_4O_7$ crystalizes in an orthorhombic crystal system with Cmma space group (Figure 4) [13]. There are four formula units per unit cell in this structure. Only one crystallographic site exists for the strontium atom while three different sites (two tetrahedra and one octahedra) exist for the aluminum atoms. The strontium ion is coordinated to 10 oxygen atoms with the average distance of 0.262 nm. The Sr-O distances in the crystal structure of β-$SrAl_4O_7$ are provided in Table 3.

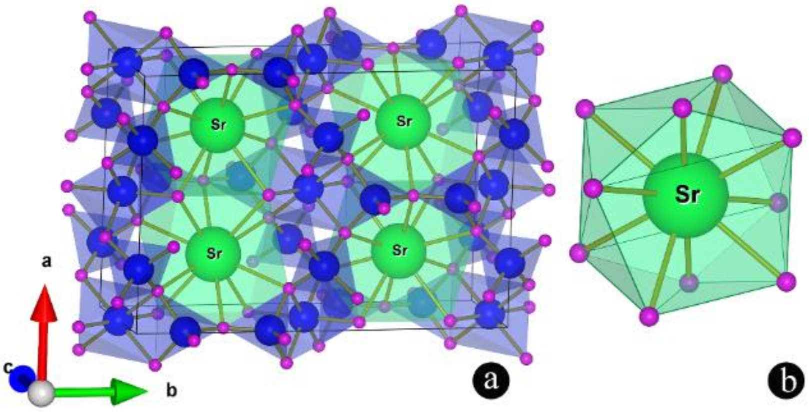

Figure 4. Unit cell of β-$SrAl_4O_7$ and local coordination geometry of Sr^{2+} ions.

Table 3. Sr-O distances in β-$SrAl_4O_7$.

Atoms	Distance (nm)
Sr-O1	0.250
Sr-O1	0.250
Sr-O2	0.266
Sr-O2	0.266
Sr-O2	0.266
Sr-O2	0.266
Sr-O3	0.262
Sr-O3	0.262
Sr-O3	0.262
Sr-O3	0.262

$Sr_4Al_{14}O_{25}$

This structure crystallizes in an orthorhombic crystal system with space group Pmma (Figure 5) [14]. Projection of $Sr_4Al_{14}O_{25}$ along the crystal plane shows two layers made up of AlO_6 octahedra separated by a double layer of AlO_4 tetrahedra. The octahedra share edges to connect to one another, whereas the tetrahedra are connected by corner sharing, leading to a structure with tricoordinate oxygen atoms. There are two different crystallographic sites for strontium ions with the coordination numbers 7(+2) and 10. The average Sr-O bond lengths for the 7 and 10 coordinated strontium ions are 0.264(279) and 0.281 nm, respectively. Table 4 presents the Sr-O distances in this structure. As the average bond length suggests, the interaction between strontium and oxygen ions in the case of the 7(+2)-fold coordinated site is stronger than the 10-fold one. For Al^{3+} ions there are six different crystallographic sites in this structure (three AlO_6 octahedral and three AlO_4 tetrahedral sites).

Note: The “(+n)” Eu-O coordination is indicated with a “(+)” in the corresponding table of distances of each crystal phase.

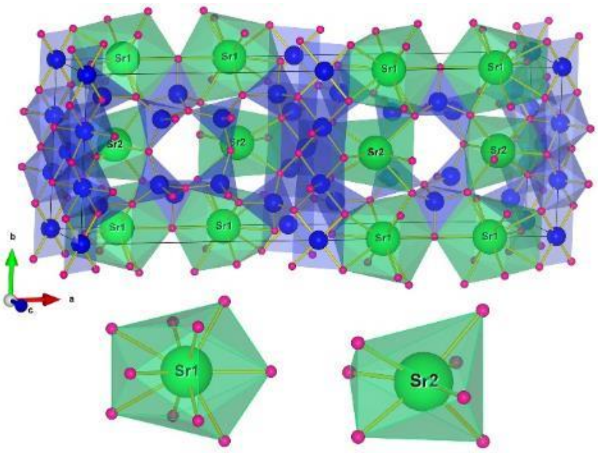

Figure 5. Unit cell of $Sr_4Al_{14}O_{19}$ and local coordination geometry of Sr^{2+} ions.

Table 4. Sr-O distances in $Sr_4Al_{14}O_{25}$.

Atoms	Distance (nm)	Atoms	Distance (nm)
Sr1-O2	0.303	Sr2-O1	0.261
Sr1-O2	0.303	Sr2-O1	0.261
Sr1-O2	0.275	Sr2-O2	0.331 (+)
Sr1-O2	0.275	Sr2-O2	0.331 (+)
Sr1-O3	0.267	Sr2-O3	0.270
Sr1-O3	0.267	Sr2-O3	0.270
Sr1-O6	0.265	Sr2-O5	0.251
Sr1-O8	0.287	Sr2-O7	0.249
Sr1-O8	0.287	Sr2-O7	0.283
Sr1-O9	0.279		

$Sr_2Al_6O_{11}$

$Sr_2Al_6O_{11}$ crystalized in an orthorhombic structure with space group Pnnm (Figure 6) [4]. Its unit cell consists of four formula unit with two different crystallographic sites for strontium atom and five different aluminum sites (three octahedra and two tetrahedra). The strontium atoms are coordinated to 7(+2) and 10 oxygen atoms, respectively. As presented in Table 5 the Sr-O distance ranges from 0.253 to 0.331 nm [average d = 0.277 (0.285)] for the former strontium and from 0.251-0.309 nm (average d = 0.277 nm) for the latter one.

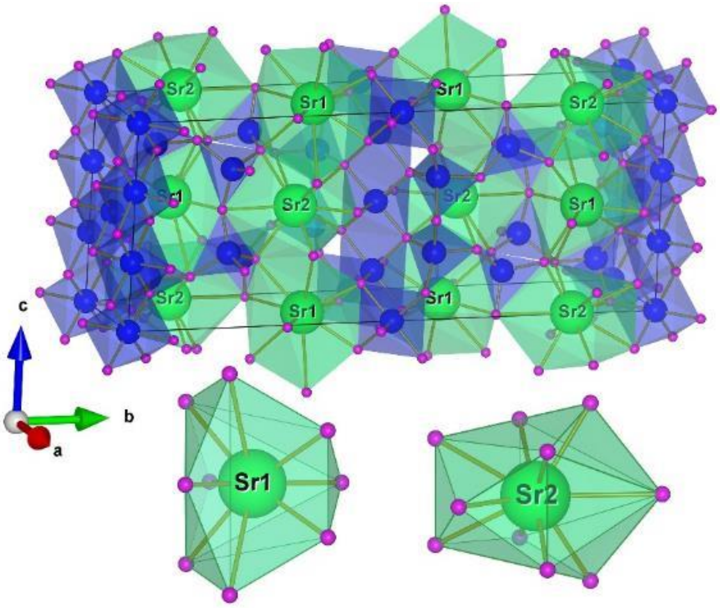

Figure 6. Crystal structure of $Sr_2Al_6O_{11}$ and local coordination geometry of Sr^{2+} ions.

Table 5. Sr-O distances in $Sr_2Al_6O_{11}$ crystal structure.

Atoms	Distance (nm)	Atoms	Distance (nm)
Sr1-O2	0.259	Sr2-O1	0.251
Sr1-O2	0.304	Sr2-O2	0.309
Sr1-O3	0.261	Sr2-O4	0.267
Sr1-O3	0.261	Sr2-O4	0.267
Sr1-O4	0.331 (+)	Sr2-O4	0.301
Sr1-O4	0.331 (+)	Sr2-O4	0.301
Sr1-O5	0.253	Sr2-O6	0.283
Sr1-O7	0.280	Sr2-O6	0.283
Sr1-O7	0.280	Sr2-O7	0.263
		Sr2-O7	0.263

$SrAl_2O_4$

Similar to $SrAl_4O_7$, $SrAl_2O_4$ has two different polymorphs; α-$SrAl_2O_4$ and β-$SrAl_2O_4$ (Figure 7). The α polymorph crystalizes in a monoclinic crystal system with $P2_1$ space group [15]. The monoclinic phase exists at room temperature and it transforms into the hexagonal phase above 650 °C. Even though $SrAl_2O_4$ belongs to the AB_2O_4 spinel structure, the large size of Sr^{2+} ion inhibits it from formation of a spinel structure. It has a crystal structure of stuffed tridymite type consisting of six corner-sharing AlO_4 tetrahedra. Four different crystallographic sites exist for aluminum atoms (all with AlO_4 tetrahedra structure) and the strontium ions are located within the hexagonal cavity formed by these tetrahedra layers. There are two nonequivalent sites for strontium in this structure. In both sites, Sr^{2+} ions are coordinated to 7(+2) oxygen atoms with the average distances being 0.269(0.288) nm and 0.267(0.284) nm for these two sites (See Table 6 for Sr-O distances). The two sites differ only by a slight distortion of their square planes.

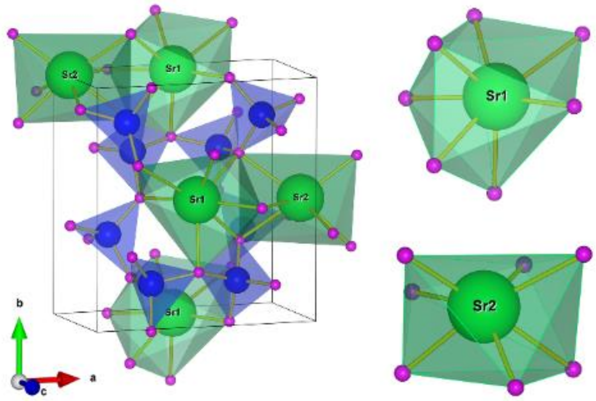

Figure 7. Crystal structures of α-$SrAl_2O_4$ and local coordination geometry of Sr^{2+} ions.

Table 6. Sr-O distances in α-$SrAl_2O_4$ (monoclinic) crystal structure.

Atoms	Distance (nm)	Atoms	Distance (nm)
Sr1-O1	0.267	Sr2-O1	0.277
Sr1-O2	0.268	Sr2-O2	0.270
Sr1-O3	0.252	Sr2-O4	0.261
Sr1-O3	0.352 (+)	Sr2-O5	0.328 (+)
Sr1-O4	0.256	Sr2-O5	0.251
Sr1-O5	0.353 (+)	Sr2-O6	0.256
Sr1-O6	0.311	Sr2-O8	0.299
Sr1-O7	0.273	Sr2-O8	0.254
Sr1-O5	0.257	Sr2-O8	0.357 (+)

β-$SrAl_2O_4$ phase crystalized in a hexagonal crystal system with $P6_322$ space group (Figure 8) [16]. This structure is normally instable below 650 °C [17]. Its unit cell accommodates six formula units. In this structure, Al^{3+} ion occupies two different AlO_4 tetrahedra sites, and Sr^{2+} ions experience three different crystallographic sites. The strontium ions are coordinated to 9, 6(+3), and 8 oxygen atoms with the average Sr-O distance of 0.289, 0.27(0.299) and 0.280 nm, respectively. The two aluminum tetrahedra form a corner-sharing structure with a cavity, which is filled by the Sr^{2+} ions. Table 7 provides the Sr-O distance in this structure.

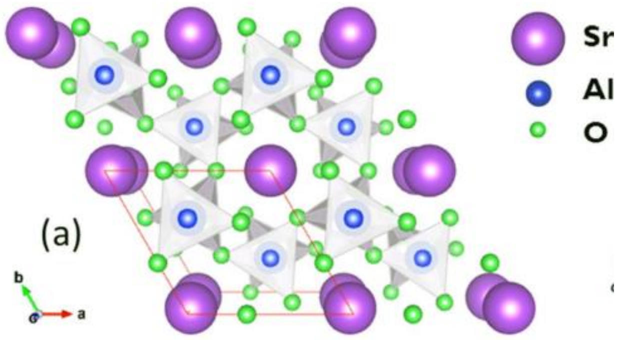

Figure 8. Crystal structures of β-$SrAl_2O_4$ and local coordination geometry of Sr^{2+} ions (Figure reproduced from ref. [13]).

Table 7. Sr-O distances in β-$SrAl_2O_4$ (hexagonal) crystal structure.

Atoms	Distance (nm)	Atoms	Distance (nm)	Atoms	Distance (nm)
Sr1-O1	0.293	Sr2-O1	0.348 (+)	Sr3-O1	0.260
Sr1-O1	0.293	Sr2-O1	0.348 (+)	Sr3-O1	0.260
Sr1-O1	0.293	Sr2-O1	0.348 (+)	Sr3-O1	0.260
Sr1-O2	0.257	Sr2-O3	0.282	Sr3-O3	0.285
Sr1-O2	0.257	Sr2-O3	0.282	Sr3-O3	0.285
Sr1-O2	0.257	Sr2-O3	0.282	Sr3-O4	0.296
Sr1-O2	0.318	Sr2-O4	0.268	Sr3-O4	0.296
Sr1-O2	0.318	Sr2-O4	0.268	Sr3-O4	0.296
Sr1-O2	0.318	Sr2-O4	0.268		

Although β-$SrAl_2O_4$ is known to be unstable below 650 °C [17], it has been stabilized at room temperature as a solid solution after firing to 900-1300 °C in the presence of silicon, Ca or excess amount of aluminum atoms. Singh et al [18] showed that addition of ZnO to the reaction mixture can stabilize the β-$SrAl_2O_4$ at room temperature. In a combustion synthesis, they added 20 wt% of ZnO to the reaction mixture to obtain the precursor material, which was then annealing at 700 °C to yield the β-$SrAl_2O_4$ as the dominant phase. However, increasing the annealing temperature to above 1000 °, again resulted in α-$SrAl_2O_4$.

Avdeev et al [17] studied the reversibility of the α-$SrAl_2O_4$ and β-$SrAl_2O_4$ polymorphs phase transformation and suggested that a monoclinic ↔ hexagonal process takes place at ≈680 °C (Figure 9). This phase transition process was monitored with in situ high-temperature X-ray and neutron powder diffraction. The XRD data collected in the range of 670-688 °C, clearly indicate a phase transformation taking place. At 670 °C the monoclinic phase dominates. At 678 °C, a mixture of the monoclinic and hexagonal phase is present and increasing the temperature to 686 °C results in complete transformation to the hexagonal phase.

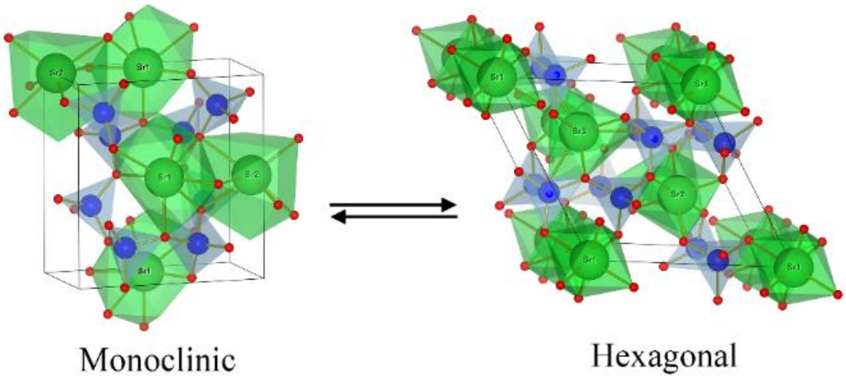

Figure 9. Transition between the monoclinic and hexagonal phases of $SrAl_2O_4$.

$Sr_3Al_2O_6$

Tristrontium dialuminum hexaoxide has a similar structure to the ABO_3 perovskite, which crystallizes in the cubic Pa3 space group (Figure 10) [19]. In this structure, the unit cell consists of 24 formula units which accommodates 48 Al^{3+}, 72 Sr^{2+}, and 144 O^{2-} ions. Six different crystallographic sites exist for strontium in this lattice. Three strontium ions coordinate to six oxygen atoms, which form a 3-dimentional cubic matrix. Two of the remaining three strontium atoms coordinate to 8 oxygen atoms and the last strontium coordinates to 7(+1) oxygen atoms. The average Sr-O distances in these six sites are 0.248, 0.250, 0.248, 0.281, 0.275 and 0.264(0.273) nm, respectively. These values are in average shorter than the other members of the family covered before and indicates greater crystal field effect on the central atom. Table 8 provides the Sr-O distances for this structure.

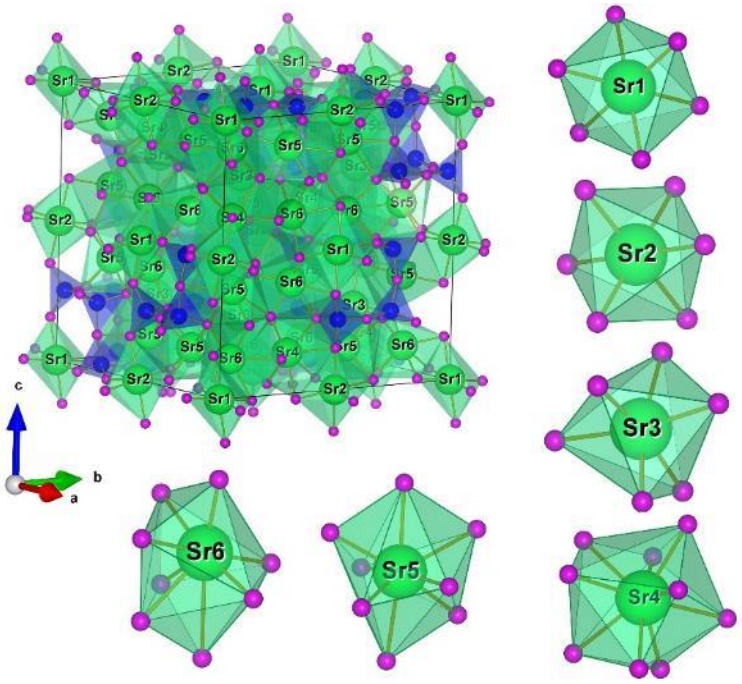

Figure 10. Crystal structure of $Sr_3Al_2O_6$ and local coordination geometry of Sr^{2+} ions.

Table 8. Sr-O distances in $Sr_3Al_2O_6$ crystal structure.

Atoms	Distance (nm)	Atoms	Distance (nm)
Sr1-O6	0.249	Sr4-O1	0.270
Sr1-O6	0.249	Sr4-O1	0.270
Sr1-O6	0.249	Sr4-O4	0.275
Sr1-O6	0.249	Sr4-O4	0.275
Sr1-O6	0.249	Sr4-O4	0.275
Sr1-O6	0.249	Sr4-O5	0.293
Sr2-O5	0.250	Sr4-O5	0.293
Sr2-O5	0.250	Sr4-O5	0.293
Sr2-O5	0.250	Sr5-O1	0.273
Sr2-O5	0.250	Sr5-O2	0.257
Sr2-O5	0.250	Sr5-O2	0.292
Sr2-O5	0.250	Sr5-O3	0.286
Sr3-O3	0.250	Sr5-O3	0.270
Sr3-O3	0.250	Sr5-O4	0.287
Sr3-O3	0.250	Sr5-O5	0.289
Sr3-O4	0.250	Sr5-O5	0.243
Sr3-O4	0.250	Sr6-O1	0.289
Sr3-O4	0.250	Sr6-O2	0.273
		Sr6-O3	0.248
		Sr6-O4	0.338 (+)
		Sr6-O4	0.246
		Sr6-O6	0.278
		Sr6-O6	0.272
		Sr6-O6	0.243

References

[1] F. Massazza, The system SrO–Al_2O_3, Chim. Ind.(Milan), 41 (1959) 108-115.

[2] F. Ganits, T.Y. Chemekova, Y.P. Udalov, The SrO-Al_2O_3 system, Zhurnal Neorganicheskoj Khimii, 24 (1979) 471-475.

[3] D. Dutczak, T. Jüstel, C. Ronda, A. Meijerink, Eu^{2+} luminescence in strontium aluminates, Phys. Chem. Chem. Phys., 17 (2015) 15236-15249.

[4] L.D. Merkle, B. Zandi, R. Moncorgé, Y. Guyot, H.R. Verdun, B. McIntosh, Spectroscopy and laser operation of Pr,Mg:$SrAl_{12}O_{19}$, J. Appl. Phys., 79 (1996) 1849-1856.

[5] M. Fechner, F. Reichert, N.-O. Hansen, K. Petermann, G. Huber, Crystal growth, spectroscopy, and diode pumped laser performance of Pr, Mg:$SrAl_{12}O_{19}$, Appl. Phys. B, 102 (2011) 731-735.

[6] Y. Pan, B. Liu, J. Liu, Q. Song, J. Xu, D. Li, P. Liu, J. Ma, X. Xu, H. Lin, Polarized spectral properties and laser operation of Nd:$SrAl_{12}O_{19}$ crystal, J. Lumin., 235 (2021) 118034.

[7] L. Wang, Y. Xu, D. Wang, R. Zhou, N. Ding, M. Shi, Y. Chen, Y. Jiang, Y. Wang, Deep red phosphors $SrAl_{12}O_{19}$:Mn^{4+}, M (M= Li^+, Na^+, K^+, Mg^{2+}) for high colour rendering white LED s, physica status solidi (a), 210 (2013) 1433-1437.

[8] X. Lin, K. Deng, H. Wu, B. Du, B. Viana, Y. Li, Y. Hu, Photon energy conversion and management in $SrAl_{12}O_{19}$:Mn^{2+},Gd^{3+} for rewritable optical information storage, Chem. Eng. J., 420 (2021) 129844.

[9] V. Sharma, A. Das, V. Kumar, O. Ntwaeaborwa, H. Swart, Potential of $Sr_4Al_{14}O_{25}$:Eu^{2+},Dy^{3+} inorganic oxide-based nanophosphor in Latent fingermark detection, J. Mater. Sci., 49 (2014) 2225-2234.

[10] W. Piotrowski, K. Trejgis, K. Maciejewska, K. Ledwa, B. Fond, L. Marciniak, Thermochromic luminescent nanomaterials based on Mn^{4+}/Tb^{3+} codoping for temperature imaging with digital cameras, ACS appl. mater. interfaces, 12 (2020) 44039-44048.

[11] F. Farzaneh, M.K. Maleki, E. Rashtizadeh, Expedient catalytic access to Knöevenagel condensation using Sr 3 Al 2 O 6 nanocomposite in room temperature, J. Clust. Sci., 28 (2017) 3253-3263.

[12] H. Hagemann, J. Afshani, Chapter 321: Synthesis, luminescence and persistent luminescence of europium-doped strontium aluminates, Handbook on the Physics and Chemistry of Rare Earths, Elsevier, Vol 60 (2021) p.163-225, ISSN 0168-1273, https://doi.org/10.1016/bs.hpcre.2021.06.001.

[13] M. Capron, A. Douy, Strontium dialuminate $SrAl_4O_7$: Synthesis and stability, J. Am. Ceram. Soc., 85 (2002) 3036-3040.

[14] T. Takeda, K. Takahashi, K. Uheda, H. Takizawa, T. Endo, Crystal structure and luminescence properties of $Sr_2Al_6O_{11}$:Eu^{2+}, Journal of the Japan Society of Powder and Powder Metallurgy, 49 (2002) 1128-1133.

[15] H. Akasaka, H. Tada, T. Ooki, A. Nakamura, K. Komatsu, S. Tsuchida, S. Ohshio, N. Nambu, H. Saitoh, New Violet Phosphor $Sr_7Al_{12}O_{25}$:Eu^{2+} Synthesized from Sr–Al–O: Eu Powder Mounted on Polycrystalline Alumina, JPN. J. Appl. Phys., 49 (2010) 122601.

[16] C.-H. Huang, Rare earth coordination chemistry: fundamentals and applications, John Wiley & Sons, 2011.

[17] K. Kimura, M. Ohgaki, K. Tanaka, H. Morikawa, F. Marumo, Study of the bipyramidal site in magnetoplumbite-like compounds, $SrM_{12}O_{19}$ (M= Al, Fe, Ga), J. Solid State Chem., 87 (1990) 186-194.

[18] A.J. Lindop, C. Matthews, D.W. Goodwin, The refined structure of SrO.6Al_2O_3, Acta Crystallographica Section B, 31 (1975) 2940-2941.

[19] K. Gedekar, S. Wankhede, S. Moharil, R. Belekar, Ce^{3+} and Eu^{2+} luminescence in calcium and strontium aluminates, J. Mater. Sci.: Mater. Electron., 29 (2018) 4466-4477.

2. Synthesis methods

The synthesis method used for the preparation of strontium aluminate greatly influences the particle size and crystallinity. These in turn, dramatically affect the optical properties of luminescent dopants such as fluorescent quantum efficiency, and afterglow intensity and duration. Solid-state method is the conventional route for synthesizing strontium aluminates. Usually, this method leads to products with big grain sizes in between 20-100 µm, which limits their applications, remarkably. In recent years, with the emergence of new applications, extensive research has been dedicated to the synthesis of nanosized particles of these compounds. This consequently has led to development of new synthesis methods. On the other hand, the conventional solid-state method requires high temperatures, normally above 1300 °C for several hours, which consume huge amount of energy. Therefore, development of alternative synthesis methods is essential. Different methods for the preparation of inorganic materials have been comprehensively covered in several books and review papers [1-5]. Here, we will discuss those used for the preparation of $SrO-Al_2O_3$ compounds.

2.1. Solid-state method

As the most commonly applied method for preparation of inorganic materials, solid state method involves decomposition and reaction of a mixture of solid reactants at elevated temperatures to produce a solid product [6, 7]. This process is normally accompanied by release of gasses as by-products. A variety of reactants such as metal oxides, carbonates, nitrates, hydroxides, oxalates, alkoxides, sulfates, and others can be used in this method. A phase diagram is generally very helpful for obtaining desired compositions.

Since in this method the reaction takes places at considerably high temperatures, choosing a suitable container is extremely important. While platinum, silica, and alumina containers are generally used for the synthesis of oxides, for sulfides, chalcogenides, and pnictides usually graphite containers are employed. For volatile and sensitive reactants, the reaction may be carried out in a sealed evacuated capsule. Basically, grinding the precursor components to mix properly before running the synthesis, is essential to obtain a product with a homogeneous composition. In some cases, several steps of annealing and milling of the intermediate products are inevitable to obtain a pure-phase product.

The conventional solid-state method remains still the primary choice for the preparation of commercially available strontium aluminate phosphors, due to the superior brightness and luminescence of the particles obtained by this method. Nevertheless, the high temperatures (>1300 °C) applied for considerably long reaction times (>10 h) required in this method, results in huge energy consumption for the mass production. Indeed, high temperature is essential for obtaining good afterglow in LPPs, since it increases the population of thermal defects in the crystal structure. These defects and distortions are believed to improve the afterglow properties. Nevertheless, the solid-state method is always accompanied with inevitable shortcomings such as large grain size, irregular morphology and, in many cases, inhomogeneous composition.

To reduce the particle size, intensive mechanical procedures such as ball milling is required. By high-energy dry-milling approach, it is possible to reduce the grain size. However, an agglomeration state is generated during this process. Particle sizes as small as 4 µm was achieved through wet-milling employing ethanol as a milling medium. Nonetheless, they exhibited dramatically inferior luminescence properties [8]. Willson et al. [9], successfully prepared $SrAl_2O_4:Eu^{2+},Dy^{3+}$ nanoparticles with the size distribution in between 100-500 nm after 7-9 days of milling and size distribution isolation through differentia centrifugation. The luminescence properties of these particles were retained after the milling process. In this study ethyl acetate was employed as the wet medium.

Hsiang et al [10] investigated effect of milling treatment of the $SrCO_3$ precursor on the formation and physical properties of $SrAl_2O_4:Eu^{2+},Dy^{3+}$ phosphor. According to their results, the smaller particle size and hence larger specific surface area of the milled $SrCO_3$, resulted in increasing the contact area between the reactants. Consequently, the average required diffusion distance was reduced, which facilitated and accelerated the reaction. Furthermore, increasing the nucleation sites as a result of finer $SrCO_3$ particles, resulted in smaller particle size of the product. 12 h milling of the $SrCO_3$ resulted in pure-phase SrA_2O_4 at the reaction temperature as low as 950 °C in only 3 h, whereas less than 6h milling led to the formation of undesired $Sr_3Al_2O_6$ phase as well.

Recently, influence of soft mechanochemical pretreatment of precursors on the photoluminescence (PL) and mechanoluminescence (ML) properties of $SrAl_2O_4:Eu^{2+},Dy^{3+}$ phosphor was investigated [11]. The soft mechanochemical pretreatment of the reactant mixture reduced the reaction temperature down to 1200 ° and improved the crystal growth. On the other hand, the untreated mixture had to be calcined at 1400 °C to yield this product. The former sample showed superior PL and ML properties, despite being obtained at a lower temperature. The authors attributed this to creation of more traps inside the crystal structures due to easier diffusion of Eu and Dy ions into the particles.

To obtain a pure-phase product via solid-state method, introduction of a flux agent to the reaction mixture seems inevitable. In many works, application of borates as flux agents has improved the phase-purity of the final product. Luo et al. [12] reported a 200 °C decrease in the synthesis temperature in the presence of using B_2O_3. According to the authors, the flux also enhanced the afterglow properties of the product by facilitating diffusion of Eu^{2+} and Dy^{3+} ions into the grains. In the absence of the flux, precipitation of the dopants in the grain boundaries was observed. Hsiang et al. [13] suggested that formation of intermediate B_2O_4 and $SrAl_2B_2O_7$ compounds facilitated the formation of $SrAl_2O_4$ and led to superior luminescence properties. Nevertheless, introduction of more than 5% B_2O_3 to the reaction mixture resulted in formation of a secondary $Sr_4Al_{14}O_{25}$ phase. Chang et al. [14] investigated effect of B_2O_3 on the phase composition, porosity, density, microstructure, and luminescence properties of the $SrAl_4O_7$ compound. The flux contributed to obtaining a purer phase $SrAl_4O_7$ and enhanced the afterglow properties.

Haranath et al. [15] studied the effect of thermal treatment on the initial brightness and afterglow properties of strontium aluminate phosphor. According to their observation, heating rates higher than 625 $°C\ h^{-1}$, constant heating time of less than 2h, and cooling rates higher than 250 $°C\ h^{-1}$ result in non-uniform luminescent compound. In contrast, heating rates lower than 300 $°C\ h^{-1}$, constant heating times more than 4h at 1200 °C, and cooling rates lower than 100 $°C\ h^{-1}$ produced phosphors with good initial brightness and considerably long afterglow.

Solid state synthesis has been used to obtain other members of the $SrO-Al_2O_3$ family than $SrAl_2O_4$ structure. Takeda et al [16] prepared $Sr_2Al_6O_{11}:Eu^{2+}$ phosphor at 1100-1300 °C in the presence of B_2O_3. Red-emitting $Sr_4Al_{14}O_{25}:Mn^{4+}$ and blue-emitting $Sr_4Al_{14}O_{25}:Eu^{2+}$ [17, 18], $Sr_3Al_2O_6$ [19], and red-orange $SrAl_{12}O_{19}:Sm^{3+}$ [20] are a few other examples prepared by solid state method.

2.2. Combustion method

Combustion method or self-propagating high temperature synthesis, is a spontaneous and highly exothermic reaction between the reactants, which then yields either the desired product or its precursors [21]. The reaction is complete within only a few minutes, during which time huge amount of gasses is released. In order for the combustion to take place, the initial mixture of the reactants needs to be highly dispersed and contain high chemical energy. The commonly used fuels in this method are glycine, citric acid, carbohydrazide, and urea. Varma et al, published an excellent review paper on application of solution combustion method for synthesis of nanoscale material [22].

Similar to solid-state method, combustion method has been broadly utilized for preparation of strontium aluminates. The solution combustion method used for the preparation of $SrAl_2O_4:Eu^{2+},Dy^{3+},Cr^{3+}$ phosphor is illustrated in Figure 1 [23]. In a typical procedure, the metals precursors are dissolved in a solvent or a mixture of solvents along with a fuel. The mixture is heated to obtain a gel, which is then put in a preheated furnace at elevated temperatures. To prepare a well-crystallized product, post-annealing treatment is usually required.

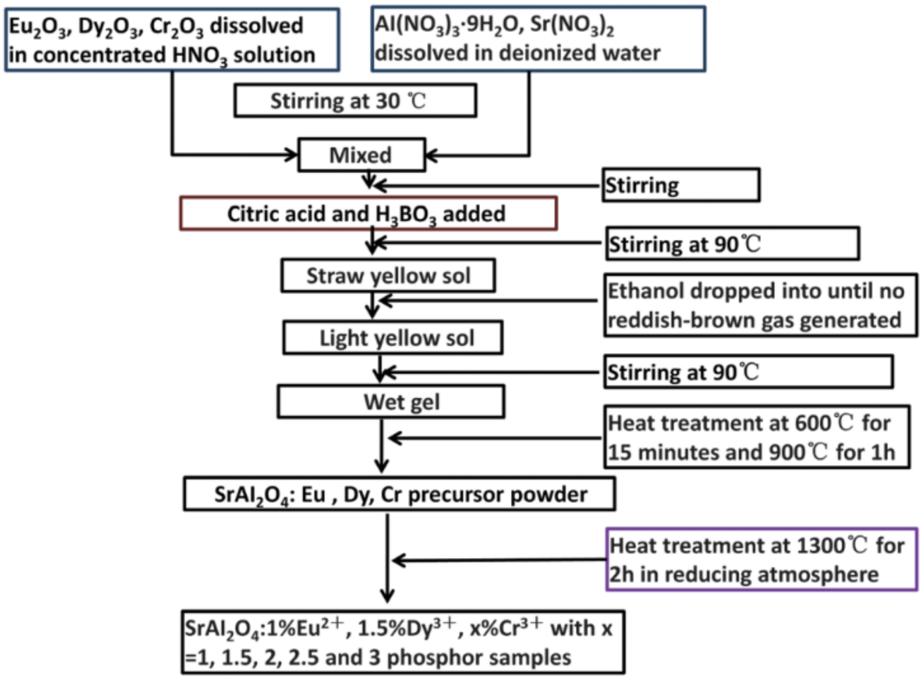

Figure 1. Synthesis process of $SrAl_2O_4:Eu^{2+},Dy^{3+},Cr^{3+}$ samples via a combustion method (Figure reproduced from ref. 23).

Many reports can be found in the literature on the synthesis of Sr-Al-O compounds via combustion method. In 2004, Haranath et al. [24] reported a modified combustion method for preparation of nanocrystalline $SrAl_2O_4:Eu^{2+},Dy^{3+}$ phosphor. They mixed nitrates salts of strontium and aluminum along with urea/camphor and heated the mixture at 400-600 °C in a partially closed quartz/ceramic tube. Before the heating process, deionized water was added to the mixture to obtain a homogeneous paste. The whole reaction was complete within only 5 minutes. In another study, they reported a green chemistry mediated combustion process for preparation of $SrAl_2O_4:Eu^{2+},Dy^{3+}$ phosphor [25]. In this method, the evolution of hazardous N_xO_x gases during the reaction was completely eliminated, by applying an in situ complex formation reaction, leading to the release of non-hazardous gasses. Later in 2006, $Sr_4Al_{14}O_{25}:Eu^{2+},Dy^{3+}$ was prepared via solution combustion method as well [26]. The reaction was carried out at 500 °C, where initially the water evaporated rapidly and the remaining mixture underwent decomposition and spontaneous ignition to produce the precursor material as a white foamy and volumous ash. The ash was then well-milled and annealed at 1300 °C to obtain crystalline $Sr_4Al_{14}O_{25}:Eu^{2+},Dy^{3+}$ product. $SrAl_{12}O_{19}:Eu^{2+}$ was also prepared with this method [27].

Effect of the combustion temperature was studied on the $SrAl_2O_4:Eu^{2+},Dy^{3+},Tb^{3+}$ particles [28]. This study covered temperatures in the range of 400-900 °C for the combustion reaction. According to the authors, crystalline $SrAl_2O_4:Eu^{2+},Dy^{3+},Tb^{3+}$ particles were obtained at a temperature as low as 400 °C. Increasing the reaction temperature improved crystallinity of the particles. A brightness equal to 3.55 cd/m^2 and afterglow duration of 2743 s was obtained with this method.

Effect of annealing temperature was investigated on $Sr_3Al_2O_6:Eu^{2+}$ samples obtained via a combustion method [29]. A series of samples were annealed at temperatures ranging from 900 °C to 1250 °C. A well-crystallized product was obtained at 1200 °C. The emission intensity of this phosphor enhanced by increasing the annealing temperature up to 1200 °, and then decreased for the sample annealed at 1250 °C. Similarly, the red afterglow of this phosphor improved by increasing the annealing temperature from 1050 °C to 1200 °C and lasted for 600 s for the latest sample. Han et al [30], monitored effect of annealing temperature on the morphology of the $SrAl_2O_4:Eu^{2+},Dy^{3+}$ phosphor using transmission electron microscopy. At temperatures below 1150 °C, hollow nanoparticles were formed, while increasing the reaction temperature to 1200 °C resulted in needle/rod-shape nanoparticles.

Lanos et al. [31] compared the effects of single-fuel and mixed-fuels on the product in combustion synthesis. $SrAl_2O_4$ was not acquired directly from the combustion reaction, when employing either urea or glycine as the fuel, due to the release of low amount of energy during the combustion process. The maximum combustion temperatures measured by thermal imaging were 482 °C and 941 °C for urea and glycine batch, respectively. These values were much lower than the calculated adiabatic temperature (1864 °C for urea and 2147 °C for glycine). On the other hand, employing a mixture of urea and glycine as the fuel delivered crystalline $SrAl_2O_4$ directly from the combustion reaction. The maximum temperature measured in the latter reaction was 1559 °C, which is much closer to the calculated adiabatic temperature. According to this study, appropriate choice of fuel can improve the generation of critical concentration of hypergolic gases, which subsequently lead to ignition.

Role of the oxidizing agent was also investigated in the preparation and phase formation of strontium aluminate phosphors via combustion method [32]. Although urea as a fuel plays a crucial role in the combustion synthesis, addition of large amounts can prohibit incorporation of strontium into the structure. However, the results in this work indicated that, adding nitric acid as an oxidizing agent allows introduction of large amounts of urea to the reaction mixture. Stoichiometric addition of urea resulted in a product with major crystalline $SrAl_2O_4$ structure along with $SrCO_3$ and minor quantities of unreacted $Sr(NO_3)_2$. The $SrCO_3$ is formed during the carbon dioxide release in the combustion reaction. The presence of unreacted $Sr(NO_3)_2$ was assigned to insufficient amount of urea in the mixture. Increasing the urea ratio by a factor of 2, resulted in mainly $SrAl_2O_4$ phase with minor $Sr_3Al_2O_6$ as well as $Sr_4Al_{14}O_{25}$, as secondary phases. In this sample, minor amount of $SrCO_3$ was detected as well, but not unreacted

$Sr(NO_3)_2$. 3-fold increasing the quantity of urea inhibited the formation of the strontium aluminate structure.

However, even larger quantities of urea (m = 3, 4, 5) resulted in formation of a well-crystallized $SrAl_2O_4$ compound, when HNO_3 was introduced into the reaction mixture as the oxidizing agent. The crystalline phases obtained at different combustion temperatures in the presence of 3-fold urea (m = 3), where $SrAl_2O_4$ phase was acquire at 600 °C with minor secondary phases. On the right-hand side, it is possible to clearly observe the improvement of the product crystallinity obtained at 600 °C as a function of urea quantity in the presence of HNO_3. Larger amounts of urea improved the brightness of the prepared phosphor, by obviously improving the crystallinity and further facilitating the reduction of Eu^{3+} to Eu^{2+}.

As in the case of solid-state method, many authors have reported positive effect of borates as flux agents in the synthesis of strontium aluminate compound via combustion method. Effect of using H_3BO_3 in the reaction mixture was studied on the crystal phase, morphology, photoluminescence, afterglow, and thermoluminescence properties of $SrAl_2O_4:Eu^{2+},Dy^{3+}$ phosphor [33]. Introduction of 2 mol% of H_3BO_3 in the mixture produced pure-phase $SrAl_2O_4$ phosphor. Morphology of the particles changed dramatically by varying the H_3BO_3 quantity. Initially, irregular morphologies were observed for the samples prepared in the absence of the flux. Addition of 2 mol% of H_3BO_3 resulted in flower-like particles with sharp petals. Thickness of the petals increased by increasing the flux in the mixture, and then employment of higher than 12 % H_3BO_3 resulted in irregular morphologies again. The particle size also kept increasing constantly as a function of the flux concentration. Luminescence intensity of the phosphors constantly increased as a function of the flux concentration, until it reached its maximum at 20 mol %. It then started decreasing at higher concentrations. A similar trend was observed for the afterglow duration, as well as the trap depths of the samples. However, in another study, the optimal concentration of H_3BO_3 for obtaining best photoluminescence and mechanoluminescence properties was reported as 7.5 % [34].

With careful control of the synthesis condition, it is possible to obtain nanoparticles with narrow size distribution via combustion method. An organic fuel can further contribute to the size and/or morphology control. For instance, application of triethanolamine as the fuel in the synthesis of $SrAl_2O_4$ resulted in nanosheet morphology, which then transformed into crystalline semi-curled nanobelts following a post-annealing process [35].

Indeed, combustion method has been accepted and widely used for the synthesis of aluminum-based nanoparticles. In 2003, Peng et al. [36] synthesized $SrAl_2O_4$:Eu,Dy nanoparticles with a size distribution in between 15-45 nm. They used a solution combustion method, where nitrate salts of the metals were dissolved in distilled water together with excess amount of glycine. Then the mixture was reacted at 500 °C, which was complete in only 3 minutes. In the next step, the foamy ash product was well-milled and annealed at 1100 °C to obtain the final nanoparticles. Taxak et al. [37] reported the preparation of $Sr_9Al_6O_{18}:Sm^{3+}$ nanocubes via a low-temperature combustion synthesis. $SrAl_{12}O_{19}$ nanorods have also been reported with this method [38].

In line with the previous efforts, Rojas-Hernandez et al. [39] used a combustion method followed by post dry-grinding to prepare strontium aluminate nanoparticles. The initial powder was obtained by a reaction at 400-600 °C, which was then dry-milled using zirconium dioxide balls of 0.5 mm diameter for 5-25 minutes. The milled powder was subsequently annealed at 900 °C to acquire the final product as nanosheets of submicron width. The nanoparticles obtained with this method showed good optical properties in spite of the photoluminescence degradation resulted from the grinding process. The post-annealing process enhanced the luminescence properties of the particles by improving the crystallinity.

2.3. Sol-gel method

The sol-gel method is a widely used technique for preparation of nanosized particles. It is a well-stablished approach for obtaining high quality nanoparticles including metal oxides. In general, the sol-gel method consists of five steps; hydrolysis, polycondensation, aging, drying, and thermal decomposition (Figure 2). The hydrolysis takes place in either water or an organic solvent like alcohols. This is then followed by condensation of adjacent molecules to form colloidal dispersion. The condensation or polycondensation leads to higher viscosity. During the aging step, polycondensation continues along with the reprecipitation of the gel network, which ultimately increases the thickness between the colloidal particles. Later in the drying process, water or organic solvents are evaporated off the gel structure. In the last step, to obtain the final powder, the remaining volatiles are removed by thermal treatment, which is also referred to as calcination. Generally, post-thermal treatments are necessary for obtaining crystalline structures.

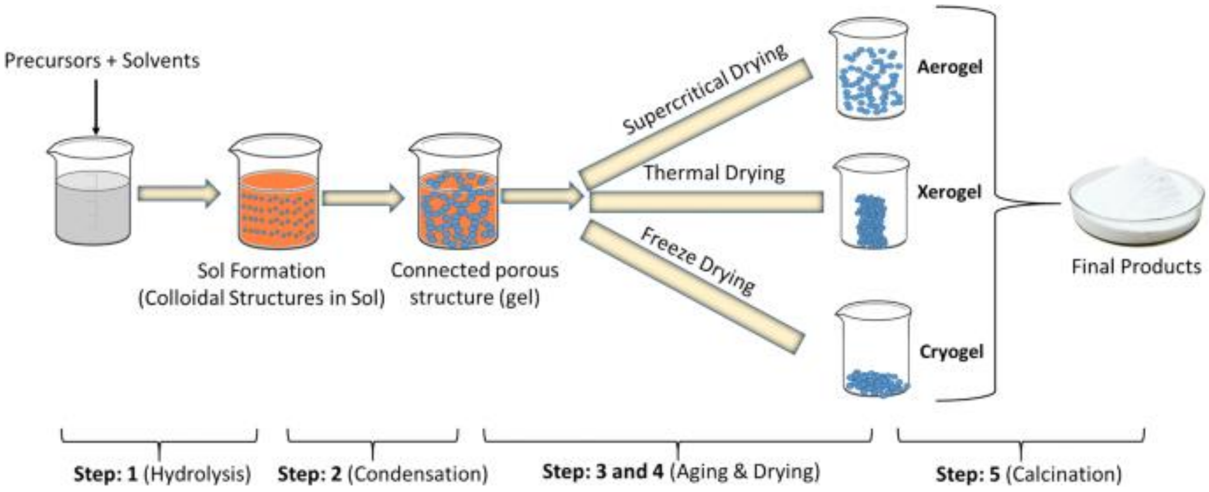

Figure 2. Steps involved in a sol-gel process (Figure reproduced from ref [40].

The precursors used in metal oxide synthesis through sol-gel method generally includes metal salts or alkoxides, citric acid as a chelating ligand, and alcohol as a cross-linking agent. The gel is normally heated at 100 °C for 10-24 h to obtain a dry powder. Then, the powder is annealed at high temperatures to improve the crystallinity of the particles. For strontium aluminates, these temperatures are usually in the range of 1100-1400 °C.

The main disadvantage of the sol-gel method is the large volume of solvent required. Moreover, it has been shown that decreasing the size of the particles comes in expense of decreasing the afterglow intensity and duration. Nevertheless, nanoparticles with the sizes about 60 nm have been obtained at 900 °C, which showed an afterglow duration of 14 h [41].

Liu and Xu published a base-catalyzed sol-gel method for the preparation of europium-doped strontium aluminate particles [42]. They applied ammonia in a water solution of the precursors to drive the hydrolysis, which was followed by Sr(Eu)-O-Al system formation. They monitored the effect of annealing temperature and observed that at 750 °C a mixture of $SrAl_2O_4$ and $Sr_3Al_2O_6$ phases were formed (Figure 3). At 1000 °C $SrAl_2O_4$ was predominant phase and further increase the annealing temperature to 1300 and 1400 °C resulted in a highly crystalline $SrAl_2O_4$ phosphor. Almost a decade before, in 1993, Suib and Kurihara had presented a general sol-gel synthesis method for preparation of ternary metal oxides (MAl_2O_4) including $SrAl_2O_4$ [43].

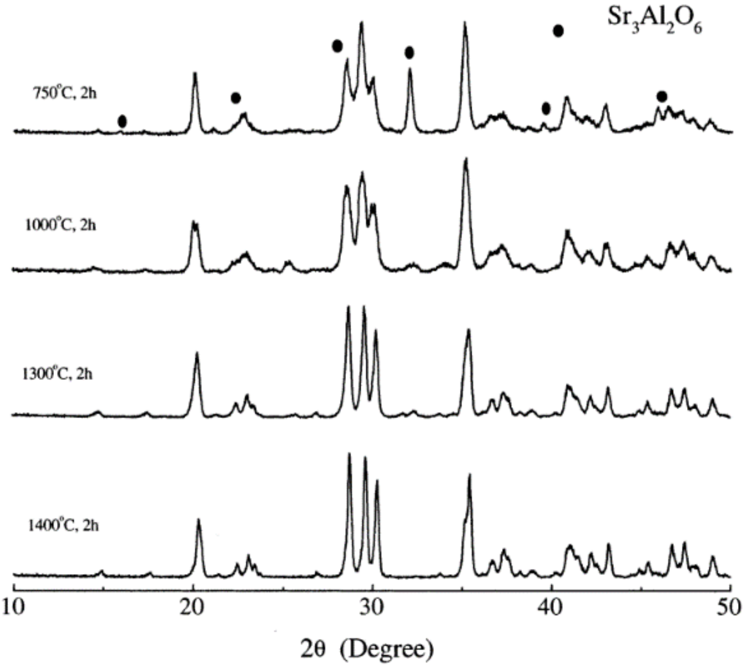

Figure 3. XRD patterns of the Eu-doped strontium aluminate particles calcined at different temperatures (Figure reproduced from ref. [42]).

nanometer sized particles of $SrAl_2O_4:Eu^{2+},Dy^{3+}$ were also prepared by the sol-gel method [41]. The particle size was drastically reduced compared to the ones obtained through the conventional solid-state method. However, brightness of these nanoparticles was considerably lower than that of the of the particles prepared via solid-state method. Moreover, the emission and excitation spectra of the Eu^{2+} doped in these nanoparticles sowed blue shifts peaking at 323 and 500 nm, respectively. The authors attributed this to the high surface energy of the nanoparticles.

Fan et al. [44] reported preparation of highly efficient $SrAl_2O_4:Eu^{2+}$ microsphere phosphors with cage-like morphology via an epoxy-driven sol-gel method. They prepared a water-ethanol-formamide solution of chloride salts of the constituent metals together with polyethylene oxide. After stirring the mixture at 25 °C for 1 h, a transparent solution was obtained. To initiate the condensation, propylene oxide was rapidly introduced into the solution while stirring. In about only two minutes, a cream-like semi-solid was obtained, which was then dried to obtain a smooth powder consisting of micro-sized spheres (Figure 4). Annealing this precursor powder at above 1000 °C in a reductive atmosphere resulted in cage-like $SrAl_2O_4:Eu^{2+}$ microspheres. These microspheres consisted of numerous tiny $SrAl_2O_4$ singe crystals and they showed an excellent quantum yield of 94.94%. The authors explained that the unique cage-like structure of the particles supposedly let the excitation light inside and facilitated excitation of the Eu^{2+} ions inside the spheres. This in turn enhanced the luminescence intensity.

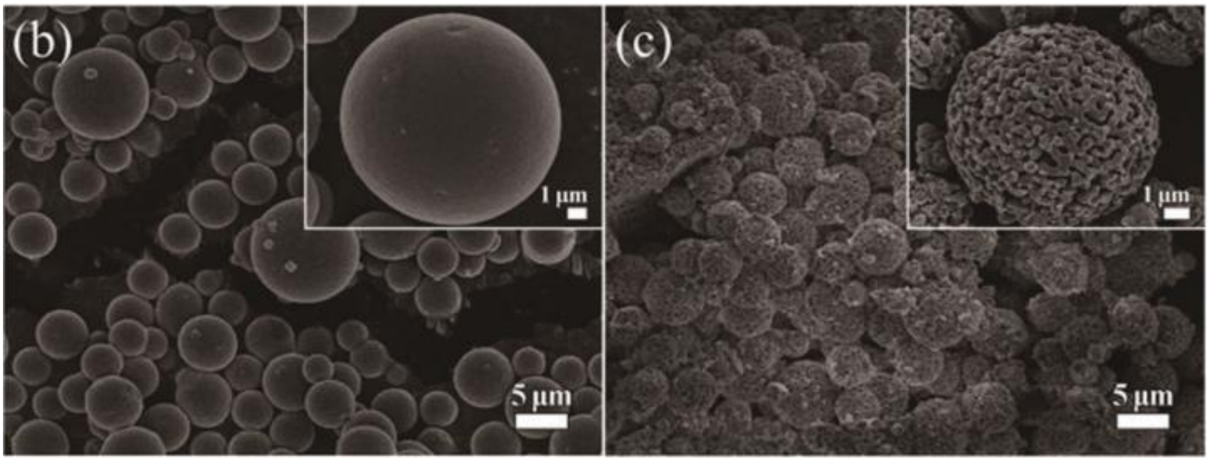

Figure 4. SEM images of b) as-dried precursor microspheres and c) $SrAl_2O_4:Eu^{2+}$cage-like microspheres annealed at 1200 °C for 2 h (Figure reproduced from ref. [44].

Misevicius et al [45] prepared $Sr_4Al_{14}O_{25}:Ce^{3+}$ particles via the sol-gel method followed by a post-annealing step at 1300 °C. The particles agglomerated during the annealing process. Interestingly, when boric acid was used as flux in the reaction mixture, hexagonal plates with well-defined edges were obtained (Figure 5).

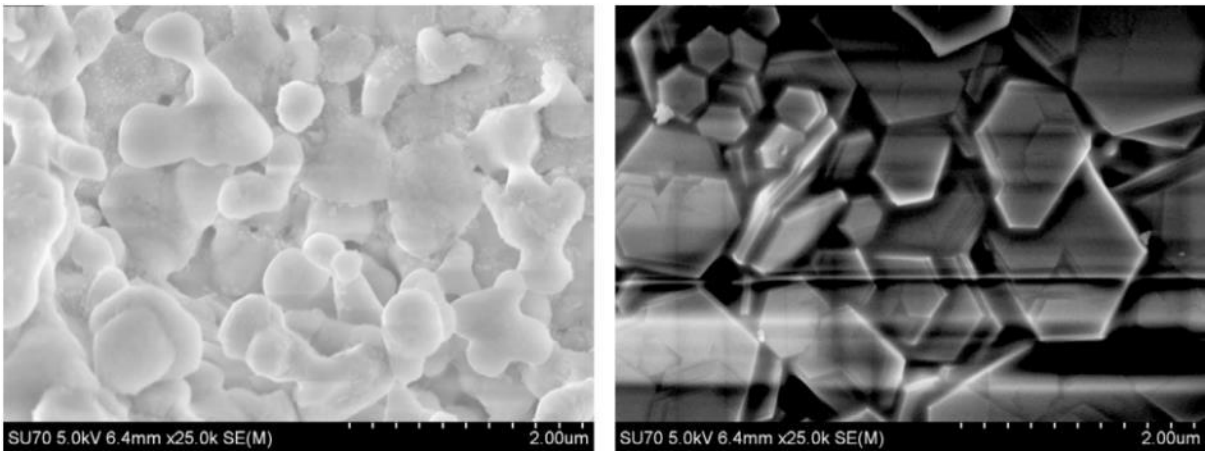

Figure 5. $Sr_4Al_{14}O_{25}:Ce^{3+}$ particles annealed in the absence (left-hand side) and presence of (right-hand side) of boric acid (Figure reproduced from ref. 45).

Similar to the solid-state and combustion methods, employment of borates improved the luminescence and afterglow properties of the strontium aluminate phosphors prepared by the sol-gel method [46]. Ow-Yang et al [47] investigated the effects of boron on the microstructure and luminescence of $Sr_4Al_{14}O_{25}:Eu^{2+},Dy^{3+}$ through nanoscale-resolved cathodoluminescence mapping technique. They applied the same sol-gel method for preparation of the precursor material in the presence and absence of B_2O_3 in the reaction mixture. Pure-phase $Sr_4Al_{14}O_{25}$ was obtained when B_2O_3 was employed, whereas the reaction mixture without B_2O_3 resulted in a polycrystalline product. The authors showed that, boron facilitates evolution of the equilibrium crystalline structure and enhances homogeneous distribution of Eu^{2+} into both Sr sites. As a result, the afterglow of the boron-doped phosphor lasted for over 14 h, which is remarkably longer than that of the boron-free phosphor (about 10 minutes). The short afterglow for the latter phosphor was attributed to the concentration quenching. The fact that Eu^{3+} was found uniformly distributed throughout the structure indicates dependence of the Eu^{2+} to the local coordination of the Sr site.

2.4. Hydro(solvo)thermal

Hydrothermal synthesis is defined as a method to prepare inorganic materials in aqueous solutions above ambient pressure and temperature [48, 49]. Solvothermal term is applied for the reactions performed in organic solvents. Usually, the reaction is carried out in sealed reaction vessels defined as autoclaves. Heating the reaction mixture at temperatures above the boiling point of the employed solvent increases the pressure inside the reactor, dramatically. Due to the synergistic effect of high temperature and pressure, highly crystalline materials can be produced without the need for post-annealing treatments. In addition to obtaining homogeneous composition, utilization of organic additives and/or surfactants can offer control over the size and morphology of the particles.

This method has been broadly used for preparation of a wide range of materials including metal oxides. However, application if this method for mass production is not very convenient due to the need for expensive and sophisticated reaction vessels as well as safety issues. Moreover, observing and analysis of the reaction process is not possible in this method.

A series of hydrothermal and solvothermal reactions were carried out to prepare strontium aluminates particles with four different morphologies [50]. Changing the reaction conditions influenced the morphology of the particles, dramatically. In a typical procedure, $Sr(NO_3)_2$ and $AlCl_3$ were dissolved in a solvent (H_2O or glycol) along with CTAB. $Eu(NO_3)_3$ prepared in HNO_3 was then added to the mixture. When NaOH was added into the mixture prepared in H_2O, needle cluster-like particles formed.

1-D nanowire precursor particles of $Sr_3Al_2O_6$ were synthesized starting from the nitrate salts of strontium and aluminum in the presence of different quantities of $CO(NH_2)_2$ [51]. Addition of sodium citrate to the reaction mixture resulted in quasi-sphere precursor particles. The reaction was carried out in H_2O at 120 °C for 12 h, during which time the precursor particles consisting crystalline $SrCO_3$ and $NH_4Al(OH)_2CO_3$ were formed. Annealing these precursor particles at 1000 °C resulted in formation of the crystalline $Sr_3Al_2O_6$ phase along with residual crystalline $SrCO_3$ and some unidentified components in the compound. Little amount of $SrCO_3$ was left in the structure upon increasing the temperature to 1100 °C. At 1200 °C in pure-phase $Sr_3Al_2O_6$ was obtained.

Ye, et al [52] used a hydrothermal method followed by post-annealing to prepare crystalline $SrAl_2O_4$ nanotubes. A mixed solution of cetyltrimethylammonium bromide (CTAB)/n-butanol/water was used as the reaction medium. Urea was used to adjust the pH of the medium gradually upon hydrolysis at 120 °C. After 16 h at this temperature, amorphous whisker-like morphology was obtained. Well-crystallized $SrAl_2O_4$ nanotubes were obtained after annealing these amorphous tubes at 1300 °C for 4 h.

In 2009, Pinna et al [53] could successfully synthesize $SrAl_4O_7$ along with $CaAl_4O_7$ and $BaAl_4O_7$ compound via a one-pot solvothermal reaction. According to the authors, these crystalline structures could be prepared at 275 °C, which is remarkably lower than the temperature required for conventional solid-state method or post annealing step in the sol-gel method.

2.5. Co-precipitation

In coprecipitation method, normally precursor materials such as metals chlorides, nitrates, and acetates are dissolved in a solvent. The mixture is kept stirring and then a precipitating agent is added slowly, which causes the precipitation of the desired compound to take place. After evaporating the solvent off the product, usually a mild calcination step is required for the final products to form. Like in the case of the sol-gel method, for obtaining crystalline structures, post-annealing treatments are necessary.

Co-precipitation is an excellent method for nanoparticles owing to the homogeneous mixing of the precursors in the molecular level, which can lead to a homogeneous product. Furthermore, it offers good control over the particle morphology. It’s simplicity as well as in addition to the great potential for scale up production has added to the popularity of this method.

Precipitation of the constituents to obtain the precursor $SrO\text{-}Al_2O_3$ normally takes place by adjusting the pH value of the solution to basic values. NH_4OH, $(NH_4)_2CO_3$, and $CO(NH_2)_2$ are the commonly used bases for this purpose. Using $CO(NH_2)_2$ can in principle provide more control over the synthesis as it gradually hydrolyses to yield NH_3 and CO, which later lead to the precipitation of $AlOOH/Al(OH)_3$ and $SrCO_3$, respectively. Figure 6 shows the hydrolysis process for $CO(NH_2)_2$. This process require heat and normally is used in coupled coprecipitation-hydrothermal reactions [54].

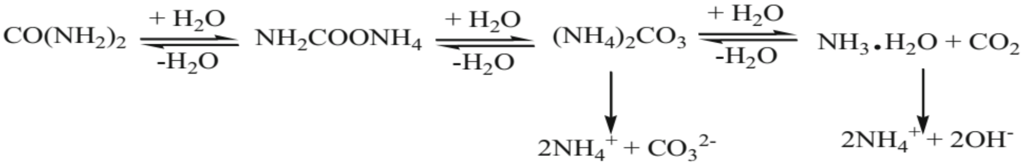

Figure 6. Schematic illustration of the hydrolysis of $CO(NH_2)_2$ (Figure reproduced from ref. [54]).

Co-precipitation method was used to prepare the precursor micro-donats of $SrAl_2O_4{:}Eu^{2+},Dy^{3+}$ [55]. In this work, acetate salts of aluminum, strontium, europium, and dysprosium were dissolved in ethylene glycol along with $CO(NH_2)_2$ and polyvinyl pyrrolidone (PVP). The authors described the formation of micro-donats as a result of AlOOH and $SrCO_3$ precipitation onto the PVP micelles formed in the solution. The powder XRD analysis showed that these precursor particles contained crystalline phases of both $SrCO_3$ and AlOOH. Annealing at temperature above 1050 °C resulted in formation of crystalline $SrAl_2O_4$.

The precursor particles of red-emitting $SrAl_2O_4{:}Mn^{4+}$ phosphor was obtained [56] by introducing NH_4OH to a solution containing the nitrate salts of Sr^{2+}, Al^{3+}, and Mn^{2+}. Increasing the pH of the solution resulted in precipitating these metal salts in their hydroxide forms. The pure-phase product was obtained after a post annealing process at 1200 °C. Cheng et al [57] reported a co-precipitation method for the synthesis of $SrAl_2O_4{:}Eu^{2+},Dy^{3+}$ Long persistent phosphor nanotubes (Figure 7). They combined a homogeneous coprecipitation of $SrCO_3$ and γ-AlOOH with soft-template assembly to prepare the precursor material.

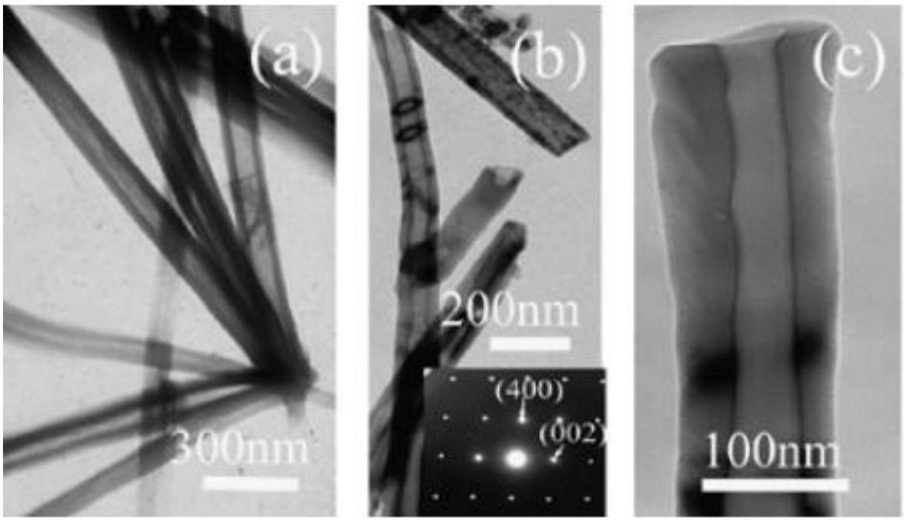

Figure 7. Bright-field TEM images of the nanotubes: a) as synthesized from solution; b) and c) calcined at 1300 °C (figure reproduced from ref. [57].

2.6. Microwave-assisted

The microwave -assisted synthesis has attracted a lot of attention in nanomaterial synthesis [58-60]. Microwave generators for the synthesis purposes have continuously been the subject of technological improvement for the last three decades. Today, the microwave ovens used for the synthesis purposes are equipped with the in situ measurement of pressure and temperature with IR sensors, which can offer more control on the synthesis procedure and quality of the nanoparticles over the conventional heating. Rapid and homogenous heating can in principle lead to remarkably fast reaction time and homogenous morphology and size distribution of the nanoparticles. Solvents with high dielectric constants absorb the microwave radiation and generate heat through dipole-dipole interactions with the alternating electric field. Conventional heating can have an uneven impact of the nucleation and growth of the nanoparticles due to creating a thermal gradient, which can in turn result in big size distribution, different morphologies and poor quality. On the other hand, microwave heating induces uniform heating in the entire solution, which can in principle lead to uniform nucleation and growth kinetics. Nevertheless, application of microwaves is not limited to the wet synthesis. Grefory et al [61] have published a thorough review on the modern microwave methods in solid-state chemistry, where they describe in detail both fundamentals and application of the microwaves in the manufacturing processes.

Wu et al [62] employed a microwave-assisted sol-gel method to prepare $SrAl_2O_4:Eu^{2+}$ phosphor. Both preparation of the precursor material and calcining process took place in a microwave oven. They studied the effects of microwave-calcining temperature as well as the heating and cooling rates on the crystal structure and optical properties of the phosphor. A crystalline structure was obtained at a temperature as low as 750 °C for only 30 minutes. Progressive increase of the annealing temperature from 750 °C to 900 °C indicated improvement in the crystalline structure. At 900 °C, only 15 minutes was sufficient to obtain a crystalline phosphor. Over 20 h afterglow was reported for the sample annealed at 900 °C. According to the authors, this was comparable to the samples prepared through solid-state method at around 1400 °C. Further increase of the temperature over 950 °C adversely influenced the crystal structure and luminescence properties of the phosphor. In another work

[63] the crystallization process was reported to complete in only 10-20 min. With the conventional heating for the precursors prepared by the same sol-gel method this process was reported as 2h at 1200 °C [118]. Table 3 in the appended book chapter (Section) presents some examples of the different method used for the synthesis of strontium aluminates.

References

[1] J.N. Lalena, D.A. Cleary, E.E. Carpenter, N.F. Dean, Inorganic materials synthesis and fabrication, Wiley Online Library, 2008.

[2] U. Schubert, N. Hüsing, Synthesis of inorganic materials, John Wiley & Sons, 2019.

[3] C.N.R. Rao, K. Biswas, Essentials of inorganic materials synthesis, Wiley Online Library, 2015.

[4] A. Nikam, B. Prasad, A. Kulkarni, Wet chemical synthesis of metal oxide nanoparticles: a review, CrystEngComm, 20 (2018) 5091-5107.

[5] J.A. Darr, J. Zhang, N.M. Makwana, X. Weng, Continuous hydrothermal synthesis of inorganic nanoparticles: applications and future directions, Chem. Rev., 117 (2017) 11125-11238.

[6] C. Rao, Chemical synthesis of solid inorganic materials, Mater. Sci. Engin.: B, 18 (1993) 1-21.

[7] A. Buekenhoudt, A. Kovalevsky, J. Luyten, F. Snijkers, L. Giorno, 1.11 Basic Aspects in Inorganic Membrane Preparation, in-Chief: Enrico, G. Lidietta (Eds.), Comprehensive Membrane Science and Engineering, Elsevier, Oxford, (2010) 217-252.

[8] R. Rojas-Hernandez, F. Rubio-Marcos, E. Enríquez, M. De La Rubia, J. Fernandez, A low-energy milling approach to reduce particle size maintains the luminescence of strontium aluminates, RSC Adv., 5 (2015) 42559-42567.

[9] A.S. Paterson, B. Raja, G. Garvey, A. Kolhatkar, A.E. Hagström, K. Kourentzi, T.R. Lee, R.C. Willson, Persistent luminescence strontium aluminate nanoparticles as reporters in lateral flow assays, Analyt. chem., 86 (2014) 9481-9488.

[10] Y.-L. Chang, H.-I. Hsiang, M.-T. Liang, Characterization of strontium aluminate phosphors prepared from milled $SrCO_3$, Ceramics international, 35 (2009) 1027-1032.

[11] H. Lv, Z. Pan, Y. Wang, Synthesis and mechanoluminescent property of (Eu^{2+}, Dy^{3+})-co-doped strontium aluminate phosphor by soft mechanochemistry-assisted solid-state method, J. Lumin., 209 (2019) 129-140.

[12] X. Luo, W. Cao, Z. Xiao, Investigation on the distribution of rare earth ions in strontium aluminate phosphors, J. Alloys Compd., 416 (2006) 250-255.

[13] Y.-L. Chang, H.-I. Hsiang, M.-T. Liang, Characterizations of Eu, Dy co-doped SrAl2O4 phosphors prepared by the solid-state reaction with B_2O_3 addition, J. Alloys Compd., 461 (2008) 598-603.

[14] C. Chang, D. Mao, J. Shen, C. Feng, Preparation of long persistent $SrO{\cdot}2A_{l2}O_3$ ceramics and their luminescent properties, J. Alloys Compd., 348 (2003) 224-230.

[15] D. Haranath, V. Shanker, H. Chander, P. Sharma, Studies on the decay characteristics of strontium aluminate phosphor on thermal treatment, Mater. Chem. Phys., 78 (2003) 6-10.

[16] T. Takeda, K. Takahashi, K. Uheda, H. Takizawa, T. Endo, Crystal structure and luminescence properties of $Sr_2Al_6O_{11}:Eu^{2+}$, Journal of the Japan Society of Powder and Powder Metallurgy, 49 (2002) 1128-1133.

[17] M. Peng, X. Yin, P.A. Tanner, C. Liang, P. Li, Q. Zhang, J. Qiu, Orderly-Layered Tetravalent Manganese-Doped Strontium Aluminate $Sr_4Al_{14}O_{25}:Mn^{4+}$: An Efficient Red Phosphor for Warm White Light Emitting Diodes, J. Am. Ceram. Soc., 96 (2013) 2870-2876.

[18] W. Minquan, D. Wang, L. Guanglie, Research on fluorescence spectra and structure of single-phase $4SrO·7Al_2O_3$:Eu^{2+} phosphor prepared by solid-state reaction method, Mater. Sci. Eng.: B, 57 (1998) 18-23.

[19] C. Chang, W. Li, X. Huang, Z. Wang, X. Chen, X. Qian, R. Guo, Y. Ding, D. Mao, Photoluminescence and afterglow behavior of Eu^{2+}, Dy^{3+} and Eu^{3+}, Dy^{3+} in $Sr_3Al_2O_6$ matrix, J. Lumin., 130 (2010) 347-350.

[20] J. Liu, Q. Song, D. Li, X. Xu, J. Xu, Growth and red-orange emission of Sm^{3+} doped $SrAl_{12}O_{19}$ single crystals, Opt. Materi., 101 (2020) 109754.

[21] A. Varma, J.-P. Lebrat, Combustion synthesis of advanced materials, Chem. Engin. Sci., 47 (1992) 2179-2194.

[22] A. Varma, A.S. Mukasyan, A.S. Rogachev, K.V. Manukyan, Solution combustion synthesis of nanoscale materials, Chem. Rev., 116 (2016) 14493-14586.

[23] Y. Teng, J. Zhou, S.N. Khisro, S. Zhou, J. Qiu, Persistent luminescence of $SrAl_2O_4$:Eu^{2+}, Dy^{3+},Cr^{3+} phosphors in the tissue transparency window, Mater. Chem. Phys., 147 (2014) 772-776.

[24] H. Chander, D. Haranath, V. Shanker, P. Sharma, Synthesis of nanocrystals of long persisting phosphor by modified combustion technique, Journal of crystal growth, 271 (2004) 307-312.

[25] P. Sharma, D. Haranath, H. Chander, S. Singh, Green chemistry-mediated synthesis of nanostructures of afterglow phosphor, Appl. Surf. Sci., 254 (2008) 4052-4055.

[26] C. Zhao, D. Chen, Y. Yuan, M. Wu, Synthesis of $Sr_4Al_{14}O_{25}$:Eu^{2+},Dy^{3+} phosphor nanometer powders by combustion processes and its optical properties, Mater. Sci. Eng.: B, 133 (2006) 200-204.

[27] V. Singh, T.G. Rao, J.-J. Zhu, Preparation, luminescence and defect studies of Eu^{2+}-activated strontium hexa-aluminate phosphor prepared via combustion method, J. Solid State Chem., 179 (2006) 2589-2594.

[28] H. Song, D. Chen, Combustion synthesis and luminescence properties of $SrAl_2O_4$:Eu^{2+},Dy^{3+},Tb^{3+} phosphor, Luminescence: The journal of biological and chemical luminescence, 22 (2007) 554-558.

[29] P. Huang, C.-e. Cui, S. Wang, Influence of calcination temperature on luminescent properties of $Sr_3Al_2O_6$:Eu^{2+},Dy^{3+} phosphors prepared by sol–gel-combustion processing, Opt. Mater., 32 (2009) 184-189.

[30] R. Zhang, G. Han, L. Zhang, B. Yang, Gel combustion synthesis and luminescence properties of nanoparticles of monoclinic $SrAl_2O_4$:Eu^{2+},Dy^{3+}, Mater. Chem. Phys., 113 (2009) 255-259.

[31] R. Ianoş, R. Istratie, C. Păcurariu, R. Lazău, Solution combustion synthesis of strontium aluminate, $SrAl_2O_4$, powders: single-fuel versus fuel-mixture approach, Phys. Chem. Chem. Phys., 18 (2016) 1150-1157.

[32] R. Rojas-Hernandez, M. Rodriguez, J. Fernandez, Role of the oxidizing agent to complete the synthesis of strontium aluminate based phosphors by the combustion method, RSC Adv., 5 (2015) 3104-3112.

[33] W. Xie, C. Zou, M. Xie, Effect of H_3BO_3 on phases, micromorphology and persistent luminescence properties of $SrAl_2O_4$:Eu^{2+},Dy^{3+} phosphors, J. Mater. Sci.: Mater Electron., 28 (2017) 6328-6334.

[34] R. Sharma, U. Sharma, Influence of fluxing agent on the luminescence properties of $SrAl_2O_4$:Eu^{2+} nanophosphors, J. Alloys Compd., 649 (2015) 440-446.

[35] B. Cheng, Z. Zhang, Z. Han, Y. Xiao, S. Lei, SrAl2O4: Eu2+, Dy3+ nanobelts: synthesis by combustion and properties of long-persistent phosphorescence, J. Mater. Res., 26 (2011) 2311.

[36] T. Peng, H. Yang, X. Pu, B. Hu, Z. Jiang, C. Yan, Combustion synthesis and photoluminescence of $SrAl_2O_4$:Eu,Dy phosphor nanoparticles, Mater. Lett., 58 (2004) 352-356.

[37] P. Sehrawat, P. Boora, R. Malik, S. Khatkar, V. Taxak, Achieving orange red emission with high color purity from novel perovskite based $Sr_9Al_6O_{18}:Sm^{3+}$ nano-cubes for advanced optoelectronic applications, Ceramics International, 47 (2021) 5432-5445.

[38] R. Zhong, J. Zhang, X. Zhang, S. Lu, X.-j. Wang, Efficient energy transfer and photoluminescent characteristics in $SrAl_{12}O_{19}:Eu^{2+},Cr^{3+}$ nano-rods, Nanotech., 18 (2007) 445707.

[39] R.E. Rojas-Hernandez, M.A. Rodriguez, F. Rubio-Marcos, A. Serrano, J.F. Fernandez, Designing nanostructured strontium aluminate particles with high luminescence properties, J. Mater. Chem. C, 3 (2015) 1268-1276.

[40] M. Parashar, V.K. Shukla, R. Singh, Metal oxides nanoparticles via sol–gel method: A review on synthesis, characterization and applications, Journal of Materials Science: Materials in Electronics, 31 (2020) 3729-3749.

[41] Z. Tang, F. Zhang, Z. Zhang, C. Huang, Y. Lin, Luminescent properties of $SrAl_2O_4$:Eu,Dy material prepared by the gel method, J. Eur. Ceram. Soc., 20 (2000) 2129-2132.

[42] Y. Liu, C.-N. Xu, Influence of calcining temperature on photoluminescence and triboluminescence of europium-doped strontium aluminate particles prepared by sol− gel process, J. Phys. Chem. B, 107 (2003) 3991-3995.

[43] L.K. Kurihara, S.L. Suib, Sol-gel synthesis of ternary metal oxides. 1. Synthesis and characterization of MAl_2O_4 (M= Mg, Ni, Co, Cu, Fe, Zn, Mn, Cd, Ca, Hg, Sr, and Ba) and lead aluminum oxide ($Pb_2Al_2O_5$), Chem. Mater., 5 (1993) 609-613.

[44] J. Wan, Y. Zhang, Y. Wang, R. Ma, Y. Wu, X. Qiao, X. Fan, Facile synthesis of monodisperse $SrAl_2O_4:Eu^{2+}$ cage-like microspheres with an excellent luminescence quantum yield, J. Mater. Chem. C, 6 (2018) 3346-3351.

[45] M. Misevicius, M. Kilmanas, S. Culunlu, S. Sakirzanovas, A.U. Morkan, A. Beganskiene, A. Kareiva, On the sol–gel fabrication and characterization of undoped and cerium-doped $Sr_4Al_{14}O_{25}$, J. Alloys Compd., 614 (2014) 44-48.

[46] I.-C. Chen, T.-M. Chen, Sol-gel synthesis and the effect of boron addition on the phosphorescent properties of $SrAl_2O_4:Eu^{2+},Dy^{3+}$ phosphors, J. Mater. Res., 16 (2001) 644-651.

[47] G. Inan Akmehmet, S. Šturm, L. Bocher, M. Kociak, B. Ambrožič, C.W. Ow-Yang, Structure and luminescence in long persistence Eu, Dy, and B codoped strontium aluminate phosphors: the boron effect, J. Am. Ceram. Soc., 99 (2016) 2175-2180.

[48] W.L. Suchanek, R.E. Riman, Hydrothermal synthesis of advanced ceramic powders, in: Advances in Science and Technology, Trans Tech Publ, 2006, pp. 184-193.

[49] S.-H. Feng, G.-H. Li, Hydrothermal and solvothermal syntheses, in: Modern inorganic synthetic chemistry, Elsevier, 2017, pp. 73-104.

[50] D. Si, B. Geng, S. Wang, One-step synthesis and morphology evolution of luminescent Eu2+ doped strontium aluminate nanostructures, CrystEngComm, 12 (2010) 2722-2727.

[51] X.Y. Chen, S.P. Bao, Y.C. Wu, Controlled synthesis and luminescent properties of Eu^{2+} (Eu^{3+}), Dy^{3+}-doped $Sr_3Al_2O_6$ phosphors by hydrothermal treatment and postannealing approach, J. Solid State Chem., 183 (2010) 2004-2011.

[52] C. Ye, Y. Bando, G. Shen, D. Golberg, Formation of crystalline $SrAl_2O_4$ nanotubes by a roll-up and post-annealing approach, Angew. Chem., 118 (2006) 5044-5048.

[53] M. Karmaoui, M.-G. Willinger, L. Mafra, T. Herntrich, N. Pinna, A general nonaqueous route to crystalline alkaline earth aluminate nanostructures, Nanoscale, 1 (2009) 360-365.

[54] X. Liyuan, X. Qin, L. Yingliang, Preparation and characterization of flower-like $SrAl_2O_4:Eu^{2+},Dy^{3+}$ phosphors by sol-gel process, J. Rare Earths, 29 (2011) 39-43.

[55] X. Zhiping, D. Suqing, L. Yingliang, L. Bingfu, X. Yong, M. ZHENG, Synthesis and luminescence properties of $SrAl_2O_4:Eu^{2+},Dy^{3+}$ hollow microspheres via a solvothermal co-precipitation method, J. Rare Earths, 31 (2013) 241-246.
[56] N. Chi, N. Tuan, N. Lien, D. Nguyen, Red emission of $SrAl_2O_4:Mn^{4+}$ phosphor for warm white light-emitting diodes, J. Electron. Mater., 47 (2018) 4571-4578.
[57] B. Cheng, H. Liu, M. Fang, Y. Xiao, S. Lei, L. Zhang, Long-persistent phosphorescent $SrAl_2O_4:Eu^{2+},Dy^{3+}$ nanotubes, Chem. Commun., (2009) 944-946.
[58] I. Bilecka, M. Niederberger, Microwave chemistry for inorganic nanomaterials synthesis, Nanoscale, 2 (2010) 1358-1374.
[59] M. Baghbanzadeh, L. Carbone, P.D. Cozzoli, C.O. Kappe, Microwave-assisted synthesis of colloidal inorganic nanocrystals, Angewandte Chemie International Edition, 50 (2011) 11312-11359.
[60] Y.-J. Zhu, F. Chen, Microwave-assisted preparation of inorganic nanostructures in liquid phase, Chemical reviews, 114 (2014) 6462-6555.
[61] H.J. Kitchen, S.R. Vallance, J.L. Kennedy, N. Tapia-Ruiz, L. Carassiti, A. Harrison, A.G. Whittaker, T.D. Drysdale, S.W. Kingman, D.H. Gregory, Modern microwave methods in solid-state inorganic materials chemistry: from fundamentals to manufacturing, Chemical reviews, 114 (2014) 1170-1206.
[62] S. Wu, S. Zhang, J. Yang, Influence of microwave process on photoluminescence of europium-doped strontium aluminate phosphor prepared by a novel sol–gel-microwave process, Mater. Chem. Phys., 102 (2007) 80-85.
[63] Y. Tian, P. Zhang, Z. Zheng, Y. Chai, A novel approach for preparation of $Sr_3Al_2O_6:Eu^{2+},Dy^{3+}$ nanoparticles by sol–gel–microwave processing, Mater. Lett., 73 (2012) 157-160.

Luminescence of europium

As discussed above, strontium aluminates can be doped with rare-earth and transition metal-ions as luminescent activators 1. While transition metal ions such as Cr^{3+} and Mn^{4+} substitute for Al^{3+} in the crystal lattice due to their similar ionic radiuses, RE ions in both divalent and trivalent states replace the Sr^{2+}. Europium has been widely studied in these structures in both divalent and trivalent forms.

3.1. Trivalent europium

Trivalent europium is well-known for its intense red photoluminescence with characteristic sharp and narrow transitions in a wide variety of materials, such as crystalline inorganic hosts [2-5], glasses [6, 7], polymers [8], liquid crystals [9], metal-organic frameworks (MOFs) [10-13], functionalized materials [14], Eu(III) complexes [15], and etc. $Y_2O_3:Eu^{3+}$ is an important material used in fluorescent lamps [16]. $Y_2O_2S:Eu^{3+}$ was used in old-fashion color television and computer screens [17]. EURO banknotes take advantage of europium in their anti-counterfeiting ink [18]. Eu^{3+} provides a great spectroscopic tool to probe its local geometry, in particular, in glasses and crystals. Indeed, it is possible to determine the local symmetry of Eu^{3+} by analyzing its luminescence spectrum.

Trivalent europium has 60 electrons, including 6 electrons in the 4f shell, which are well-screened from their environments by $5s^2$ and $5p^6$ outer shells. The 6 electrons in the 4f shell can be arranged in 3003 (total degeneracy of Eu^{3+}) different ways into the 7 orbitals in this shell according to the following binominal coefficient:

$$\binom{14}{n} = \frac{14!}{n!(14-n)!} \tag{1}$$

where, n is the number of electrons in the 4f shell. As shown in Figure 1, internal perturbations (electron repulsion, spin-orbit coupling, and crystal-field effect) can lift the degeneracy of the $4f^6$ configuration. Electron repulsion results from the electrostatic interaction of electrons in the same shell. The spin-orbit coupling is referred to the interaction between the spin magnetic momentum of the electron and the magnetic field generated by the movement of the electron around the nucleus. This usually causes a splitting of $\approx 1000\ cm^{-1}$. The crystal field (CF) effect originates from the interaction of the electrons of the ligands with the electrons in the 4f shell of Eu^{3+}. The splitting caused by the CF effect is normally about a few hundred cm^{-1} or less. In low symmetry structures, all degeneracy is lifted by the CF.

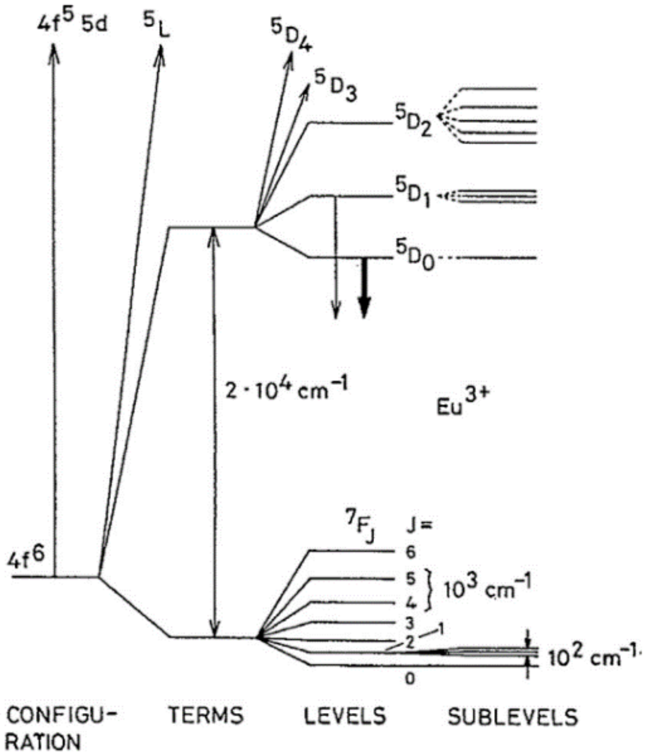

Figure 1. Energy diagram of Eu^{3+} ($4f^6$) (figure reproduced from ref. [19].

Eu^{3+} compounds emit strong photoluminescence as a result of intra-configurational f-f transitions between the $^5D_0$ excited state and the ^7F_J (J=0-6) ground state (Table). There are only few examples, where mission from the higher excited states of Eu^{3+} ($^5D_{1-3}$) have been observed [20]. As shown in Table x, all the $^5D_0 \rightarrow {}^7F_J$ transitions are of electric dipole (ED) nature, except for the magnetic dipole (MD) $^5D_0 \rightarrow {}^7F_1$ transition. Intra-configurational ED transitions like f-f transitions are forbidden by the Laporte selection rule. However, this rule relaxes for Eu^{3+} ion embedded in a medium (non-gas phase) due to vibronic coupling and/or admixture of higher configurations into the 4f wavefunction as a result of CF effect. Since these transitions are normally much weaker than the allowed ED transitions, they are called "induced" ED transitions. Intra-configurational MD transitions are allowed within by the Laporte selection rule. Nevertheless, in general, they are weak and their intensities are comparable to the induced ED transitions [21].

Table , Overview of the transitions observed in luminescence spectra of Eu^{3+} (Reproduced from ref. [19]).

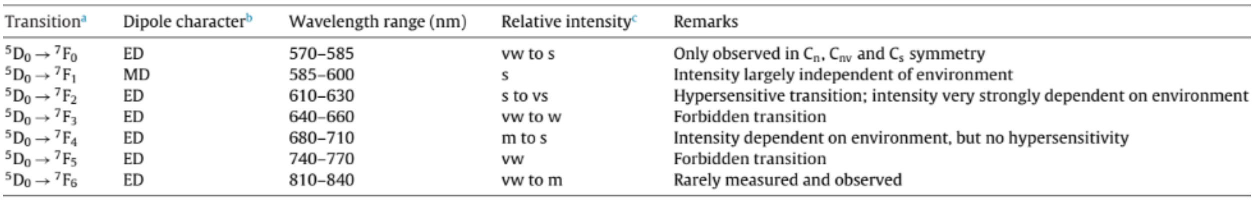

Transition[a]	Dipole character[b]	Wavelength range (nm)	Relative intensity[c]	Remarks
$^5D_0 \rightarrow {}^7F_0$	ED	570–585	vw to s	Only observed in C_n, C_{nv} and C_s symmetry
$^5D_0 \rightarrow {}^7F_1$	MD	585–600	s	Intensity largely independent of environment
$^5D_0 \rightarrow {}^7F_2$	ED	610–630	s to vs	Hypersensitive transition; intensity very strongly dependent on environment
$^5D_0 \rightarrow {}^7F_3$	ED	640–660	vw to w	Forbidden transition
$^5D_0 \rightarrow {}^7F_4$	ED	680–710	m to s	Intensity dependent on environment, but no hypersensitivity
$^5D_0 \rightarrow {}^7F_5$	ED	740–770	vw	Forbidden transition
$^5D_0 \rightarrow {}^7F_6$	ED	810–840	vw to m	Rarely measured and observed

Transition between the $^5D_0$ and $^7F_0$ states is strictly forbidden within the framework of Judd-Ofelt theory. According to the ΔJ selection rule, a 0-0 transition is forbidden. However, the

$^5D_0 \rightarrow {}^7F_0$ transition can be observed for the compounds, where Eu^{3+} experiences a local environment with a C_{nv}, C_n or C_s (non-centrosymmetric sites) symmetry. The violation of this selection rule has been explained by the admixture of the charge transfer (CT) band into the wavefunction of the $4f^6$ configuration [22] or by the J-mixing [23, 24] caused by the CF perturbation. The $^5D_0 \rightarrow {}^7F_0$ transition is not split and appears as a singlet band. Hagemann et al [25] observed this transition at 578 nm as a weak band in the spectrum of crystalline $SrAl_2O_4:Eu^{3+}$. In some cases, it is observed as a doublet, triplet, and etc., which is due to the presence of at least two or more crystallographic sites for the Eu^{3+} ion in the compound. In general, the $^5D_0 \rightarrow {}^7F_0$ transition occurs as a very weak band. However, in some β-diketonate complexes [26], where Eu^{3+} occupies a C_3 symmetry, it was observed to be unusually intense.

Since the intensity of the MD $^5D_0 \rightarrow {}^7F_1$ transition is to a great extent independent of the local environment of the Eu^{3+} ion [21], it is normally used to normalize two spectra to compare their intensities. It must be noted that the integrated intensity must be considered rather than the individual intensities of the CF components. The $^5D_0 \rightarrow {}^7F_1$ transition appears as a singlet band in the icosahedral and cubic crystals, since in these structures the $^7F_1$ level is not split. This level is split into a nondegenerate and a twofold degenerate in trigonal, tetragonal, and hexagonal crystals. Consequently, in these structures, the $^5D_0 \rightarrow {}^7F_1$ transition is observed as a doublet band. As the CF degeneracies are totally lifted in the orthorhombic or lower symmetries, this transition is observed as a triplet. In the monoclinic crystal structure of $SrAl_2O_4$, the $^5D_0 \rightarrow {}^7F_1$ transition was observed as a triplet at 587, 592, and 597 nm, respectively [25]. However, considering a C_3 local symmetry for the two Sr^{2+} sites in this structure, only a doublet was expected. Observation of these 3 distinct components was assigned to the local distortion of the Eu^{3+} ion from the C_3 symmetry due to the charge compensation process. In exceptional cases, under large CF splitting of the $^5D_0 \rightarrow {}^7F_1$ transition, an overlap is possible with the CF lines of the $^5D_0 \rightarrow {}^7F_2$ transition [27]. In some compound such as $Ba_2GdNbO_6:Eu^{3+}$ and $Gd_2Ti_2O_7:Eu^{3+}$ with the centrosymmetric crystal structure, the $^5D_0 \rightarrow {}^7F_1$ transition has been observed to be the most intense band [28]. In some Eu^{3+}-doped rare-earth fluorides including LaF_3, GdF_3, and $KGdF_4$, this transition was reported to generate the most intense band in the Eu^{3+} spectrum.

In majority of Eu^{3+}-based phosphors, the $^5D_0 \rightarrow {}^7F_2$ transition generates the most intense emission band, and therefore, it is the responsible for their typical red color. It is called a hypersensitive transition, since its intensity is dramatically influenced by the nature and local geometry of the Eu^{3+} ion. The intensity of this transition is considered as a measure for the local symmetry of the Eu^{3+} ion (see section 7 of ref. [19] for more information). The CF can split it into a quintet or lower, depending on the site symmetry of Eu^{3+} ion. In $SrAl_{12}O_{19}$ with the Sr^{2+} ion in a D_{3h} symmetry, it appears as a sharp singlet band [29], because there is only one CF band allowed for the $^5D_0 \rightarrow {}^7F_2$ transition. It splits into two in the D_3 symmetry (sometimes it is not resolved) [30].

Similar to the $^5D_0 \rightarrow {}^7F_0$ transition, the $^5D_0 \rightarrow {}^7F_3$ transition is forbidden by the Jude-Ofelt theory and appear very weak in the Eu^{3+} spectra. Its intensity can increase by a strong CF effect and J-mixing. The higher intensity of this transition compared to the $^5D_0 \rightarrow {}^7F_4$ transition in the C_{2V} site of $BaFCl:Eu^{3+}$ [22] was attributed to the strong J-mixing. It was also observed anomalously strong for the Eu^{3+} ion in the $Mg_3F_3BO_3$ host [27]. However, the authors suggested that, this intense band originates from the $^5D_0 \rightarrow {}^7F_2$ transition with a huge CF splitting (1750 cm^{-1}).

The $^5D_0 \rightarrow {}^7F_4$ transition lies in a region of the spectrum, where many commonly used photomultiplier tubes have low sensitivity. This must be considered when comparing its intensity with the other transition bands of the Eu^{3+} ion. With several exceptions, the intensity of this transition is normally lower than that of the $^5D_0 \rightarrow {}^7F_2$ transition. In particular, dominant emission have been observed for this transition in compounds with D_{4d} symmetry for the Eu^{3+} ion. The $^5D_0 \rightarrow ^7F_4$ transition is intense in D_{4d} symmetry due to the absence of a center of symmetry, whereas the $^5D_0 \rightarrow ^7F_2$ transition is forbidden. $YF_3:Eu^{3+}$, $Na_3YSi_3O_9:Eu^{3+}$: and $Ga_3Ga_2Ge_3O_{12}:Eu^{3+}$ are examples of the compounds, where the $^5D_0 \rightarrow ^7F_4$ transition is the strongest.

3.2. Eu^{3+} as a probe

Eu^{3+} is often used as a spectroscopic probe, because interpretation of its spectra is usually straightforward. In majority of cases, it emits light only from the non-degenerate $^5D_0$ excited state. On the other hand, the $^7F_0$ ground level is also non-degenerate and only one emission band is expected for the transition from the $^5D_0$ state to the $^7F_0$ level, regardless of the CF effect. Other important transitions of Eu^{3+} takes place in between the $^5D_0$ state and the $^7F_{1,2}$ levels. The maximum number of CF splitting for these two levels are 3 and 5, respectively, which are rather low numbers. The accurate calculation of the energy levels of the $4f^6$ configuration is possible due to the limited J-mixing and only slight relaxation in the selection rules. In line with other simplicities in the interpretation of Eu^{3+} spectra, the $^5D_0 \rightarrow ^7F_J$ transition bands are well separated, and therefore confusions are not caused by the overlapping of different emission bands. Moreover, the bright luminescence of Eu^{3+} falls in the visible range. Finally, due to the very weak vibronic coupling, Eu^{3+} has very narrow emission bands even at room temperature. This facilitates resolving the fine structures resulted from the CF.

There are two crystallographic sites in the structure of $SrAl_2O_4$ compound. Therefore, maximum 2 emission bands are expected for the $^5D_0 \rightarrow ^7F_0$ transition in this structure, as reported in an experimental and theoretical study [31] of $SrAl_2O_4:Eu^{2+}$. In this study, the two bands were reported at 575 and 576, respectively. Nonetheless, spectroscopically probing the Eu^{3+} sites revealed that there were multiple sites for the Eu^{3+} ion in the crystal structure of $SrAl_2O_4$ [49]. According to the authors, the different charge compensation processes taking place, distorted the local geometry of the Eu^{3+} ion, resulting in multiple sites. Interestingly, the $^5D_0 \rightarrow ^7F_0$ transition was not observed in the luminescence spectra of $SrAl_2O_4:Eu^{3+}$ co-doped with B^{3+} and Li^+ [32], which indicates that the Eu^{3+} ion occupies a centrosymmetric site in this compound.

References

[1] H. Hagemann, J. Afshani, Chapter 321: Synthesis, luminescence and persistent luminescence of europium-doped strontium aluminates, Handbook on the Physics and Chemistry of Rare Earths, Elsevier, Vol 60 (2021) p.163-225, ISSN 0168-1273, https://doi.org/10.1016/bs.hpcre.2021.06.001.

[2] J. Bierwagen, T. Delgado, J. Afshani, S. Yoon, N. Gartmann, B. Walfort, H. Hagemann, Observation of multiple sites for trivalent europium ions in $SrAl_2O_4$, Journal of Luminescence, 239 (2021) 118348.

[3] A.M. Cross, P.S. May, F.C.v. Veggel, M.T. Berry, Dipicolinate sensitization of europium luminescence in dispersible 5% Eu:LaF_3 nanoparticles. The Journal of Physical Chemistry C, 2010. **114**(35): p. 14740-14747.

[4] J. Wang, Y. Cheng, Y. Huang, P. Cai, S.I. Kim, H.J. Seo, Structural and luminescent properties of red-emitting Eu^{3+}-doped ternary rare earth antimonates R_3SbO_7 (R= La, Gd, Y). Journal of Materials Chemistry C, 2014. **2**(28): p. 5559-5569.

[5] E. Chaudan, J. Kim, S. Tusseau-Nenez, P. Goldner, O.L. Malta, J. Peretti, T. Gacoin, Polarized luminescence of anisotropic $LaPO_4$:Eu nanocrystal polymorphs. Journal of the American Chemical Society, 2018. **140** (30): p. 9512-9517.

[6] T. Rao, A.R. Kumar, K. Neeraja, N. Veeraiah, M.R. Reddy, Optical and structural investigation of Eu^{3+} ions in Nd^{3+} co-doped magnesium lead borosilicate glasses. Journal of alloys and compounds, 2013. **557**: p. 209-217.

[7] I. Kindrat, B. Padlyak, Luminescence properties and quantum efficiency of the Eu-doped borate glasses. Optical Materials, 2018. **77**: p. 93-103.

[8] F. Cao, T. Huang, Y. Wang, F. Liu, L. Chen, J. Ling, J. Sun, Novel lanthanide–polymer complexes for dye-free dual modal probes for MRI and fluorescence imaging. Polymer Chemistry, 2015. **6**(46): p. 7949-7957.

[9] K. Binnemans, C. Görller-Walrand, Lanthanide-containing liquid crystals and surfactants. Chemical reviews, 2002. **102**(6): p. 2303-2346.

[10] J.-N. Hao, B. Yan, Highly sensitive and selective fluorescent probe for Ag^{+} based on a Eu^{3+} post-functionalized metal–organic framework in aqueous media. Journal of Materials Chemistry A, 2014. **2**(42): p. 18018-18025.

[11] R. He, Y.-L. Wang, H.-F. Ma, S.-G. Yin, Q.-Y. Liu, Eu3+-functionalized metal-organic framework composite as ratiometric fluorescent sensor for highly selective detecting urinary 1-hydroxypyrene. Dyes and Pigments, 2018. **151**: p. 342-347.

[12] J. Luo, B.-S. Liu, X.-R. Zhang, R.-T. Liu, A Eu^{3+} post-functionalized metal-organic framework as fluorescent probe for highly selective sensing of Cu^{2+} in aqueous media. Journal of Molecular Structure, 2019. **1177**, 444.

[13] C. Nico, R. Fernandes, M. Graça, M. Elisa, B. Sava, R. Monteiro, L. Rino, T. Monteiro, Eu^{3+} luminescence in aluminophosphate glasses. Journal of luminescence, 2014. **145**, 582.

[14] S. Gago, J.A. Fernandes, J.P. Rainho, R.A. Sá Ferreira, M. Pillinger, A.A. Valente, T.M. Santos, L.D. Carlos, P.J. Ribeiro-Claro, I.S. Gonçalves, Highly luminescent tris (β-diketonate) europium (III) complexes immobilized in a functionalized mesoporous silica. Chemistry of materials, 2005. **17**(20) 5077.

[15] S. Petoud, S.M. Cohen, J.-C.G. Bünzli, K.N. Raymond, Stable lanthanide luminescence agents highly emissive in aqueous solution: multidentate 2-hydroxyisophthalamide complexes of Sm^{3+}, Eu^{3+}, Tb^{3+}, Dy^{3+}. Journal of the American Chemical Society, 2003. **125**(44) 13324.

[16] C. Ronda, T. Jüstel, H. Nikol, Rare earth phosphors: fundamentals and applications. Journal of Alloys and Compounds, 1998. **275**, 669.

[17] L. Ozawa, M. Itoh, Cathode ray tube phosphors. Chemical reviews, 2003. **103**(10) 3835.

[18] J. Liu, H. Rijckaert, M. Zeng, K. Haustraete, B. Laforce, L. Vincze, I. Van Driessche, A.M. Kaczmarek, R. Van Deun, Simultaneously excited downshifting/upconversion luminescence from lanthanide-doped core/shell fluoride nanoparticles for multimode anticounterfeiting. Advanced Functional Materials, 2018. **28**(17) 1707365.

[19] K. Binnemans, Interpretation of europium (III) spectra. Coordination Chemistry Reviews, 2015. **295** 1.

[20] K. Biswas, A.D. Sontakke, K. Annapurna, Synthesis and structural probing of Eu3+ doped BaYF5 nano-crystals in transparent oxyfluoride glass-ceramics. International Journal of Applied Glass Science, 2012. **3**(2) 154.

[21] C. Görller-Walrand, K. Binnemans, Spectral intensities of f-f transitions. Handbook on the physics and chemistry of rare earths, 1998. **25** 101.

[22] X. Chen, G. Liu, The standard and anomalous crystal-field spectra of Eu^{3+}. Journal of Solid State Chemistry, 2005. **178**(2) 419.

[23] O. Malta, W. Azevedo, E. Gouveia, G. De Sá, On the $^5D_0 \rightarrow {}^7F_0$ transition of the Eu^{3+} ion in the $\{(C_4H_9)_4N\}_3Y(NCS)_6$ host. Journal of Luminescence, 1982. **26**(3) 337.

[24] M. Tanaka, T. Kushida, Effects of static crystal field on the homogeneous width of the $^5D_0 – {}^7F_0$ line of Eu^{3+} and Sm^{2+} in solids. Physical Review B, 1995. **52**(6) 4171.

[25] J. Bierwagen, T. Delgado, J. Afshani, S. Yoon, N. Gartmann, B. Walfort, H. Hagemann, Observation of multiple sites for trivalent europium ions in $SrAl_2O_4$, Journal of Luminescence, 239 (2021) 118348.

[26] A.F. Kirby, F. Richardson, Detailed analysis of the optical absorption and emission spectra of europium (3+) in the trigonal (C3) Eu $(DBM)_3.H_2O$ system. The Journal of Physical Chemistry, 1983. **87**(14) 2544.

[27] D. Van der Voort, G. Blasse, Anomalous rare-earth emission in magnesium fluoroborate. Journal of Physics and Chemistry of Solids, 1991. **52**(9) 1149.

[28] G. Blasse, A. Bril, W. Nieuwpoort, On the Eu^{3+} fluorescence in mixed metal oxides: Part I—The crystal structure sensitivity of thr intensity ratio of electric and magnetic dipole emission. Journal of Physics and Chemistry of Solids, 1966. **27**(10) 1587.

[29] S. Chawla, A. Yadav, Role of valence state of dopant (Eu^{2+}, Eu^{3+}) and growth environment in luminescence and morphology of SrAl12O19 nano-and microcrystals. Materials Chemistry and Physics, 2010. **122**(2-3) 582.

[30] M.H. Werts, R.T. Jukes, J.W. Verhoeven, The emission spectrum and the radiative lifetime of Eu^{3+} in luminescent lanthanide complexes. Physical Chemistry Chemical Physics, 2002. **4**(9) 1542.

[31] B.F. dos Santos Jr, M.V. dos Santos Rezende, P.J. Montes, R.M. Araujo, M.A. Dos Santos, M.E. Valerio, Spectroscopy study of $SrAl_2O_4:Eu^{3+}$. Journal of luminescence, 2012. **132**(4) 1015.

[32] R. Qiang, S. Xiao, J. Ding, W. Yuan, C. Zhu, Red emission in B^{3+}-and Li^{+}-doped $SrAl_2O_4:Eu^{3+}$ phosphor under UV excitation. Journal of luminescence, 2009. **129**(8) 826.

Spectroscopy of Eu^{2+}

The spectroscopy of Eu^{2+} is governed by f-d transitions, leading to emission spectra ranging from the near UV to the red, depending on the CF splitting and centroid shifts related to the contribution of covalency to the bonding, as discussed in detail in the review chapter reproduced below.

The structural descriptions and synthetic methods outlined above were included in the review chapter : Synthesis, luminescence and persistent luminescence of europium-doped strontium aluminates,by H. Hagemann and J. Afshani, Handbook on the Physics and Chemistry of Rare Earths, Elsevier, 2021,, ISSN 0168-1273, https://doi.org/10.1016/bs.hpcre.2021.06.001. which is appended hereafter.

Book Chapter

Synthesis, luminescence and persistent luminescence of europium-doped strontium

1. Introduction

Persistent phosphorescence is a phenomenon in which a material re-emits light over long periods (hours) after stopping the excitation irradiation [1-8]. The term "persistent phosphorescence" is not unique in the scientific literature to describe this phenomenon, other expressions are "long lasting phosphorescence (LLP)", "long afterglow" or simply phosphorescence. Smet et al. [6] have presented in an earlier chapter of this Handbook the history, synthesis, models, analysis and applications of persistent phosphors, and other reviews have been recently published [1-5,7,8].

The discovery of persistent phosphorescence in strontium aluminates [9] has stimulated a considerable research effort on strontium aluminates and other persistent phosphor materials. Presently, more than 270 papers are published each year with keywords related to persistent phosphors [7]. Strontium aluminates find however also a great variety of other applications. Some examples of these applications are mentioned hereafter, but this list is by far not exhaustive.

The compound $SrAl_{12}O_{19}$ is a useful ingredient for the cement industry [10], as this compound has an excellent thermal conductivity of 11 W/m·K and high Moh's hardness of 9 [11]. Nd- or Pr- doped $SrAl_{12}O_{19}$ crystals can be used for laser applications [11, 12]. Mn^{2+}, Gd^{3+} doped $SrAl_{12}O_{19}$ has been proposed as rewritable optical data storage compound [13]. $Sr_3Al_2O_6$ has been used as heterogeneous Lewis Base catalyst for Knövenagel condensation reactions [14].

Mn^{4+}, Tb^{3+} co-doped $Sr_4Al_{14}O_{25}$ is a thermographic material for temperature imaging, as the emission color strongly changes due to the thermal quenching of the Mn^{4+} emission [15]. Eu^{2+},Eu^{3+} co-doped $Sr_4Al_{14}O_{25}$ also shows important color changes from 298 to 523 K [16].

Many very diverse applications of persistent phosphors can be found in the literature [1-7]. Traditional applications are safety signs for emergency exits, toys or luminescent watch dials [1-7]. However, quite a few new applications are emerging. Mechanoluminescence can be observed in $SrAl_2O_4:Eu^{2+}$ [6, 17], and this property is connected to persistent phosphorescence [18]. Electron microscopy experiments indicate that the mechanoluminescence in $SrAl_2O_4:Eu^{2+}$ is associated with rearrangements of morphology variants of the monoclinic phase [19]. A recent study [17] observed that increasing the number of dislocations decreases the stress-free persistent emission, but increased the mechanoluminescence intensity. The persistent afterglow of $Sr_4Al_{14}O_{25}:Eu^{2+}$ can be used to reduce the flicker for white LED's [20]. Composite materials including strontium aluminate persistent phosphors can be applied as photocatalysts [21-24], improve solar cell performance [25, 26], anticounterfeiting [27], fingerprint detection [28, 29], or oxygen sensing [30]. The use of persistent strontium aluminates as road markings for improved safety has also been addressed [31, 32].

A light charged pressure sensitive paint was obtained by the combination of the persistent phosphor material $Sr_4Al_{14}O_{25}$:Eu,Dy combined with a pressure sensitive luminophore [33].

One promising future application of persistent phosphors concerns bio-sensing and bio-imaging applications [34, 35]. Persistent emission (ca 10 minutes) in the NIR was reported the first time in 2009 for $SrAl_2O_4$ codoped with Eu^{2+},Dy^{3+} and Er^{3+}. The NIR emission is obtained from the energy transfer from Eu^{2+} to Er^{3+} [36]. Cr^{3+} can also be used as NIR emitter [37]. Nanoparticles of $SrAl_2O_4$ do not appear to be cytotoxic [38], which is an important condition for potential biological applications.

In this chapter we address first the crystal structures and syntheses of rare earth doped strontium aluminates, and discuss then in more detail the spectroscopy of europium-doped compounds, and present finally experimental results related to the persistent phosphorescence mechanisms which apply to the currently best performing materials $SrAl_2O_4:Eu^{2+}$, Dy^{3+} and $Sr_4Al_{14}O_{25}:Eu^{2+}$, Dy^{3+}. The emphasis of this chapter is based on experimental results, but of course theoretical approaches do provide additional insights into various aspects of the persistent phosphorescence mechanism. Our current understanding of this mechanism is outlined at the end of this chapter, as well as remaining questions to be addressed.

2. The phase diagram and crystal structures of the SrO-Al_2O_3 system

2.1. Phase diagram

The phase diagram of the SrO-Al_2O_3 system has been studied by F. Massazza [39] and F. Ganits [40]. This diagram was completed by M. Capron and A. Douy who studied in detail the formation of $SrAl_4O_7$ [41]. Figure 1 illustrates the resulting combined phase diagram, which also defines the short notations used for the different compounds formed from the reaction of SrO with Al_2O_3. The compound $SrAl_4O_7$ is formed from 1 SrO and 2 Al_2O_3, resulting in the notation **SA_2**. This phase diagram highlights the fact that between 1273 and 1773 K (1000 and 1500 °C), several phases can transform into each other, and thus a combination of thermodynamic and kinetic factors come into play to prepare specifically one pure species, as will be discussed below. There are some species missing in this phase diagram. For instance, Akasaka et al. [42] report the preparation of $Sr_7Al_{12}O_{25}$ (**S_7A_6**) from a mixture Sr+Eu:Al = 7:8 at 1673 K. This complexity is not fully reproduced by the CALPHAD calculation of this system [43] which does not contain the **SA_2** data from [41].

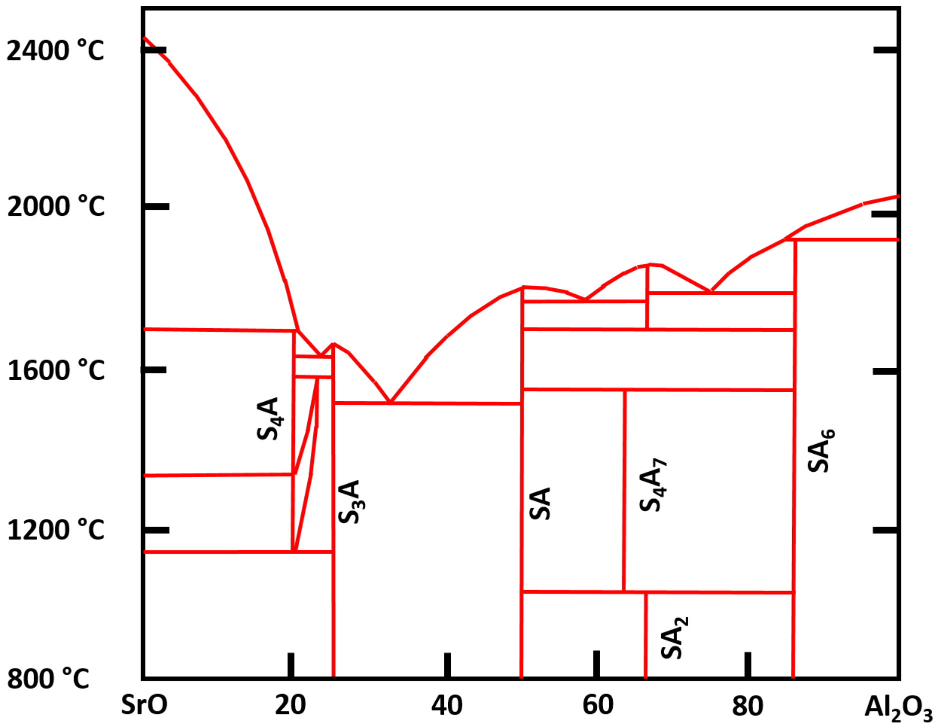

Figure 1: Phase diagram of the SrO – Al_2O_3 system after [39-41]. There is a small field of solid solutions for β-$Sr_4Al_2O_7$ (**S_4A**). More detailed data of the region between **S_3A** and **S_4A** are given in [39].

According to [39] and [40], the 3 compounds **S_3A**, **SA** and **SA_2** are congruently melting, while **SA_6** is incongruently melting (peritectic point). However, the values of the corresponding melting points differ somewhat: Massassa [39] indicates 1933 K and 2063 K for **S_3A** and **SA** respectively, while Ganits [40] reports higher melting points of 2009, 2233 and 2053 K for **S_3A**, **SA** and **SA_2** respectively. Boyko et al. [44] give a melting point of 2043 +/-15 K for **SA_2**. For **SA_2**, Capron and Douy [41] have shown that this compound can be obtained from **SA** and γ-Al_2O_3 by annealing at 1223-1273 K. Above 1373 K, $Sr_4Al_{14}O_{25}$ (**S_4A_7**) (which is stable up to 1773 K) is formed, which decomposes at higher temperatures into **SA** and **SA_6**. Close to its melting point, **SA_2** is again stable. Glassy **S_3A** can be obtained by rapid quenching from the melt at 2073 K. Upon heating, a glass transition is observed at 958 K and crystallization at 1035 K. Treating the glass at 1113 K for 5 h yielded a transparent polycrystalline material [45]. As many preparations of strontium aluminate phosphors involve annealing steps between 1173 and 1673 K, the resulting phase purity of the target compound is subject to both thermodynamic (phase diagram) and kinetic constraints, requiring thus precise preparation protocols to ensure reproducible results.

A very dense (d = 4.84 g/cm^3) orthorhombic phase has been reported for **SA_2** prepared in the presence of water in a cubic anvil apparatus under up to 5 MPa pressure and 1273 -1573 K [46].

Thermodynamic data for strontium aluminates are scarce. Temperature dependent data for **SA** can be found in [47]. At 298 K, $\Delta_f H° = -2324.6$ kJ/mol, $S^{°} = 106.69$ J/(mol.K), $\Delta_f G° = -2200.6$ kJ/mol. Jakob and Shreyas [48] have recently studied potentiometrically the stability of **SA_6** and **SA_2**. Ye et al. [43] have calculated the phase diagram including also data from [49], but as mentioned above, without the data for **SA_2**. A full description is therefore still lacking.

2.2. Crystal structures

2.2.1. Survey of crystal structures

Tables 1 and 2 summarize crystal structure data and some properties of the most stable compounds in this system. It is important to note that with the exception of **SA_6** and the high-pressure phase of **SA_2**, the density of all other compounds is less than the average density of SrO and Al_2O_3 for these compounds. This lower density results in voids in the structure which can in principle allow to incorporate charge compensating anions, when the divalent Sr^{2+} ion is replaced with a trivalent rare earth ion (see below). The structures of **SA** and **S_4A_7** which are the host crystals for the best performing persistent phosphors are described in more detail below.

Table 1. Crystallographic data for strontium aluminates.

		a (nm)	b(nm)	c (nm)	α (°)	β (°)	γ (°)	V (nm^3)	Z	Space group	d (g/cm^3)	Ref.
SrO		5.1600	5.1600	5.1600	90	90	90	1.3739	4	Fm-3m	5.01	[50]
$Sr_{10}Al_6O_{19}$	**$Sr_{10}A_3$**	3.4582	0.7846	1.5749	90	103.7	90	4.1519	8	C2/c	4.29	[51]
$Sr_3Al_2O_6$	**S_3A**	1.5842	1.5842	1.5842	90	90	90	3.9762	24	Pa3	4.14	[52]
$Sr_7Al_{12}O_{25}$	**S_7A_6**	1.791	1.791	0.716	90	90	120	1.9890	3	P3	3.35	[53]
α-$SrAl_2O_4$ β-$SrAl_2O_4$	**SA**	0.8447 0.8926	0.8816 0.8926	0.5163 0.8499	90 90	93.42 90	90 120	0.3838 0.5864	4 6	$P2_1$ $P6_3$	3.561 3.49	[54] [55]
$Sr_2Al_6O_{11}$	**S_2A_3**	2.1914	0.4884	0.8404	90	90	90	0.8995	4	Pnnm	3.79	[56]
$Sr_4Al_{14}O_{25}$	**S_4A_7**	2.4745	0.8473	0.4881	90	90	90	1.0234	2	Pmma	3.66	[57]
α-$SrAl_4O_7$ β-$SrAl_4O_7$	**SA_2**	1.3039 0.8085	0.9011 1.1845	0.5536 0.4407	90 90	106.5 90	90 90	0.6249 0.4220	4 4	C2/c Cmma	3.269 4.84	[58] [46]
$SrAl_{12}O_{19}$	**SA_6**	0.55666	0.5567	2.2002	90	90	120	0.5904	2	$P6_3$/mmc	4.02	[59]
$Sr_{0.5}Al_{11}O_{17}$	**$SrAl_{11}$**	0.5622	0.5622	3.3500	90	90	120	0.9169	3	R-3mH	3.33	[60]
Al_2O_3		1.18	0.290	0.570	90	104.5	90	0.1888	4	C12/m1	3.59	[61]

Table 2. Strontium-oxygen bond length, refractive index, thermal expansion and conductivity data for strontium aluminates

Compound	Space group	Number of Sr sites	C.N.	average Sr-O distance (nm)	n	α (10^{-6} K^{-1})	Conductivity at 1273K (S/cm)	Ref.
$Sr_{10}Al_6O_{19}$	C2/c	11	8(+1) 7(+2) 6 8 6 7(+2) 7(+2) 7 6(+2) 4(+4) 8(+1)	0.274 (0.280) 0.265 (0.282) 0.246 0.278 0.246 0.274 (0.287) 0.274 (0.287) 0.266 0.261 (0.276) 0.247 (0.286) 0.279 (0.283)				[51]
$Sr_3Al_2O_6$	Pa3	6	6 6 6 8 8 7(+1)	0.248 0.250 0.248 0.281 0.275 0.264 (0.273)	1.643-1.654	10.6 (333-873K)	3.5 10^{-6}	[39, 52, 62]
α-$SrAl_2O_4$ β-$SrAl_2O_4$	$P2_1$ $P6_3$	2 3	7(+2) 7(+2) 9 6(+3) 8	0.269 (0.288) 0.267 (0.284) 0.289 0.27 (0.299) 0.280	1.613-1.649	9.2 (333-943K)	1.4 10^{-6}	[39, 54, 55]
$Sr_2Al_6O_{11}$	Pnnm	2	7(+2) 10	0.277 (0.285) 0.279				[56]
$Sr_4Al_{14}O_{25}$	Pmma	2	7(+2) 10	0.264 (0.279) 0.281		7.6 (333-773K)	4 10^{-5}	[57, 62]
α-$SrAl_4O_7$ β-$SrAl_4O_7$	C2/c Cmma	1 1	7 10	0.262 0.262	1.62-1.644			[44, 46, 58]
$SrAl_{12}O_{19}$	$P6_3$/mmc	1	12	0.276	1.757,1.763			[39][59]

2.2.2. $SrAl_2O_4$ (**SA**)

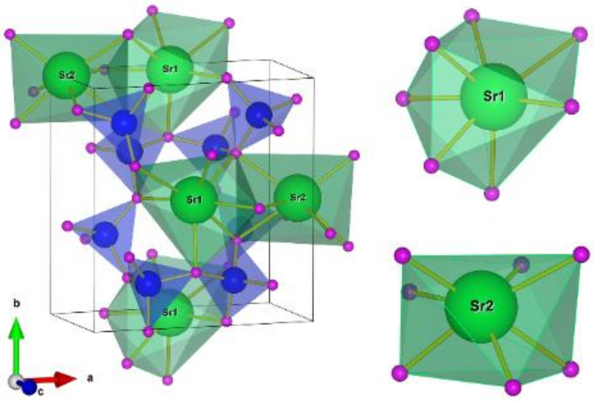

Figure 2: Illustration of the crystal structure of **SA [54]** in the monoclinic phase

SA has a monoclinic crystal structure (space group P21, No. 4), with four formula units per one unit cell [54]. The main motif of the structure are the corner-sharing AlO_4 tetrahedra, which are tilted with respect to each other. Large Sr ions are positioned in the cavities between those tetrahedra (Figure 2) [63]. There are 2 different Sr sites. The bandgap of **SA** is 6.6 eV [64]. DFT calculations [65] show that the highest levels in the valence band originate from the 2p states of oxygen, and the lowest levels of the conduction band originate mainly from Sr 5s states. Around 943 K, there is a structural phase transition leading to a hexagonal phase with space group P_3 [55], and another transition is observed around 1133 K, resulting in a structure with space group $P6_322$. The transition at 943 K presents a hysteresis of about 12 K, and is associated upon heating with a small unit cell volume decrease (about 0.25%) [66].

2.2.3. $Sr_4Al_{14}O_{25}$ (**S_4A_7**)

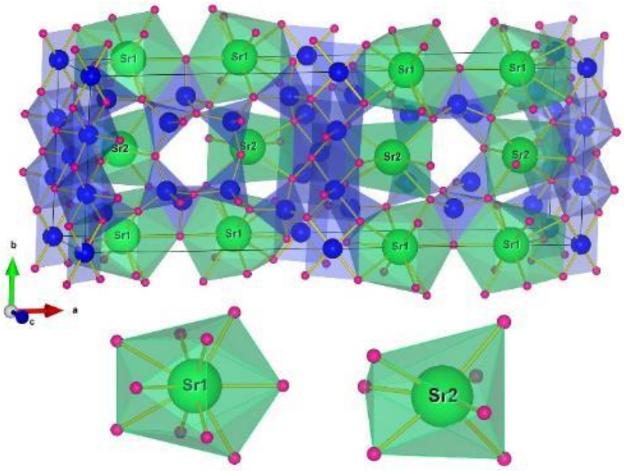

Figure 3: Illustration of the crystal structure of **S_4A_7** [57, 67] in the monoclinic phase

This compound crystallizes in an orthorhombic crystal system with space group Pmma [57, 67]. There are two different crystallographic sites for strontium ions with the coordination numbers 7 and 10 (see Figure 3). The covalency and crystal field strength is expected to be higher for the 7-fold coordinated site. The average Sr-O bond lengths for the 7 and 10 coordinated strontium atoms are 2.64 and 2.81 Å, respectively. There are six different Al^{3+} crystallographic sites in this structure (three AlO_6 octahedral sites and three AlO_4 tetrahedral sites) [57, 67]. The structure is stable up to 1773 K, above this temperature, it dissociates into **SA** and **SA$_6$** (see Figure 1).

3 Synthesis of strontium aluminates

3.1. Single crystal growth

Due to the incongruent melting behavior of **SA$_6$**, single crystals of Nd-doped $SrAl_{12}O_{19}$ were grown using the Czochralski method in the presence of an excess of $SrCO_3$ for laser applications [12]. Single crystals of **SA$_2$** were equally obtained using the Czochralski method [58]. Katsumata et al. [68] reported the preparation of single crystals (maximum 6 mm diameter 40 mm length), of rare earth-doped **SA** by the floating zone method.

3.2. Solid state synthesis

Many papers have reported the solid state synthesis of strontium aluminates by annealing between 1273 and 1773 K. Some compounds can only be obtained using additionally boron oxide in the reaction mixture. For **S$_4$A$_7$**, Thomson et al. [69] report that the title compound is obtained as a single phase in the presence of 5% and more of B_2O_3. Without boron oxide, **SA** is the main product at the reaction temperature of 1373 K. With more than 30% B_2O_3, **SA$_6$** is obtained. Akmehmet et al. [70] investigated the effects of boron on the microstructure and luminescence of **S$_4$A$_7$**:Eu^{2+},Dy^{3+} by nanoscale-resolved cathodoluminescence mapping technique. They applied the same sol-gel method for preparation of the precursor material in the presence and absence of B_2O_3 in the reaction mixture. Pure-phase **S$_4$A$_7$** was obtained when B_2O_3 was employed in the reaction mixture, whereas the absence of B_2O_3 resulted in a mixture of **S$_4$A$_7$**, **SA$_6$**, **SA$_2$** and **SA**. The authors showed that boron facilitates evolution of the equilibrium crystalline structure and enhances homogeneous distribution of Eu^{2+} into both Sr sites.

The unit cell volume of **S$_4$A$_7$** decreases regularly from V =1035 Å^3 for 0% B_2O_3 to V = 1019 Å^3 for 30% B_2O_3 for a single step calcination (heated at a rate of 10 K/min to 1373 K in a reducing atmosphere (5% H_2+ 95% N_2) which was maintained for 3 h) , but much less (from 1028.8 to 1026.3 Å^3) for a 2 step calcination (pre-calcination at 1273 K in an ambient atmosphere for 2 h, addition of B_2O_3, heated to 1373 K in reducing atmosphere).

S$_2$A$_3$ is obtained only by solid state synthesis in the presence of boron oxide under specific conditions. Takeda et al. [56] report that at 1473 K, **S$_2$A$_3$** is formed predominantly with a boron to aluminum ratio of 0.05. With lower boron content, **SA** and Al_2O_3 are found, while with a ratio of 0.1, the formation of **S$_4$A$_7$** dominates. This latter compound is also favored at higher reaction temperatures (1573 K).

The choice of starting materials is also important. Using nanosized Al_2O_3 as source of Al, together with $SrCO_3$ and boric acid, single phase SA_2 was obtained at 1223 K, while normal Al_2O_3 or $Al(OH)_3$ did not allow to obtain the pure phase.

3.3. Other synthesis methods

Inorganic materials can be prepared in many different ways. The solid state preparation has been the most popular in the past, and the products obtained are typically powders with particle size between 5 and 50 μm. Other synthesis methods which are currently the subject of many studies aim at the preparation of nano-sized particles with not only good shape and size control, but also with good emission properties. These methods have been described in detail in various reviews [71-74]. The examples cited below for the preparation of strontium aluminates are by far not exhaustive, but aim to illustrate some recent results.

3.3.1. Molten salt method

In 2015, Rojas-Hernandez et al. [75] reported in detail the application of this method for the preparation of highly crystalline **SA** powder. They employed a eutectic mixture of NaCl-KCl salts medium to obtain nanosized crystals in only 1 h at 1173 K. Later in 2018 [76], this method was used once again for the preparation of **SA** nanoparticles. Although the luminescence emission intensity had improved compared to the former work, the afterglow duration was observed to be only 7 minutes. Using sapphire (Al_2O_3(0001)) substrates, this research group recently obtained textured **SA** samples on this reactive Al_2O_3 crystal surface which showed a twofold enhancement of the luminescence as compared with unoriented films [77]. It is important to note that **SA** is moisture sensitive, which can cause difficulties to separate the product from the flux. Guo et al. [78] have studied the hydrolysis behavior of **SA**. After suspending **SA** in water for several days, they observed the formation of **SA$_2$** and **SA$_6$**. Heating **SA** together with $NH_4.HF_2$ at 873-973 K for 2 h leads to the formation of a SrF_2 protecting surface layer which effectively improves the water stability of the phosphor [78]. Other authors propose coating with polymers [79] or with phosphates [80].

3.3.2. Combustion method

This method or self-propagating high temperature synthesis, is a spontaneous and highly exothermic reaction between the reactants, which then yields either the desired product or its precursors [81]. The reaction is complete within only a few minutes, during which time a huge amount of gasses is released. In order for the combustion to take place, the initial mixture of the reactants needs to be highly dispersed and contain high chemical energy. The notably used fuel in this method are glycine, citric acid, carbohydrazide, and urea. Varma et al. published an excellent review paper on the application of the solution combustion method for synthesis of nanoscale materials [72]. To obtain a well-crystallized product, post-annealing treatment is usually required.

The effect of the combustion temperature was studied on **SA**: Eu^{2+},Dy^{3+},Tb^{3+} particles [82]. This study covered temperatures in the range of 673-1173 K for the combustion reaction. Crystalline **SA**: Eu^{2+},Dy^{3+},Tb^{3+} particles were obtained at a temperature as low as 673 K. By increasing the reaction temperature, the crystallinity of the particles improved as well. A brightness equal to 3.55 cd/m^2 and afterglow duration of 2743 s was obtained for these particles.

The influence of the annealing temperature was investigated on **S$_3$A**:Eu^{2+} samples obtained via the combustion method [83]. A series of samples were annealed at temperatures ranging from 1173 K to 1523 K. The results showed that a well-crystallized product was obtained following annealing at 1473 K. Moreover, the emission intensity increased by increasing the annealing temperature up to 1473 K, and then decreased for the sample annealed at 1523 K. The red afterglow of the samples improved by increasing the annealing temperature from 1323 K to 1473 K and lasted for 600 s for the latest sample. In another study [84], effect of the annealing temperature was monitored on the morphology of the **SA**:Eu^{2+},Dy^{3+} product. At temperatures below 1423 K, hollow nanoparticles were formed, while increasing the reaction temperature to 1473 K resulted in needle/rod-shape nanoparticles.

The addition of borates as flux agents in the synthesis of strontium aluminate compounds via the combustion method has positive effects [85, 86]. Effect of application of H_3BO_3 in the synthesis of **SA**:Eu^{2+},Dy^{3+} was studied on the crystal phase, morphology, as well as photoluminescence, afterglow properties, and thermoluminescence properties. The addition of 2 mol% H_3BO_3 resulted in the preparation of pure-phase **SA**:Eu^{2+},Dy^{3+} phosphor [85]. The morphology of the particles changed dramatically by varying the amount of H_3BO_3 in the reaction mixture. In the absence of boric acid, irregular morphology of the resulting powder was observed. With 2 mol% H_3BO_3, flower like particles with sharp petals were obtained. The thickness of the petals increased by increasing the H_3BO_3 content and at around 12 % H_3BO_3, the morphology looked irregular again. The luminescence intensity of the phosphors constantly increased as a function of boric acid content, until it reached its maximum at 20 mol %, where it started decreasing. A similar trend was observed for the afterglow duration, as well as the trap depths of the samples. However, in another study, the optimal amount of H_3BO_3 for obtaining best photoluminescence and mechanoluminescence properties was reported as 7.5 % [86].

3.3.3. Sol-gel

The sol-gel method is a widely used technique for the preparation of nanosized particles [71]. It is a well-stablished approach for obtaining high quality nanoparticles including metal oxides. In general, the sol-gel method consists of five steps; hydrolysis, polycondensation, aging, drying, and thermal decomposition. The hydrolysis takes place in either water or an organic solvent like alcohols. This is then followed by condensation of adjacent molecules to form a colloidal dispersion. Condensation or polycondensation leads to higher viscosity. During the aging step, polycondensation continues along with the reprecipitation of the gel network, which ultimately increases the thickness between the colloidal particles. Later in the drying process, water or organic solvents are evaporated off the gel structure. Finally, to obtain the final powder, remaining volatiles are removed by thermal treatment which is also referred to as calcination. Generally, post-thermal treatments are necessary for obtaining crystalline structures. The precursors used in metal oxide synthesis through the sol-gel method generally includes metal salts or alkoxides, citric acid as a chelating ligand, and alcohol as a cross-linking agent. The gel is normally heated at 373 K for 10-24 h to obtain a dry powder. Then, the powder is annealed at high temperatures to improve the crystallinity of the particles. For strontium aluminates, these temperatures are usually in the range of 1373-1673 K, which results in the growth of the particle size. The main disadvantage of the sol-gel method is the large volume of solvent required. Moreover, it has been shown that decreasing the size of the particles comes to the expense of decreasing the afterglow intensity and duration. Nevertheless, nanoparticles with a size of about 60 nm have been obtained at 1173 K, which showed an afterglow duration of 14 h [87].

The effect of the cooling rate on the ratio of monoclinic to hexagonal **SA** was studied in [88]. After keeping undoped as well as Eu- and Dy-doped **SA** samples at 1373 K for 4h, they studied the effect of different cooling rates from 2 K/min to 20 K/min. They observed the formation of both monoclinic and hexagonal **SA**, with a maximum hexagonal content of 26.8% in the Dy-doped sample cooled at 2 K/min. For this composition, the cooling rate of 10 K/min yielded 97.6% of the monoclinic modification. This observation shows that also the cooling speed can have a dramatic effect on the phase purity of the sample.

Misevicius et al. [89] prepared **S_4A_7**:Ce^{3+} particles via the sol-gel method followed by a post-annealing step at 1573 K. The precursor particles agglomerated during the annealing process. Interestingly, when boric acid was used as flux in the reaction mixture, hexagonal plates (ca 5 μm diameter) with well-defined edges were obtained.

3.3.4. Microwave heating

In some cases, microwave heating has been applied instead of the conventional heating methods. Application of microwave heating is well-known for uniform heating of the reaction mixture and decreasing the reaction time. It is not only used for the preparation of the precursor materials, but also for the calcination and crystallization process. Wu et al. [90] showed that it was possible to obtain crystalline **SA**:Eu^{2+} structure using microwave heating for only 30 minutes at a temperature as low as 1023 K. The authors reported over 20 h afterglow for the sample annealed at 1173 K, which was comparable to the phosphors prepared via the solid-state method at 1673 K. At 1173 K, nicely crystalline **SA** was obtained in only 15 minutes. In another work [91] the crystallization process was reported to complete in only 10-20 min. With the conventional heating of the precursors prepared by the same sol-gel method this process was completed in 2h at 1473 K [92].

3.3.5. Hydro (solvo) –thermal synthesis

Hydrothermal synthesis is defined as a method to prepare inorganic materials in aqueous solutions above ambient pressure and temperature [73, 74]. Solvothermal term is applied for the reactions performed in organic solvents. Usually, the reaction is carried out in sealed reaction vessels defined as autoclaves. Heating the reaction mixture at temperatures above the boiling point of the employed solvent increases the pressure inside the reactor, dramatically. Due to the synergistic effect of high temperature and pressure, highly crystalline materials can be produced without the need for post-annealing treatments. In addition to obtaining homogeneous composition, utilization of organic additives and/or surfactants can offer control over the size and morphology of the particles. Ye et al. reported the formation of crystalline **SA** nanotubes which were obtained from a solvothermal reaction in a cetyltrimethylammonium bromide/n-butanol/water mixture at 393 K for 16h followed by annealing at 1573 K for 4h [93]. These nanotubes had a diameter of ca 150 nm. **SA** nanosheets were obtained from hydrothermal synthesis (443 K, 24h) starting from metal nitrate solution, followed by 2h annealing at 1573 K [94]. In 2009, Karmaoui et al. [95] could successfully synthesize $SrAl_4O_7$ (**SA_2**) along with $CaAl_4O_7$ and $BaAl_4O_7$ compounds via a one-pot solvothermal reaction, starting from metal alkoxides. Lack of water in the reaction mixture made it easier to achieve similar reactivity for the metal precursors. According to the authors, these crystalline structures could be prepared by a reaction carried out at 548 K, which is remarkably lower than the temperature required for conventional solid-state method or post annealing step in the sol-gel method.

We have recently synthesized **SA_6**:Eu^{3+} precursor nanoparticles with excellent morphology and narrow size distribution in the range of 200-300 nm via a solvothermal method. Annealing these particles at 1423 K resulted in nanocrystalline particles with hexagonal morphology, as shown in Figure 4 [96].

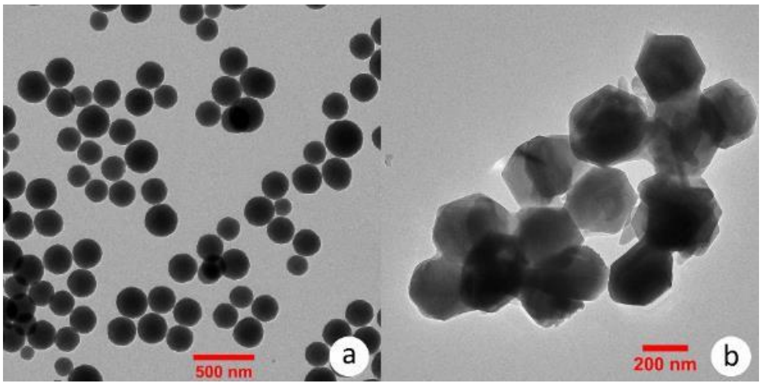

Figure 4: a) $SrAl_{12}O_{19}:Eu^{3+}$ precursor nanospheres and, b) $SrAl_{12}O_{19}:Eu^{3+}$ particles obtained upon annealing at 1423 K for 3 h [96]

The table 3 below summarizes some of the synthesis experiments reported in the literature.

Table 3. Representative examples of the synthesis of strontium aluminates with different methods.

Compound	Synthesis method	Temperature (K)/time	B_2O_3 content	Particle size	Afterglow duration	Ref.
S$_4$A	Solid state	1537-1773/3h	0	< 50 µm		[97]
S$_3$A	Solid state	1573-1623/4h	small		Several h	[56, 98]
S$_3$A	Solid state	1423/4h	30mol%	0.5-15 µm	> 1 h	[99]
S$_3$A	Solid state	1273-1523/2h	< 7 wt%		> 600 s	[83, 100]
S$_3$A	hydrothermal	1273-1773/3-4h	0	< 3 µm	Several min.	[101, 102]
S$_3$A	hydrothermal	513/12h	0	< 5 µm		[103]
S$_3$A	Sol-gel	680 W (microwave)/10-20 min.	0	1 µm	20 min.	[91]
S$_3$A	Sol-gel	1373-1473/2h	0	1-2 µm	Several min.	[92, 104, 105]
S$_3$A	Sol-gel	1173/16h	0			[106]
SA	Solid state	1573-1623/3-4h	0-15 mol%	< 15 µm	> 10 min.	[107-111]
SA	Solid state	1073-1693	3 mol%	< 30 µm	16-100 h	[112]
SA	Combustion	673-1173	small	30-100 nm	2743 s	[82, 113-116]
SA	Combustion	1373/2h	0	15-45 nm	16 h	[117]
SA	Combustion	1573/2h	0	<3 µm	> 1000 s	[37]
SA	Combustion	873-1073 (detonation)	0	20-50 nm		[118]
SA	Combustion	873-1173	0	10 µm		[119]
SA	Combustion	723	2 wt%	200-500 nm		[120]
β-SA	Combustion	1173/3h	0			[121]
SA	Sol-gel	1273/3h	0	100-150 nm		[122]
SA	Sol-gel	1273-1773/2-3h	0	1-5 µm	Several min.	[123-125]
SA	Sol-gel	1023-1273 (microwave)/15-120 min.	< 20 wt%		> 20 h	[90]
SA	Sol-gel	1173-1773/1-10h	small			[126]
SA	Solid state Sol-gel	1573-1773/2h 1373-1673/2h	0 0	ca 3 µm < 100 nm		[87]
SA	Sol-gel	1373-1473/3h	0	1-2 µm	Several min.	[127]
SA	Sol-gel	1473/4h	0	20-200 µm	253 min.	[128]
SA	Hydrothermal	1373-1473/3-4h	0	< 15 µm		[93, 129, 130]
SA	Hydrothermal	773-1073/12-48h	0			[131]

SA	Hydrothermal	1373/4h	0.5 wt%	1-2 µm	> 3000 s	[132]
SA	Hydrothermal-coprecipitation	1323-1473/4h	0	0.15-1 µm	Several min.	[133]
SA	Microwave	1523-1873/30min	0			[131]
SA	Solvothermal-coprecipitation	1423-1473/4h	0	3 µm	Several min.	[134]
SA	coprecipitation	1573/3h	0	< 10 µm	200 min.	[135]
SA	coprecipitation	1173-1573/6h	0	300-400 nm		[136]
SA	Microemulsion	1173-1273/3h	0	40 nm		[137]
SA	Microemulsion-coprecipitation	1173-1473/2h	small	< 200 nm	> 8 h	[138]
SA	Spray pyrolysis	1173-1773/2h	0	< 1.5 µm	> 7000 s	[139-142]
β-SA	Spray pyrolysis	1573/2h	0	< 1 µm		[143]
S_2A_3	Solid state	1473/12h	2.5 %	1-10 µm		[56]
S_2A_3	Solid state	1273/2h	small		240 min.	[144]
S_4A_7	Solid state	1473/10h	small			[56]
S_4A_7:	Solid state	1473-1823/5h	small			[16, 109, 145, 146]
S_4A_7	Solid state	1623/3h	small		> 15 h	[147]
S_4A_7	Solid state	1573/7h	small			[148]
S_4A_7:	Combustion	1373/6h	small		(NIR) 31 min	[149]
S_4A_7	Combustion	1573/3h	0		Blue: > 10 h Red: several min.	[150]
S_4A_7	Combustion	1573/3h	0	20-300nm	Several min.	[121, 151]
S_4A_7	Sol-gel	1573/4h	2.5 wt%	0.2-1 µm		[89]
S_4A_7	Sol-gel	1423/10h	10-30 at%		> 14 h	[70]
S_4A_7	coprecipitation	1523/3h	small	< 2 µm		[152]
S_4A_7	Microemulsion	1273-1473/5h	small	50 nm	Several sec.	[153]
S_4A_7	Microemulsion	1373/3h	5-20%	50-200 nm	850 s	[69]
SA_2	Solid state	1223/5h	2.5-7.5wt %		5-10 min.	[154, 155]
SA_2	Solid state	1673	0-20 mol%			[156]
SA_2	Combustion	1373/3h	0	< 300 nm		[121]
SA_2	Combustion	1073/1.5h	0	Several µm		[157]
SA_2	Combustion	873/5min.	5-15 mol%		> 30 min.	[158]
SA_2	Sol-gel	1273/3h	0	< 50 µm		[159]
SA_2	solvothermal	548/2days	0	few µm		[95]
SA_6	Solid state	1573-1873/2-4h	< 10 mol%			[109, 160-162]
SA_6	Combustion	1073-1673/4h	0	< 5 µm		[163-165]
SA_6	Combustion	773/<5min.	0	0.4-1 µm		[166]
SA_6	Sol-gel	1373/2h	0			[167]

4. Rare earth doping in strontium aluminates

Aluminates can be doped with transition metal ions or rare earth ions. In the case of Cr^{3+} and Mn^{4+}, these ions substitute for Al^{3+} in the lattice [168] while, as shown below, both divalent and trivalent rare earth ions will be located on the Sr^{2+} sites.

4.1. Trivalent ions

Trivalent rare earth ions can be doped into the strontium aluminates, as shown by the examples presented in Table 4 below. For **SA**, high resolution X-ray and neutron diffraction data [169] showed that the bond valency of Al^{3+} is normal (2.96-3.06 for the different sites), while the bond valency of Sr^{2+} is low (1.69 and 1.89 for Sr1 and Sr2 respectively). This low value is in principle not favorable for substitution by a trivalent lanthanide. The experimental results presented in [169] showed also that for **SA** doped with 1% of Eu^{3+} or Nd^{3+} which were prepared by heating in air, small amounts of $EuAlO_3$ and $NdAlO_3$ were also formed, indicating that the solubility of trivalent rare earth ions in **SA** remains low. The solubility of Ln^{3+} (Ln=Eu, Nd) decreases from $CaAl_2O_4$ to $BaAl_2O_4$, and the effective doping level of trivalent rare earth ions in these aluminates is found to be much lower than the nominal doping [170].

High frequency EPR of the S-state ion Gd^{3+} in $Sr_{0.98}Al_{2.0}O_4$:$Dy_{0.018}Gd_{0.002}$ showed the presence of 2 signals with similar intensity and similar zero-field splitting parameters than Eu^{2+} and confirm that the trivalent rare earth ions occupy indeed both Sr^{2+} sites in the strontium aluminates [171]. The luminescence of Ce^{3+} and Eu^{2+} in **SA₂** and **SA₆** has been studied by Gedekar et al. [157] Using the correlations between emission properties of divalent (see below) and trivalent rare earth ions in crystals developed by Dorenbos [172-176] the spectroscopic properties (crystal field (CF) splitting, centroid shift, red shift and Stokes shift) of Eu^{2+} were well predicted using the data for Ce^{3+} in the same host, and confirm that both trivalent Ce and divalent Eu occupy the Sr^{2+} sites in the crystal. Shi et al. [177] also obtained this result. Additionally, they have studied theoretically the substitution of Sr^{2+} by Ce^{3+} and Na^+ and found that the substitution of Sr^{2+} by Ce^{3+} is favored on site 2. Recently, STEM studies of **S_4A_7**: Eu,Dy single crystals confirmed that the rare earth ions are found on the Sr sites [178]. In this work, DFT simulations also indicate that Eu and Dy would incorporate onto adjacent Sr sites along the [012] direction, which can enable the energy transfer related to the persistent emission. The doping of **SA** with Eu^{3+} has been studied experimentally and theoretically by dos Santos et al. [179]. These authors considered theoretically the following substitution reactions:

Substitution at the Al site: $\frac{1}{2}Eu_2O_3 + Al_{Al} \rightarrow Eu_{Al} + \frac{1}{2}Al_2O_3$

Substitution at the Sr site (compensation by Sr vacancy): $Eu_2O_3 + 3Sr_{Sr} \rightarrow \left(2Eu_{Sr}^{\cdot} - V_{Sr}^{''}\right) + 3SrO$

Substitution at the Sr site (compensation by Sr^{2+}/Al^{3+} substitution)

Substitution at the Sr site (compensation by O^{2-} interstitial): $Eu_2O_3 + 2Sr_{Sr} \rightarrow (2Eu_{Sr}^{\cdot} - O_i') + 2SrO$

Substitution at the Sr site (compensation by Al^{3+} vacancy)

The lowest-energy charge compensation mechanism involves substitution at the Sr site with oxygen interstitial compensation. The authors calculated for this process 6 situations with two Eu ions located in 2 of the 4 Sr sites of the unit cell. The extensive literature for rare-earth doped CaF_2 supports this results, as tetragonal and trigonal charge compensations with interstitial fluoride ions are commonly observed [180, 181]. The analysis of the crystal structure of **SA** [179] shows that there are two different voids labelled V1 and V2 (Figure 5). There are three voids (V1) located at 294.6, 297.2 and 308.1 pm from the strontium atom on site 2, and three voids (V2) located at 278.0,279.8 and 333.8 pm from the strontium atom on site 1. The fractional coordinates are (-0.019, 0.163, 0.682) and (0.506, 0.315, 0.313) for V1 and V2 respectively [182].

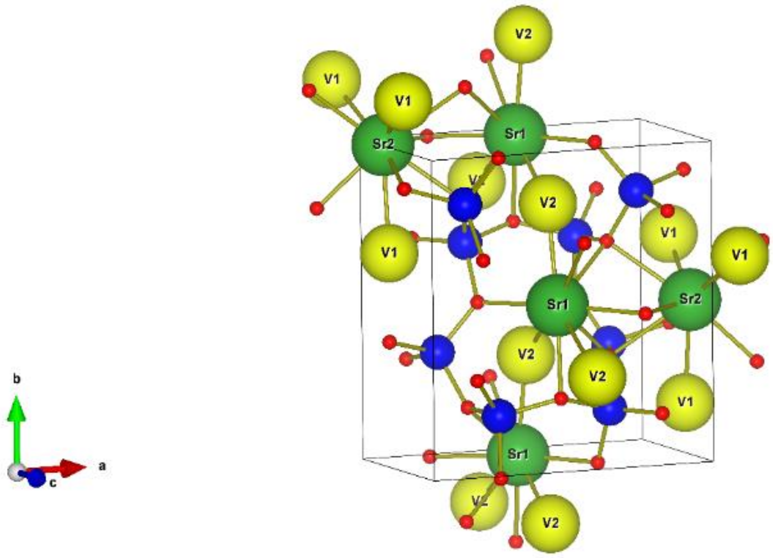

Figure 5: Crystal structure of **SA** and location of the two different voids labelled V1 and V2.[182]

If strontium is replaced by a trivalent ion such as Eu^{3+} and Dy^{3+}, the excess positive charge can be compensated by a negative charge located in these voids. This excess charge can be for instance a single electron (F-center), or an interstitial OH$^-$, O$^-$, or O^{2-} (which would compensate the charge of two trivalent ions). The presence of an interstitial compensation negative ion/charge on these void sites is expected to have a strong impact on the crystal field of the dopant trivalent rare earth ion, as it adds formally a ligand into the coordination sphere. Similar voids are also found in **Sr_4O_7**, as illustrated in Figure 6, however in this case the distances between the Sr sites and the voids are significantly larger: d(Sr1-V1) = 353.7 and 386.1 pm, d(Sr2-V2) = 319.3 nm.

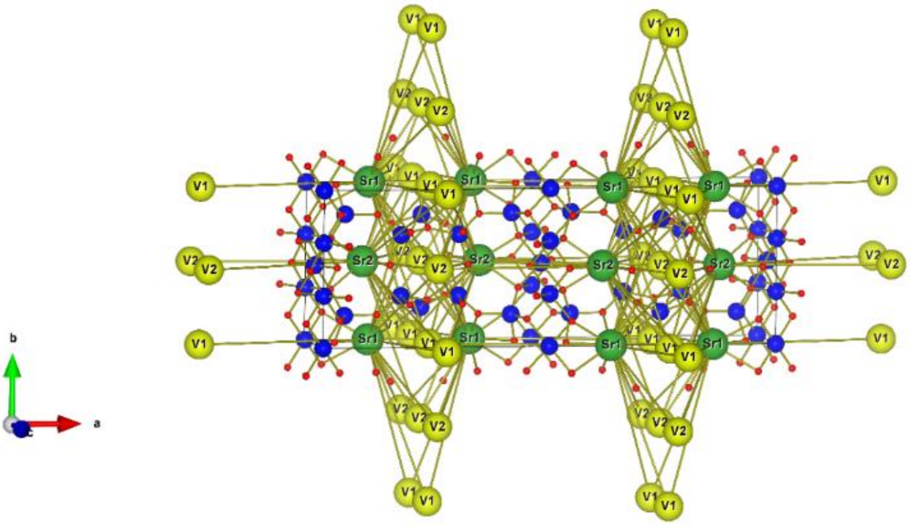

Figure 6: Crystal structure of **S_4A_7** and location of the two different voids labelled V1 and V2 [96].

Table 4. Representative examples of Strontium aluminates doped with trivalent rare earth ions.

Host crystal	RE dopant(s)	Applications	Ref
SA_6	Ce^{3+}	Blue-emitting lamp phosphor	[157, 183, 184]
SA_6	Pr^{3+}	laser	[11, 163, 185-197]
SA_6	Nd^{3+}	Laser crystal	[12, 198]
SA_6	Sm^{3+}	Laser	[199, 200]
SA_6	Gd^{3+}	UV emission	[201]
SA_6	Tb^{3+}	Phosphor, VUV sensitization	[202, 203]
SA_6	Dy^{3+}	Warm white light-emitting diodes	[164]
SA_6	Er^{3+}	Upconversion	[165]
SA_2	Ce^{3+}	Blue-emitting phosphor	[157]
SA_2	Pr^{3+}	Phosphor	[204]
SA_2	Sm^{3+}	Orange-light emitting displays	[159, 205, 206]
SA_2	Dy^{3+}	White light-emitting diodes	[206]
SA_2	Tm^{3+}	Phosphor	[207]
SA_2	Yb^{3+}, Tb^{3+}	Upconversion	[208]
S_4A_7	Ce^{3+}	Phosphor	[89, 209-212]
S_4A_7	Sm^{3+}	UV/blue-excited white LEDs	[213-215]
S_4A_7	Sm^{2+}	Luminescence conversion	[215]
S_4A_7	Tb^{3+}	Backlighting display	[211, 216, 217]
S_4A_7	Dy^{3+}	White LEDs	[214]
S_4A_7	Yb^{2+}	Persistent phosphor	[218]
SA	Ce^{3+}	Displays and solid-state lighting	[177, 219-229]
SA	Pr^{3+}	Scintilation, yellow-orange phosphor	[230-232]
SA	Nd^{3+}	Laser, NIR emission	[233, 234]
SA	Sm^{3+}	Phosphor	[235, 236]
SA	Gd^{3+}	UV emission	[237]
SA	Tb^{3+}	Blue-green Phosphor	[227, 238-241]
SA	Dy^{3+}	WLED, codopant persistent phosphor	[114, 236, 242-246]
SA	Ho^{3+}	Upconversion	[247]
SA	Er^{3+}	NIR emission	[36, 248-252]
SA	Yb^{3+}		[229]
SA	Yb^{2+}	Persistent phosphor	[253]
Sr_3A	Ce^{3+}	phosphor	[45, 100, 254]
Sr_3A	Pr^{3+}		[99]
Sr_3A	Sm^{3+}		[103]
Sr_3A	Tb^{3+}		[106]

Sr$_3$A	Er^{3+}	NIR emission	[45, 255]

4.2. Divalent ions

Reducing conditions can be achieved using either a 5%H$_2$:95%N$_2$ gas atmosphere at high temperature (typically above 1173 K), or by the addition of graphite powder to the reaction mixture [256]. In some instances, the formation of Eu^{2+} is observed even in the absence of reducing atmosphere. **S$_4$A$_7$**:Eu(0.01) prepared in air at 1673 K for 5 h with intermediate grindings presents under 365 nm excitation a broad f-d emission (Eu^{2+}) at 492nm, and weak emissions at 593 and 617 nm corresponding to the $^5D_0$ – $^7F_{1,2}$ emissions of Eu^{3+} [216], confirming previous results [257].

SA ceramics with nominal composition Sr$_{(1-x-y)}$Al$_{1.94}$B$_{0.06}$O$_4$:Eu$_x$,Dy$_y$ (x =0.001, 0.01, y =0.001, 0.005, 0.01) were prepared in air with the laser sintering technique using a CO$_2$ laser. These samples showed under 365 nm the typical Eu^{2+} emission at 512 nm, and under 280 nm excitation additionally weak bands around 610 nm from the $^5D_0$-$^7F_2$ emission of Eu^{3+} [258].

The ratio between Eu^{2+} and Eu^{3+} can be quantified using XANES measurements around the Eu LIII edge. XANES measurements by Dutczak et al. [109] show the typical Eu^{2+} peaks at 6973.90 eV for **SA**:Eu^{2+} and 6973.86 eV for **S$_4$A$_7$**:Eu^{2+} prepared with 5%H$_2$:95%N$_2$, but only a very weak signal at about 7-8 eV higher energy which would be typical for Eu^{3+}. The XANES data reported in [258] for the laser annealed sample showed in contrast a shoulder at around 6974 eV for Eu^{2+} and a strong peak at 6983 eV for Eu^{3+}. It appears thus that the observation of Eu^{2+} emission is not an indication that most of the Europium ions are indeed divalent. This can be rationalized by the fact that the allowed f-d transitions of Eu^{2+} have a much stronger extinction coefficient than the forbidden f-f transitions of Eu^{3+}. If one associates the extinction coefficient with the radiative lifetime (ca 1 µs for Eu^{2+} and 1 ms for Eu^{3+}), then already 5-10% of Eu^{2+} can mask the emission of Eu^{3+}. Heating **SA$_3$**:Eu^{2+} in air at 773 K leads to ca 50% reduction in emission intensity, while for **S$_4$A$_7$**:Eu^{2+}, the same treatment yields no intensity reduction [56]. The presence of boron can prevent the oxidation of Eu^{2+} in air. Yoon et al. [259] observed that heating **SA**:Eu^{2+} in air to 1023 K almost completely oxidized Eu^{2+}, leaving a white powder, while the same sample co-doped with boron still showed a strong Eu^{2+} emission.

The Rietveld refinement from powder X-ray diffraction of (Sr$_{0.96}$Eu$_{0.04}$)O.Al$_2$O$_3$ indicated that that fractional occupation of Eu^{2+} on the 2 Sr^{2+} sites is very similar (3.89% and 4.095%) and corresponds practically to the nominal Eu^{2+} content [260]. DFT calculations [65] on supercells of **SA** with Eu^{2+} either on site 1 or 2 showed only very small energy differences for the substitution on each site (32 meV on site 1 and 22 meV on site 2) and confirmed that no preferential site substitution of Sr^{2+} by Eu^{2+} in **SA** is expected.

Yb^{2+}-doped **SA** was prepared by solid state reaction starting from SrCO$_3$, Al$_2$O$_3$ and rare earth oxides by annealing at 1523-1873 K under reducing atmosphere, with the optimum temperature of 1723 K (based on the Yb^{2+} emission intensity) [253]. Sm^{2+} can be obtained in **S$_4$A$_7$** together with Sm^{3+} with strongly reducing conditions (20%H$_2$/80%N$_2$). For **SA$_6$**, Sm remains trivalent even under heating to 1973 K with (20%H$_2$/80%N$_2$) [215]. Tzu-Piao Tang et al. [235] have studied Sm^{3+} doped **SA** prepared both with or without boron oxide addition. Firing the sample in reducing atmosphere does not lead to the reduction of Sm^{3+}, and typical Sm^{3+} emissions are observed at 562, 596 and 643 nm.

High frequency EPR spectra of Eu^{2+} in **SA** and **S$_4$A$_7$** [261] yield in each case 2 sets of spectra which can be described with the large zero-field parameters given in Table 5. It is important to note that due to the high zero-field strength, conventional X-band EPR spectra for Eu^{2+} in **SA** give a second order spectrum with many bands between 0.03 and 0.5 T [262] which cannot be assigned without the full diagonalization of the spin Hamiltonian. Fourth-order spin Hamiltonian parameters were obtained for Eu^{2+} in a mixture of 5:1 mixture of **SA** and **S_4A_7** powders [263]. The spectra showed two pairs of centers with relative intensity 5:1, confirming that the two different Sr sites in both hosts are equally substituted with Eu^{2+}.

Table 5. Spin Hamiltonian parameters for Eu^{2+} and Gd^{3+} in **SA** and **S_4A_7**.

Host	Ion	g	ǀDǀ (cm^{-1})	ǀE/Dǀ
$SrAl_2O_4$	Eu^{2+}	1.989	0.140	0.258
	Eu^{2+}	1.989	0.112	0.306
	Gd^{3+}	1.986	0.138	0.333
	Gd^{3+}	1.986	0.091	0.333
$Sr_4Al_{14}O_{25}$	Eu^{2+}	1.984	0.102	0.333
	Eu^{2+}	1.984	0.092	0.333

5. Eu^{2+} emission in strontium aluminates

The emission spectra of Europium (2+) have been the object of many investigations [109, 172]. As the 5d energy levels depend strongly on the environment, Eu^{2+} emissions can be observed from the near UV to the red. P. Dorenbos [172] has rationalized the position of the lowest energy $4f^7 \rightarrow 4f^6 5d^1$ transition in the following way (see Figure 7). The redshift **D** can be expressed as follows (note that the red shift **D** is specific for each different host crystal as well as for each different site in the host crystal):

$$D = \Delta\varepsilon_c + \frac{\varepsilon_{CFS}}{r} + \Delta\varepsilon_{CFS}(free) = \Delta\varepsilon_c + \Delta\varepsilon_{CFS} + \Delta\varepsilon_{CFS}(free)$$

where $\Delta\varepsilon_c$ is the centroid shift of Eu^{2+} on the site in the crystal, ε_{CFS} is the crystal field splitting, and **r** is a parameter expressing the fraction of ε_{CFS} that contributes to the redshift. The dashed line on the top of the figure corresponds to E_{free} (= 34000 cm^{-1} for Eu^{2+}) [172] which is a constant for each lanthanide ion with a value equal or close to the fd-transition energies for the free (gaseous) lanthanide ions. $\Delta\varepsilon_{CFS}$(free) corresponds to the weight-averaged contribution of the $4f^6$ levels, and is numerically equal to 1900 cm^{-1}. The centroid shift is related to the nephelauxetic effect which can be associated with the covalency of the europium-ligand (in this case oxygen) bonds [173, 264]. It is important to note that polarizability effects also come into play [71]. The crystal field splitting can by related to the rare-earth ligand (= oxygen) bond length. An empirical relation for the crystal field splitting is:

$$\varepsilon_{CFS} = \beta_{poly}^{Q} \cdot R_{av}^{-2} = \beta_{poly}^{Q} \cdot \left(\frac{1}{N}\sum_{i=1}^{N}(R_i - 0.6 \cdot \Delta R)\right)^{-2}$$

β_{poly}^{Q} is a constant related to the type of coordination polyhedron and the valence of the rare earth ion, R_i the bond length with each of the N coordinated anions (oxygen dianions) and ΔR the difference in ionic radii between the host cation (strontium) and the lanthanide dopant. For lower coordination numbers of Eu^{2+}, one expects on one side a higher crystal field splitting (as the europium oxygen bonds are shorter), and also a higher covalency, leading to a larger centroid shift. The combination of both effects leads to emissions shifted to the red, and is illustrated on the right hand side of Figure 7.

The position of the absorption band is given by:

$$E_{abs} = E_{free} - D$$

And the position of the emission band:

$$E_{em} = E_{free} - D - \Delta S$$

where ΔS is the Stokes shift.

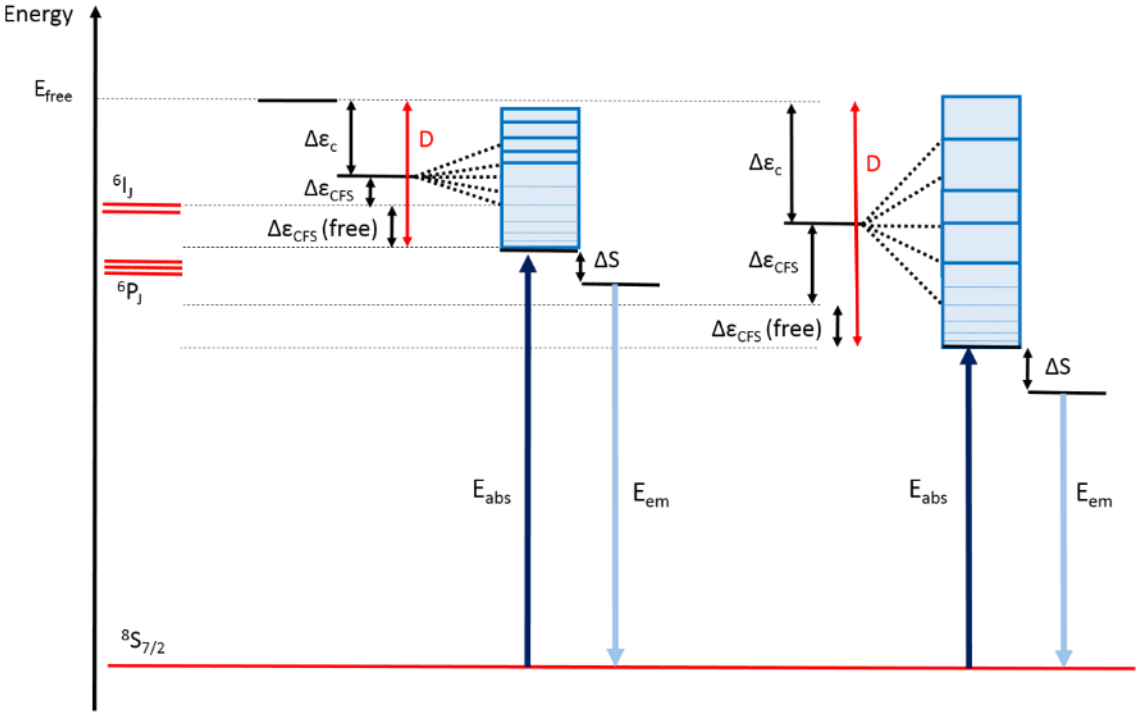

Figure 7. Schematic illustration of the higher energy levels of Eu^{2+} (see text for explanations). At the left side, the first excited levels of the $4f^7$ configuration ^6P_J with J = 7/2, 5/2 and 3/2 which are observed around 28000 cm^{-1} and two of the ^6I_J levels (around 31000 cm^{-1}) are shown. In the center, a case with low crystal field splitting and low centroid shift is illustrated, and the right hand side depicts the case with high crystal field splitting and high centroid shift.

The luminescence of Eu^{2+} in strontium aluminates has been studied by many authors [56, 97, 109, 265-268]. Many different facets of Eu^{2+} luminescence properties are observed in this family of compounds. Dutczak et al. [109] have compared systematically the emissions in different hosts. Their data, combined with the results for **S_2A_3** [56], and **S_4A** [97] and others, are compiled in the Table 6. All these emission bands have lifetimes around 1 µs which are typical for Eu^{2+} f-d transitions [144].

Table 6. Emission properties of Eu^{2+} in strontium aluminates. The thermal quenching temperature TQ_{50} is the temperature at which the emission intensity is half the low temperature emission intensity.

Compound		Emission wavelength (nm)	τ at 4K (µs)	τ at 298 K (µs)	Quantum yield int/ext	TQ_{50} (K)	Band gap at 4 K (eV)	Ref.
$Sr_4Al_2O_7$	**S_4A**	607			0.25/0.19			[97]
$Sr_3Al_2O_6$	**S_3A**	535	0.6			80	6.2	
		625	1.1			135		[105, 269]
$Sr_7Al_{12}O_{25}$	**S_7A_6**	410						[42]
$SrAl_2O_4$	**SA**	445	0.4			230	6.6	[270]
		520	1.2-1.7	0.7	0.55	440		[265, 270]
$Sr_2Al_6O_{11}$	**S_2A_3**	462						[56]
		493						[56]
$Sr_4Al_{14}O_{25}$	**S_4A_7**	425 400	0.6	0.24 0.24			6.3	[267]
		490	0.94	0.83		400		[266, 267]
$SrAl_4O_7$	**SA_2**	390 470				260	6.3	[156] [271]
$SrAl_{12}O_{19}$	**SA_6**	397		8		380	7.76	

The lowest emission wavelength is observed for Eu^{2+} in **SA_6**. As shown in Table 2, the coordination number for Eu^{2+} is 12 and the Sr(Eu) – O bond length are 0.277 nm. This compound is the most ionic among the strontium aluminates (it has the highest bandgap), and due to the long bond lengths, the crystal field splitting is the smallest. This situation corresponds to the one illustrated in the middle of Figure 7.

It is interesting to note that for **SA_6**, at low temperature, only f-f transitions around 360 nm are observed [109]. With increasing temperature, energy is thermally transferred to the lowest $5d^1$ state. As illustrated in Figure 7, the corresponding energy levels are slightly lower than the lowest f-d level in the middle of the figure. The lifetime observed as a function of temperature reflects the combination of lifetimes of both types of emissions:

$$\frac{1}{\tau} = \frac{p_1 + p_2 \cdot e^{-\frac{\Delta E}{kT}}}{1 + e^{-\frac{\Delta E}{kT}}}$$

In this expression τ is the observed lifetime, and p_1 (= $1/\tau_1$) and p_2 (= $1/\tau_2$) are the individual decay rates from levels 1 and 2 to the ground state, and ΔE is the energy difference between states 1 (^6P_J) and 2 ($4f^65d^1$). At 100K, the measured lifetime of $^6P_J \rightarrow {}^8S_{7/2}$ is 0.9 ms, while at room temperature, the lifetime of the peak at 397 nm is 8 µs, which is much longer than expected for Eu^{2+} f-d transitions and which is explained by the equation above. This temperature-induced change of populations of excited Eu^{2+} states has equally an effect on the observed emission intensities, and for **SA_6** between 100 and 200 K the intensity of the f-f transition decreases, while the intensity of the f-d band increases. At room temperature, only the broad f-d emission band at 397 nm is observed [109].

The highest emission wavelength among the different Eu-doped strontium aluminates is observed for **S$_3$A** at 625 nm. In this compound, there are 6 different Sr sites, which can be divided into 2 groups of 3. The first group has a coordination number of 6, which is associated with this emission at 625 nm, the other group with coordination numbers 6+3, 7 and 9 is associated with the emission at 525 nm [109].

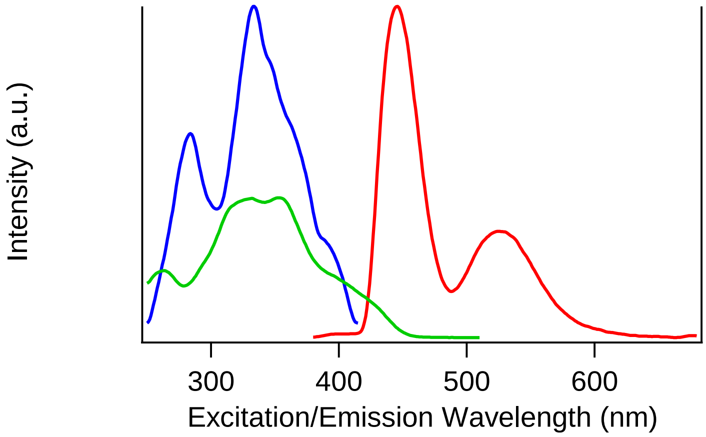

Figure 8: Excitation and emission spectra of SrAl$_2$O$_4$:Eu^{2+} doped with 0.01 mol% at 10K (data from ref [272]). Blue trace: excitation spectrum observed at 430 nm, green trace: excitation spectrum observed at 520 nm. Red trace: Emission spectrum excited at 370 nm.

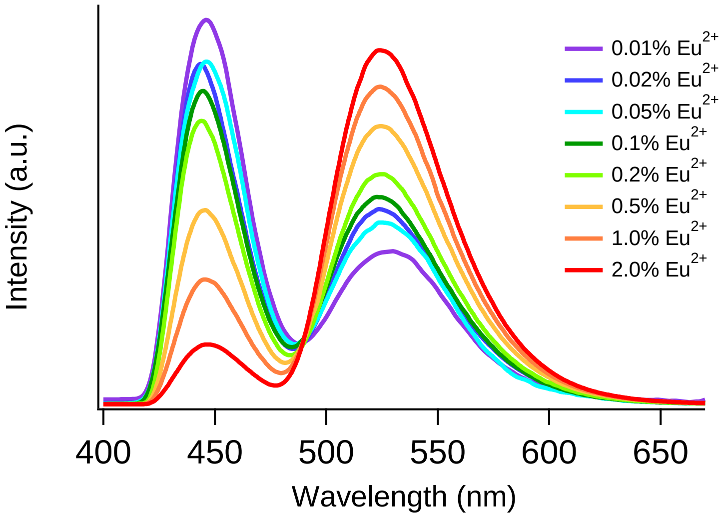

Figure 9: 10K Emission spectra excited at 370 nm of eight samples of **SA** with increasing Eu^{2+} content. The integral under the spectra were normalized. Data from ref. [272].

Eu^{2+}-doped **SA** presents at low temperature 2 emission bands observed at 445 and 520 nm. Figure 8 shows the low temperature excitation spectra for each of these two emission bands together with the emission spectrum excited at 370 nm. These spectra agree with those previously reported by Botterman et al. [273]. These authors report for the green and blue emissions at 10 K quite different values for the red shift D = 1.42 and D = 1.22 eV respectively, but similar values for the crystal field splitting (1.10 eV and 1.13 eV, respectively). The small wiggles appearing between 400 and 360 nm in the excitation spectrum observed at 430 nm (blue trace in Figure 8) correspond to the different ^7F_J states of the $4f^6$ electronic configuration, in agreement with the well resolved excitation spectrum reported in [268]. The peaks corresponding to these ^7F_J levels were observed between 24500 cm^{-1} (J=0) and 30040 cm^{-1} (J=6). Terraschke et al. [268] also observed Fano antiresonances with the ^6I_J (J = 9/2, 7/2) levels of Eu^{2+} at 31350 and 31650 cm^{-1}. The assignments of the two emission bands in **SA** is not so obvious, as the average Sr-O bond lengths of the 7 shortest bonds is very similar: 267 pm for site 1 and 269 pm for site 2. An empirical crystal field analysis [273, 274] suggests to assign the green emission to site 1 (stronger CF). However, recent multi-configurational ab initio calculations [275] assign the green luminescence unambiguously to Eu^{2+} at the Sr2 site, in agreement with the results reported previously by Shi et al. [177]. The extinction coefficient of the Eu^{2+} absorption was measured at 254 and 330 nm and found to be equal to 1289 and 1149 ± 15 $M^{-1}cm^{-1}$ respectively [276]. These values are comparable to the value of the extinction coefficient of 1130 ± 56 $M^{-1}cm^{-1}$ reported for $EuCl_2$ [277].

Figure 9 shows the low temperature emission spectra of Eu-doped **SA** with increasing Eu^{2+} content (data from [272], in agreement with previous results [273]). With increasing Eu^{2+} concentration, the relative intensity of the blue emission band at 450 nm decreases. A similar observation was also made for Eu^{2+} in $\mathbf{S_4A_7}$ [21], where the relative intensity of the 400 nm emission band decreases with respect to the 494 nm emission band with increasing Eu^{2+} concentration. The energy transfer in SA has been studied quantitatively in detail [272] with both lifetime and emission intensity measurements. Figure 10 illustrates the processes which were considered to analyze the data. This figure additionally indicates the separation from the top of the valence band to the lowest energy level of Eu^{2+} in **SA** which can be measured from the oxygen-to-Eu^{3+} charge transfer band in the same host [278]. In Eu^{3+}-doped **SA**, this band is observed at 275 nm and has a half-width of 40 nm [182, 273]. Botterman et al. [273] calculate that the ground states for the two different Eu^{2+} ions are at 4.53 and 4.45 eV above the valence band.

The decay rates for the blue (k_{blue}) and green (k_{green}) emissions are:

$$k_{green} = k_{fl_g} + k_{q_g}$$

$$k_{blue} = k_{fl_b} + k_{q_b} + k_{ET}$$

where $k_{q(green,blue)}$ are the quenching rates and k_{ET} expresses the energy transfer in the Dexter model [279]. Using these relations, the normalized luminescence intensity I (i.e. I = 1 if neither energy transfer nor quenching occurs) of the blue and the green emission can be expressed as follows:

$$I_{green}(r,T) \propto \frac{k_{fl_g}}{k_{fl_g} + k_{q_g}} + \frac{k_{fl_g}}{k_{fl_g} + k_{q_g}} * \frac{k_{ET}}{k_{fl_b} + k_{q_b} + k_{ET}}$$

$$I_{blue}(r,T) \propto \frac{k_{fl_b}}{k_{fl_b} + k_{q_b} + k_{ET}}$$

where I_{blue} and I_{green} represent the normalized luminescence intensity of the blue and green peak. Assuming further an Arrhenius process for the quenching and Dexter energy transfer mechanism [279], one obtains:

$$I_{blue}(r,T) \propto \frac{k_{fl_b}}{k_{fl_b} + A_b * e^{-{E_{a_b}}/{k_B*T}} + J * e^{-{2r}/{r_c}}}$$

A_b is a pre-exponential frequency-factor representing the quenching rate at infinite temperature (attempt rate). $E_{a,b}$ is the activation energy needed for thermal quenching of the blue emission. Furthermore, J is a pre-factor for the energy transfer, representing the spectral overlap and r is the average distance between two inequivalent Eu^{2+} ions; r_c is the critical radius, for which the transition probability is (1-1/e). The average distance between two inequivalent Eu^{2+} ions was calculated, assuming an even distribution of the Eu^{2+}, regardless the doping concentration c, with the expression:

$$r(\mathrm{Eu}^{2+}) = \sqrt[3]{\frac{V}{c/m * n}}$$

The volume V of the unit-cell of $SrAl_2O_4$ is 0.384 nm^3. Within this volume n = 2 formula units are incorporated and the structure has m = 2 inequivalent Sr sites.

Bierwagen et al. [272] obtained for the blue emission $E_a = 0.21\pm0.02$ eV and $r_c = 2.6\pm0.3$ nm using the luminescence intensities and $E_a = 0.18\pm0.01$ eV and $r_c = 3.4\pm0.7$ nm using the lifetime measurements. Very recently, the emission decay curves were measured at 77K using picosecond sources at 375 and 440 nm for a series of samples. These data revealed a strongly non-exponential behavior which could be analytically fitted using a Förster model, yielding a value for r_c of 1.6 ± 0.05 nm [280].

The values for the attempt rate A_b showed a large variation. The mean value for A_b is $1.5\pm1.3\cdot10^{11}$ Hz which is considerably smaller than for A_g, which is found to be $2.0\pm1.0\cdot10^{13}$ Hz. This attempt rate is related to the phonon frequencies [281]. The strongest Raman band of **SA** is observed at 465 cm^{-1} (1.4 10^{13} Hz) [282]. This value is quite close to the value obtained for A_g. The activation energy for the quenching of the green emission was found to be $E_a = 0.68\pm0.1$ eV. These latter values are in agreement with previous studies [281, 283].

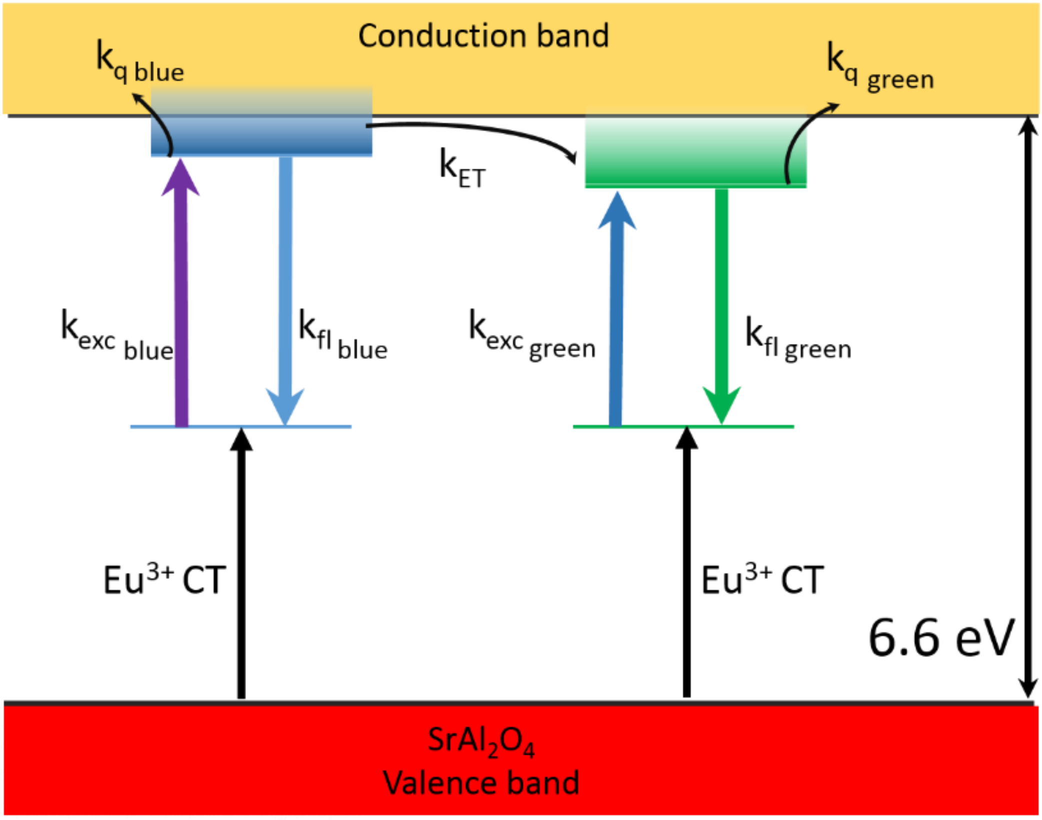

Figure 10: Energy level scheme of Eu^{2+} ions in **SA** and luminescence, quenching and energy transfer processes as described in the text.

The effect of Eu concentration in $Sr_{1-x}Eu_xAl_2O_4$ (high temperature synthesis) was studied [265]. While the quantum yield for a lightly doped **SA** was found to be 55%, it decreases only to about 34% in

$EuAl_2O_4$, i.e. the concentration quenching is not very strong. The decay of several $Eu_{1-x}Sr_xAl_2O_4$ samples (0<x<1) was measured at 23 K for all samples and a lifetime of ca 1.2 µs (comparable to the value of 1.7 µs observed by Blasse [270]) was observed [265]. Nakauchi et al. [284] have measured the room temperature lifetime of the green emission as a function of Eu^{2+} content in single crystals and observed an increase of the lifetime from 795 ns (0.5%Eu) to 847 ns (3%Eu) under 365nm excitation, which is also an indication of energy transfer between the different Eu^{2+} ions in the crystal.

In $EuAl_2O_4$, high pressure experiments up to 7 GPa show a continuous red shift of -230 cm-^{1}/GPa [285]. For SA doped with 1% Eu^{2+}, we observed a similar pressure shift of -250 cm-^{1}/GPa, measuring up to 4 GPa [286].

Europium-doped **S_4A_7** presents at room temperature 2 emission bands observed at 400 and 490 nm. These emission bands are assigned to the Sr sites with C.N. = 10 and 7 respectively [266, 267]. As for **SA**, the relative intensity of the 425 nm band decreases with increasing Eu^{2+} content, indicating that also in this compound energy transfer between Eu^{2+} ions on different sites takes place [21, 266]. The emission at 490 nm is quenched at TQ_{50} = 390 K for a very lightly doped sample ($Sr_{4(1-x)}Al_{14}O_{25}$:$4xEu^{2+}$ with x = 0.02%), but the quenching temperature is shifted to TQ_{50} = 410 K for samples with x = 1% [68]. The emission at 425 nm (observed at low temperature) shifts to 400 nm at room temperature. Dutczak et al. [267] have studied this evolution in detail. They assign the 400 nm emission band to the d-f emission, and the 425 nm emission to a europium trapped exciton (“anomalous emission” [287]). This anomalous emission is observed more frequently on sites with high C.N. and is characterized by a large Stokes shift and low quenching temperature [287]. The lifetime of the 425 nm emission band is 0.52 µs at 100 K and drops to 0.24 µs at 300 K, and the Stokes shift is estimated to be ca 5000 cm^{-1}, while the Stokes shift of the 400 nm emission is ca 3600 cm^{-1} [267].

6. Persistent luminescence in SA and S_4A_7 doped with Eu^{2+},Dy^{3+} and B^{3+}

6.1. Experimental aspects

Persistent luminescence is associated to the presence of emission centers and defects which can act as electron or hole traps following irradiation. These traps are released thermally and transfer their energy to the emitter, resulting in the long afterglow. The persistent luminescence is generally probed using afterglow and thermoluminescence (TL) experiments.

Afterglow measurements have been reported in many studies, however the precise protocol of the measurement is not systematically mentioned and this makes quantitative comparisons difficult. The norm ISO 17514:2004 [288] describes a standard procedure as follows: “30 mg of phosphor should be applied evenly on 1 cm^2 of surface and stored for at least 8h in the dark. Irradiate using a D65 light source [289] at 200 lx for 30 min or 400 lx for 20 min, and then store it in the dark. Measure the luminous intensity of the test sample 30 min, 90 min and 180 min after its storage. The ambient temperature should be 296 ± 2 K, and the relative humidity 50±15%.”

The amount of material exposed to light is a first parameter to control. Up to the abovementioned value of 30mg/cm^2, the afterglow after irradiation increases linearly with the amount of phosphor [290] above this value, a saturation is observed. The intensity of the irradiation is also important, as will be discussed further below.

The data presented in the Figure 11 below (taken from ref [291]) have been measured with this norm ISO17514:2004 and show quantitatively the effect of different nominal dopant concentrations on the observed afterglow. The presence of boron leads to a higher afterglow intensity (additional traps) and a significant flattening of the afterglow curve (deeper traps). The further addition of Dy^{3+} results in about 10 times higher afterglow intensity.

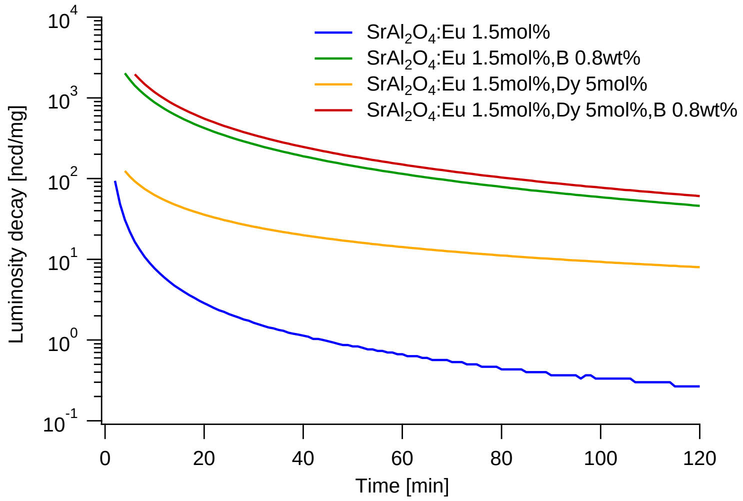

Figure 11: Afterglow curves measured at room temperature for different samples. Experimental conditions: 30 mg sample, mixed properly with 30 mg of varnish A206 and applied on a 1 cm^2 white coated aluminum plate, Illumination 400Lx, 20 Min. Data taken from [291].

Representing the data of Figure 11 on a log-log scale shows that all these afterglow data are non-linear, i.e. that these afterglow curves cannot be associated with a simple power law. In the literature, these afterglow curves are sometimes fitted with a sum of 2 or 3 exponentials, however the physical meaning of this treatment is questionable, not only because there is a large variation of parameters depending on the fitting domain (e.g. 1-60 minutes, 1-90 minutes, 1-120 minutes), but also because in **SA**, there is a great variety of traps from different origins which contribute to the observed afterglow (see below).

Thermoluminescence (TL) experiments can be performed with different excitation (loading) sources ranging from γ-rays as well as α and β radiation, or from the VUV to the visible, either broadband or at single wavelength, at different irradiation temperatures and with different temperature ramps. With high energy radiation, electrons are directly transferred from the valence band to the conduction band, leading also to the radiation-induced formation of color centers. Prior to the TL experiment, the samples are typically heated to 473-523 K in order to empty all the traps. Recently, Van der Heggen et al. [292] reported the presence of very deep traps with TL peaks above 523 K that have a very high trapping probability. It appears thus that heating to 523 K does not empty all the traps of the persistent phosphor, and this can potentially impact on the analysis of the data

6.2. Intrinsic traps

Several studies have addressed properties of intrinsic defects which can be expected in strontium aluminates [244, 293-298]. A first type of defects are the oxygen vacancies V_O^0, V_O^+ and V_O^{2+}. There is also a different notation for these defects in the literature on Al_2O_3 as shown in the table below [296, 297]. Recent density functional theory (DFT) calculations have shown that oxygen vacancies are likely to occur in **SA** both in the presence or absence of Eu^{2+} [293]. These defect states are calculated to be about 0.67 eV below the conduction band and can, therefore, act as electron traps.

Table 7: Summary of oxygen defects nomenclature in α-Al_2O_3.

Description		Symbol				
	F^{2+}	**F^{+}**	**F**	**F_2**	**F_2^{+}**	**F_2^{2+}**
	V_O^{2+}	V_O^{+}	V_O^{0}			
	Oxygen monovacancy with no electron	Oxygen monovacancy with one electron	Oxygen monovacancy with two electrons	Oxygen di-vacancy with four electrons	Oxygen di-vacancy with three electrons	Oxygen di-vacancy with two electrons

The V_O^+ can be in principle by observed by ESR spectroscopy. Another type of vacancy are those related to Sr vacancies (V_{Sr}) or to aluminum vacancies (V_{Al}). DFT calculations on defects in **SA** yield the energies of 0.13, 0.46 and 0.64 eV below the conduction band and 1.72 eV above the valence band for oxygen vacancies, of 0.008 and 0.062 eV above the valence band for Sr vacancies and of 0.29, 0.5 and 0.65 eV above the valence band for Al vacancies [244].

Takeyama et al. [295] studied the EPR of $Sr_xAl_2O_4$ (x=0.99, 1.00, 1.01) with and without Dy^{3+} doping. The EPR spectra of the sample with x=0.99 shows a superposition of eleven hyperfine bands with an anisotropic signal at g=2.007. The signal with the hyperfine bands was assigned to an [AlO_4^0] species (aluminum oxide hole species) and results from the coupling of the oxygen electron with the 2 adjacent Al nuclei with spin I=5/2. The anisotropic signal is assigned to a trapped hole. For x = 1.00 and 1.01, an additional signal at g=1.999 is assigned to a trapped electron in the host. Under UV irradiation, the intensity of the [AlO_4^0] increases significantly. This signal decays over hours, the decay rate decreases from x=1.01 to x=0.99 and shows that this [AlO_4^0] species is rather stable. Further, for x=1.00 and 1.01, the intensity of the signal at g=1.999 did not change.

In the presence of Dy^{3+}, the anisotropic signal at g=2.007 is clearly observed, indicating that this trivalent dopant leads to the formation of a hole trap. After UV irradiation, the [AlO_4^0] signals decay much faster, while the signals at g=2.007 (trapped hole) and 1.999 (trapped electron) decay very slowly (about 50% intensity loss after 12 h). Boutinaud et al. observed also that transition metal impurities (Mn^{2+},Mn^{4+}, Cr^{3+} and Fe^{3+}) can contribute to the EPR spectra observed in nominally undoped **SA** [299].

Vitola et al. [294] observed at 10K in undoped **SA** two emission bands at 435 and 510 nm which were excited at 229 nm and 246 nm. These bands were assigned to F and F_2 centers, by analogy with the results reported for Al_2O_3 [296, 297]. At room temperature, these emission bands become very weak under UV excitation, However, under X-ray excitation, these emissions become much stronger at low temperature, but are also quenched at room temperature. An additional broad emission band appears around 800 nm, but this emission is also quenched at room temperature. The TSL curve after X-ray excitation of the 800 nm emission band shows a peak at 100 K, a weak peak at 260 K and another strong peak at 400 K.

Nakauchi et al. [284] observed in undoped **SA** single crystals at room temperature weak emission bands at 480 and 560 nm upon excitation at 316 nm, in line with the observations by Vitola [294]. The luminescence decay curve for both peaks were fitted with a double exponential function with lifetimes of 5-6 and 15-20 ns, respectively.

Nazarov et al. [298] studied the emission of **SA** (1% Eu) using different excitations. The cathodoluminescence experiment revealed a new emission at 375 nm, in addtion to the Eu^{2+} emission at 520 nm and Eu^{3+} emission bands at ca 610, 650 and 700 nm. The emission at 375 nm is quenched at

200K, while the emissions at 520, 610, 650 and 700 nm keep their intensity. Under 8 eV irradiation, 2 emission peaks at 250 and 375 nm were observed at 10K. The excitation spectrum of the emission at 250 nm shows an onset at 6.7-6.8 eV, i.e. at the band gap of **SA** and is assigned to a self-trapped exciton. The other emission is excited at 6 eV (208 nm) and assigned to an intrinsic defect.

Table 8. Thermoluminescence experiments for undoped or Eu-only doped **SA** (w=weak)

Sample	Irradiation	Exposure time or dose	Temperature	TL Peaks (K)	heating rate	Ref
SA:Eu^{2+}:	200-300nm	30 min	10 K	55, 215, 270		[300]
SA:Eu^{2+}, Dy^{3+}	200-300 nm	30 min	10 K	215, 270		[300]
SA:0.02%Eu	375 nm	10 min	173 K	215, 270	0.17 K/s	[291]
SA:0.02%Eu	445 nm	10 min	173 K	215w,270	0.17 K/s	[291]
SA:1% Eu	254 nm	5 min	10 K	100, 200, 270 w	0.5 K/s	[301]
SA	X-ray		10 K	100, 260w,400	0.1 K/s	[294]
SA	X-ray	2 Gy	300 K	~740	1 K/s	[284]
SA:Eu^{2+}:	Hg lamp	1 min	80 K	150, 230, 360	0.13 K/s.	[302]
SA:Eu 5%	366nm	60 min	80 K	170, 195, 210	0.08 K/s	[303]
SA:Eu	X-ray	2Gy	300 K	370-470, 720	1K/s	[284]

Several authors have measured thermoluminescence of pure or Eu-doped **SA**, as shown in Table 8. These samples present TL peaks which can be divided into 4 temperature regions: very low temperatures (below 110 K), below 200 K, below 300 K and above 300 K. The peaks below 110 K are assigned to intrinsic defects [294] and the peaks at 215 and 270 K are assigned tentatively to hole traps at the 2 different strontium sites [300]. It is interesting to note that very deep traps can also be created by X-ray irradiation, as seen by the TL peaks above 700K [284].

Recent experiments on nitride-doped **S$_4$A$_7$** [304] suggest that the incorporation of N^{3+} favors the generation of V_O^{2+} defects which contribute to an increased afterglow. Nitride-doped **SA** also shows improved afterglow [305].

6.3. Traps related to boron

As mentioned in Section 3.2. on the high temperature solid state synthesis of strontium aluminates, boron oxide (B_2O_3) or boric acid (H_3BO_3) are frequently added as flux. This flux not only lowers the reaction temperature, but contributes also to the phase purity of the desired compound. Nag and Kutty [306] have studied the effect of boron additions in **SA** and **S$_4$A$_7$** and showed from IR spectra and magic angle ^{27}Al NMR spectra that boron is incorporated at the Al sites as BO_4 tetrahedra. The incorporation of boron is also observed by the small decrease of unit cell volume in the presence of boron oxide in the reaction mixture both for **SA** [244, 259] and **S$_4$A$_7$** [69], as well by the shift to higher temperatures of the monoclinic to hexagonal phase transition for **SA** [259]. For **SA** in the presence of boron, the crystallite size estimated from the Scherrer equation is about twice that of the one for the sample prepared without boric acid (256 nm vs 134 nm) [259]; however, Vitola et al. [307] report a much smaller increase (from 39 to 55 nm) of the crystallite size with increasing nominal boron doping. **SA** samples prepared with boron oxide present much smoother grain surfaces than those prepared without boron oxide [259, 307], and these samples also show an increased protection against oxidation by air at 973 K [307]. Nag and Kutty [308] postulated that, as the negative charge of BO_4 is larger than the one of AlO_4, the trivalent Dy^{3+} prefers to occupy the Sr site in the neighborhood of boron. Delgado et al. [243] observed for Dy-doped **SA** that codoping with boron significantly changes the emission and excitation spectra, which can indeed be associated to local distortions induced by the close vicinity of boron and dysprosium. In the STEM study mentioned above [178], the authors concluded that boron facilitates the clustering of dopant rare earth ions and accommodates the misfit strains associated with these pair formations.

As reported by many authors [243, 259, 306-309], the presence of boron improves the afterglow performance. This is also illustrated in Figure 11 which shows that the afterglow intensity of europium-doped **SA** is about 7-10 times smaller than the one of a sample containing additional boron. Vitola et al. [307] observed TL at very low temperature in boron co-doped **SA**:Eu^{2+},Dy^{3+} which they attribute to boron-induced defects lying close to the emitting Eu^{2+} ion.

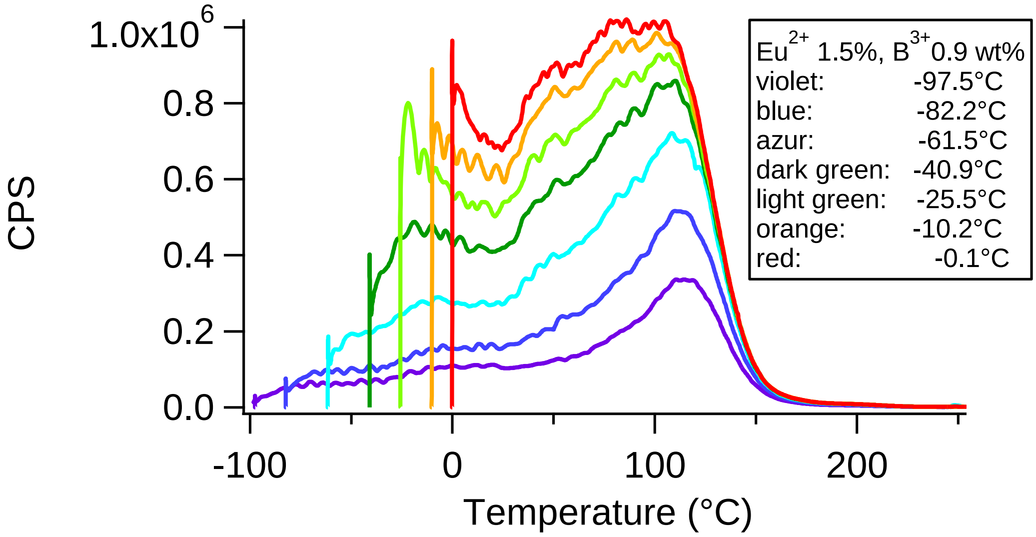

Figure 12: Temperature dependent TL of **SA**:1.5%Eu^{2+},0.9wt%B excited at 445 nm at increasing temperatures from 175.65 K to 273.05 K (data from ref. [291])

Figure 12 shows the TL measured after excitation at 445 nm (which excites only the green emitting Eu^{2+} ion) of **SA**:1.5%Eu^{2+},0.9wt%B at different temperatures (data from [291]). After excitation at 175.65 K, the most prominent TL peak is observed at ca 385 K (112 °C) as well as weaker TL peaks at 200 and 265 K. This strong TL peak and can be thus associated with a boron-induced defect related to Eu^{2+} on site 2 in **SA**. Excitation at 375nm reveals additional Tl peaks observed at ca 199, 264, 309, 345 K. It is interesting to note that the TL peak at 345 K observed under 375 nm excitation at 178 K is also observed under 445 nm excitation at 273 K. This observation suggests that under 375 nm irradiation, one does not only reach boron-induced additional traps related to Eu^{2+} on site 1, but also other traps via the conduction band, which are only thermally accessed under 445 nm irradiation. The high temperature TL peak at 385 K contributes to the flattening of the afterglow curve at long afterglow times (see Figure 11).

6.4. Traps related to Dy^{3+} (and/or other rare earth ions)

The performance of the afterglow in **SA** and **S_4A_7** is strongly improved by co-doping with Dy^{3+} [68, 310], as illustrated in Figure 11. This improvement can be rationalized with the Dorenbos approach which allows to relate for a given host compound (e.g. **SA** or **S_4A_7**) the position of the rare earth ion energy levels in the band gap, starting from one reference data point obtained from experiment (e.g. for Eu^{2+}) [278]. The result is the well-known scheme of zig-zag curves of divalent and trivalent rare earth energy levels in the band gap and in the valence and conduction bands. According to this approach, the energy level of the ground state of Dy^{2+} is located about 0.9 eV below the energy level of the lowest excited $4f^65d^1$ level of Eu^{2+} and can thus act as an electron trap. Recently, electron trapping by Dy^{3+} was demonstrated in

S_4A_7:Eu^{2+},Dy^{3+} [311]. The energy levels of Ho^{2+}, Er^{2+} and Nd^{2+} are in the same range as Dy^{2+} and can thus also act as efficient electron traps in **SA**.

The effect of rare earth co-doping was systematically addressed by Nakazawa et al. [310] in **SA** and **S_4A_7**. Persistent emission was observed for co-doping with Pr, Nd, Dy, Ho, and Er. Using a pulsed (0.09 Hz) 365 nm excitation as a function of temperature, they estimated the trap depth for the different rare earth ions from the maxima of the afterglow intensity observed after a specific delay after switch-off. The obtained trap depths for Pr, Nd, Dy, Ho, Er are 0.81, 0.73, 0,91, 0.71, 0.59 eV respectively in **S_4A_7**; in **SA** the trap depths amount to 0.84, 1.18, 1.03, 0.99 eV for Nd, Dy, Ho, Er, respectively. In both cases, the trap depth of Dy is the lowest, i.e. the trap depletion is faster than for the other rare earth co-doped ions. Katsumata et al. [68] prepared a series of single crystals of Eu^{2+}-doped **SA** codoped with other rare earth ions. Long afterglow (more than 120 minutes) was observed for samples codoped with Dy, Pr, Nd, Tm and Ce, however for Ho, the afterglow was practically finished after 60 minutes. These authors also estimated the trap depth from the fitting of the first TL peak observed for all samples studied and obtained values ranging from 0.45 eV for Tm to 1.0 eV for Yb. Note that for Tm, a second very strong TL peak is observed at 475 K, and for Er and Yb a second TL peak around 510 K. In the case of Sm^{3+}, the trap depth is found to be 0.56 eV, however the corresponding integrated afterglow is about 10,000 times weaker than with Dy codoping. Very low afterglow in Sm co-doped samples have also been observed in [312]. Györi et al. [313] have studied the effect of combined codoping with Dy and Ho on the afterglow in **SA.** They observed that the presence of Ho leads to higher initial emission intensity and faster decay of the afterglow.

7. Mechanism of the afterglow in SA and S_4A_7

Long afterglow can be induced by high energy radiation, as well as by irradiation within the band gap. In the following, we will focus on the afterglow induced by UV and visible light in **SA** and **S_4A_7**. Different mechanisms for the afterglow in **SA** and **S_4A_7** have been proposed in the literature, involving either holes or electrons as the charge carriers [9, 314-316]. These mechanisms have also been recently reviewed in the literature [4, 5, 8].

The currently accepted model for persistent luminescence in **SA** is an electron trapping-detrapping process, induced by the $4f^7$-$4f^65d^1$ absorptions of the Eu^{2+}. Several fundamental results support this model. Ueda et al. [283] measured photocurrent excitation spectra (PCE) of **SA**:Eu^{2+}:Dy^{3+}. Above 300 K, the PCE spectrum is similar to the photoluminescence excitation spectrum measured at 520 nm. At low temperatures, the PCE spectrum resembles more the photoluminescence excitation spectrum measured at 440 nm. Thus, below 100 K, no photocurrent is observed for wavelengths longer than 400 nm. The authors further show that there is an anti-correlation between photoluminescence intensity and measured photocurrent as a function of temperature, confirming thus that the Eu^{2+} emission is quenched via the conduction band [283].

The excitation wavelengths required to obtain persistent luminescence can be probed by thermoluminescence excitation spectroscopy (TLES) [317]. In this technique, monochromatic light is coupled to a TL instrument which allows one to integrate the total TL emission as a function of excitation wavelength and probes thus exclusively the excitations leading to the afterglow. This experiment was performed on commercial afterglow phosphors **SA** and **S_4A_7** co-doped with Eu^{2+} and Dy^{3+} and showed that these TLES spectra overlap with the photoluminescence excitation spectra of Eu^{2+} (such as shown in Figure 8), however with a different shape [317]. The authors conclude that the afterglow is initiated by the f-d absorption of Eu^{2+} followed by trapping.

Figure 13 shows schematically the different processes which come into play for the observed afterglow in **SA** and **S$_4$A$_7$**.

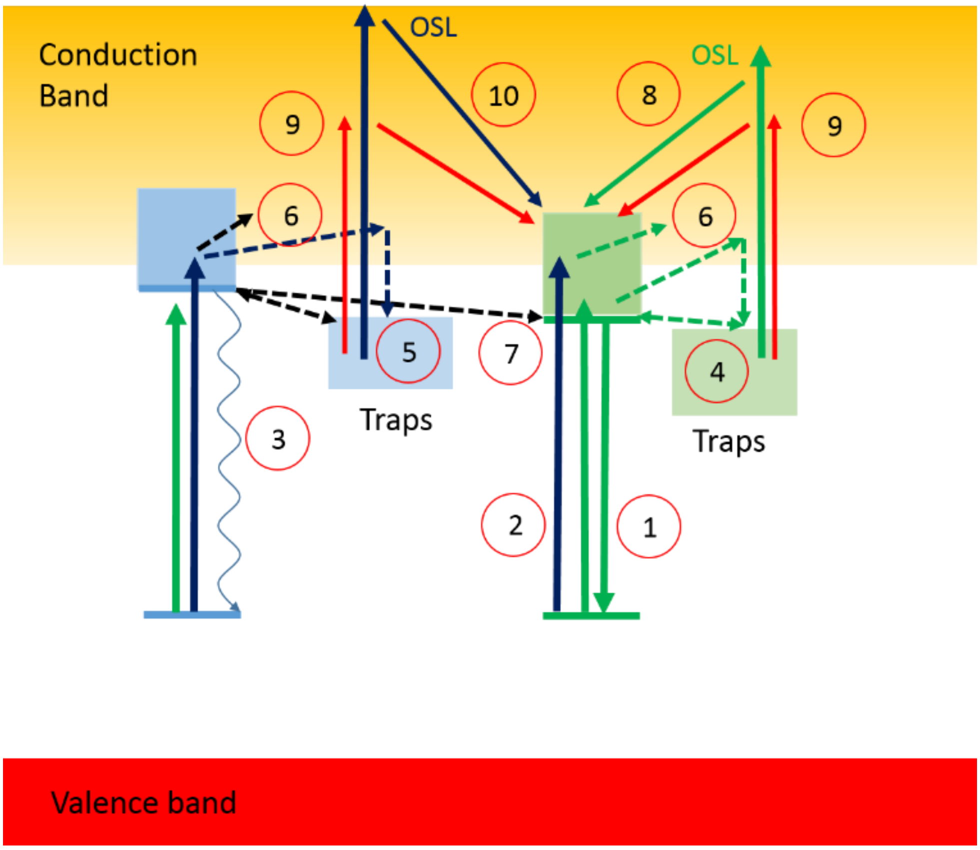

Figure 13: Schematic illustration of the different processes coming into play for the afterglow in **SA** and **S$_4$A$_7$**.

The downwards pointing arrow **1** corresponds to the 520 nm emission of **SA**:Eu^{2+},Dy^{3+}, which corresponds also to the persistent emission. It is important to note here that the afterglow spectra of **SA**:Eu^{2+},Dy^{3+} observed around ambient temperature show only the 520 nm Eu^{2+} emission, but no peaks corresponding to Dy^{3+} or Eu^{3+} emissions.

This implies that all the traps involved in the persistent emission must transfer their energy back to the green emitting 5d level of Eu^{2+}. The upward pointing green (e.g. 445 nm) and blue (e.g. 375 nm) arrows **2** excite either exclusively the green emitting europium ion (λ>405nm), or both different Eu^{2+} ions or from the Eu^{2+} ground state to the conduction band (via the excited 4f^{6}5d^1 levels, as shown by the photocurrent experiments reported above [283]. The undulating arrow **3** indicates non-radiative decay, as the blue emitting Eu^{2+} ion is quenched at room temperature [272, 273]. There is of course also some non-radiative decay of the green emission, which is not shown in the figure for better clarity. The room temperature quantum yield of SA:Eu^{2+} was reported to be 0.55 [265] for a lightly Eu^{2+}-doped sample, and even close to 68% under 445 nm, as reported in [318] and in line with the ratio of lifetimes measured at room temperature and 3 K (850ns/1180ns) in the same work. The energy levels associated to the blue-emitting Eu^{2+} ions are shown in blue, those to the green-emitting Eu^{2+} ion in green. For each different Eu^{2+} ion, a set of accessible trap states is associated with the same color (numbered **4** and **5**). The different TL curves measured with 445 nm and 375 nm excitation [291] show that more shallow traps are accessed with the excitation of the blue emitting Eu^{2+} ion at 173 K (see Figure 14). The trap states **4** and **5** assemble generically all possible traps which can be present: intrinsic defects [294, 296-298], boron related traps [306-309] and rare earth (Dy^{3+}) related traps [68, 310], as discussed above. Different types of traps can thus in principle be specifically addressed using differently doped samples. As shown in the comparative afterglow data presented in Figure 11, the dominant contribution of the afterglow is associated with Dy^{3+}.

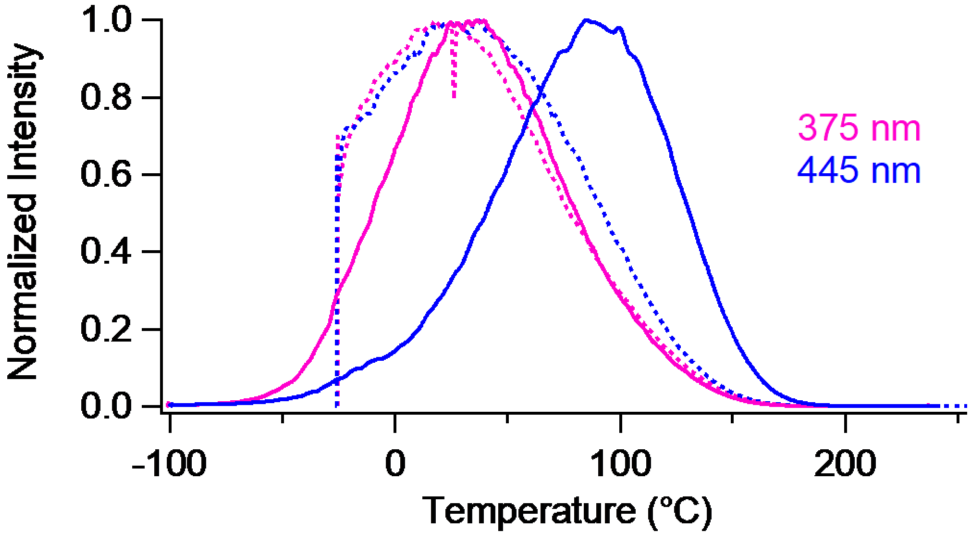

Figure 14. Normalized TL curves of **SA**:Eu^{2+},Dy^{3+},B^{3+} (sample 5 in [291]) excited with 375 nm and 445 nm at 173 K (full lines) and 248 K (dotted lines).

Once the green-emitting Eu^{2+} ion is excited, it can either emit (green downwards pointing arrow in Figure 13) or fill the traps either directly (thermally-assisted process [273] and/or tunneling) or via the conduction band (dashed arrows in Figure 13) [292]. These processes are generically labelled **6** in the scheme and apply also to the trap filling processes from the excited state of the blue emitting Eu^{2+} ion. The depletion of the traps can take place either from thermal excitation (not shown in this scheme), or by optically stimulated luminescence (OSL), labelled **8** in Figure 13 [273, 319, 320]. With 375 nm excitation, also the blue-emitting europium ion is excited, adding the processes **10** on the left hand side of Figure 13. The arrows pointing directly into the conduction band indicate transfers to the conduction band which have been associated with the measured photoconductivity [283]. This process is also included in **6** in Figure 13**,** as the transfer to the conduction band can lead either to trap filling or energy dissipation. Finally, process **9** in Figure 13 corresponds to the trap depletion under NIR irradiation, which has been reported by several authors [321-323]. Upon excitation in the near UV (arrow **2**), also the blue-emitting Eu^{2+} is excited, and can thus lead to filling of associated traps, transferring electrons to the conduction band and fill all available traps, and also lead to energy transfer to the green-emitting Eu^{2+} ion (process **7**), as discussed in detail above. A first conclusion from this scheme is that one expects to observe different afterglow curves under excitation at 445 nm and 375 nm, and this is indeed observed [280, 318].

The fundamental understanding of the trapping and detrapping processes is challenging, as these processes take place on extremely different time scales. The typical emission lifetime of divalent europium is in the microsecond range (see above), and energy transfer processes are typically much faster, while the afterglow extends over hours. One way to study the filling of the traps during irradiation is the measure of so-called “loading curves”, i.e. the measure of the luminescence intensity as a function of irradiation time. Several studies have reported that the luminescence intensity of **SA**:Eu^{2+},Dy^{3+} samples that were previously either kept in the dark for a long time or heated in the dark before the experiment to release all the thermal traps, increases upon irradiation in the blue or near UV over a timespan of about 5 to 10 min. before reaching a steady state [273, 292, 319, 324].

Botterman et al. [273] were the first to systematically compare loading and afterglow curves under 370 and 435 nm irradiation, and observed that, independently of the temperature, the steady state emission of the loading curve was reached much faster under 370 nm (within 100-200 seconds), while under 435 nm irradiation, the steady state was reached after 600 seconds or more. Additionally, van der Heggen et al. [319] observed that with higher irradiation intensity, the steady state is reached after shorter irradiation times. He et al. [325] observed for **SA** that under very high irradiation intensity, the observed emission intensity increased very fast, reached a maximum and then showed a slightly decreasing trend over longer irradiation times (up to 4000 s). The afterglow after 4000 seconds of irradiation was much stronger than after 10 seconds of irradiation. Similar results were reported for $\mathbf{S_4A_7}$:Eu^{2+},Dy^{3+} [326]: with 70 mW LED at 395 nm on 200 mg sample, the PL intensity is maximum after ca 300 s, and then decreases slowly (7% less after 10,000 s) with increasing illumination time. The maximum integrated afterglow is however obtained after ca 60 min illumination, after 10 min of illumination about 90% of this maximum is achieved. The main difference between the data for these two illumination times is the stronger long-lived (after 2 h) afterglow intensity for the longer illumination.

This behavior has been quantitatively modeled the first time by Jia [324] who considered a simplified 3 level system (Eu^{2+} ground state, Eu^{2+} excited state and the trap state). The solution of the corresponding differential equations qualitatively reproduces the observed loading curve, however the fitting of the experimental data required a superposition of 3 sets of curves. He et al. [325] proposed a quenching mechanism via cross relaxation of Eu^{2+} ions to account for the changes observed as a function of irradiation intensity. More recently, Van der Heggen et al. [319] included an additional optically stimulated luminescence (OSL) process induced by the loading irradiation and which competes with the loading of the traps to describe the observed loading curves (green and blue OSL arrows in Figure 13). These models also show that the intensity of the irradiation has a direct impact on the shape of the loading curves.

Careful luminescence lifetime measurements in **SA** [272, 273, 318] and $\mathbf{S_4A_7}$ [266] doped with Eu^{2+} show that at room temperature, the decay can only be fitted using a bi-exponential function. The integrated fraction of the faster decay curve (with a lifetime of ca 350ns) over the total integrated decay curve was shown to increase from 0 % at 80 K to 36% at ca 285 K [273]. Delgado et al. [318] further found that lifetimes and ratio between fast and slower components are strongly sample dependent. The corresponding values also correlate with the observed quantum yields for these different samples [318]. The fraction of the faster decay curve increases strongly with the number of available traps, induced for instance by the Dy^{3+} co-doping. This fast component is assigned to the fraction of excited Eu^{2+} ions which fill these available traps, while the remaining Eu^{2+} ions emit normally. A critical parameter which appeared in this study [318] is the ratio of accessible traps to excitable Eu^{2+} ions. This ratio can be modulated not only by different doping ions (europium, boron, dysprosium), but also by temperature, as more traps become accessible with increasing temperature, as was illustrated for the TL curves for boron-doped **SA** (see Figure 12) and for Dy-doped **SA** (Figure 14).

The qualitative picture which emerges from the combined observations in the literature is that upon excitation at room temperature of the Eu^{2+} ions, there is either a fast transfer to traps (with a fast time scale) or the normal Eu^{2+} emission with a lifetime of ca 800 ns or less (with additional thermal quenching processes). As shown by the results of [273, 318], the fraction of trapping can be substantial, as indicated by the value of 36% mentioned above. This suggests that basically each excited Eu^{2+} ion can reach a trap, but once this trap is filled, the other Eu^{2+} ions emit normally, leading thus to a splitting of the excited population which results in the observed bi-exponential decay curves. The trapping fraction decreases with increasing loading time, as the filled traps cannot accept additional electrons. Alternatively, this fast component could originate from OSL, as the superposition of a continuous UV irradiation to the excitation pulses at 355 nm added a strong component with 110 ns lifetime to the normal single exponential decay curve with a normal Eu^{2+} lifetime (ca 800 ns) observed without this additional irradiation [327].

On the other side, the traps are also thermally released during charging, and, as shown by [319], the blue or near UV irradiation can additionally empty traps by an OSL process. The increased afterglow intensity after very long irradiations suggests that this extended irradiation also leads to increase in the number of filled deeper traps with respect to the shallower traps.

An important question is whether the trapping and detrapping processes are local or imply migrations through the conduction band. The combined STEM and DFT study on **S_4A_7**:Eu, Dy [178] indicates that Eu^{2+} and Dy^{3+} could be preferentially located on adjacent Sr^{2+} sites which can favor direct energy transfers. The normalized TL curves measured for **SA**:Eu^{2+},Dy^{3+},B^{3+} [291] under 375 nm and 445nm excitation were shown in Figure 14. Upon excitation at 445 nm at 173 K, the photon energy is not sufficient to reach the conduction band, and thus the blue full trace corresponds to Dy^{3+}-related traps connected to the green-emitting Eu^{2+} ion, either directly or via tunneling. The irradiation at 375 nm can excite both different Eu^{2+} ions, and also reach directly the conduction band, and thus the corresponding TL curve can contain several contributions. Upon excitation at 248 K, the TL signal intensity increases dramatically under 445 nm irradiation [291], and the shape resembles now the one observed under 375 nm irradiation (dashed lines in Figure 14). At 248 K, there is also a significant increase of TL intensity between 248 K and 293 K compared to the TL intensity observed under 375 nm at 173 K, indicating that shallow traps are additionally filled with increasing temperature. It is tempting to assign this additional contribution to a fraction of traps filled through the conduction band, as the normalized intensity is very similar under both irradiations. Note that these traps correspond also to those which are the fastest to be emptied, also during the loading of the traps.

8. Conclusions and outlook

Van der Heggen et al. [290] have estimated that only 1.6% of the Eu^{2+} ions participate in the energy storage process in **SA**. However, this fraction is probably doubled considering the presence of very deep traps with a TL peak around 648 K [292]. In the recent study by Joos et al. [311], about 3 % of the Eu^{2+} ions and a corresponding number of Dy^{3+} ions are involved in the afterglow process which is identified as the charge transfer from Eu^{2+} to Dy^{3+}. This process is reversed by NIR irradiation, but reinforced with UV light. This value of 3% is about one order of magnitude smaller than the value of 36% estimated from the double exponential decay curves [273]. It appears that each persistent phosphor has an optimum afterglow temperature which is correlated to the temperature of the TL maximum [328]. Additionally, **SA** and **S_4A_7** showed a maximum of integrated TL + afterglow intensity around 273 K and 293 K, respectively, i.e. for these persistent phosphors, temperature-assisted loading is important, which is then competing with the onset of strong afterglow. This does not appear to be the case for $LaAlO_3$:Mn^{4+},Na^{+}, as for this material, the integrated TL and afterglow intensity is constant within 20% for charging temperatures between 213 K and 413 K. The understanding of the mechanisms underlying the persistent emissions is continuously increasing by the design of pertinent experimental approaches which allow to isolate a specific contribution of interest. One of the challenges for future work will be to address the origin of the above-mentioned temperature-assisted loading.

The quality of ab initio theoretical approaches to energy transfer processes has improved significantly over the last years and allows now to analyze charge transfer processes, as was recently done for Eu^{2+}/Eu^{3+} in MF_2 (M=Ca, Sr, Ba) [329]. Applying this type of approach to the more complex structures of **SA** and **S_4A_7**, exploring also the potential presence of interstitial charge compensators, will be certainly challenging but can highlight possible energetic landscapes for the energy transfer between Eu^{2+} and Dy^{3+}.

ABBREVIATIONS

CALPHAD	Calculation of Phase Diagram
CF	Crystal Field
C.N.	Coordination Number
DFT	Density Functional Theory
EPR	Electron Paramagnetic Resonance
LED	Light Emitting Diode
LLP	Long lasting phosphorescence
ML	Mechanoluminescence
NIR	Near-infrared
NMR	Nuclear Magnetic Resonance
OSL	Optically stimulated luminescence
PCE	Photocurrent excitation spectra
PL	Photoluminescence
STEM	Scanning transmission electron microscopy
TL	Thermoluminescence
TLES	Thermoluminescence Excitation spectroscopy
TQ_{50}	Emission quenching temperature at which the emission intensity is half of the low temperature intensity
UV	Ultra-violet
VUV	Vacuum ultra-violet

References

[1] Y. Li, M. Gecevicius, J. Qiu, Long persistent phosphors—from fundamentals to applications, Chem. Soc. Rev., 45 (2016) 2090-2136.

[2] J. Xu, S. Tanabe, Persistent luminescence instead of phosphorescence: History, mechanism, and perspective, J. Lumin., 205 (2019) 581-620.

[3] K. Van den Eeckhout, P.F. Smet, D. Poelman, Persistent luminescence in Eu^{2+}-doped compounds: a review, Materials, 3 (2010) 2536-2566.

[4] R.E. Rojas-Hernandez, F. Rubio-Marcos, M.Á. Rodriguez, J.F. Fernandez, Long lasting phosphors: $SrAl_2O_4$:Eu,Dy as the most studied material, Renew. Sustain. Energy Rev., 81 (2018) 2759-2770.

[5] V. Vitola, D. Millers, I. Bite, K. Smits, A. Spustaka, Recent progress in understanding the persistent luminescence in $SrAl_2O_4$:Eu,Dy, Mater. Sci. Technol., 35 (2019) 1661-1677.

[6] K.V.d.E. Philippe F.Smet, Olivier Q. De Clercq, Dirk Poelman, Handbook on the physics and chemistry of rare earths, Chapter 274 - Persistent Phosphors, (2015).

[7] D. Poelman, D. Van der Heggen, J. Du, E. Cosaert, P.F. Smet, Persistent phosphors for the future: Fit for the right application, J. Appl. Phys., 128 (2020) 240903.

[8] D. Kim, Recent developments in lanthanide-doped alkaline earth aluminate phosphors with enhanced and long-persistent luminescence, Nanomaterials, 11 (2021) 723.

[9] T. Matsuzawa, Y. Aoki, N. Takeuchi, Y. Murayama, A new long phosphorescent phosphor with high brightness, $SrAl_2O_4:Eu^{2+},Dy^{3+}$, J. Electrochem. Soc., 143 (1996) 2670.

[10] K. Vishista, F. Gnanam, Microstructural development of $SrAl_{12}O_{19}$ in alumina–strontia composites, J. Eur. Ceram. Soc., 29 (2009) 77-83.

[11] M. Fechner, F. Reichert, N.-O. Hansen, K. Petermann, G. Huber, Crystal growth, spectroscopy, and diode pumped laser performance of Pr, Mg:$SrAl_{12}O_{19}$, Appl. Phys. B, 102 (2011) 731-735.

[12] Y. Pan, B. Liu, J. Liu, Q. Song, J. Xu, D. Li, P. Liu, J. Ma, X. Xu, H. Lin, Polarized spectral properties and laser operation of Nd:$SrAl_{12}O_{19}$ crystal, J. Lumin., 235 (2021) 118034.

[13] X. Lin, K. Deng, H. Wu, B. Du, B. Viana, Y. Li, Y. Hu, Photon energy conversion and management in $SrAl_{12}O_{19}:Mn^{2+},Gd^{3+}$ for rewritable optical information storage, Chem. Eng. J., 420 (2021) 129844.

[14] F. Farzaneh, M.K. Maleki, E. Rashtizadeh, Expedient catalytic access to Knöevenagel condensation using $Sr_3Al_2O_6$ nanocomposite in room temperature, J. Clust. Sci., 28 (2017) 3253-3263.

[15] W. Piotrowski, K. Trejgis, K. Maciejewska, K. Ledwa, B. Fond, L. Marciniak, Thermochromic luminescent nanomaterials based on Mn^{4+}/Tb^{3+} codoping for temperature imaging with digital cameras, ACS appl. mater. interfaces, 12 (2020) 44039-44048.

[16] Z. Wang, X. Luan, G. Ma, J. Chen, Y. Liu, Dual-emitting phosphor $Sr_4Al_{14}O_{25}:Eu^{2+/3+}$ prepared in air for ratiometric temperature sensing, J. Mater. Sci.: Mater. Electron., (2021) 1-8.

[17] J.R.N. Gnidakouong, G.J. Yun, Dislocation density level induced divergence between stress-free afterglow and mechanoluminescence in $SrAl_2O_4:Eu^{2+},Dy^{3+}$, Ceram. Int., 45 (2019) 1794-1802.

[18] A. Feng, P.F. Smet, A review of mechanoluminescence in inorganic solids: compounds, mechanisms, models and applications, Materials, 11 (2018) 484.

[19] H. Matsuo, K. Ikeda, S. Hata, H. Nakashima, H. Yamada, C. Xu, Phase transformation behavior and pseudoelastic deformation in $SrAl_2O_4$, J. Alloys Compd., 577 (2013) S507-S516.

[20] L. Wang, W. Wang, Z. Shang, P. Cao, M. Shi, B. Yang, J. Zou, Optical and reliability properties studies of $Sr_4Al_{14}O_{25}:Eu^{2+}$ film for high-CRI white LEDs, J. Mater. Sci.: Mater. Electron., 31 (2020) 13561-13569.

[21] S.G. Menon, A. Bedyal, T. Pathak, V. Kumar, H.C. Swart, $Sr_4Al_{14}O_{25}:Eu^{2+},Dy^{3+}$@ZnO nanocomposites as highly efficient visible light photocatalysts for the degradation of aqueous methyl orange, J. Alloys Compd., 860 (2021) 158370.

[22] X. Liu, X. Chen, Y. Li, B. Wu, X. Luo, S. Ouyang, S. Luo, A.A. Al Kheraif, J. Lin, A g-C_3N_4@Au@$SrAl_2O_4:Eu^{2+},Dy^{3+}$ composite as an efficient plasmonic photocatalyst for round-the-clock environmental purification and hydrogen evolution, J. Mater. Chem. A, 7 (2019) 19173-19186.

[23] S.-R. Eun, S. Mavengere, J.-S. Kim, Preparation of Ag-$TiO_2/Sr_4Al_{14}O_{25}:Eu^{2+},Dy^{3+}$ Photocatalyst on phosphor beads and its photoreaction characteristics, Catalysts, 11 (2021) 261.

[24] F. Kang, G. Sun, P. Boutinaud, H. Wu, F.-X. Ma, J. Lu, J. Gan, H. Bian, F. Gao, S. Xiao, Recent advances and prospects of persistent luminescent materials as inner secondary self-luminous light source for photocatalytic applications, Chem. Eng. J., 403 (2020) 126099.

[25] H. Sun, L. Pan, X. Piao, Z. Sun, Enhanced performance of cadmium selenide quantum dot-sensitized solar cells by incorporating long afterglow europium, dysprosium co-doped strontium aluminate phosphors, J. Colloid Interface Sci., 416 (2014) 81-85.

[26] H. Sun, L. Pan, G. Zhu, X. Piao, L. Zhang, Z. Sun, Long afterglow $Sr_4Al_{14}O_{25}$:Eu,Dy phosphors as both scattering and down converting layer for CdS quantum dot-sensitized solar cells, Dalton Trans., 43 (2014) 14936-14941.

[27] X. Shen, S. Tang, Q. Hu, M. Ge, Doping $SrAl_2O_4:Eu^{2+},Dy^{3+}$ and thermochromic materials for the generation of anticounterfeiting membrane, ECS J. Solid State Sci. Technol., 9 (2020) 076001.

[28] L. Liu, Z. Zhang, L. Zhang, Y. Zhai, The effectiveness of strong afterglow phosphor powder in the detection of fingermarks, Forensic Sci. Int., 183 (2009) 45-49.

[29] V. Sharma, A. Das, V. Kumar, Eu^{2+},Dy^{3+} codoped $SrAl_2O_4$ nanocrystalline phosphor for latent fingerprint detection in forensic applications, Mater. Res. Express, 3 (2016) 015004.

[30] I. Aydin, K. Ertekin, S. Demirci, S. Gultekin, E. Celik, Sol-gel synthesized $Sr_4Al_{14}O_{25}:Eu^{2+}/Dy^{3+}$ blue–green phosphorous as oxygen sensing materials, Opt. Mater., 62 (2016) 285-296.

[31] J. Botterman, P.F. Smet, Persistent phosphor $SrAl_2O_4$:Eu,Dy in outdoor conditions: saved by the trap distribution, Opt. Express, 23 (2015) A868-A881.

[32] J. Nance, T.D. Sparks, From streetlights to phosphors: A review on the visibility of roadway markings, Prog. Org. Coat., 148 (2020) 105749.

[33] D. Peng, Z. Zhong, T. Cai, S. Guo, X. Zhao, Y. Liu, Integration of pressure-sensitive paint with persistent phosphor: A light-charged pressure-sensing system, Rev. Sci. Instrum., 89 (2018) 085003.

[34] S. Wu, Y. Li, W. Ding, L. Xu, Y. Ma, L. Zhang, Recent advances of persistent luminescence nanoparticles in bioapplications, Nano-Micro Lett., 12 (2020) 1-26.

[35] X. Qin, J. Wang, Q. Yuan, Synthesis and biomedical applications of lanthanides-doped persistent luminescence phosphors with NIR emissions, Front. Chem., 8 (2020) 608578.

[36] N. Yu, F. Liu, X. Li, Z. Pan, Near infrared long-persistent phosphorescence in $SrAl_2O_4:Eu^{2+},Dy^{3+},Er^{3+}$ phosphors based on persistent energy transfer, Appl. Phys. Lett., 95 (2009) 231110.

[37] Y. Teng, J. Zhou, S.N. Khisro, S. Zhou, J. Qiu, Persistent luminescence of $SrAl_2O_4:Eu^{2+}$, Dy^{3+},Cr^{3+} phosphors in the tissue transparency window, Mater. Chem. Phys., 147 (2014) 772-776.

[38] J. Montes-Frausto, K. Juarez-Moreno, B. Can-Uc, G. Hirata-Flores, Synthesis and cytotoxic effects of $SrAl_2O_4$ persistent luminescence nanoparticles co-doped with Eu^{2+}/Dy^{3+} ions, Opt. Mater. Express, 6 (2016) 1488-1499.

[39] F. Massazza, The system $SrO–Al_2O_3$, Chim. Ind. (Milan), 41 (1959) 108-115.

[40] F. Ganits, T.Y. Chemekova, Y.P. Udalov, The $SrO-Al_2O_3$ system, Zh.Neorg.Khim., 24 (1979) 471-475.

[41] M. Capron, A. Douy, Strontium dialuminate $SrAl_4O_7$: Synthesis and stability, J. Am. Ceram. Soc., 85 (2002) 3036-3040.

[42] H. Akasaka, H. Tada, T. Ooki, A. Nakamura, K. Komatsu, S. Tsuchida, S. Ohshio, N. Nambu, H. Saitoh, New violet phosphor $Sr_7Al_{12}O_{25}:Eu^{2+}$ synthesized from Sr–Al–O:Eu powder mounted on polycrystalline alumina, JPN. J. Appl. Phys., 49 (2010) 122601.

[43] X. Ye, W. Zhuang, J. Wang, W. Yuan, Z. Qiao, Thermodynamic description of $SrO-Al_2O_3$ system and comparison with similar systems, J. Phase Equilibria Diffus., 28 (2007) 362-368.

[44] E. Boyko, L. Wisnyl, The optical properties and structures of $CaO.2Al_2O_3$ and $SrO.2Al_2O_3$, Acta Crystallogr., 11 (1958) 444-445.

[45] S. Alahraché, K. Al Saghir, S.b. Chenu, E. Veron, D. de Sousa Meneses, A.I. Becerro, M. Ocana, F. Moretti, G. Patton, C. Dujardin, F. Cussó, J.-P. Guin, M. Nivard, J.-C. Sangleboeuf, G. Matzen, M. Allix, Perfectly transparent $Sr_3Al_2O_6$ polycrystalline ceramic elaborated from glass crystallization, Chem. Mater., 25 (2013) 4017-4024.

[46] K.-I. Machida, G.-Y. Adachi, J. Shiokawa, M. Shimada, M. Koizumi, Structure of strontium tetraaluminate β-$SrAl_4O_7$, Acta Crystallogr. Sec. B: Struct. Crystallogr. Cryst. Chem., 38 (1982) 889-891.

[47] I. Barin, Thermochemical data of pure substances, 3rd ed., in, VCH Weinheim, 1995.

[48] K. Jacob, V. Shreyas, Thermodynamic properties of $SrAl_{12}O_{19}$ and $SrAl_4O_7$, J. Mater. Sci., 53 (2018) 1723-1730.

[49] C. Brisi, F. Abbattista, Searches on the heats of formation of the strontium aluminated one, Ann. Chimica, 50 (1960) 165-169.

[50] M. Zinkevich, Constitution of the Sr–Ni–O system, J. Solid State Chem., 178 (2005) 2818-2824.

[51] V. Kahlenberg, Synthesis and crystal structure of $Sr_{10}Al_6O_{19}$: a derivative of the perovskite structure type in the system SrO–Al_2O_3, Mater. Res. Bull., 37 (2002) 715-726.

[52] J. Alonso, I. Rasines, J. Soubeyroux, Tristrontium dialuminum hexaoxide: an intricate superstructure of perovskite, Inorg. Chem., 29 (1990) 4768-4771.

[53] N. Nevskij, L. Glasser, V.V. Ilyukhin, N.V.e. Belov, Crystal structure of simplest strontium aluminate with three-dimensional skeleton, Dokl. Akad. Nauk SSSR, 241 (1978) 821-824.

[54] A.R. Schulze, H.M. Buschbaum, Zur Verbindungsbildung von MeO:M_2O_3. IV. Zur Struktur von monoklinem $SrAl_2O_4$, Zeitschrift für anorganische und allgemeine Chemie, 475 (1981) 205-210.

[55] K. Fukuda, K. Fukushima, Crystal structure of hexagonal $SrAl_2O_4$ at 1073 K, J. Solid State Chem., 178 (2005) 2709-2714.

[56] T. Takeda, K. Takahashi, K. Uheda, H. Takizawa, T. Endo, Crystal structure and luminescence properties of $Sr_2Al_6O_{11}$:Eu^{2+}, J. Jpn Soc. Powder Powder Metall., 49 (2002) 1128-1133.

[57] D. Wang, M. Wang, G. Lü, Synthesis, crystal structure and X-ray powder diffraction data of the phosphor matrix $4SrO\cdot 7Al_2O_3$, J. Mater. Sci., 34 (1999) 4959-4964.

[58] A. Lindop, D. Goodwin, The refined structure of $SrO.2Al_2O_3$, Acta Crystallogr. Sect. B: Struct. Crystallogr. Crys. Chem., 28 (1972) 2625-2626.

[59] K. Kimura, M. Ohgaki, K. Tanaka, H. Morikawa, F. Marumo, Study of the bipyramidal site in magnetoplumbite-like compounds, $SrM_{12}O_{19}$ (M= Al, Fe, Ga), J. Solid State Chem., 87 (1990) 186-194.

[60] J. Boilot, M. Lee, P. Colomban, G. Collin, R. Comes, Fast divalent ion conduction—Ion ordering in β AND β ″alumina (Sr^{2+}, Cd^{2+}, Pb^{2+}), J. Phys. Chem. Solids, 47 (1986) 693-706.

[61] R.-S. Zhou, R.L. Snyder, Structures and transformation mechanisms of the η, γ and θ transition aluminas, Acta Crystallogr. Sect. B: Struct. Sci., 47 (1991) 617-630.

[62] K. Zakharchuk, A. Yaremchenko, D. Fagg, Electrical properties and thermal expansion of strontium aluminates, J. Alloys Compd., 613 (2014) 232-237.

[63] M.G. Brik, M. Nazarov, B. Tsukerblat, S.C.M. Calyn, A. Nor Nazida, M.N. Ahmad-Fauzi, Ab-initio calculations and theoretical study of the electronic structure of $SrAl_2O_4$:Eu^{2+}, Conference Proceeding, (2013).

[64] J. Hölsä, T. Laamanen, M. Lastusaari, J. Niittykoski, P. Novák, Electronic structure of the $SrAl_2O_4$:Eu^{2+} persistent luminescence material, J. Rare Earths, 27 (2009) 550-554.

[65] Y. Obukuro, S. Matsushima, H. Nakamura, M. Arai, H. Yamada, C.-N. Xu, Electronic structure of Eu^{2+}-doped $SrAl_2O_4$ using modified Becke–Johnson exchange potential, Solid State Commun., 186 (2014) 46-49.

[66] M. Avdeev, S. Yakovlev, A.A. Yaremchenko, V.V. Kharton, Transitions between $P2_1$, $P6_3$ (√3A), and $P6_322$ modifications of $SrAl_2O_4$ by in situ high-temperature X-ray and neutron diffraction, J. Solid State Chem., 180 (2007) 3535-3544.

[67] M. Capron, F. Fayon, D. Massiot, A. Douy, $Sr_4Al_{14}O_{25}$: formation, stability, and ^{27}Al high-resolution NMR characterization, Chem. Mater., 15 (2003) 575-579.

[68] T. Katsumata, S. Toyomane, R. Sakai, S. Komuro, T. Morikawa, Trap levels in Eu-doped $SrAl_2O_4$ phosphor crystals co-doped with rare-earth elements, J. Am. Ceram. Soc., 89 (2006) 932-936.

[69] N. Thompson, P. Murugaraj, C. Rix, D.E. Mainwaring, Role of oxidative pre-calcination in extending blue emission of $Sr_4Al_{14}O_{25}$ nanophosphors formed with microemulsions, J. Alloys Compd, 537 (2012) 147-153.

[70] G. Inan Akmehmet, S. Šturm, L. Bocher, M. Kociak, B. Ambrožič, C.W. Ow-Yang, Structure and luminescence in long persistence Eu, Dy, and B codoped strontium aluminate phosphors: the boron effect, J. Am. Ceram. Soc., 99 (2016) 2175-2180.

[71] X. Qin, X. Liu, W. Huang, M. Bettinelli, X. Liu, Lanthanide-activated phosphors based on 4f-5d optical transitions: theoretical and experimental aspects, Chem. Rev., 117 (2017) 4488-4527.

[72] A. Varma, A.S. Mukasyan, A.S. Rogachev, K.V. Manukyan, Solution combustion synthesis of nanoscale materials, Chem. Rev., 116 (2016) 14493-14586.

[73] W.L. Suchanek, R.E. Riman, Hydrothermal synthesis of advanced ceramic powders, Adv. Sci. Technol., 45 (2006) 184-193.

[74] S.-H. Feng, G.-H. Li, Modern inorganic synthetic chemistry 2nd Edition, Chapter 4, Hydrothermal and solvothermal syntheses Elsevier, (2017) 73-104.

[75] R.E. Rojas-Hernandez, F. Rubio-Marcos, R.H. Goncalves, M.A.n. Rodriguez, E. Veron, M. Allix, C. Bessada, J.F. Fernandez, Original synthetic route to obtain a $SrAl_2O_4$ phosphor by the molten salt method: insights into the reaction mechanism and enhancement of the persistent luminescence, Inorg. Chem., 54 (2015) 9896-9907.

[76] G. Hernández-Alvarado, S.M. Montemayor, I. Moggio, E. Arias, E. Trujillo-Vázquez, J. Díaz-Guillén, C. Ávila-Orta, O. Rodríguez-Fernández, Synthesis at room atmosphere conditions of phosphorescent emitter $SrAl_2O_4$:Eu,Dy, Ceram. Int., 44 (2018) 12789-12796.

[77] R.E. Rojas-Hernandez, F. Rubio-Marcos, A. Serrano, I. Hussainova, J.F. Fernandez, Boosting phosphorescence efficiency by crystal anisotropy in $SrAl_2O_4$:Eu,Dy textured ceramic layers, J. Eur. Ceram. Soc., 40 (2020) 1677-1683.

[78] C. Guo, L. Luan, D. Huang, Q. Su, Y. Lv, Study on the stability of phosphor $SrAl_2O_4:Eu^{2+},Dy^{3+}$ in water and method to improve its moisture resistance, Mater. Chem. Phys., 106 (2007) 268-272.

[79] M. Tayebi, S.O. Movahed, A. Ahmadpour, The effect of the surface coating of a strontium mono-aluminate europium dysprosium-based ($SrAl_2O_4:Eu^{2+},Dy^{3+}$) phosphor by polyethylene (PE), polystyrene (PS) and their dual system on the photoluminescence properties of the pigment, RSC Adv., 9 (2019) 38703-38712.

[80] Y. Zhu, J. Zeng, W. Li, L. Xu, Q. Guan, Y. Liu, Encapsulation of strontium aluminate phosphors to enhance water resistance and luminescence, Appl. Surf. Sci., 255 (2009) 7580-7585.

[81] A. Varma, J.-P. Lebrat, Combustion synthesis of advanced materials, Chem. Eng. Sci., 47 (1992) 2179-2194.

[82] H. Song, D. Chen, Combustion synthesis and luminescence properties of $SrAl_2O_4:Eu^{2+},Dy^{3+},Tb^{3+}$ phosphor, Luminescence, 22 (2007) 554-558.

[83] P. Huang, C.-e. Cui, S. Wang, Influence of calcination temperature on luminescent properties of $Sr_3Al_2O_6:Eu^{2+},Dy^{3+}$ phosphors prepared by sol–gel-combustion processing, Opt. Mater., 32 (2009) 184-189.

[84] R. Zhang, G. Han, L. Zhang, B. Yang, Gel combustion synthesis and luminescence properties of nanoparticles of monoclinic $SrAl_2O_4:Eu^{2+},Dy^{3+}$, Mater. Chem. Phys., 113 (2009) 255-259.

[85] W. Xie, C. Zou, M. Xie, Effect of H_3BO_3 on phases, micromorphology and persistent luminescence properties of $SrAl_2O_4:Eu^{2+},Dy^{3+}$ phosphors, J. Mater. Sci.: Mater Electron., 28 (2017) 6328-6334.

[86] R. Sharma, U. Sharma, Influence of fluxing agent on the luminescence properties of $SrAl_2O_4:Eu^{2+}$ nanophosphors, J. Alloys Compd., 649 (2015) 440-446.

[87] Z. Tang, F. Zhang, Z. Zhang, C. Huang, Y. Lin, Luminescent properties of $SrAl_2O_4$:Eu,Dy material prepared by the gel method, J. Eur. Ceram. Soc., 20 (2000) 2129-2132.

[88] C.d.S. Bezerra, A.B. Andrade, P.J. Montes, M.V.d.S. Rezende, M.E. Valerio, The effects of cooling rate on the structure and luminescent properties of undoped and doped $SrAl_2O_4$ phosphors, Opt. Mater., 72 (2017) 71-77.

[89] M. Misevicius, M. Kilmanas, S. Culunlu, S. Sakirzanovas, A.U. Morkan, A. Beganskiene, A. Kareiva, On the sol–gel fabrication and characterization of undoped and cerium-doped $Sr_4Al_{14}O_{25}$, J. Alloys Compd., 614 (2014) 44-48.

[90] S. Wu, S. Zhang, J. Yang, Influence of microwave process on photoluminescence of europium-doped strontium aluminate phosphor prepared by a novel sol–gel-microwave process, Mater. Chem. Phys., 102 (2007) 80-85.

[91] Y. Tian, P. Zhang, Z. Zheng, Y. Chai, A novel approach for preparation of $Sr_3Al_2O_6:Eu^{2+},Dy^{3+}$ nanoparticles by sol–gel–microwave processing, Mater. Lett., 73 (2012) 157-160.

[92] C. Yuesheng, Z. Ping, Z. Zhentai, Eu^{2+} and Dy^{3+} co-doped $Sr_3Al_2O_6$ red long-afterglow phosphors with new flower-like morphology, Physica B: Condens. Matter, 403 (2008) 4120-4122.

[93] C. Ye, Y. Bando, G. Shen, D. Golberg, Formation of crystalline $SrAl_2O_4$ nanotubes by a roll-up and post-annealing approach, Angew. Chem., 118 (2006) 5044-5048.

[94] Y.-F. Xu, D.-K. Ma, M.-L. Guan, X.-A. Chen, Q.-Q. Pan, S.-M. Huang, Controlled synthesis of single-crystal $SrAl_2O_4:Eu^{2+},Dy^{3+}$ nanosheets with long-lasting phosphorescence, J. Alloys Compd., 502 (2010) 38-42.

[95] M. Karmaoui, M.-G. Willinger, L. Mafra, T. Herntrich, N. Pinna, A general nonaqueous route to crystalline alkaline earth aluminate nanostructures, Nanoscale, 1 (2009) 360-365.

[96] J. Afshani, T. Delgado, H. Hagemann, To be published.

[97] S.J. Kim, H.I. Won, N. Hayk, C.W. Won, D.Y. Jeon, A.G. Kirakosyan, Preparation and characterization of $Sr_4Al_2O_7$:Eu^{3+},Eu^{2+} phosphors, Mater. Sci. Eng.: B, 176 (2011) 1521-1525.

[98] C. Chang, W. Li, X. Huang, Z. Wang, X. Chen, X. Qian, R. Guo, Y. Ding, D. Mao, Photoluminescence and afterglow behavior of Eu^{2+}, Dy^{3+} and Eu^{3+}, Dy^{3+} in $Sr_3Al_2O_6$ matrix, J. Lumin., 130 (2010) 347-350.

[99] S. Liu, M. Wu, W. Chen, Y. Sun, Z. Zheng, G. Chen, Y. Zeng, L. Huang, Photoluminescence and afterglow behavior of orange-reddish Pr^{3+}-activated $Sr_3Al_2O_6$ phosphor, J. Solid State Chem., 294 (2021) 121861.

[100] W. Zhang, F. Liu, S. Feng, S. Hao, Y. Xu, J. Guan, Synthesis and luminescence of $Sr_3Al_2O_6$:Ce^{3+} powders synthesized by solid state reaction method with addition of H_3BO_3, J. Mater. Sci.: Mater. Electron., 25 (2014) 2355-2358.

[101] X.Y. Chen, S.P. Bao, Y.C. Wu, Controlled synthesis and luminescent properties of Eu^{2+} (Eu^{3+}), Dy^{3+}-doped $Sr_3Al_2O_6$ phosphors by hydrothermal treatment and postannealing approach, J. Solid State Chem., 183 (2010) 2004-2011.

[102] X. Li, H. Pan, A. Tang, J. Zhang, L. Guan, H. Su, G. Dong, Z. Yang, H. Wang, F. Teng, Hydrothermal synthesis and luminescent properties of Eu^{3+} doped $Sr_3Al_2O_6$ phosphor for white LED, J. Nanosci. Nanotechnol., 16 (2016) 3474-3479.

[103] Y. Yang, H. Pan, L. Guan, D. Wang, J. Zhao, J. Yang, Z. Yang, X. Li, Electronic structure and luminescent properties of $Sr_3Al_2O_6$:Sm^{3+} orange phosphor prepared by hydrothermal method, J. Mater. Res. Technol., 9 (2020) 3847-3855.

[104] P. Zhang, M. Xu, L. Liu, L. Li, Luminescent properties of $Sr_3Al_2O_6$:Eu,Pr prepared by sol–gel method, J. Solgel Sci. Technol., 50 (2009) 267-270.

[105] P. Zhang, M. Xu, Z. Zheng, L. Liu, L. Li, Synthesis and characterization of europium-doped $Sr_3Al_2O_6$ phosphors by sol–gel technique, J. Solgel Sci. Technol., 43 (2007) 59-64.

[106] P. Page, R. Ghildiyal, K. Murthy, Photoluminescence and thermoluminescence properties of $Sr_3Al_2O_6$:Tb^{3+}, Mater. Res. Bull., 43 (2008) 353-360.

[107] H. Ryu, K. Bartwal, Defect structure and its relevance to photoluminescence in $SrAl_2O_4$:Eu^{2+},Nd^{3+}, Phys. B: Condens. Matter, 404 (2009) 1714-1718.

[108] Y.-T. Yu, B.-G. Kim, Effects of adding B_2O_3 as a flux on phosphorescent properties in synthesis of $SrAl_2O_4$:(Eu^{2+}, Dy^{3+} phosphor, Korean J. Chem. Eng., 20 (2003) 973-976.

[109] D. Dutczak, T. Jüstel, C. Ronda, A. Meijerink, Eu^{2+} luminescence in strontium aluminates, Phys. Chem. Chem. Phys., 17 (2015) 15236-15249.

[110] H. Lv, Z. Pan, Y. Wang, Synthesis and mechanoluminescent property of (Eu^{2+}, Dy^{3+})-co-doped strontium aluminate phosphor by soft mechanochemistry-assisted solid-state method, J. Lumin., 209 (2019) 129-140.

[111] Z. Wu, J. Shi, J. Wang, H. Wu, Q. Su, M. Gong, Synthesis and luminescent properties of $SrAl_2O_4$:Eu^{2+} green-emitting phosphor for white LEDs, Mater. Lett., 60 (2006) 3499-3501.

[112] X. Luo, W. Cao, Z. Xiao, Investigation on the distribution of rare earth ions in strontium aluminate phosphors, J. Alloys Compd., 416 (2006) 250-255.

[113] Y.M. Huang, Q.-l. Ma, Long afterglow of trivalent dysprosium doped strontium aluminate, J. Lumin., 160 (2015) 271-275.

[114] I.P. Sahu, D. Bisen, N. Brahme, R.K. Tamrakar, R. Shrivastava, Luminescence studies of dysprosium doped strontium aluminate white light emitting phosphor by combustion route, J. Mater. Sci.: Mater. Electron., 26 (2015) 8824-8839.

[115] H. Tanaka, A. Gubarevich, H. Wada, O. Odawara, Process stages during solution combustion synthesis of strontium aluminates, Int. J. Self-Propag. High-Temp. Synth., 22 (2013) 151-156.

[116] H. Song, D. Chen, W. Tang, Y. Peng, Synthesis of $SrAl_2O_4$:Eu^{2+},Dy^{3+},Gd^{3+} phosphor by combustion method and its phosphorescence properties, Displays, 29 (2008) 41-44.

[117] T. Peng, H. Yang, X. Pu, B. Hu, Z. Jiang, C. Yan, Combustion synthesis and photoluminescence of $SrAl_2O_4$:Eu,Dy phosphor nanoparticles, Mater. Lett., 58 (2004) 352-356.

[118] X. Li, Y. Qu, X. Xie, Z. Wang, R. Li, Preparation of $SrAl_2O_4$:Eu^{2+},Dy^{3+} nanometer phosphors by detonation method, Mater. Lett., 60 (2006) 3673-3677.

[119] R. Rojas-Hernandez, M. Rodriguez, J. Fernandez, Role of the oxidizing agent to complete the synthesis of strontium aluminate based phosphors by the combustion method, RSC Adv., 5 (2015) 3104-3112.

[120] R. Ianoş, R. Istratie, C. Păcurariu, R. Lazău, Solution combustion synthesis of strontium aluminate, $SrAl_2O_4$, powders: single-fuel versus fuel-mixture approach, Phys. Chem. Chem. Phys., 18 (2016) 1150-1157.

[121] B. Cheng, Z. Zhang, Z. Han, Y. Xiao, S. Lei, $SrAl_xO_y:Eu^{2+},Dy^{3+}(x=4)$ nanostructures: Structure and morphology transformations and long-lasting phosphorescence properties, CrystEngComm, 13 (2011) 3545-3550.

[122] A. De, A.K. Dey, B. Samanta, U.K. Ghorai, Enhanced red photoluminescence in chain-like $SrAl_2O_4:Eu^{3+}$ nanophosphors: utilizing charge compensation by modulating Na^+ co-doping concentration, J. Mater. Sci.: Mater. Electron., 32 (2021) 8648-8656.

[123] D. Xu, D. Lv, F. Guo, G. Zhang, H. Wang, L. Xiong, J. Luo, W. Wang, H. Jiang, Facile fabrication of $SrAl_2O_4:Eu^{2+},Dy^{3+}$ hollow microsphere by a chemical induction self-transformation process, Ceram. Int., 46 (2020) 10807-10813.

[124] J. Wan, Y. Zhang, Y. Wang, R. Ma, Y. Wu, X. Qiao, X. Fan, Facile synthesis of monodisperse $SrAl_2O_4:Eu^{2+}$ cage-like microspheres with an excellent luminescence quantum yield, J. Mater. Chem. C, 6 (2018) 3346-3351.

[125] Y. Liu, C.-N. Xu, Influence of calcining temperature on photoluminescence and triboluminescence of europium-doped strontium aluminate particles prepared by sol−gel process, J. Phys. Chem. B, 107 (2003) 3991-3995.

[126] P. Escribano, M. Marchal, M.L. Sanjuán, P. Alonso-Gutiérrez, B. Julián, E. Cordoncillo, Low-temperature synthesis of $SrAl_2O_4$ by a modified sol–gel route: XRD and Raman characterization, J. Solid State Chem., 178 (2005) 1978-1987.

[127] X. Liyuan, X. Qin, L. Yingliang, Preparation and characterization of flower-like $SrAl_2O_4:Eu^{2+},Dy^{3+}$ phosphors by sol-gel process, J. Rare Earths, 29 (2011) 39-43.

[128] Y. Yang, H. Jiang, D. Xu, O. Hai, T. Yang, Preparation of $SrAl_2O_4:Eu^{2+},Dy^{3+}$ phosphors using propylene oxide as gel agent and its optical properties, Mater. Res. Express, 5 (2018) 016201.

[129] K. Song, J.-G. Mo, W. Chen, K. Feng, Hydrothermal synthesis and luminescence of $SrAl_2O_4:Eu^{2+}/Yb^{3+}$ hierarchical nanostructures, J. Mater. Sci.: Mater. Electron., 27 (2016) 49-53.

[130] B.-G. Park, Characteristics of Eu^{2+},Dy^{3+}-doped $SrAl_2O_4$ synthesized by hydrothermal reaction and its photocatalytic properties, J. Mater. Sci. Chem. Eng., 6 (2018) 12.

[131] D. Ravichandran, S.T. Johnson, S. Erdei, R. Roy, W.B. White, Crystal chemistry and luminescence of the Eu^{2+}-activated alkaline earth aluminate phosphors, Displays, 19 (1999) 197-203.

[132] C.-Y. Wu, C.-M. Lei, R. Wu, T. Takei, C.-C. Chou, S.-H. Wang, H.-Y. Chang, Nanothick aluminate long-afterglow phosphors using inherited hydrothermal deriving, J. Lumin., 206 (2019) 593-602.

[133] Q. Xiao, L. Xiao, Y. Liu, X. Chen, Y. Li, Synthesis and luminescence properties of needle-like $SrAl_2O_4$: Eu, Dy phosphor via a hydrothermal co-precipitation method, J. Phys. Chem. Solids, 71 (2010) 1026-1030.

[134] X. Zhiping, D. Suqing, L. Yingliang, L. Bingfu, X. Yong, M. ZHENG, Synthesis and luminescence properties of $SrAl_2O_4:Eu^{2+},Dy^{3+}$ hollow microspheres via a solvothermal co-precipitation method, J. Rare Earths, 31 (2013) 241-246.

[135] B. Cheng, H. Liu, M. Fang, Y. Xiao, S. Lei, L. Zhang, Long-persistent phosphorescent $SrAl_2O_4:Eu^{2+},Dy^{3+}$ nanotubes, Chem. Commun., (2009) 944-946.

[136] N. Chi, N. Tuan, N. Lien, D. Nguyen, Red emission of $SrAl_2O_4:Mn^{4+}$ phosphor for warm white light-emitting diodes, J. Electron. Mater., 47 (2018) 4571-4578.

[137] C.-H. Lu, S.-Y. Chen, C.-H. Hsu, Nanosized strontium aluminate phosphors prepared via a reverse microemulsion route, Mater. Sci. Eng.: B, 140 (2007) 218-221.

[138] S. Yanbin, Q. Guanming, L. Xikun, S. Zhang, Y. Changhao, X. Zhang, Synthesis of $SrAl_2O_4:Eu^{2+},Dy^{3+}$ phosphors by the coupling route of microemulsion with coprecipitation method, Rare Met., 25 (2006) 615-619.

[139] W. Shi, H. Yamada, K. Nishikubo, H. Kusaba, C. Xu, Novel structural behavior of strontium aluminate doped with europium, J. Electrochem. Soc., 151 (2004) H97.

[140] C. Li, Y. Imai, Y. Adachi, H. Yamada, K. Nishikubo, C.N. Xu, One-step synthesis of luminescent nanoparticles of complex oxide, strontium aluminate, J. Am. Ceram. Soc., 90 (2007) 2273-2275.

[141] W. Chung, H.J. Yu, S.H. Park, B.-H. Chun, J. Kim, S.H. Kim, Spray pyrolysis synthesis of $MAl_2O_4:Eu^{2+}$ (M= Ba, Sr) phosphor for UV LED excitation, J. crys. growth, 326 (2011) 73-76.

[142] S. Gültekin, S. Yıldırım, O. Yılmaz, İ.Ç. Keskin, M.İ. Katı, E. Çelik, Structural and optical properties of $SrAl_2O_4:Eu^{2+}/Dy^{3+}$ phosphors synthesized by flame spray pyrolysis technique, J. Lumin., 206 (2019) 59-69.

[143] W. Shi, H. Yamada, K. Nishikubo, H. Kusaba, C. Xu, Stabilization of beta-$SrAl_2O_4$ with Eu prepared by spray pyrolysis, MRS Online Proceedings Library, 755 (2002) 1-6.

[144] J. Han, Z. Jiang, W. Zhang, L. Hao, Y. Ni, C. Lu, Z. Xu, A facile and effective strategy to synthesize orthorhombic $Sr_2Al_6O_{11}:Eu^{2+},Dy^{3+}$ with blue-green persistent luminescence, IOP Conference Series: Mater. Sci. Eng., IOP Publishing, (2017) 012050.

[145] M. Peng, X. Yin, P.A. Tanner, C. Liang, P. Li, Q. Zhang, J. Qiu, Orderly-layered tetravalent manganese-doped strontium aluminate $Sr_4Al_{14}O_{25}:Mn^{4+}$: an efficient red phosphor for warm white light emitting diodes, J. Am. Ceram. Soc., 96 (2013) 2870-2876.

[146] L. Luo, R. Liu, Y. Liu, W. Zhuang, Y. Li, S. Qin, Enhanced luminescence performances of Mn^{4+}-activated $Sr_4Al_{14}O_{25}$ red phosphors by doping with Sc^{3+} ions, J. Rare Earths, 39 (2021) 380-385.

[147] Y. Lin, Z. Tang, Z. Zhang, Preparation of long-afterglow $Sr_4Al_{14}O_{25}$-based luminescent material and its optical properties, Mater. Lett., 51 (2001) 14-18.

[148] W. Minquan, D. Wang, L. Guanglie, Research on fluorescence spectra and structure of single-phase $4SrO·7Al_2O_3:Eu^{2+}$ phosphor prepared by solid-state reaction method, Mater. Sci. Eng.: B, 57 (1998) 18-23.

[149] M. Guzmán-Rocha, J. Oliva, L. Diaz-Torres, E. Montes, Effect of the reducing atmospheres on the photoluminescent and phosphorescent properties of $Sr_4Al_{14}O_{25}:Eu^{2+},Dy^{3+},Cr^{3+}$ phosphors, J. Solgel Sci. Technol., 95 (2020) 423-431.

[150] H.N. Luitel, T. Watari, T. Torikai, M. Yada, Luminescent properties of Cr^{3+} doped $Sr_4Al_{14}O_{25}$:Eu/Dy blue–green and red phosphor, Opt. Mater., 31 (2009) 1200-1204.

[151] C. Zhao, D. Chen, Y. Yuan, M. Wu, Synthesis of $Sr_4Al_{14}O_{25}:Eu^{2+},Dy^{3+}$ phosphor nanometer powders by combustion processes and its optical properties, Mater. Sci. Eng.: B, 133 (2006) 200-204.

[152] Z. Wu, M. Gong, J. Shi, Q. Su, Comparative investigation on synthesis and luminescence of $Sr_4Al_{14}O_{25}:Eu^{2+}$ applied in InGaN LEDs, J. Alloys Compd., 458 (2008) 134-137.

[153] C.-C. Chang, C.-Y. Yang, C.-H. Lu, Preparation and photoluminescence properties of $Sr_4Al_{14}O_{25}:Eu^{2+}$ phosphors synthesized via the microemulsion route, J. Mater. Sci.: Mater. Electron., 24 (2013) 1458-1462.

[154] M. Misevicius, V. Balevicius, Solid-state synthesis of $SrAl_4O_7$ and luminescence of Eu^{3+}-doped samples, Mater. Chem. Phys., 249 (2020) 122998.

[155] M. Misevicius, J. Pinkas, V. Balevicius, Solid-state synthesis and luminescence of europium doped and co-doped with dysprosium $SrAl_4O_7$, J. Alloys Compd., 820 (2020) 153110.

[156] C. Chang, D. Mao, J. Shen, C. Feng, Preparation of long persistent $SrO·2Al_2O_3$ ceramics and their luminescent properties, J. Alloys Compd., 348 (2003) 224-230.

[157] K. Gedekar, S. Wankhede, S. Moharil, R. Belekar, Ce^{3+} and Eu^{2+} luminescence in calcium and strontium aluminates, J. Mater. Sci.: Mater. Electron., 29 (2018) 4466-4477.

[158] D. Singh, V. Tanwar, A.P. Simantilleke, S. Bhagwan, B. Mari, P.S. Kadyan, K.C. Singh, I. Singh, Synthesis and enhanced luminescent characterization of $SrAl_4O_7:Eu^{2+}$, RE^{3+} (RE= Nd, Dy) nanophosphors for light emitting applications, J. Mater. Sci.: Mater. Electron., 27 (2016) 5303-5308.

[159] V. Singh, G. Lakshminarayana, A. Wagh, Sol-gel synthesis and fluorescence features of $SrAl_4O_7:Sm^{3+}$ phosphors, Optik, 204 (2020) 163908.

[160] S. Chawla, A. Yadav, Role of valence state of dopant (Eu^{2+}, Eu^{3+}) and growth environment in luminescence and morphology of $SrAl_{12}O_{19}$ nano-and microcrystals, Mater. Chemis. Phys., 122 (2010) 582-587.

[161] Y. Zhu, C. Li, D. Deng, B. Chen, H. Yu, H. Li, L. Wang, C. Shen, X. Jing, S. Xu, A high-sensitivity dual-mode optical thermometry based on one-step synthesis of Mn^{2+}: $BaAl_{12}O_{19}$–Mn^{4+}: $SrAl_{12}O_{19}$ solid solution phosphors, J. Alloys Compd., 853 (2021) 157262.

[162] L. Wang, Y. Xu, D. Wang, R. Zhou, N. Ding, M. Shi, Y. Chen, Y. Jiang, Y. Wang, Deep red phosphors $SrAl_{12}O_{19}$:Mn^{4+}, M (M= Li^+, Na^+, K^+, Mg^{2+}) for high colour rendering white LED s, physica status solidi (a), 210 (2013) 1433-1437.
[163] Z. Nie, J. Zhang, X. Zhang, K.-S. Lim, $SrAl_{12}O_{19}$:Pr^{3+} nanodisks and nanoplates: New processing technique and photon cascade emission, J. Mater. Res., 24 (2009) 1771-1779.
[164] K. Dev, A. Selot, G.B. Nair, C.M. Mehare, F.Z. Haque, M. Aynyas, S. Dhoble, Synthesis and photoluminescence study of Dy^{3+} activated $SrAl_{12}O_{19}$ phosphor, Optik, 194 (2019) 163051.
[165] V. Singh, M. Seshadri, M. Radha, N. Singh, S.H. Nandyala, Intense infrared, visible up and down emissions in Er^{3+}/Yb^{3+} co-doped $SrAl_{12}O_{19}$ obtained by urea assisted combustion route, J. Mater. Sci.: Mater. Electron., 29 (2018) 16516-16522.
[166] V. Singh, T.G. Rao, J.-J. Zhu, Preparation, luminescence and defect studies of Eu^{2+}-activated strontium hexa-aluminate phosphor prepared via combustion method, J. Solid State Chem., 179 (2006) 2589-2594.
[167] K. Mori, H. Onoda, T. Toyama, Y. Kojima, Synthesis and fluorescence studies of Eu^{3+}-doped $SrAl_{12}O_{19}$ phosphor, Optik, 180 (2019) 183-188.
[168] M. Peng, X. Yin, P.A. Tanner, M. Brik, P. Li, Site occupancy preference, enhancement mechanism, and thermal resistance of Mn^{4+} red luminescence in $Sr_4Al_{14}O_{25}$:Mn^{4+} for warm WLEDs, Chem. Mater., 27 (2015) 2938-2945.
[169] P.J. Saines, M.M. Elcombe, B.J. Kennedy, Lanthanide distribution in some doped alkaline earth aluminates and gallates, J. Solid State Chem., 179 (2006) 613-622.
[170] P.J. Saines, B.J. Kennedy, Implications of the solubility of trivalent lanthanides in AAl_2O_4 (A= Ca, Sr, and Ba) for their role in phosphors, Powder Diffr., 21 (2006) 285-288.
[171] T. Nakamura, K. Kaiya, N. Takahashi, T. Matsuzawa, M. Ohta, C. Rowlands, G. Smith, P. Riedi, High frequency EPR investigations of gadolinium (III)-doped strontium aluminates, Phys. Chem. Chem. Phys., 3 (2001) 1721-1723.
[172] P. Dorenbos, Energy of the first $4f^7 \rightarrow 4f^6 5d$ transition of Eu^{2+} in inorganic compounds, J. Lumin., 104 (2003) 239-260.
[173] P. Dorenbos, 5d-level energies of Ce^{3+} Fluoride I. and the crystalline environment. compounds, Phys. Rev. B -Condens. Matter Mater. Phys., 62, (2000) 15640-15649.
[174] P. Dorenbos, Relating the energy of the $[Xe]5d^1$ configuration of Ce^{3+} in inorganic compounds with anion polarizability and cation electronegativity, Phys. Rev. B, 65 (2002) 235110.
[175] P. Dorenbos, 5d-level energies of Ce^{3+} and the crystalline environment. IV. Aluminates and "simple" oxides, J. Lumin., 99 (2002) 283-299.
[176] P. Dorenbos, Relation between Eu^{2+} and Ce^{3+} f↔ d-transition energies in inorganic compounds, J. Phys.: Condens. Matter, 15 (2003) 4797.
[177] R. Shi, M. Qi, L. Ning, F. Pan, L. Zhou, W. Zhou, Y. Huang, H. Liang, Combined experimental and ab initio study of site preference of Ce^{3+} in $SrA_{l2}O_4$, J. Phys. Chem. C, 119 (2015) 19326-19332.
[178] G.I. Akmehmet, S. Šturm, M. Komelj, Z. Samardžija, B. Ambrožič, M. Sezen, M. Čeh, C.W. Ow-Yang, Origin of long afterglow in strontium aluminate phosphors: Atomic scale imaging of rare earth dopant clustering, Ceram. Int., 45 (2019) 20073-20077.
[179] B.F. dos Santos Jr, M.V. dos Santos Rezende, P.J. Montes, R.M. Araujo, M.A. Dos Santos, M.E. Valerio, Spectroscopy study of $SrAl_2O_4$:Eu^{3+}, J. Lumin., 132 (2012) 1015-1020.
[180] N.M. Strickland, G.D. Jones, Site-selective spectroscopy of Tm^{3+} centers in CaF_2:Tm^{3+}, Phys. Rev. B, 56 (1997) 10916.
[181] J. Corish, C. Catlow, P. Jacobs, S.H. Ong, Defect aggregation in anion-excess fluorites. Dopant monomers and dimers, Phys. Rev. B, 25 (1982) 6425.
[182] T. Delgado, Jakob Bierwagen, J. Afshani, S. Yoon, G. Nando, B. Walfort, H. Hagemann, Observation of multiple sites for trivalent Europium ions in $SrAl_2O_4$, resubmitted to J. Lumin may 2021.
[183] V. Panse, S. Choubey, R. Pandey, S. Dhoble, Photoluminescence analytical study of Ce^{3+}-activated blue-emitting $SrAl_{12}O_{19}$ lamp phosphors, Macromol. Symp., Wiley Online Library, (2020) 2000099.
[184] J. Choi, S. Baek, S. Kim, S. Lee, H. Park, S.-I. Mho, T. Kim, Y. Hwang, Energy transfer between Ce^{3+} and Eu^{2+} in $SrAl_{12}O_{19}$:Ce_x^{3+},$Eu_{0.01}^{2+}$(x= 0.01–0.09), Mater. Res. Bull., 34 (1999) 551-556.

[185] S.M. Loureiro, A. Setlur, W. Heward, S.T. Taylor, H. Comanzo, M. Manoharan, A. Srivastava, P. Schmidt, U. Happek, First observation of quantum splitting behavior in nanocrystalline $SrAl_{12}O_{19}$:Pr,Mg phosphor, Chem. Mater., 17 (2005) 3108-3113.
[186] Y. Ikeda, K. Masada, H. Kurokawa, H. Motomura, M. Jinno, K. Tachibana, Fluorescence properties of $SrAl_{12}O_{19}:Pr^{3+}$ quantum cutting phosphor, J. Phys. D: Appl. Phys., 46 (2013) 065305.
[187] J. Zhang, F. Liu, X.-j. Wang, J. Zhang, Calculating line intensities of 1S0 emission through standard and modified Judd–Ofelt theories in Pr^{3+}-doped $CaAl_{12}O_{19}$ and $SrAl_{12}O_{19}$, J. Phys.: Condens. Matter, 22 (2010) 155501.
[188] Z. Nie, J. Zhang, X. Zhang, X. Ren, W. Di, G. Zhang, D. Zhang, X. Wang, Spectroscopic investigation of $CaAl_{12}O_{19}:M^{3+}$ upon UV/vacuum–UV excitation: a comparison with $SrAl_{12}O_{19}:M^{3+}$ (M= Pr, Cr), J. Phys.: Condens. Matter, 19 (2007) 076204.
[189] Z. Nie, J. Zhang, X. Zhang, X. Ren, G. Zhang, X.-j. Wang, Evidence for visible quantum cutting via energy transfer in $SrAl_{12}O_{19}$:Pr,Cr, Opt. Lett., 32 (2007) 991-993.
[190] D. Wang, S. Huang, F. You, S. Qi, H. Peng, Application of original and modified Judd–Ofelt theories to the 1S0 state of Pr^{3+}-doped $SrAl_{12}O_{19}$ and LaF_3, Physica B: Condens. Matter, 387 (2007) 86-91.
[191] F. Liu, J. Zhang, S. Lu, S. Liu, S. Huang, X.-j. Wang, Explicit effects of 4f5d configuration on $4f^2 \rightarrow 4f^2$ electric dipole transitions in Pr^{3+}-doped $SrAl_{12}O_{19}$, Phys. Rev. B, 74 (2006) 115112.
[192] F. Liu, J.-h. Zhang, S.-z. Lu, S.-x. Liu, S.-h. Huang, X.-j. Wang, Selection rules for $4f^2 \rightarrow 4f^2$ electric dipole transitions by considering mixing with 4f5d components of Pr^{3+} in $SrAl_{12}O_{19}$, J. Lumin., 119 (2006) 492-495.
[193] S.-h. Huang, X.-j. Wang, B.-j. Chen, D. Jia, W. Yen, Photon cascade emission and quantum efficiency of the $3P_0$ level in Pr^{3+}-doped $SrAl_{12}O_{19}$ system, J. Lumin., 102 (2003) 344-348.
[194] P. Rodnyi, S. Mikhrin, P. Dorenbos, E. Van der Kolk, C. Van Eijk, A. Vink, A. Avanesov, The observation of photon cascade emission in Pr^{3+}-doped compounds under X-ray excitation, Opt. commun., 204 (2002) 237-245.
[195] P. Rodnyi, P. Dorenbos, G. Stryganyuk, A. Voloshinovskii, A. Potapov, C. Van Eijk, Emission of Pr^{3+} in $SrAl_{12}O_{19}$ under vacuum ultraviolet synchrotron excitation, Journal of Physics: Condens. Matter, 15 (2003) 719.
[196] A. Srivastava, W. Beers, Luminescence of Pr^{3+} in $SrAl_{12}O_{19}$: Observation of two photon luminescence in oxide lattice, J. Lumin., 71 (1997) 285-290.
[197] B. Zandi, L.D. Merkle, J.B. Gruber, D.E. Wortman, C.A. Morrison, Optical spectra and analysis for Pr^{3+} in $SrAl_{12}O_{19}$, J. Appl. Phys., 81 (1997) 1047-1054.
[198] H. Verdun, D. Wortman, C. Morrison, J. Bradshaw, Optical properties of Nd^{3+} in single crystal $SrAl_{12}O_{19}$, Opt. Mater., 7 (1997) 117-128.
[199] J. Liu, Q. Song, D. Li, X. Xu, J. Xu, Growth and red-orange emission of Sm^{3+} doped $SrAl_{12}O_{19}$ single crystals, Opt. Mater.., 101 (2020) 109754.
[200] D.-T. Marzahl, P.W. Metz, C. Kränkel, G. Huber, Spectroscopy and laser operation of Sm^{3+}-doped lithium lutetium tetrafluoride ($LiLuF_4$) and strontium hexaaluminate ($SrAl_{12}O_{19}$), Opt. express, 23 (2015) 21118-21127.
[201] V. Singh, G. Sivaramaiah, N. Singh, J. Rao, P.K. Singh, M. Pathak, D. Hakeem, EPR and PL studies on UVB-emitting gadolinium-doped $SrAl_{12}O_{19}$ phosphors, Optik, 158 (2018) 1227-1233.
[202] V. Mikhailik, VUV sensitization of Mn^{2+} emission by Tb^{3+} in strontium aluminate phosphor, Mater. Lett., 63 (2009) 803-805.
[203] V. Mikhailik, H. Kraus, Feasibility Study of VUV Sensitization Effect of Tb^{3+}, Spectrosc. Lett., 43 (2010) 350-356.
[204] X.-j. Wang, S. Huang, J. Zhang, W.M. Yen, Spectral properties and quantum efficiency of optical emission in rare earth doped crystals, J. Phys.: Conference Series, IOP Publishing, 28 (2006) 18-24.
[205] M. Puchalska, E. Zych, The effect of charge compensation through alkali metal co-doping on the luminescence behaviour of $SrAl_4O_7:Sm^{3+}$ phosphor, J. Lumin., 197 (2018) 211-218.
[206] A.N. Yerpude, S.J. Dhoble, B. Ramesh, B.D.P. Raju, Photoluminescence and decay properties of Sm^{3+} and Dy^{3+} in $SrAl_4O_7$ phosphor, Adv. Mater. Lett, 6 (2015) 1111-1115.
[207] N. Giri, S. Singh, D. Rai, S. Rai, $SrAl_4O_7:Tm^{3+}/Yb^{3+}$ nanocrystalline blue phosphor: structural, thermal and optical properties, Appl. Phys. B, 99 (2010) 271-277.

[208] M. Puchalska, E. Zych, A. Watras, Cooperative up-conversion processes in $SrAl_4O_7$:Yb and $SrAl_4O_7$:Yb,Tb and their dependence on charge compensation by Na, J. Lumin., 183 (2017) 185-192.

[209] G. Nikhare, S. Gedam, S. Dhoble, Luminescence in $Sr_4Al_{14}O_{25}$:Ce^{3+} aluminate phosphor, Luminescence, 30 (2015) 163-167.

[210] S.K. Sharma, S.S. Pitale, M.M. Malik, R. Dubey, M. Qureshi, Luminescence studies on the blue–green emitting $Sr_4Al_{14}O_{25}$:Ce^{3+} phosphor synthesized through solution combustion route, J. Lumin., 129 (2009) 140-147.

[211] H. Li, Y. Liang, S. Liu, W. Zhang, Y. Bi, Y. Gong, Y. Chen, W. Lei, Highly efficient green-emitting phosphor $Sr_4Al_{14}O_{25}$:Ce,Tb with low thermal quenching and wide color gamut upon UV-light excitation for backlighting display applications, J. Mater. Chem. C, 9 (2021) 2569-2581.

[212] S.H. Han, Y.J. Kim, Luminescent properties of Ce and Eu doped $Sr_4Al_{14}O_{25}$ phosphors, Opt. Materi., 28 (2006) 626-630.

[213] H.N. Luitel, T. Watari, R. Chand, T. Torikai, M. Yada, Photoluminescence properties of a novel orange red emitting $Sr_4Al_{14}O_{25}$:Sm^{3+} phosphor and PL enhancement by Bi^{3+} co-doping, Opt. Materi., 34 (2012) 1375-1380.

[214] V. Hedaoo, V. Bhatkar, S. Omanwar, Combustion synthesis and characterization of nanocrystalline alkaline earth aluminate $Sr_4Al_{14}O_{25}$:RE (RE= Eu, Dy, Sm), Int. J. Nanosci., 12 (2013) 1350023.

[215] S. Šakirzanovas, Novel $Sm^{2+/3+}$ phosphors as luminescence converter for near UV radiation, (2011).

[216] Z. Wang, B. Wang, Y. Liu, Z. Huang, Single-phased chromaticity-tunable phosphor of $Sr_4Al_{14}O_{25}$:$Eu^{2+/3+}$ co-doped with Tb^{3+} for white-light-emitting diodes, Mater. Res. Express, 6 (2019) 115903.

[217] S. Zhang, R. Pang, C. Li, Q. Su, Green photoluminescence, but blue afterglow of Tb^{3+} activated $Sr_4Al_{14}O_{25}$, J. Lumin., 130 (2010) 2223-2225.

[218] H. Kanno, K. Noda, K. Matsui, New long-afterglow phosphors: Yb^{2+}-doped strontium aluminates, Chem. Phys. Lett., 580 (2013) 103-107.

[219] L. Diaz-Torres, J. Oliva, D. Chavez, C. Garcia, Enhancing the white light emission of $SrAl_2O_4$:Ce^{3+} phosphors by codoping with Li^+ ions, Ceram. Int., 42 (2016) 16235-16241.

[220] X. Xu, Y. Wang, X. Yu, Y. Li, Y. Gong, Investigation of Ce–Mn energy transfer in $SrAl_2O_4$:Ce^{3+},Mn^{2+}, J. Am. Ceram. Soc., 94 (2011) 160-163.

[221] R. Neema, M. Saleem, P. Sharma, M. Mittal, Structural and photoluminescent studies of $SrAl_2O_4$:Dy^{3+},Ce^{3+} phosphors, in: AIP Conference Proceedings, AIP Publishing LLC, 2019, pp. 020189.

[222] K. Gedekar, S. Wankhede, S. Moharil, R. Belekar, d–f luminescence of Ce^{3+} and Eu^{2+} ions in $BaAl_2O_4$, $SrAl_2O_4$ and $CaAl_2O_4$ phosphors, J. Adv. Ceram., 6 (2017) 341-350.

[223] D. Nakauchi, G. Okada, M. Koshimizu, T. Yanagida, Evaluation of Ce:$SrAl_2O_4$ crystalline scintillators, Nucl. Instrum. Methods Phys. Res. B: Beam Interactions with Materials and Atoms, 377 (2016) 89-93.

[224] K. Foka, F. Dejene, H. Swart, Photoluminescence properties of Ce^{3+}-doped $SrAl_2O_4$ prepared using the solution combustion method, Physica B: Condens. Matter, 439 (2014) 177-180.

[225] R. Zheng, L. Xu, W. Qin, J. Chen, B. Dong, L. Zhang, H. Song, Electrospinning preparation and photoluminescence properties of $SrAl_2O_4$:Ce^{3+} nanowires, J. Mater. Sci., 46 (2011) 7517-7524.

[226] N.K. Zurba, I. Bdikin, A. Kholkin, D. Golberg, J.M. Ferreira, Intercrystalline distal-effect on the afterglow phenomenon in photoluminescent $SrAl_2O_4$:Ce(III), Ln nanotube growth, Nanotechnology, 21 (2010) 325707.

[227] B. Geng, J. Ma, F. Zhan, A solution chemistry approach for one-dimensional needle-like $SrAl_2O_4$ nanostructures with Ln (Ce^{3+}, Eu^{2+} and Tb^{3+}) as activator/dopant, J. Alloys Compd., 473 (2009) 530-533.

[228] D. Jia, Relocalization of Ce^{3+} 5d electrons from host conduction band, J. Lumin., 117 (2006) 170-178.

[229] Z. Fu, S. Zhou, S. Zhang, Study on optical properties of rare-earth ions in nanocrystalline monoclinic $SrAl_2O_4$:Ln (Ln= Ce^{3+}, Pr^{3+}, Tb^{3+}), J. Phys. Chem. B, 109 (2005) 14396-14400.

[230] D. Nakauchi, G. Okada, M. Koshimizu, T. Yanagida, Scintillation and thermally-stimulated luminescence properties of Pr-doped $SrAl_2O_4$ single crystals, Radiat. Meas., 106 (2017) 170-174.

[231] S. Chawla, N. Kumar, H. Chander, Broad yellow orange emission from $SrAl_2O_4:Pr^{3+}$ phosphor with blue excitation for application to white LEDs, J. Lumin., 129 (2009) 114-118.

[232] X. Feng, W. Feng, K. Wang, Experimental and theoretical spectroscopic study of praseodymium (III) doped strontium aluminate phosphors, J. Alloys Compd., 628 (2015) 343-346.

[233] D. Nakauchi, G. Okada, M. Koshimizu, T. Yanagida, Optical and scintillation properties of Nd-doped $SrAl_2O_4$ crystals, J. Rare Earths, 34 (2016) 757-762.

[234] M. Ayvacıkli, Z. Kotan, E. Ekdal, Y. Karabulut, A. Canimoglu, J.G. Guinea, A. Khatab, M. Henini, N. Can, Solid state synthesis of $SrAl_2O_4:Mn^{2+}$ co-doped with Nd^{3+} phosphor and its optical properties, J. Lumin., 144 (2013) 128-132.

[235] T.-P. Tang, C.-M. Lee, F.-C. Yen, The photoluminescence of $SrAl_2O_4$: Sm phosphors, Ceram. Int., 32 (2006) 665-671.

[236] M. Ayvacıklı, A. Ege, N. Can, Radioluminescence of $SrAl_2O_4:Ln^{3+}$ (Ln= Eu, Sm, Dy) phosphor ceramic, Opt. Materi., 34 (2011) 138-142.

[237] V. Singh, N. Singh, M. Pathak, V. Natarajan, Annealing effect on the structural, optical and EPR properties of UV radiation emitting Gd^{3+} doped $SrAl_2O_4$ host, J. Electron. Mater., 48 (2019) 238-243.

[238] B. Jamalaiah, N. Venkatramaiah, T.S. Rao, S.N. Rasool, B.N. Rao, D.R. Ram, A.S.N. Reddy, UV excited $SrAl_2O_4:Tb^{3+}$ nanophosphors for photonic applications, Mater. Sci. Semicond. Process., 105 (2020) 104722.

[239] B. Jamalaiah, N. Madhu, Luminescence properties of $SrAl_2O_4:Tb^{3+}/Bi^{3+}$ nanophosphors for photonic applications, J. Mol. Struct., 1205 (2020) 127599.

[240] B.-g. Zhai, Y.M. Huang, Green photoluminescence and afterglow of Tb-doped $SrAl_2O_4$, J. Mater. Sci., 52 (2017) 1813-1822.

[241] I. Mindru, D. Gingasu, L. Patron, G. Marinescu, J.M. Calderon-Moreno, L. Diamandescu, M. Secu, O. Oprea, Tb^{3+}-doped alkaline-earth aluminates: Synthesis, characterization and optical properties, Mater. Res. Bull., 85 (2017) 240-248.

[242] K.G. Kumar, P.B. Bhargav, K. Aravinth, R. Arumugam, P. Ramasamy, Dysprosium activated strontium aluminate phosphor: A potential candidate for WLED applications, J. Lumin., 223 (2020) 117126.

[243] T. Delgado, S. Ajoubipour, J. Afshani, S. Yoon, B. Walfort, H. Hagemann, Spectroscopic properties of Dy^{3+}-and Dy^{3+}, B^{3+}-doped $SrAl_2O_4$, Opt. Materi., 89 (2019) 268-275.

[244] B.-g. Zhai, L. Yang, Q.-l. Ma, X. Liu, Y.M. Huang, Mechanism of the prolongation of the green afterglow of $SrAl_2O_4:Dy^{3+}$ caused by the use of H_3BO_3 flux, J. Lumin., 181 (2017) 78-87.

[245] B.C. Jamalaiah, Y.R. Babu, Near UV excited $SrAl_2O_4:Dy^{3+}$ phosphors for white LED applications, Mater. Chemis. Phys., 211 (2018) 181-191.

[246] R. Sharma, D. Bisen, B. Chandra, Mechanoluminescence of Dy doped strontium aluminate nanophosphors, J. Lumin., 168 (2015) 49-53.

[247] M. Tang, X. Wang, D. Peng, W. Wang, H. Sun, X. Yao, Strong green and red up-conversion emission in Ho^{3+}, Yb^{3+} and Li^+ co-or tri-doped $SrAl_2O_4$ ceramics, J. Alloys Compd., 529 (2012) 49-51.

[248] L. De Herval, Y.T. Arslanlar, M. Ayvacikli, F. Iikawa, J. Nobrega, P. Pizani, Y.G. Gobato, N. Can, M. Henini, M. de Godoy, Enhancement of the luminescence intensity by co-doping Mn^{2+} into Er^{3+}-doped $SrAl_2O_4$, J. Lumin., 163 (2015) 17-20.

[249] M. Ayvacıklı, A. Ege, S. Yerci, N. Can, Synthesis and optical properties of Er^{3+} and Eu^{3+} doped $SrAl_2O_4$ phosphor ceramic, J. Lumin., 131 (2011) 2432-2439.

[250] A. Choudhary, A. Dwivedi, A. Bahadur, S. Rai, Enhanced upconversion from Er^{3+}/Yb^{3+} co-doped alkaline earth aluminates phosphor in presence Zn^{2+}: A comparative study, J. Lumin., 210 (2019) 135-141.

[251] A.K. Choudhary, A. Dwivedi, A. Bahadur, S. Rai, Effect of the concentration of the dopants (Er^{3+}, Yb^{3+} and Zn^{2+}) and temperature on the upconversion emission behavior of Er^{3+}/Yb^{3+} co-doped $SrAl_2O_4$ phosphor, Spectrochim. Acta Part A: Mol. Biomol. Spectrosc., 185 (2017) 155-162.

[252] S. Pawar, R.S. Kumaran, M. Kumar, K. Yun, S. Dhoble, V. Singh, On the infrared emissions of Er^{3+}/Yb^{3+} co-doped $SrAl_2O_4$, Optik, 136 (2017) 581-585.

[253] F. Yu, Y. Yang, X. Su, C. Mi, H.J. Seo, Novel long persistent luminescence phosphors: Yb^{2+} codoped MAl_2O_4 (M= Ba, Sr), Opt. Mater. Express, 5 (2015) 585-595.

[254] G. Li, Y. Lai, T. Cui, H. Yu, D. Liu, S. Gan, Luminescence properties and charge compensation of $Sr_3Al_2O_6$ doped with Ce^{3+} and alkali metal ions, Mater. Chem.. Phys., 124 (2010) 1094-1099.

[255] V. Singh, M. Seshadri, N. Singh, M. Mohapatra, Radiative properties of Er^{3+} doped and Er^{3+}/Yb^{3+} co-doped $Sr_3Al_2O_6$ phosphors: exploring the usefulness as a phosphor material, J. Mater. Sci.: Mater. Electron., 30 (2019) 2927-2934.

[256] S.-D. Han, K.C. Singh, T.-Y. Cho, H.-S. Lee, D. Jakhar, J.P. Hulme, C.-H. Han, J.-D. Kim, I.-S. Chun, J. Gwak, Preparation and characterization of long persistence strontium aluminate phosphor, J. Lumin., 128 (2008) 301-305.

[257] M. Peng, Z. Pei, G. Hong, Q. Su, Study on the reduction of $Eu^{3+}\rightarrow Eu^{2+}$ in $Sr_4Al_{14}O_{25}$:Eu prepared in air atmosphere, Chem. Phys. Lett., 371 (2003) 1-6.

[258] Y. Alves, D. Sampaio, J. Santos, M. Rezende, N. Souza, C. Kucera, J. Ballato, R. Silva, Laser sintering and optical characterization of $SrAl_{2-x}B_xO_4$:Eu,Dy ceramics, Optik, 221 (2020) 165338.

[259] S. Yoon, J. Bierwagen, M. Trottmann, B. Walfort, N. Gartmann, A. Weidenkaff, H. Hagemann, S. Pokrant, The influence of boric acid on improved persistent luminescence and thermal oxidation resistance of $SrA_{l2}O_4:Eu^{2+}$, J. Lumin., 167 (2015) 126-131.

[260] D. Wang, Q. Yin, Y. Li, M. Wang, Concentration quenching of Eu^{2+} in $SrO{\cdot}Al_2O_3:Eu^{2+}$ phosphor, J. Lumin., 97 (2002) 1-6.

[261] K. Kaiya, N. Takahashi, T. Nakamura, T. Matsuzawa, G. Smith, P. Riedi, EPR studies of europium (II)-doped strontium aluminate phosphors, J. Lumin., 87 (2000) 1073-1075.

[262] T. Nakamura, T. Matsuzawa, C. Rowlands, V. Beltran-Lopez, G. Smith, P. Riedi, EPR investigations on europium (II)-doped aluminates, J. Chem. Soc., Faraday Trans., 94 (1998) 3009-3012.

[263] H. Matsuoka, K. Furukawa, K. Sato, D. Shiomi, Y. Kojima, K. Hirotsu, N. Furuno, T. Kato, T. Takui, Importance of fourth-order zero-field splitting terms in random-orientation EPR spectra of Eu(II)-doped strontium aluminate, J. Phys. Chem. A, 107 (2003) 11539-11546.

[264] C.K. Jørgensen: Modern aspects of ligand field theory. North-Holland Publishing Co. 1971. 538 p.

[265] F. Meister, M. Batentschuk, S. Dröscher, A. Osvet, A. Stiegelschmitt, M. Weidner, A. Winnacker, Eu^{2+} luminescence in the $EuAl_2O_4$ concentrated phosphor, Radiat. Meas., 42 (2007) 771-774.

[266] H. Liu, X. Liu, X. Wang, M. Peng, P. Xiong, Y. Chen, Y. Wang, B. Lei, Q. Zeng, Unusual concentration induced antithermal quenching of the Eu^{2+} emission at 490 nm in $Sr_4Al_{14}O_{25}$: Eu^{2+} for near ultraviolet excited white LEDs, J. Am. Ceram. Soc., 103 (2020) 5758-5768.

[267] D. Dutczak, C. Ronda, T. Jüstel, A. Meijerink, Anomalous trapped exciton and d–f emission in $Sr_4Al_{14}O_{25}:Eu^{2+}$, J. Phys. Chem. A, 118 (2014) 1617-1621.

[268] H. Terraschke, M. Suta, M. Adlung, S. Mammadova, N. Musayeva, R. Jabbarov, M. Nazarov, C. Wickleder, $SrAl_2O_4:Eu^{2+}$(, Dy^{3+}) nanosized particles: synthesis and interpretation of temperature-dependent optical properties, J. Spectrosc., 2015 (2015).

[269] P. Zhang, L. Li, M. Xu, L. Liu, The new red luminescent $Sr_3Al_2O_6:Eu^{2+}$ phosphor powders synthesized via sol–gel route by microwave-assisted, J. Alloys Compd., 456 (2008) 216-219.

[270] S. Poort, A. Meyerink, G. Blasse, Lifetime measurements in Eu^{2+}-doped host lattices, J. Phys. Chem. Solids, 58 (1997) 1451-1456.

[271] H. Yamamoto, T. Matsuzawa, Mechanism of long phosphorescence of $SrAl_2O_4:Eu^{2+},Dy^{3+}$ and $CaAl_2O_4:Eu^{2+},Nd^{3+}$, J. Lumin., 72 (1997) 287-289.

[272] J. Bierwagen, S. Yoon, N. Gartmann, B. Walfort, H. Hagemann, Thermal and concentration dependent energy transfer of Eu^{2+} in $SrAl_2O_4$, Opt. Materi. Express, 6 (2016) 793-803.

[273] J. Botterman, J.J. Joos, P.F. Smet, Trapping and detrapping in SrAl 2 O 4: Eu, Dy persistent phosphors: Influence of excitation wavelength and temperature, Phys. Rev. B, 90 (2014) 085147.

[274] M. Nazarov, M.G. Brik, D. Spassky, B. Tsukerblat, Crystal field splitting of 5d states and luminescence mechanism in $SrAl_2O_4:Eu^{2+}$ phosphor, J. Lumin., 182 (2017) 79-86.

[275] L. Ning, X. Huang, Y. Huang, P.A. Tanner, Origin of the green persistent luminescence of Eu-doped $SrAl_2O_4$ from a multiconfigurational ab initio study of $4f^7\rightarrow 4f^65d^1$ transitions, J. Mater. Chem. C, 6 (2018) 6637-6640.

[276] T. Delgado, J. Afshani, H. Hagemann, Spectroscopic study of a single crystal of $SrAl_2O_4:Eu^{2+},Dy^{3+}$, J. Phys. Chem. C, 123 (2019) 8607-8613.

[277] A. Uehara, O. Shirai, T. Nagai, T. Fujii, H. Yamana, Spectroelectrochemistry and electrochemistry of europium ions in alkali chloride melts, Zeitschrift für Naturforschung A, 62 (2007) 191-196.

[278] P. Dorenbos, Locating lanthanide impurity levels in the forbidden band of host crystals, J. Lumin., 108 (2004) 301-305.
[279] D.L. Dexter, A theory of sensitized luminescence in solids, J. Chem. Phys., 21 (1953) 836-850.
[280] B. Walfort, N. Gartmann, J. Afshani, A. Rosspeintner, H. Hagemann, Effect of excitation wavelength (blue vs near UV) and dopant concentrations on the afterglow and fast decay of the persistent phosphor $SrAl_2O_4:Eu^{2+},Dy^{3+}$, Submitted to J. Rare Earth (2021).
[281] P. Dorenbos, Thermal quenching of Eu^{2+} 5d–4f luminescence in inorganic compounds, J. Phys.: Condens. Matter, 17 (2005) 8103.
[282] R.E. Rojas-Hernandez, W. More, F. Rubio-Marcos, J.F. Fernandez, Investigating Raman spectra and density functional theory calculations on $SrAl_2O_4$ polymorphs, J. Raman Spectrosc., 50 (2019) 91-101.
[283] J. Ueda, T. Nakanishi, Y. Katayama, S. Tanabe, Optical and optoelectronic analysis of persistent luminescence in Eu^{2+}-Dy^{3+} codoped $SrAl_2O_4$ ceramic phosphor, physica status solidi (c), 9 (2012) 2322-2325.
[284] D. Nakauchi, G. Okada, M. Koshimizu, T. Yanagida, Storage luminescence and scintillation properties of Eu-doped $SrAl_2O_4$ crystals, J. Lumin., 176 (2016) 342-346.
[285] Y. Zorenko, V. Gorbenko, M. Grinberg, R. Turos-Matysiak, B. Kukliński, High-pressure luminescence spectroscopy of $EuAl_2O_4$ phosphor, Radiat. Meas., 42 (2007) 652-656.
[286] H. Hagemann, P. Pal,, Unpublished data.
[287] P. Dorenbos, Anomalous luminescence of Eu^{2+} and Yb^{2+} in inorganic compounds, J. Phys.: Condens. Matter, 15 (2003) 2645.
[288] https://www.iso.org/standard/31404.html.
[289] O.R. Noboru, Alan R., "3.9: Standard and Supplementary Illuminants". Colorimetry. Wiley. pp. 92–96. doi:10.1002/0470094745.ch3. ISBN 978-0-470-09472-3., (2005).
[290] D. Van der Heggen, J.J. Joos, D.C. Rodríguez Burbano, J.A. Capobianco, P.F. Smet, Counting the photons: Determining the absolute storage capacity of persistent phosphors, Materials, 10 (2017) 867.
[291] J. Bierwagen, T. Delgado, G. Jiranek, S. Yoon, N. Gartmann, B. Walfort, M. Pollnau, H. Hagemann, Probing traps in the persistent phosphor $SrAl_2O_4:Eu^{2+},Dy^{3+},B^{3+}$-A wavelength, temperature and sample dependent thermoluminescence investigation, J. Lumin., 222 (2020) 117113.
[292] D. Van der Heggen, D. Vandenberghe, N.K. Moayed, J. De Grave, P.F. Smet, J.J. Joos, The almost hidden role of deep traps when measuring afterglow and thermoluminescence of persistent phosphors, J. Lumin., 226 (2020) 117496.
[293] E. Finley, A. Mansouri Tehrani, J. Brgoch, Intrinsic defects drive persistent luminescence in monoclinic $SrAl_2O_4:Eu^{2+}$, J. Phys. Chem. C, 122 (2018) 16309-16314.
[294] V. Vitola, D. Millers, K. Smits, I. Bite, A. Zolotarjovs, The search for defects in undoped $SrAl_2O_4$ material, Opt. Materi., 87 (2019) 48-52.
[295] T. Takeyama, T. Nakamura, N. Takahashi, M. Ohta, Electron paramagnetic resonance studies on the defects formed in the Dy (III)-doped $SrAl_2O_4$, Solid state Sci., 6 (2004) 345-348.
[296] A. Surdo, V. Kortov, V. Pustovarov, Luminescence of F and F^+ centers in corundum upon excitation in the interval from 4 to 40eV, Radiat. Meas., 33 (2001) 587-591.
[297] J. Valbis, N. Itoh, Electronic excitations, luminescence and lattice defect formation in α-Al_2O_3 crystals, Radiat. Eff. Defects Solids, 116 (1991) 171-189.
[298] M. Nazarov, S. Mammadova, D. Spassky, S. Vielhauer, S. Abdullayeva, A. Huseynov, R. Jabbarov, $SrAl_2O_4:Eu^{2+}$ (1%) luminescence under UV, VUV and electron beam excitation, Opt. Materi., 75 (2018) 448-452.
[299] P. Boutinaud, D. Boyer, A. Perthue, R. Mahiou, E. Cavalli, M. Brik, Spectroscopic investigations on $SrAl_2O_4$ polymorphs, J. Lumin., 159 (2015) 158-165.
[300] Y. Kamiyanagi, M. Kitaura, M. Kaneyoshi, Temperature dependence of long-lasting afterglow in $SrAl_2O_4$:Eu,Dy phosphor, J. Lumin., 122 (2007) 509-511.
[301] F. Clabau, X. Rocquefelte, S. Jobic, P. Deniard, M.-H. Whangbo, A. Garcia, T. Le Mercier, On the phosphorescence mechanism in $SrAl_2O_4:Eu^{2+}$ and its codoped derivatives, Solid State Sci., 9 (2007) 608-612.

[302] K. Kato, Y. Ogura, M. Sengiku, K. Shinbo, F. Kaneko, Y. Oda, K. Yatsui, Luminescent Properties of $SrAl_2O_4$:Eu thin films deposited by intense pulsed ion-beam evaporation, Japanese J. Appl. Phys., 40 (2001) 1038.
[303] V. Abbruscato, Optical and electrical properties of $SrAl_2O_4:Eu^{2+}$, J. Electrochem. Soc., 118 (1971) 930.
[304] S.-F. Ye, L.-Y. Hao, X. Xu, S. Agathopoulos, Nitride-doped $Sr_4Al_{14}O_{25}:Eu^{2+}$ phosphor with improved photoluminescence and long afterglow, ECS J. Solid State Sci. Technol., 8 (2019) R75.
[305] L. Ma, Z. Xia, Q. Liu, Effect of AlN addition on the photoluminescence and phosphorescence properties of $SrAl_2O_4:Eu^{2+},Dy^{3+}$ phosphors, Opt. Eng., 54 (2015) 067105.
[306] A. Nag, T. Kutty, The mechanism of long phosphorescence of $SrAl_{2-x}B_xO_4$ (0< x< 0.2) and $Sr_4Al_{14-x}B_xO_{25}$ (0.1< x< 0.4) co-doped with Eu^{2+} and Dy^{3+}, Mater. Res. Bull., 39 (2004) 331-342.
[307] V. Vitola, I. Bite, D. Millers, A. Zolotarjovs, K. Laganovska, K. Smits, A. Spustaka, The boron effect on low temperature luminescence of $SrAl_2O_4$:Eu,Dy, Ceram. Int., 46 (2020) 26377-26381.
[308] A. Nag, T. Kutty, Role of B_2O_3 on the phase stability and long phosphorescence of $SrAl_2O_4$:Eu,Dy, J. Alloys Compd., 354 (2003) 221-231.
[309] I.-C. Chen, T.-M. Chen, Sol-gel synthesis and the effect of boron addition on the phosphorescent properties of $SrAl_2O_4:Eu^{2+},Dy^{3+}$ phosphors, J. Mater. Res., 16 (2001) 644-651.
[310] E. Nakazawa, Y. Murazaki, S. Saito, Mechanism of the persistent phosphorescence in $Sr_4Al_{14}O_{25}$:Eu and $SrAl_2O_4$:Eu codoped with rare earth ions, J. Appl. Phys., 100 (2006) 113113.
[311] J.J. Joos, K. Korthout, L. Amidani, P. Glatzel, D. Poelman, P.F. Smet, Identification of Dy^{3+}/Dy^{2+} as electron trap in persistent phosphors, Phys. Rev. Lett., 125 (2020) 033001.
[312] F. Pelle, T. Aitasalo, M. Lastusaari, J. Niittykoski, J. Hölsä, Optically stimulated luminescence of persistent luminescence materials, J. Lumin., 119 (2006) 64-68.
[313] Z. Győri, V. Havasi, D. Madarász, D. Tátrai, T. Brigancz, G. Szabó, Z. Kónya, Á. Kukovecz, Luminescence properties of Ho^{3+} co-doped $SrAl_2O_4:Eu^{2+},Dy^{3+}$ long-persistent phosphors synthesized with a solid-state method, J. Mol. Struct., 1044 (2013) 87-93.
[314] T. Aitasalo, J. Hölsä, H. Jungner, J.-C. Krupa, M. Lastusaari, J. Legendziewicz, J. Niittykoski, Effect of temperature on the luminescence processes of $SrAl_2O_4:Eu^{2+}$, Radiat. Meas., 38 (2004) 727-730.
[315] F. Clabau, X. Rocquefelte, S. Jobic, P. Deniard, M.-H. Whangbo, A. Garcia, T. Le Mercier, Mechanism of phosphorescence appropriate for the long-lasting phosphors Eu^{2+}-doped $SrAl_2O_4$ with codopants Dy^{3+} and B^{3+}, Chem. Mater., 17 (2005) 3904-3912.
[316] P. Dorenbos, Mechanism of persistent luminescence in Eu^{2+} and Dy^{3+} codoped aluminate and silicate compounds, J. Electrochem. Soc., 152 (2005) H107.
[317] A.J. Bos, R.M. Van Duijvenvoorde, E. Van der Kolk, W. Drozdowski, P. Dorenbos, Thermoluminescence excitation spectroscopy: A versatile technique to study persistent luminescence phosphors, J. Lumin., 131 (2011) 1465-1471.
[318] T. Delgado, G. Nando, B. Walfort, F. La Mattina, M. Pollnau; J. Afshani, J. Olchowka, H. Hagemann, Fundamental loading-curve characteristics of the persistent phosphor $SrAl_2O_4:Eu^{2+},Dy^{3+},B^{3+}$: the effect of temperature and excitation density, To be submitted, (2021).
[319] D. Van der Heggen, J.J. Joos, P.F. Smet, Importance of evaluating the intensity dependency of the quantum efficiency: impact on LEDs and persistent phosphors, ACS Photonics, 5 (2018) 4529-4537.
[320] C. Tydtgat, K.W. Meert, D. Poelman, P.F. Smet, Optically stimulated detrapping during charging of persistent phosphors, Opt. Mat. Express, 6 (2016) 844-858.
[321] P. Zeng, X. Wei, M. Yin, Y. Chen, Investigation of the long afterglow mechanism in $SrAl_2O_4:Eu^{2+}/Dy^{3+}$ by optically stimulated luminescence and thermoluminescence, J. Lumin., 199 (2018) 400-406.
[322] M. Chithambo, Thermal assistance in the optically stimulated luminescence of superluminous $Sr_4Al_{14}O_{25}:Eu^{2+},Dy^{3+}$, Physica B: Condens. Matter, 603 (2021) 412722.
[323] H. Liu, B. Feng, L. Luo, C. Han, P.A. Tanner, Near infrared photostimulated persistent luminescence and information storage of $SrAl_2O_4:Eu^{2+},Dy^{3+}$ phosphor, Opt. Mat. Express, 6 (2016) 3375-3385.
[324] D. Jia, Charging curves and excitation spectrum of long persistent phosphor $SrAl_2O_4:Eu^{2+},Dy^{3+}$, Opt. Mat., 22 (2003) 65-69.

[325] Z. He, X.-j. Wang, W. Yen, Investigation on charging processes and phosphorescent efficiency of $SrAl_2O_4$: Eu, Dy, J. Lumin., 119 (2006) 309-313.

[326] V. Havasi, D. Tátrai, G. Szabó, G. Sipos, Z. Kónya, Á. Kukovecz, Systematic comparison of saturation effects and afterglow properties of $Sr_4Al_{14}O_{25}$:Eu,Dy phosphor excited by alpha and beta ionizing sources and UV light, J. Mol. Struct., 1140 (2017) 89-98.

[327] W. Jia, H. Yuan, S. Holmstrom, H. Liu, W. Yen, Photo-stimulated luminescence in $SrAl_2O_4:Eu^{2+},Dy^{3+}$ single crystal fibers, J. Lumin., 83 (1999) 465-469.

[328] J. Du, O.Q. De Clercq, D. Poelman, Temperature dependent persistent luminescence: Evaluating the optimum working temperature, Sci. Rep., 9 (2019) 1-11.

[329] J.J. Joos, L. Seijo, Z. Barandiarán, Direct evidence of intervalence charge-transfer states of Eu-doped luminescent materials, J. Phys. Chem. Lett., 10 (2019) 1581-1586.

Paper I: Controlled preparation of deep-red-emitting $CaAl_{12}O_{19}:Eu^{3+}$ and $SrAl_{12}O_{19}:Eu^{3+}$ hexagonal nanoparticles by a cooperative microgel formation and subsequent self-transformation process

In this first main paper for the thesis, the controlled synthesis protocol of nanoparticles of $SrAl_{12}O_{19}$ and $CaAl_{12}O_{19}$ is addressed. A new solvothermal synthesis method was developed, which shows promising results for the controlled synthesis of not only, strontium aluminate NPs with different Sr^{2+}:Al^{3+} ratios, but also for the synthesis of calcium aluminates as well. Investigation of the synthesis mechanism clearly shows the formation of micro-sized gels, consisting of polyvinylpyrrolidone (PVP) and Al^{3+} ions. These gels act as micro-sized reactors and provide excellent control over the morphology and size distribution of the $SrAl_{12}O_{19}:Eu^{3+}$, and $CaAl_{12}O_{19}:Eu^{3+}$ precursor NPs in between 200 and 300 nm. These NPs were then annealed at 1150 °C to obtain their respective crystalline phases. During the annealing process a shape transformation occurred from spherical amorphous NPs to hexagonal platelets. This method looks promising for the preparation of other bi- or multi-metallic oxide NPs. Studying the luminescence properties of Eu^{3+} in these crystalline NPs, interestingly, revealed a deep-red luminescence (680 nm) originating from the $^5D_0 \rightarrow {}^7F_4$ transition of the Eu^{3+} ion.

This paper is still under development.

Controlled preparation of deep-red-emitting $CaAl_{12}O_{19}:Eu^{3+}$ and $SrAl_{12}O_{19}:Eu^{3+}$ hexagonal nanoparticles by a cooperative microgel formation and subsequent self-transformation process

Jafar Afshani [a], Teresa Delgado [a,b], Céline Besnard [c], Yashar Sadian[d], Hans Hagemann [a]

[a] Département de Chimie Physique, Université de Genève, Quai Ernest-Ansermet 30, Genève 1211, Switzerland.

[b] Chimie ParisTech-CNRS, IRCP (PSL), 11 Rue P. et M. Curie, 75005, Paris, France

[c] Laboratoire de Cristallographie, DQMP, Université de Geneve, Quai Ernest-Ansermet 24, CH-1211 Geneva 4, Switzerland

[d] Department of Biochemistry, University of Geneva, Geneva, Switzerland

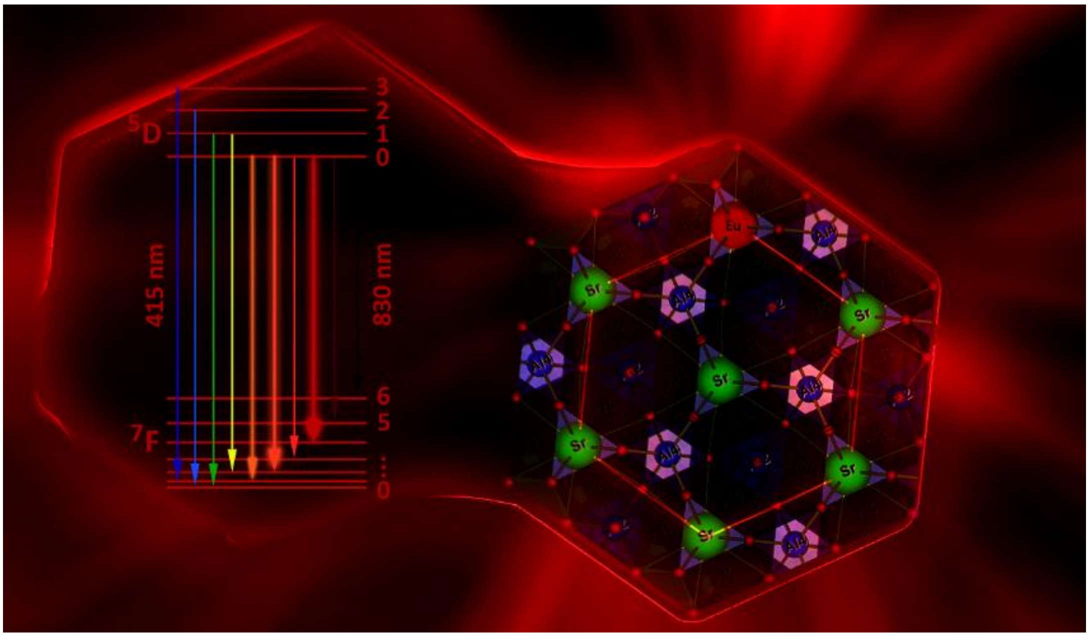

Graphical abstract

Abstract

Red-emitting phosphors attract increasing attention in a variety of fields. Biological applications, white-light emitting diodes, and plasma display panels all greatly demand red and deep-red phosphors with high luminescence efficiency and purity. Inorganic matrixes with luminescent activators show excellent properties both in terms of luminescence and chemical stability. Among them, calcium/strontium aluminates with a wide transparency window extending from the UV to near infrared (NIR) and outstandingly high thermal and chemical stability are excellent host materials for current and future optoelectronic applications. However, despite many current uses, their large grain sizes have taken the better of their huge potential. The preparation of these compounds, which takes place at significantly elevated temperatures, leaves only diminutive room for controlling their sizes and morphologies. Here, Eu^{3+}-doped $CaAl_{12}O_{19}$ and $SrAl_{12}O_{19}$ hexagonal 150-250 nm-sized nanoparticles (NPs) are successfully synthesized via a cooperative micro-sized gel formation in a solvothermal reaction. In less than 10 minutes, the gel pools self-transform into spherical NPs with homogeneous morphology and size distribution. Upon annealing, these spherical NPs transform into hexagonal crystalline platelets of $CaAl_{12}O_{19}$ and $SrAl_{12}O_{19}$.

Emission of Eu^{3+} from the $^5D_{0\text{-}3}$ excited states at room temperature, which has rarely been observed, indicates the very low non-radiative energy loss in these NPs. Moreover, unlike in the majority of the cases, where Eu^{3+} exhibits strong luminescence via the $^5D_0 \rightarrow {}^7F_2$ transition (610-630 nm), in these compounds the $^5D_0 \rightarrow {}^7F_4$ transition (680 nm) produces the strongest emission in the deep-red region of the spectrum, which can be beneficial among others for biological applications.

Keywords: Deep-Red phosphor, Eu^{3+} luminescence, calcium/strontium aluminate, hexagonal nanoparticles.

Introduction

Owing to the facile penetration of deep-red and NIR light into the body tissue, the development of phosphors emitting in this region of the electromagnetic spectrum has been the subject of extensive research for biological applications [1-3]. On the other hand, the majority of the commercially available white light-emitting diodes (WLEDs) suffers from low color rendering index (CRI) and high correlated color temperature (CCT) due to the lack of the red component [4-6]. These WLEDs are phosphor-converted LEDs made up of a blue chip with one or a combination of yellow, green, and red phosphors [7]. For instance, $Y_3Al_5O_{12}:Ce^{3+}$ (YAG) consists of a blue chip and a yellow-emitting activator [8, 9]. Even though the combination of the blue light with only one of the yellow or green components can be sufficient for generation of white light, the red component is essential to acquire high CRI and low CCT. Therefore, the development of red-emitting phosphors is a highly demanded ongoing research subject for different purposes.

Although transition metal ions such as Mn^{4+} and Cr^{3+} are commonly used as activators in inorganic matrixes, rare-earth ions are the choice for highly efficient, pure, and stable photoemission [10, 11]. Trivalent rare-earth ion-based activators generate sharp emission lines with relatively long lifetimes, since their f-f transitions are screened from their surrounding chemical environment, which can in principle result in obtaining high CRI [12, 13]. Among these ions, europium generates emission lines extending from the yellow region of the spectrum to the NIR. In the majority of the cases, the strongest emission of Eu^{3+} originates from the $^5D_0 \rightarrow {}^7F_2$ transition, which falls at the orange-red (610-630 nm) range of the visible light spectrum. Nevertheless, the luminescence properties of an activator including its brightness and color relies strongly on the host compound. Host materials with large band gaps and low vibrational energies are extremely desirable for the development of bright phosphors. $MO\text{-}Al_2O_3$ (M = Ca/Sr) compounds show high potentials for technological applications due to their high chemical, mechanical, and thermal stabilities [14, 15]. We have recently reviewed the crystal structures, synthesis, and luminescence properties of the $SrO\text{-}Al_2O_3$ system with an emphasis on the luminescence and persistent luminescence of Eu^{2+}-doped compounds [16]. $MAl_{12}O_{19}$ (M = Ca/Sr) are two important members of the $MO\text{-}Al_2O_3$ system. $CaAl_{12}O_{19}$ is interesting in astronomical studies since it’s found in meteorites [17]. $SrAl_{12}O_{19}$ co-doped with Mn^{2+} and Gd^{3+} has been proposed for optical information storage applications [18]. Among many other uses, these two compounds are, in particular, excellent hosts for luminescent activators and optoelectronic applications. The remarkably wide band gaps of $CaAl_{12}O_{19}$ (>7 eV [19]) and $SrAl_{12}O_{19}$ (7.76 eV [20]) makes them outstanding host materials, even compared to the other compounds in these $MO\text{-}Al_2O_3$ systems, for the development of bright phosphors, and also of VUV excited quantum cutting phosphors such as $SrAl_{12}O_{19}$:Pr,Cr with a theoretical quantum efficiency of 147% [21]. $MAl_{12}O_{19}$ doped with Pr^{3+} [22-25], Sm^{3+} [26, 27] or Nd^{3+} [28] are also laser materials, doped with Mn^{4+} is a deep-red phosphor [29-34], with Ce^{3+}, a blue-emitting phosphor [35-37] and with Dy^{3+} it can be used in white-light emitting diodes [38, 39]. In addition, $MAl_{12}O_{19}:Gd^{3+}$ is a UV-light emitter [40, 41] and $SrAl_{12}O_{19}:Er^{3+},Yb^{3+}$ is an up-conversion material [42].

Despite the widespread uses of the $MO\text{-}Al_2O_3$ compounds, their large grain size impedes extending their applications to many other potential areas, for instance to bioimaging. This large grain size results from the currently available synthesis methods for preparation of calcium/strontium aluminates including $MAl_{12}O_{19}$. In general, two different routes are followed for the synthesis of these compound [16]. First, the conventional solid-state method, which takes place at temperatures >1300 °C. Second, the synthesis of the precursor materials at low temperatures, followed by a post-annealing step, which again takes place at elevated temperatures (normally >1100 °C). In both methods, these very high temperatures make it extremely challenging to control the size and/or morphology of the particles of these compounds.

As an example, Willson et al [43] could prepare $SrAl_2O_4:Eu^{2+},Dy^{3+}$ NPs in the range of 100-500 nm after 7-9 days of milling. Clearly, this method results in large size distribution as well as irregular morphology. This compound was also prepared via a combustion method [44]. Despite the fact that, the application of H_3BO_3 contributed significantly to the final morphology, the obtained particles were mainly in the micron range with rather poor morphologies. Misevicius et al [45], also took advantage of H_3BO_3 to control the morphology of $Sr_4Al_{14}O_{25}$ particles. The authors used a sol-gel method in the presence of H_3BO_3 to prepare their precursor material, which evolved into crystalline hexagonal particles extending from nanometer to a few microns in size. Good morphology control was reported for $SrAl_2O_4$ compound prepared via sol-gel [46] and co-precipitation [47] methods, but the particle sizes were again in the micron range. $CaAl_{12}O_{19}:Mn^{4+}$ nanofibers have also been prepared [48]. Zhang et al [49] prepared a mixture of round and hexagonal disks of $SrAl_{12}O_{19}:Pr^{3+}$ via a combustion method ranging from nano to a few microns in size. A thorough literature review shows that, despite numerous attempts for three decades, preparation of $MO\text{-}Al_2O_3$ compounds with controlled morphology and size distribution in the nano-range, still remains frustratingly challenging.

Here, we report a novel solvothermal-coprecipitation method based on cooperative micro-sized gel formation and subsequent self-transformation into precursor $MAl_{12}O_{19}$ NPs. This method offers excellent control over the morphology of these NP. It is then followed by a post-annealing process to obtain the final NPs. In this method, controlled nucleation and growth steps occurs inside pre-formed micro-sized gel reactors, and then separate spherical NPs evolve form a self-transformation process. These spherical NPs later evolved into crystalline hexagonal NPs during the annealing step with very little aggregation. Doped into these NPs, Eu^{3+} interestingly emits strong deep-red emission resulting from the $^5D_0 \rightarrow {}^7F_4$ transition (680-705 nm). This emission is normally very weak and only a few exceptional phosphors with stronger $^5D_0 \rightarrow {}^7F_4$ than the $^5D_0 \rightarrow {}^7F_4$ (610-630 nm) have been reported [50-53].

Experimental

Materials and reagents

Strontium nitrate 99+% ACS reagent, aluminum nitrate nonahydrate 99+%, and urea 99.5% were purchased from Acros Organics. Europium nitrate pentahydrate 99.9% trace metal basis and polyvinylpyrrolidone (M.W. 58000) were purchased from Sigma Aldrich and Fluka, respectively. Ethanol absolute 99.8% was supplied by Fisher Scientific.

Instruments

A Teflon-lined stainless-steel autoclave was used for the solvothermal synthesis of the strontium aluminate precursor NPs. A Carbolite tube furnace was used for the annealing procedure. X-ray powder diffraction (XRD) data were collected on a Panalytical X'pert Pro MPD (Cu Kα = 1.5406 Å) in the Debye-Scherer geometry.

Transmission electron microscopy (TEM): Samples were dispersed in ethanol, and few drops of this dispersion were added on a carbon coated copper grid (Formvar carbon film, 200 mesh). TEM images were taken with a Tecnai G2 sphere with 120 keV electrons focused on the sample. Continuous Rotation data were collected on a single nanocrystal in nanoprobe mode in a FEI Tecnai G2 sphere microscope using a voltage of 120 kV and an Ansterdam Scientifix Cheetah camera.

Scanning electron microscopy (SEM): Samples were mounted on a conductive support (aluminium stub) with double-sided conductive carbon tape. An ultra-thin coating (ca. 10 nm) of gold was then deposited on the samples by low vacuum sputter coating prior to imaging with a Jeol JSM 7001F Scanning Electron Microscope.

Fourier transform infrared spectroscopy (FTIR) experiments on solid samples were performed with a Bruker model Tensor 27 Instrument equipped with a CsI beamsplitter and a platinum attenuated total reflection (ATR) setup. The spectral resolution was set to 2 cm^{-1}. The powdered samples were pressed between a diamond crystal and a bridge clamped sapphire anvil to ensure optimum optical contact of the powder.

The luminescence spectra were recorded on a Horiba Jobin Yvon Fluorolog 3-22, equipped with a photo multiplier tube (PMT) detector. A closed-cycle Janis-Sumitomo SHI-4.5 cryostat equipped with a programmable temperature controller (Lakeshore Model 331) was used for the luminescence measurements at 5 K. Both excitation and emission slits for all luminescence measurements were set to 0.5 nm.

Synthesis of $MAl_{12}O_{19}$:Eu^{3+} (M = Ca/Sr) NPs

For the synthesis of the precursor particles, this synthesis procedure was adapted and optimized based on the two synthesis methods reported before [47]. 1 mmol Ca/Sr$(NO_3)_2$, 6 mmol $Al(NO_3)_3$, 0.01 mmol $Eu(NO_3)_3$, and 3 g urea were all dissolved in 8 ml of distilled water. To this solution, 1.2 g PVP and then 80 ml EtOH were added. The mixture was stirred and then sonicated to obtain a clear solution, which was then heated at 170 °C in a 200 ml Teflon-lined stainless-steel autoclave for 2 h. The product was collected by centrifugation and washed with water/EtOH mixture. The wet white powder was dispersed in 30 ml of EtOH by sonication to separate the compact NPs obtained from the centrifugation process. This EtOH suspension of the NPs was transferred to a petri dish with a big surface area to evaporate the solvent. This is to minimize the contact surface area between the particles, which will later help to impede the NPs from aggregation and formation of big chunks during the annealing process. The powder was collected and heated up to 1150 °C at 10 degree/minute in the furnace in an alumina crucible. After leaving the sample at this temperature for 3 h, the furnace was cooled down to RT and nanocrystalline particles of $MAl_{12}O_{19}$:Eu^{3+} were collected. Drying the wet powder after the washing process yielded about 0.6 g of the precursor $MAl_{12}O_{19}$:Eu^{3+} NPs. After the annealing process about 0.3 g of the final product was obtained.

Results and discussion

Characterization

The powder XRD patterns of the precursor as well as the annealed $CA_6:Eu^{3+}$ and $SA_6:Eu^{3+}$ NPs are shown in Figure 1. The precursor NPs of $CA_6:Eu^{3+}$ appears amorphous, whereas weak reflections originating from crystalline $SrCO_3$ phase are clearly observed for the $SA_6:Eu^{3+}$ precursor NPs. This confirms the successful incorporation of the Sr^{2+} ion as $SrCO_3$ into the precursor NPs. Since chemistry of Ca^{2+} ion is very similar to that of Sr^{2+}, formation and precipitation of $CaCO_3$ is expected in the case of $CA_6:Eu^{3+}$ synthesis. Nonetheless, these precursor NPs are entirely amorphous, which indicates that unlike $SrCO_3$, $CaCO_3$ did not form a crystalline structure. It is likely that $CaCO_3$ species were present in the NPs, either in amorphous phase or as separate single molecules. The annealing process confirmed the successful incorporation of the Ca^{2+} into the NPs, since after 3 h at 1150 °C, the $CaAl_{12}O_{19}$ phase was obtained. Pure-phase $SrAl_{12}O_{19}$ was formed under the same annealing conditions. The patterns match perfectly with the reported patterns for $CaAl_{12}O_{19}$ and $SrAl_{12}O_{19}$ in the literature. The similar diffraction patterns of these two compounds arise from their almost identical crystal structure. Relatively smaller radii of Ca^{2+} ion slightly shifts the $CaAl_{12}O_{19}$ pattern towards the higher angles.

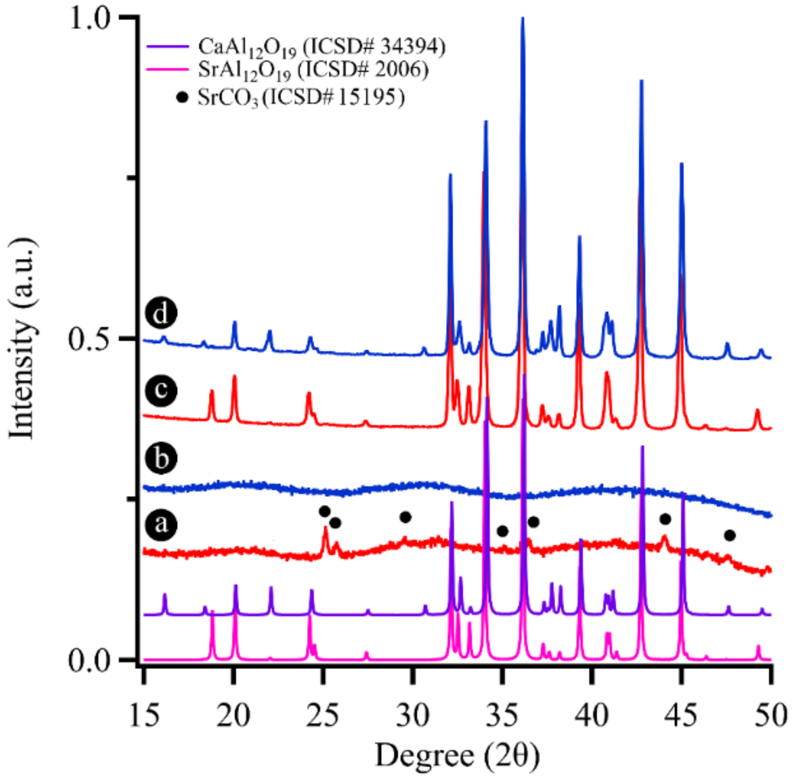

Figure 1. Powder XRD patterns of the a) $SA_6:Eu^{3+}$ precursor NPs, b) $CA_6:Eu^{3+}$ precursor NPs c) $SA_6:Eu^{3+}$ annealed at 1150 ˚C for 3h, d) $CA_6:Eu^{3+}$ annealed at 1150 ˚C for 3 h.

Figure 2 presents TEM images for the calcium and strontium aluminate precursor and the final $CaAl_{12}O_{19}:Eu^{3+}$ ($CA_6:Eu^{3+}$) and $SAl_{12}O_{19}:Eu^{3+}$ ($SA_6:Eu^{3+}$) NPs. Spherical precursor particles with homogeneous morphology and narrow size distribution in between 200-300 nm are observed for both $CA_6:Eu^{3+}$ and $SA_6:Eu^{3+}$ compounds (Figure 2a,d) . After the annealing step, hexagonal NPs with sizes about 250 nm were obtained (Figure 1b,e). Despite some aggregation taking place at 1150 °C, well-defined hexagonal morphologies are clearly observed for both NPs. This hexagonal shape also resembles structure shown in Figure S1. The electron diffraction patterns for single NPs of $CA_6:Eu^{3+}$ and $SA_6:Eu^{3+}$ are shown in Figure 2c,f. The hexagonal pattern observed for the SA_6 NP reflects the positions of strontium atoms in the 001 plane. The corresponding lattice points are indexed in the figure. The interplanar distances are presented in Figure S2.

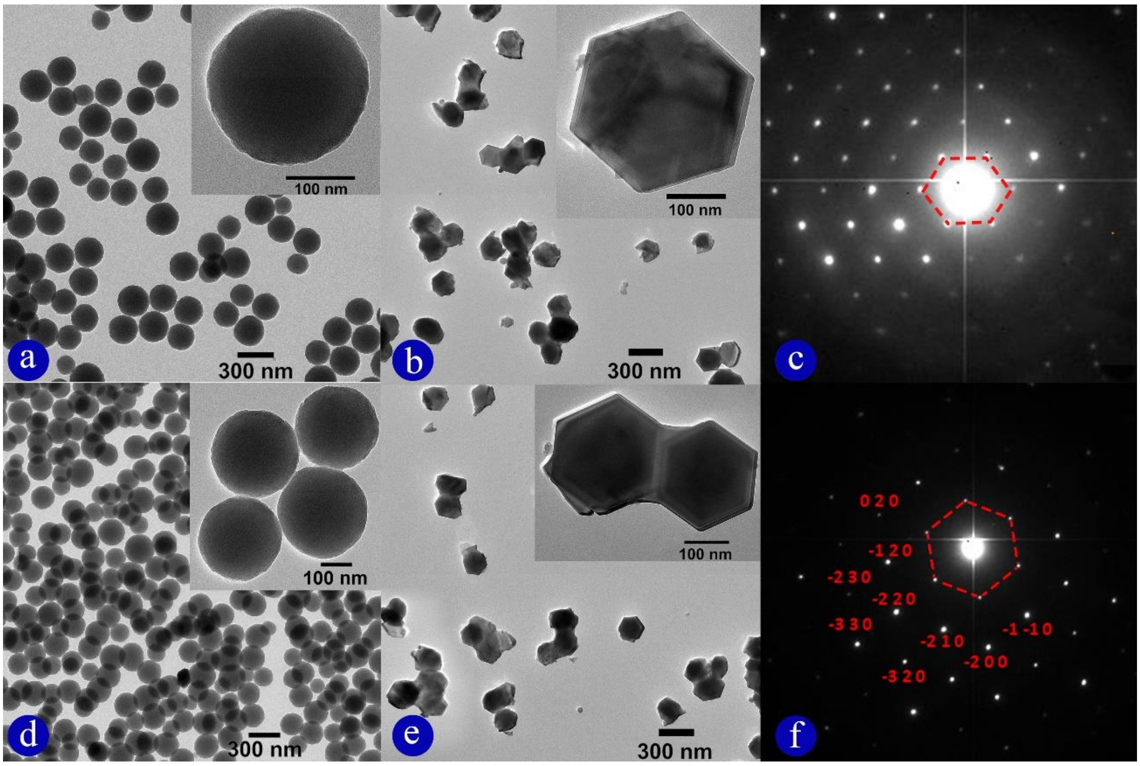

Figure 2. TEM images of a) $CA_6:Eu^{3+}$ precursor NPs before annealing, b) $CA_6:Eu^{3+}$ NPs annealed at 1150 °C for 3 h, c) electron diffraction pattern of a single $CA_6:Eu^{3+}$ NP, d) $SA_6:Eu^{3+}$ precursor NPs before annealing, e) $SA_6:Eu^{3+}$ NPs annealed at 1150 °C for 3 h, f) electron diffraction pattern of a single $SA_6:Eu^{3+}$ NP.

The SEM images in Figure S2 confirms the spherical morphology of the $SA_6:Eu^{3+}$ precursor NPs. After annealing, they transform into hexagonal platelets of about 200 nm width and 100 nm height.

FT-IR spectra were measured in the range of 200-4000 cm^{-1} (Figure 3). The $-CH_2$ and -CH stretching vibrations are observed in the range of 2840-3010 cm^{-1} for PVP. These bands are still weakly present in the spectrum of the precursor NPs at ≈2970 cm^{-1}. A strong band assigned to the C=O vibrations at 1660 cm^{-1} is observed for PVP. This band is broadened for both precursor NPs as a shoulder emerges at 1597 cm^{-1}. The presence of -CH_2/-CH as well as C=O vibrations in the spectra of the precursor NPs indicates the presence of PVP in their structure. The shoulder emerging at 1597 cm^{-1} suggest interaction of Al^{3+}/Ca^{2+}/Sr^{2+} ions with the oxygen of the C=O functional group causing a shift to lower frequencies. Both these bands disappeared following the annealing process, which confirms the successful removal of the organic component from the particles, as expected.

The IR spectra of the precursors also show a broad band around 1458 cm^{-1}, which has been reported for $SrCO_3$ [54]. The presence of $SrCO_3$ was also observed by XRD (see Figure 1). The IR spectra of the annealed sample do not show any band above 1000 cm^{-1}, which indicates that these samples are both carbonate-free (carbonates can be formed from combustion methods) and water-free. The spectra of both CA_6 and SA_6 are very similar and confirm their similar crystal structures. The expanded IR spectrum is shown in more detail in Figure S7. The spectrum of CA_6 resembles the one previously published for this compound [39], although the present one appears to be obtained with better resolution. Vibrations above 600 cm^{-1} have been assigned to Al-O stretching modes, at lower frequencies, aluminum oxygen bending modes are found [55].

The highest frequency peak for CA_6 is at slightly higher energy than the corresponding peak for SA_6, which indicates a “chemical pressure effect” on the Al-O network from the smaller Ca ion compared to Sr [56].

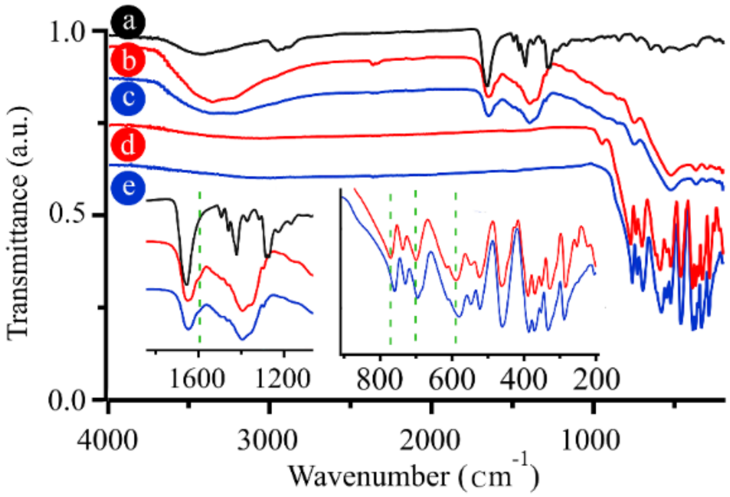

Figure 3. FTIR spectra of a) PVP, b) CA_6:Eu^{3+} precursor NPs, c) SA_6:Eu^{3+} precursor NPs, d) CA_6:Eu^{3+} annealed at 1150 °C, e) SA_6:Eu^{3+} annealed at 1150 °C.

Synthesis mechanism

It is known that urea hydrolyses in water at above 100 °C to produce NH_3 and CO [57]. These hydrolysis products react with the metal precursors in the solution to yield AlOOH and Sr/$CaCO_3$ precipitates, respectively [58]. The powder XRD results confirmed precipitation of the strontium into the precursor particles as $SrCO_3$. Moreover, our experiments showed that increasing the H_2O/EtOH ratio results in either formation of gel or losing the spherical morphology depending on other factors in the synthesis such as temperature and urea/PVP ratio. Considering the fact that, PVP is soluble in water but barely in ethanol and that we use a water to ethanol ratio of 1:10, it is safe to hypothesize that EtOH contributes to the formation and precipitation of spherical micelles. Zhip et al [47] used urea and PVP for the synthesis of donut-like micro-particles. The authors proposed the formation of spherical micelles and subsequent precipitation of AlOOH and $SrCO_3$ onto the surface of these micelles resulting in hollow micro-sized particles.

For the method presented here, the TEM image in Figure 2a,d shows a homogeneously dense spherical particle. Formation of spherical micelles and subsequent deposition of the aluminum and strontium precursors on them would result in NPs less dense towards the center. On the other hand, to obtain the final particles with the M^{2+}:Al^{3+} of 1/12, excess amount of $Ca/Sr(NO_3)_2$ was used in the reaction mixture, which suggest faster incorporation of the Al^{3+} ions into the NPs.

To shed light on the precipitation process of the metal precursors, a transparent pressure glass vessel was used instead of the autoclave to visually monitor the particle formation and growth. Under the same reaction conditions described above, except for the presence of the metal precursors, even at a 5-times longer reaction time the mixture remained a clear solution. This suggests that, under these conditions, the PVP miscalls/aggregates do not form on their own, but rather a PVP+metal-ions cooperative precipitation is taking place.

Ex-situ TEM analysis was used to understand the particle formation and growth mechanism. As the particle growth took place very fast at 170 °C, the temperature was decreased to 150 °C to be able to monitor the evolution of the spherical precursor NPs. The reaction was stopped at different particle growth times (2, 5, 10, and 20 minutes) after the initiation of the particle formation process (the beginning of transformation from a clear solution to a turbid mixture which was observed by naked eyes). The TEM images in Figures 4 and S8 show that, initially separate micro-sized gels form in the reaction mixture. The nucleation and growth of the NPs takes place inside these gels. The total process of gel formation and its evolution to the spherical NPs is complete within only 10 minutes. It should be noted that, the heating process was stopped after 10 minutes from when the precipitation was observed. The growth process continued a few minutes longer during the gradual cooling of the reaction batch.

Figure 4 shows that the micro-sized gel pools formed in the reaction mixture act as reactors, where the nucleation and growth of the particles take place. This is another indication that the precipitation and formation of these gels is a PVP+metal-ions cooperative process, and the metal-ions are dispersed throughout these gel pools. Within the 2 minutes growth time, the gels were formed and the nucleation and to some extent the growth process of the NPs had already started (Figure 4a). The particle size was mainly below 100 nm at this stage. After 5 minutes, NPs in between 100-200 nm in size with relatively higher density could be observed (Figure 4b). The borders of the gel can also be observed at this stage (Figure S9), which suggests the densification of the gel during the growth process. It appears that, the PVP inside the gel, acts both as a shape-directing and a surface-passivating agent. This gel to NP self-transformation process is complete in less than only 10 minutes (Figure 4c) and spherical particles in the range of 150-250 nm were formed. However, many of these formed spherical NPs are still inter-connected. Following further extending the reaction time to 20 minutes, the NPs further grow to 200-300 nm in size (Figure 4d). As the growth time is extended, the separation of the particles from their neighboring particles develop further.

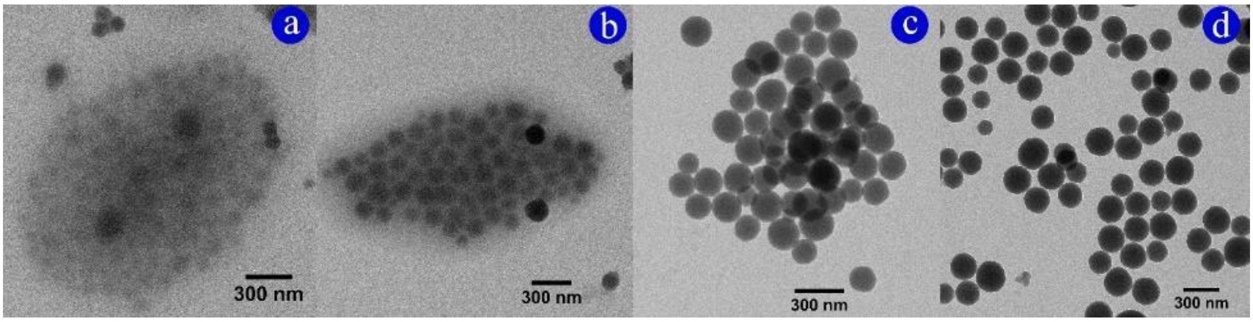

Figure 4, The evolution of the CA_6:Eu^{3+} doped NPs after 2 (a), 5 (b), 10 (c), and 20 (d) minutes.

Figure 5 takes a closer look into the evolution process of CA_6:Eu^{3+} NPs. Three different items are observed in Figure 5a. The item “1” is a pool of NPs in the growing state which are encapsulated with a gel. Unlike the item “2”, the boundaries of the gel can be observed in the picture. This is more evident in Figure S9. Towards the edges of the gel, there are no NPs present. This can further confirm a cooperative PVP+metal-ions gel formation process and subsequent condensation of metal-free PVP molecules onto these pools. Item “2”, which is enlarged in Figure 5b, looks to be in a relatively more advanced growth stage. The inset of Figure 5b shows that these entangled particles, are starting to detach from each other. The middle and top parts of the item “3”, which is magnified in Figure 5c, seem to be in different growth stages. The spherical particles confined in the dashed circle, look uniformly condensed and their surrounding is clean. On the other hand, the top part confined in the dashed square, looks very irregular. This part is enlarged in Figure 5d. The two cavities indicated with the red lines, appear next two the defined edges of the particles, because the gel in these areas is consumed entirely. The undefined edges of the particles are stretched into shady areas. These areas are the gel matrix, which is still condensing onto the particles.

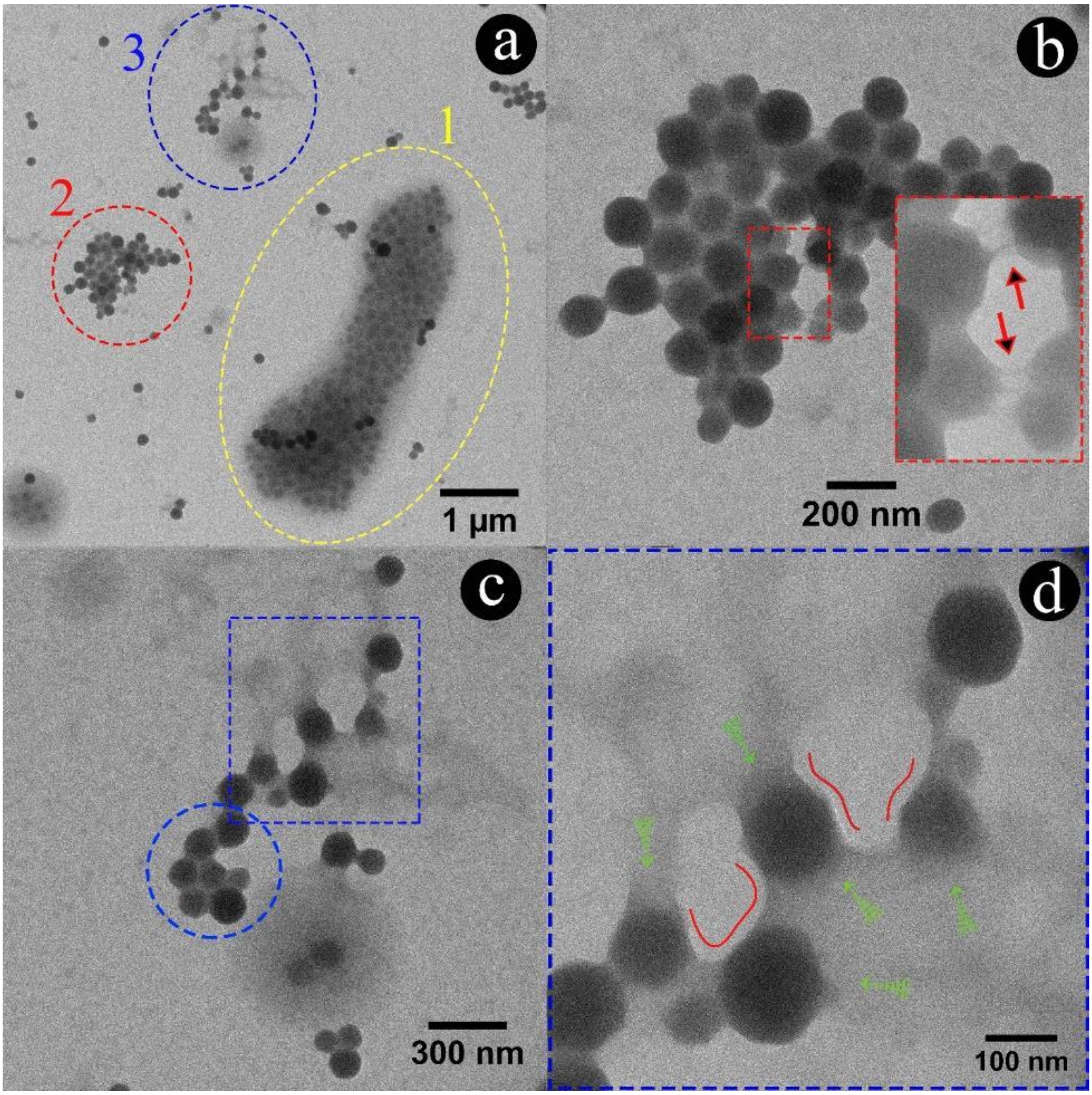

Figure 5. Illustration of different growth stages of the precursor NPs.

The powder-XRD patterns of these products annealed at 1150 °C (Figure S10) indicate that, while Al^{3+} is incorporated into the particles at very early stages of the particle growth, the Sr^{2+} precipitates in/onto the particles by extending the reaction time. In less than 5 minutes reaction time, only Al_2O_3 precursor particles are formed. Extending the reaction to 10 and then 20 minutes results in a mixture of Al_2O_3/$CaAl_{12}O_{19}$ phases and $CaAl_{12}O_{19}$, respectively. This suggests that, initially, only Al^{3+} ions bind to the PVP molecules to start the gelation process. The Ca^{2+}/Sr^{2+} ions precipitate on the particles subsequently. Based on these experimental results, the following mechanism illustrated in Figure 6 is proposed for the preparation of CA_6:Eu^{3+} and SA_6:Eu^{3+} NPs.

In the precursor NP, the residual gel binds amorphous aluminum oxide, as seen from X-ray diffraction and IR for both Sr and Ca annealed samples. $SrCO_3$ and $CaCO_3$ precipitated onto the already formed NPs as the growth time is extended. During the annealing step, upon carbonate decomposition, the nascent SrO and CaO respectively reacts with the amorphous aluminum oxide to form crystalline $MAl_{12}O_{19}$. Electrochemical studies [59] showed that for the reaction;

$SrO + 6\ Al_2O_3 \rightarrow SrAl_{12}O_{19}$,

the Gibbs free energy of reaction between 1000 and 1300 K is given by the expression

$\Delta G\ ^{o}/J\ mol^{-1}\ (\pm\ 280) = -83386 - 25.744\ (T/K)$,

which confirms that this crystallization process is spontaneous.

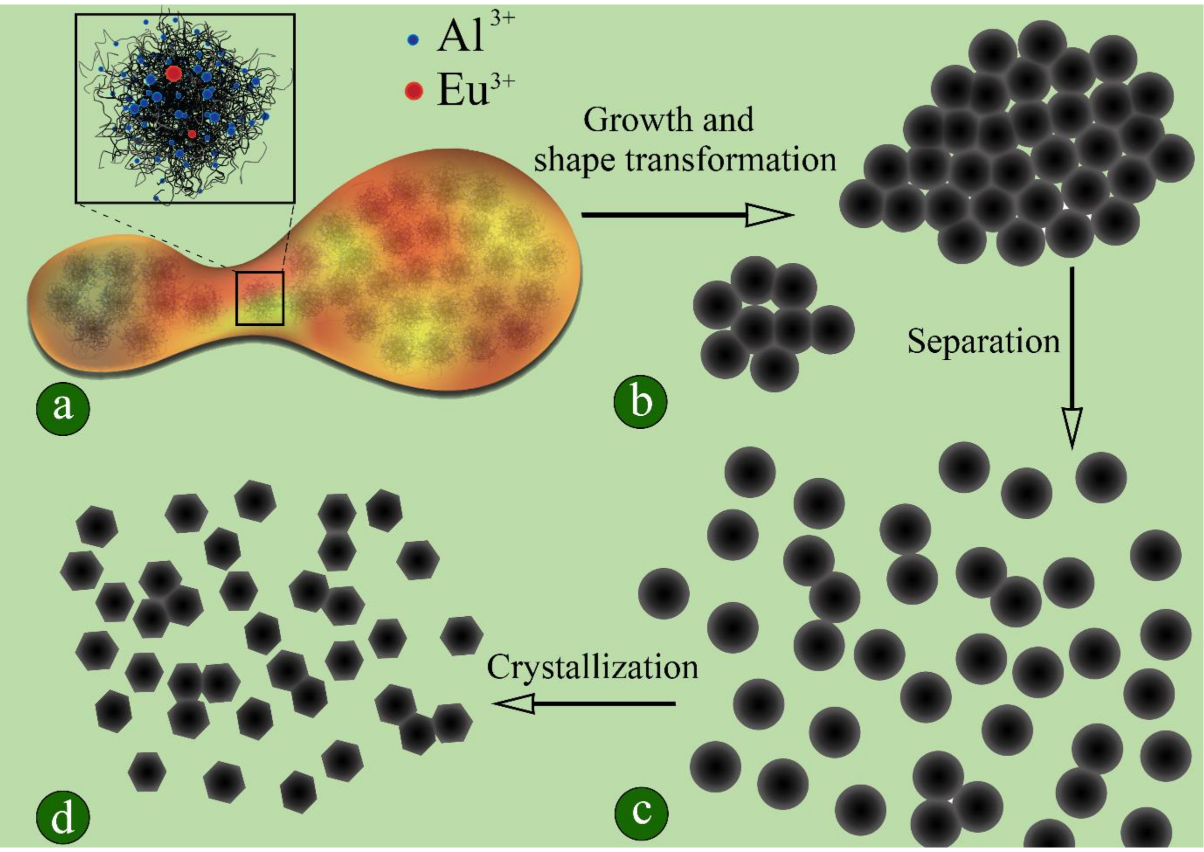

Figure 6. Illustration of $CA_6:Eu^{3+}$ and $SA_6:Eu^{3+}$ NP preparation process. a) Gelaltion and nucleation, b) growth, densification and shape transformation, b) separation of the interconnected NPs, d) crystallization at 1150 °C.

Luminescence studies

Figure 7 shows that $CA_6:Eu^{3+}$ and $SA_6:Eu^{3+}$ NPs emit light throughout the entire visible region of the spectrum at 298 K. These emission bands originate from the $^5D_{0\text{-}3}\rightarrow{}^7F_{0\text{-}6}$ transitions. Although emission from the $^5D_1$ excited state have been reported for Eu^{3+} in many cases, in particular in inorganic hosts, examples of emission from the $^5D_2$ and specially $^5D_3$ states are scares [60, 61]. Observation of these bands for Eu^{3+} in CA_6 and SA_6 at 298 K can be attributed to the huge band gap of the host compounds. Probably, the conduction bands (CB) of these host materials lie well above the excited states of the f configuration of Eu^{3+} minimizing the thermal population of the excited electrons to the CB. This in turn leads to a low nonradiative loss of energy. Nevertheless, these band are very weak compared to the $^5D_0 \rightarrow {}^7F_{0-6}$ transitions. Similar to other Eu^{3+}-activated phosphors, $CA_6:Eu^{3+}$ and $SA_6:Eu^{3+}$ NPs emit much stronger from the $^5D_0$ state. The major difference for these particles is the strong emission band originating from the $^5D_0 \rightarrow {}^7F_4$ transition in between 680-705 nm in the deep-red region of the spectrum, which normally appears very weak relative to the $^5D_0 \rightarrow {}^7F_2$ band. This strong emission with relatively low energy in the visible range is capable of penetrating the body tissues, which makes these NPs great candidates for biological applications such as bioimaging. They are also potential phosphors for application in the white-light-emitting-diodes and displays as the red component.

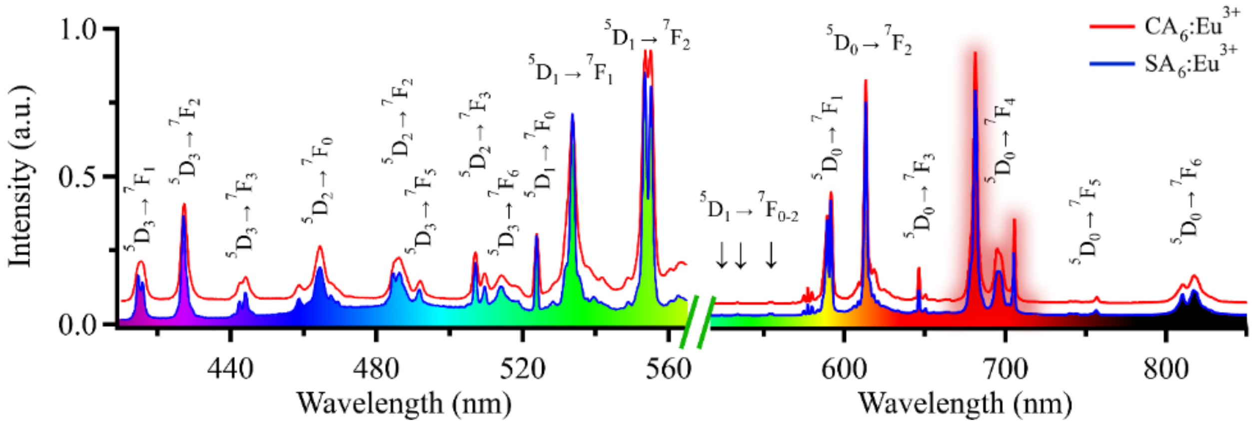

Figure 7. Emission spectra of $CA_6:Eu^{3+}$ and $SA_6:Eu^{3+}$ NPs at $\lambda_{exc.} = 397$ nm.

Chromaticity coordinates of these phosphors are illustrated in the “Commission Internationale de l’Élairage” (CIE) 1931 color spaces. The color coordinates for these NPs are located at the deep-red region (0.63. 0.37) of this diagram (Figure 8).

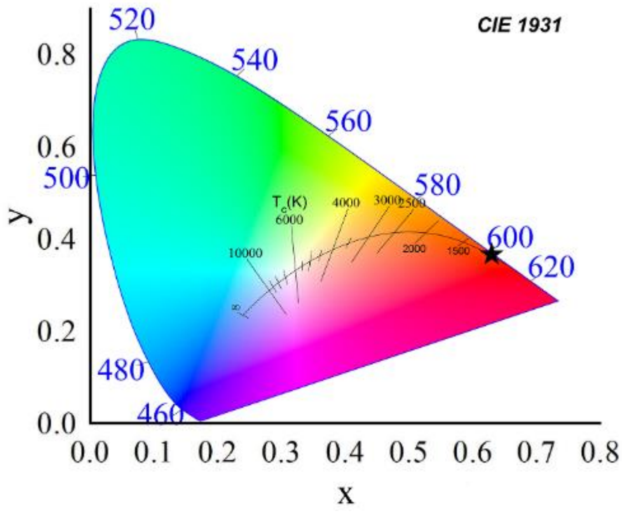

Figure 8. CIE chromaticity diagram of $CA_6:Eu^{3+}$ and $SA_6:Eu^{3+}$ NPs.

Conclusions

A novel synthesis method was developed for the synthesis of $CA_6:Eu^{3+}$ and $SA_6:Eu^{3+}$ precursor NPs. According to the powder XRD analysis, annealing these NPs at 1150 °C resulted in pure-phase crystalline $CaAl_{12}O_{19}$ and $CaAl_{12}O_{19}$ structures. The TEM images showed that spherical precursor NPs with a size distribution in the range of 200-300 nm and homogeneous spherical morphologies were obtained. These spherical NPs transformed into hexagonal platelets after the annealing process. The aggregation of the particles during the annealing step was minimal. Interestingly, the prepared $CA_6:Eu^{3+}$ and $SA_6:Eu^{3+}$ NPs emitted deep-red luminescence originating from the $^5D_0 \rightarrow {}^7F_4$ transition of the Eu^{3+} ion. Moreover, emissions from all the $^5D_{0-3}$ excited states extending from the blue to NIR region of the spectrum, were observed at room temperature, which indicates the low vibrational energy loss. Studying the precursor NP formation revealed that, the nucleation and growth process took place inside micro-sized gels. The gel formation was a cooperative process between the aluminum and PVP molecules in the reaction mixture. These gel reactors, which provided control over the nucleation and growth of the NPs, then self-transformed into the spherical NPs.

Acknowledgment

This work was supported by the Swiss National Science Foundation (projects 200020_182494,200021_169033 and P400P2_191108/1).

References

[1] A. Shao, Y. Xie, S. Zhu, Z. Guo, S. Zhu, J. Guo, P. Shi, T.D. James, H. Tian, W.H. Zhu, Far-red and near-IR AIE-active fluorescent organic nanoprobes with enhanced tumor-targeting efficacy: shape-specific effects, Angewandte Chemie, 127 (2015) 7383-7388.

[2] S. Singh, Red and near infrared persistent luminescence nano-probes for bioimaging and targeting applications, Rsc Advances, 4 (2014) 58674-58698.

[3] Y. Wang, M. Chen, N. Alifu, S. Li, W. Qin, A. Qin, B.Z. Tang, J. Qian, Aggregation-induced emission luminogen with deep-red emission for through-skull three-photon fluorescence imaging of mouse, Acs Nano, 11 (2017) 10452-10461.

[4] Q. Zhou, L. Dolgov, A.M. Srivastava, L. Zhou, Z. Wang, J. Shi, M.D. Dramićanin, M.G. Brik, M. Wu, Mn^{2+} and Mn^{4+} red phosphors: synthesis, luminescence and applications in WLEDs. A review, Journal of Materials Chemistry C, 6 (2018) 2652-2671.

[5] Y. Wang, J. Ding, Y. Wang, X. Zhou, Y. Cao, B. Ma, J. Li, X. Wang, T. Seto, Z. Zhao, Structural design of new Ce^{3+}/Eu^{2+}-doped or co-doped phosphors with excellent thermal stabilities for WLEDs, Journal of Materials Chemistry C, 7 (2019) 1792-1820.

[6] H.S. Jang, W.B. Im, D.C. Lee, D.Y. Jeon, S.S. Kim, Enhancement of red spectral emission intensity of $Y_3Al_5O_{12}$:Ce^{3+} phosphor via Pr co-doping and Tb substitution for the application to white LEDs, Journal of luminescence, 126 (2007) 371-377.

[7] P. Gaffuri, E. Stolyarova, D. Llerena, E. Appert, M. Consonni, S. Robin, V. Consonni, Potential substitutes for critical materials in white LEDs: Technological challenges and market opportunities, Renewable and Sustainable Energy Reviews, 143 (2021) 110869.

[8] V.V. Atuchin, N.F. Beisel, E.N. Galashov, E.M. Mandrik, M.S. Molokeev, A.P. Yelisseyev, A.A. Yusuf, Z. Xia, Pressure-stimulated synthesis and luminescence properties of microcrystalline $(Lu,Y)_3Al_5O_{12}$:Ce^{3+} garnet phosphors, ACS applied materials & interfaces, 7 (2015) 26235-26243.

[9] G. Blasse, A. Bril, A new phosphor for flying-spot cathode-ray tubes for color television: yellow-emitting $Y_3Al_5O_{12}$:Ce^{3+}, Applied Physics Letters, 11 (1967) 53-55.

[10] W.-R. Liu, C.-H. Huang, C.-P. Wu, Y.-C. Chiu, Y.-T. Yeh, T.-M. Chen, High efficiency and high color purity blue-emitting $NaSrBO_3$:Ce^{3+} phosphor for near-UV light-emitting diodes, Journal of Materials Chemistry, 21 (2011) 6869-6874.

[11] D. Geng, E. Cabello-Olmo, G. Lozano, H. Míguez, Photonic structuring improves the colour purity of rare-earth nanophosphors, Materials horizons, 5 (2018) 661-667.

[12] L.D. Carlos, R. Sá Ferreira, J. Rainho, V. de Zea Bermudez, Fine-Tuning of the Chromaticity of the Emission Color of Organic–Inorganic Hybrids Co-Doped with EuIII, TbIII, and TmIII, Advanced Functional Materials, 12 (2002) 819-823.

[13] L. Sun, B. Devakumar, J. Liang, S. Wang, Q. Sun, X. Huang, Highly efficient $Ce^{3+}\rightarrow Tb^{3+}$ energy transfer induced bright narrowband green emissions from garnet-type $Ca_2YZr_2(AlO_4)_3$:Ce^{3+},Tb^{3+} phosphors for white LEDs with high color rendering index, Journal of Materials Chemistry C, 7 (2019) 10471-10480.

[14] F. Ganits, T.Y. Chemekova, Y.P. Udalov, The SrO-Al_2O_3 system, Zhurnal Neorganicheskoj Khimii, 24 (1979) 471-475.

[15] D. Jerebtsov, G. Mikhailov, Phase diagram of CaO–Al_2O_3 system, Ceramics International, 27 (2001) 25-28.

[16] H. Hagemann, J. Afshani, Chapter 321: Synthesis, luminescence and persistent luminescence of europium-doped strontium aluminates, Handbook on the Physics and Chemistry of Rare Earths, Elsevier, Vol 60 (2021) p.163-225, ISSN 0168-1273, https://doi.org/10.1016/bs.hpcre.2021.06.001.

[17] L.R. Nittler, C.M.D. Alexander, R. Gallino, P. Hoppe, A.N. Nguyen, F.J. Stadermann, E.K. Zinner, Aluminum-, calcium-and titanium-rich oxide stardust in ordinary chondrite meteorites, The Astrophysical Journal, 682 (2008) 1450.

[18] X. Lin, K. Deng, H. Wu, B. Du, B. Viana, Y. Li, Y. Hu, Photon energy conversion and management in $SrAl_{12}O_{19}:Mn^{2+},Gd^{3+}$ for rewritable optical information storage, Chemical Engineering Journal, 420 (2021) 129844.
[19] R. Korpe, K. Koparkar, N. Bajaj, S. Omanwar, VUV investigation of blue emitting $MAl_{12}O_{19}:Eu$ (M= Ca, Sr, Ba) phosphors synthesized by combustion method, in: Journal of Physics: Conference Series, IOP Publishing, 2020, pp. 012056.
[20] D. Dutczak, T. Jüstel, C. Ronda, A. Meijerink, Eu^{2+} luminescence in strontium aluminates, Physical Chemistry Chemical Physics, 17 (2015) 15236-15249.
[21] Z. Nie, J. Zhang, X. Zhang, X. Ren, G. Zhang, X.-j. Wang, Evidence for visible quantum cutting via energy transfer in $SrAl_{12}O_{19}$:Pr,Cr, Optics letters, 32 (2007) 991-993.
[22] F. Reichert, D.-T. Marzahl, G. Huber, Spectroscopic characterization and laser performance of Pr, Mg: $CaAl_{12}O_{19}$, JOSA B, 31 (2014) 349-354.
[23] L.D. Merkle, B. Zandi, R. Moncorgé, Y. Guyot, H.R. Verdun, B. McIntosh, Spectroscopy and laser operation of Pr,Mg:$SrAl_{12}O_{19}$, Journal of applied physics, 79 (1996) 1849-1856.
[24] T. Calmano, J. Siebenmorgen, F. Reichert, M. Fechner, A.-G. Paschke, N.-O. Hansen, K. Petermann, G. Huber, Crystalline Pr: $SrAl_{12}O_{19}$ waveguide laser in the visible spectral region, Optics letters, 36 (2011) 4620-4622.
[25] M. Fechner, F. Reichert, N.-O. Hansen, K. Petermann, G. Huber, Crystal growth, spectroscopy, and diode pumped laser performance of Pr,Mg:$SrAl_{12}O_{19}$, Applied Physics B, 102 (2011) 731-735.
[26] J. Liu, Q. Song, D. Li, X. Xu, J. Xu, Growth and red-orange emission of Sm^{3+} doped $SrAl_{12}O_{19}$ single crystals, Optical Materials, 101 (2020) 109754.
[27] D.-T. Marzahl, P.W. Metz, C. Kränkel, G. Huber, Spectroscopy and laser operation of Sm^{3+}-doped lithium lutetium tetrafluoride ($LiLuF_4$) and strontium hexaaluminate ($SrAl_{12}O_{19}$), Optics express, 23 (2015) 21118-21127.
[28] Y. Pan, B. Liu, J. Liu, Q. Song, J. Xu, D. Li, P. Liu, J. Ma, X. Xu, H. Lin, Polarized spectral properties and laser operation of Nd: SrAl12O19 crystal, Journal of Luminescence, 235 (2021) 118034.
[29] T. Murata, T. Tanoue, M. Iwasaki, K. Morinaga, T. Hase, Fluorescence properties of Mn^{4+} in $CaAl_{12}O_{19}$ compounds as red-emitting phosphor for white LED, Journal of luminescence, 114 (2005) 207-212.
[30] Y. Xu, Y. Zhang, L. Wang, M. Shi, L. Liu, Y. Chen, Red emission enhancement for $CaAl_{12}O_{19}:Cr^{3+}$ and $CaAl_{12}O_{19}:Mn^{4+}$ phosphors, Journal of Materials Science: Materials in Electronics, 28 (2017) 12032-12038.
[31] L. Kong, Y. Liu, L. Dong, L. Zhang, L. Qiao, W. Wang, H. You, Enhanced red luminescence in $CaAl_{12}O_{19}:Mn^{4+}$ via doping Ga^{3+} for plant growth lighting, Dalton Transactions, 49 (2020) 1947-1954.
[32] Y. Wu, Y. Zhuang, R.-J. Xie, K. Ruan, X. Ouyang, Novel Mn^{4+} doped red phosphors composed of $MgAl_2O_4$ and $CaAl_{12}$ O_{19} phases for light-emitting diodes, Dalton Transactions, 49 (2020) 3606-3614.
[33] S.-H. Yang, Y.-C. Lee, Y.-C. Hung, Thermometry of red nanoflaked $SrAl_{12}O_{19}:Mn^{4+}$ synthesized with boric acid flux, Ceramics International, 44 (2018) 11665-11673.
[34] L. Wang, Y. Xu, D. Wang, R. Zhou, N. Ding, M. Shi, Y. Chen, Y. Jiang, Y. Wang, Deep red phosphors Sr $Al_{12}O_{19}:Mn^{4+}$, M (M= Li^+, Na^+, K^+, Mg^{2+}) for high colour rendering white LED s, physica status solidi (a), 210 (2013) 1433-1437.
[35] V. Panse, S. Choubey, A. Pattanaik, S. Dhoble, Combustion Synthesis and Photoluminescence Studies of Blue-Emitting $CaAl_{12}O_{19}:Ce^{3+}$ Lamp Phosphors, in: Macromolecular Symposia, Wiley Online Library, 2020, pp. 2000100.

[36] V. Panse, S. Choubey, R. Pandey, S. Dhoble, Photoluminescence Analytical Study of Ce^{3+}-Activated Blue-Emitting $SrAl_{12}O_{19}$ Lamp Phosphors, in: Macromolecular Symposia, Wiley Online Library, 2020, pp. 2000099.

[37] K. Gedekar, S. Wankhede, S. Moharil, R. Belekar, Ce^{3+} and Eu^{2+} luminescence in calcium and strontium aluminates, Journal of Materials Science: Materials in Electronics, 29 (2018) 4466-4477.

[38] K. Dev, A. Selot, G.B. Nair, C.M. Mehare, F.Z. Haque, M. Aynyas, S. Dhoble, Synthesis and photoluminescence study of Dy^{3+} activated $SrAl_{12}O_{19}$ phosphor, Optik, 194 (2019) 163051.

[39] K. Dev, A. Selot, G.B. Nair, V.L. Barai, N. Singh, F.Z. Haque, M. Aynyas, S. Dhoble, Study of luminescence properties of dysprosium-doped $CaAl_{12}O_{19}$ phosphor for white light-emitting diodes, Luminescence, 34 (2019) 804-811.

[40] V. Singh, S. Borkotoky, A. Murali, J. Rao, T.G. Rao, S. Dhoble, Electron paramagnetic resonance and photoluminescence investigation on ultraviolet-emitting gadolinium-ion-doped $CaAl_{12}O_{19}$ phosphors, Spectrochimica Acta Part A: Molecular and Biomolecular Spectroscopy, 139 (2015) 1-6.

[41] V. Singh, G. Sivaramaiah, N. Singh, J. Rao, P.K. Singh, M. Pathak, D. Hakeem, EPR and PL studies on UVB-emitting gadolinium-doped $SrAl_{12}O_{19}$ phosphors, Optik, 158 (2018) 1227-1233.

[42] V. Singh, M. Seshadri, M. Radha, N. Singh, S.H. Nandyala, Intense infrared, visible up and down emissions in Er^{3+}/Yb^{3+} co-doped $SrAl_{12}O_{19}$ obtained by urea assisted combustion route, Journal of Materials Science: Materials in Electronics, 29 (2018) 16516-16522.

[43] A.S. Paterson, B. Raja, G. Garvey, A. Kolhatkar, A.E. Hagström, K. Kourentzi, T.R. Lee, R.C. Willson, Persistent luminescence strontium aluminate nanoparticles as reporters in lateral flow assays, Analytical chemistry, 86 (2014) 9481-9488.

[44] W. Xie, C. Zou, M. Xie, Effect of H 3 BO 3 on phases, micromorphology and persistent luminescence properties of $SrAl_2O_4:Eu^{2+},Dy^{3+}$ phosphors, Journal of Materials Science: Materials in Electronics, 28 (2017) 6328-6334.

[45] M. Misevicius, M. Kilmanas, S. Culunlu, S. Sakirzanovas, A.U. Morkan, A. Beganskiene, A. Kareiva, On the sol–gel fabrication and characterization of undoped and cerium-doped $Sr_4Al_{14}O_{25}$, Journal of alloys and compounds, 614 (2014) 44-48.

[46] J. Wan, Y. Zhang, Y. Wang, R. Ma, Y. Wu, X. Qiao, X. Fan, Facile synthesis of monodisperse $SrAl_2O_4:Eu^{2+}$ cage-like microspheres with an excellent luminescence quantum yield, Journal of Materials Chemistry C, 6 (2018) 3346-3351.

[47] X. Zhiping, D. Suqing, L. Yingliang, L. Bingfu, X. Yong, M. ZHENG, Synthesis and luminescence properties of $SrAl_2O_4:Eu^{2+},Dy^{3+}$ hollow microspheres via a solvothermal co-precipitation method, Journal of Rare Earths, 31 (2013) 241-246.

[48] Z. Liu, M. Yuwen, J. Liu, C. Yu, T. Xuan, H. Li, Electrospinning, optical properties and white LED applications of one-dimensional $CaAl_{12}O_{19}:Mn^{4+}$ nanofiber phosphors, Ceramics International, 43 (2017) 5674-5679.

[49] Z. Nie, J. Zhanga, X. Zhang, K.-S. Limb, $SrAl_{12}O_{19}:Pr^{3+}$ nanodisks and nanoplates: New processing technique and photon cascade emission, J. Mater. Res, 24 (2009) 1772.

[50] F. Chi, X. Wei, S. Zhou, Y. Chen, C. Duan, M. Yin, Enhanced $^5D_0 \rightarrow {}^7F_4$ transition and optical thermometry of garnet type $Ca_3Ga_2Ge_3O_{12}:Eu^{3+}$ phosphors, Inorganic Chemistry Frontiers, 5 (2018) 1288-1293.

[51] S.U. Khan, W.U. Khan, W.U. Khan, D. Khan, S. Saeed, S. Badshah, M. Ikram, T.A. Saleh, Eu^{3+}, Sm^{3+} Deep-Red Phosphors as Novel Materials for White Light-Emitting Diodes and Simultaneous Performance Enhancement of Organic–Inorganic Perovskite Solar Cells, Small, 16 (2020) 2001551.

[52] G. Gao, L. Wondraczek, Spectral asymmetry and deep red photoluminescence in Eu^{3+}-activated $Na_3YSi_3O_9$ glass ceramics, Optical Materials Express, 4 (2014) 476-485.
[53] M. Bettinelli, A. Speghini, F. Piccinelli, A. Neto, O. Malta, Luminescence spectroscopy of Eu^{3+} in $Ca_3Sc_2Si_3O_{12}$, Journal of luminescence, 131 (2011) 1026-1028.
[54] P. Lu, X. Hu, Y. Li, M. Zhang, X. Liu, Y. He, F. Dong, M. Fu, Z. Zhang, One-step preparation of a novel $SrCO_3/gC_3N_4$ nano-composite and its application in selective adsorption of crystal violet, RSC advances, 8 (2018) 6315-6325.
[55] R.E. Rojas-Hernandez, W. More, F. Rubio-Marcos, J.F. Fernandez, Investigating Raman spectra and density functional theory calculations on $SrAl_2O_4$ polymorphs, Journal of Raman Spectroscopy, 50 (2019) 91-101.
[56] V. D’Anna, L.M.L. Daku, H. Hagemann, F. Kubel, Ionic layered BaFCl and $Ba_{1-x}Sr_xFCl$ compounds: Physical-and chemical-pressure effects, Physical Review B, 82 (2010) 024108.
[57] J. Sahu, K. Mahalik, A. Patwardhan, B. Meikap, Equilibrium and kinetic studies on the hydrolysis of urea for ammonia generation in a semibatch reactor, Industrial & engineering chemistry research, 47 (2008) 4689-4696.
[58] Y.-F. Xu, D.-K. Ma, M.-L. Guan, X.-A. Chen, Q.-Q. Pan, S.-M. Huang, Controlled synthesis of single-crystal $SrAl_2O_4:Eu^{2+},Dy^{3+}$ nanosheets with long-lasting phosphorescence, Journal of Alloys and Compounds, 502 (2010) 38-42.
[59] K. Jacob, V. Shreyas, Thermodynamic properties of $SrAl_{12}O_{19}$ and $SrAl_4O_7$, Journal of Materials Science, 53 (2018) 1723-1730.
[60] M. Dejneka, E. Snitzer, R. Riman, Blue, green and red fluorescence and energy transfer of Eu^{3+} in fluoride glasses, Journal of Luminescence, 65 (1995) 227-245.
[61] K. Biswas, A.D. Sontakke, K. Annapurna, Synthesis and structural probing of Eu^{3+} doped $BaYF_5$ nano-crystals in transparent oxyfluoride glass-ceramics, International Journal of Applied Glass Science, 3 (2012) 154-162.

Supplementary information

Controlled reparation of deep-red-emitting $CaAl_{12}O_{19}:Eu^{3+}$ and $SrAl_{12}O_{19}:Eu^{3+}$ hexagonal nanoparticles by a cooperative microgel formation and subsequent self-transformation process

Jafar Afshani [a], Teresa Delgado [b], Celine Besnard [c], Yashar Sadian[d], Hans Hagemann [a]

[a] Département de Chimie Physique, Université de Genève, Quai Ernest-Ansermet 30, Genève 1211, Switzerland.

[b] Chimie ParisTech-CNRS, IRCP (PSL), 11 Rue P. et M. Curie, 75005, Paris, France

[c] Laboratoire de Cristallographie, DQMP, Université de Geneve, Quai Ernest-Ansermet 24, CH-1211 Geneva 4, Switzerland

[d] Department of Biochemistry, University of Geneva, Geneva, Switzerland

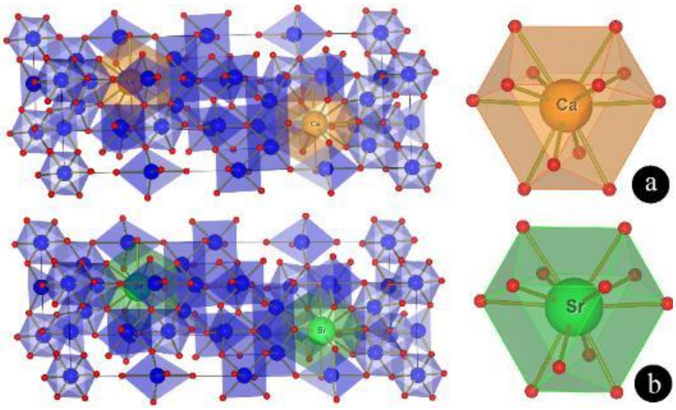

Fig S1. Unit cells of $CaAl_{12}O_{19}$ and $SrAl_{12}O_{19}$ crystal structure and the Ca^{2+}/Sr^{2+} coordination geometry.

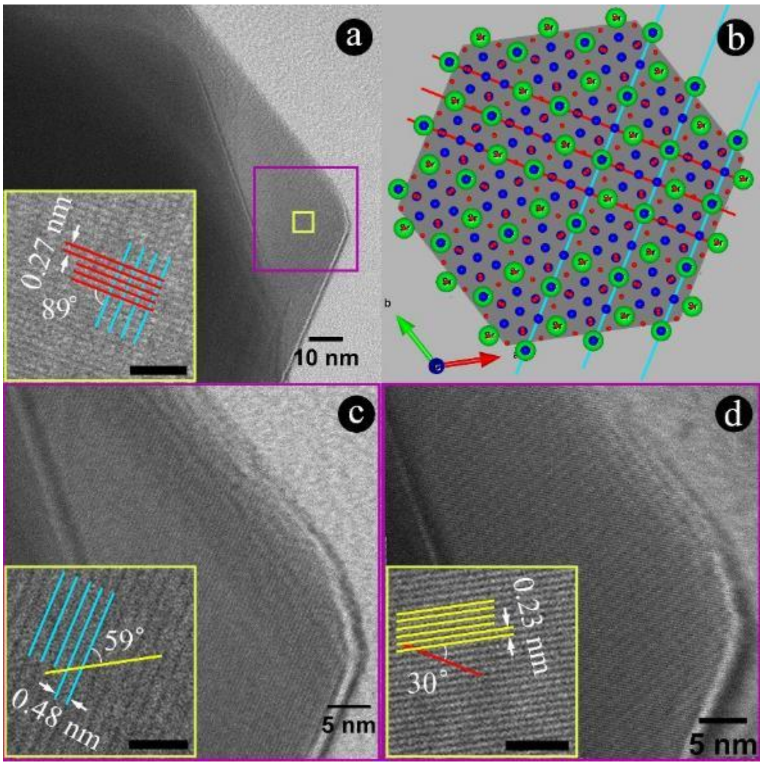

Figure S2. Inter-layer distances in SA_6 NPs. The scale bars in the inset pictures show 2 nm.

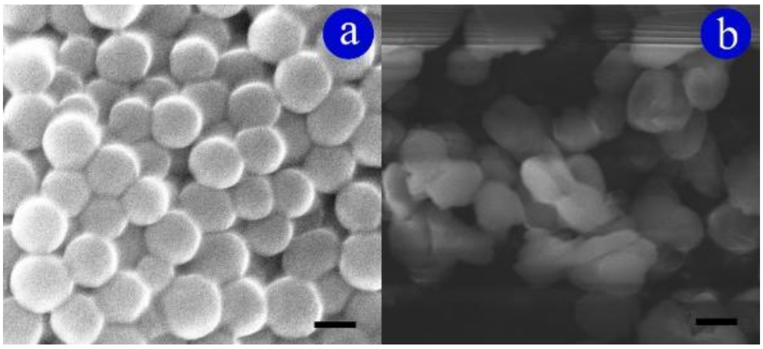

Figure S3. SEM images of the $SA_6:Eu^{3+}$ NPs precursor (a) and annealed at 1150 °C (b). The scale bar in both pictures shows 200 nm.

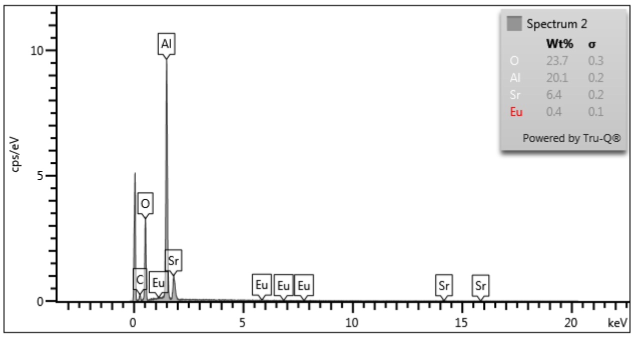

Figure S4. EDS analysis of SA_6:Eu^{3+} NPs annealed at 1150 °C.

Electron diffraction

Continuous Rotation data were collected on a single nanocrystal in nanoprobe mode in a FEI Tecnai G2 sphera microscope using a voltage of 120 kV and an Ansterdam Scientifix Cheetah camera. Figure S5 displays a typical diffraction image (rotation 0.22 degrees, exposure tine 0.5 s). Data processing was made in DIALS [1]. The data could be indexed using a hexagonal unit cell of parameters a and c of respectively 4.99 and 19.9 Å (85 percent of the reflection indexed, see figure S6). With electron diffraction data the distance and the unit cell parameters are strongly correlated so that the parameters could not be refined and are therefore very sensitive to errors in the calibration of the sample-detector distances.

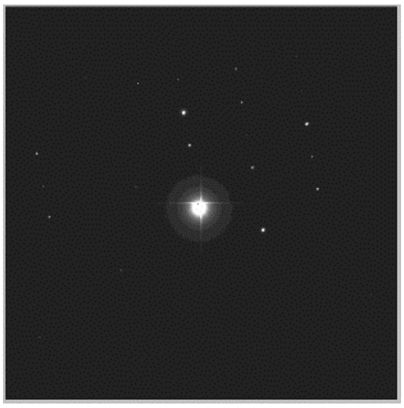

Figure S5: Typical diffraction image as recorded with the Amsterdam ScientificCheetah camera

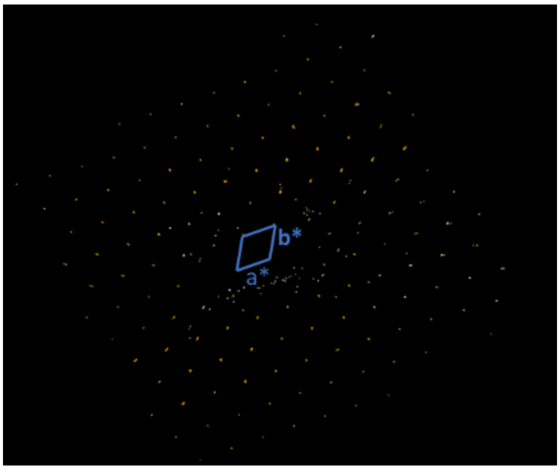

Figure S6. 3D reciprocal space reconstruction from the peak hunting done in the program DIALS. View along the 001 direction showing the a* and b* reciprocal vectors. 85 percent of the spots are indexed (indexed spots are displayed in orange) using the hexagonal unit cell.

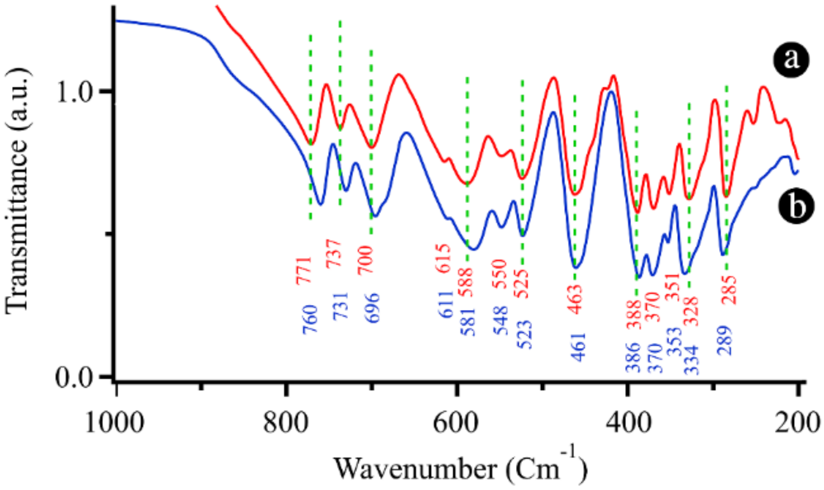

Figure S7. FTIR spectra of a) CA$_6$:Eu^{3+} annealed at 1150 °C and b) SA$_6$:Eu^{3+} annealed at 1150 °C.

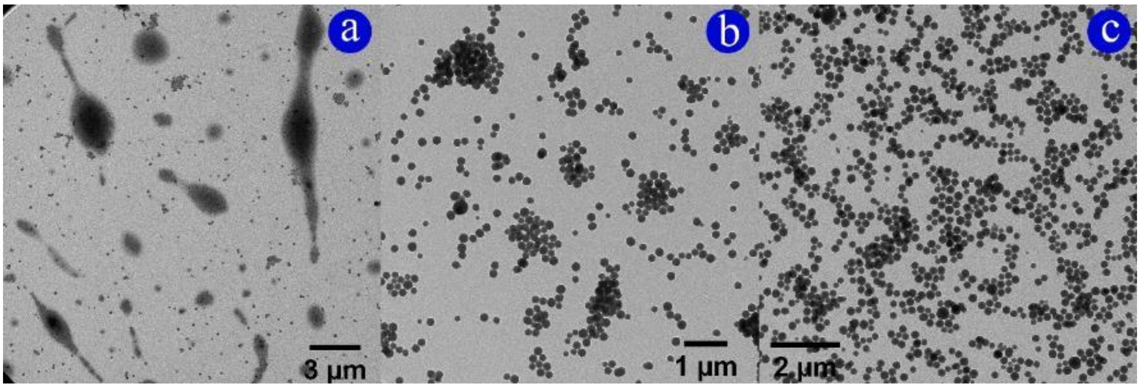

Figure S8. Evolution of $CA_6:Eu^{3+}$ NPs after 5 minutes (a), 10 minutes (b), and 20 minutes (c) growth time.

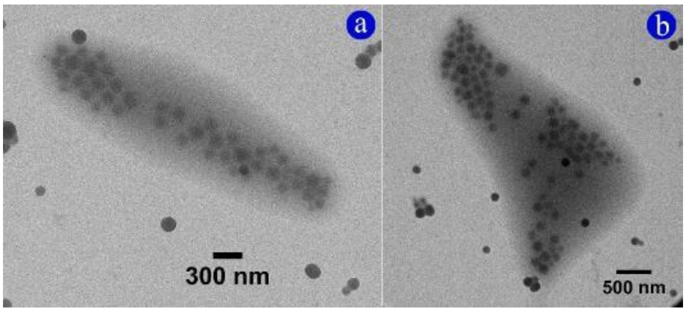

Figure S9. Growth of NPs inside micro-sized gels.

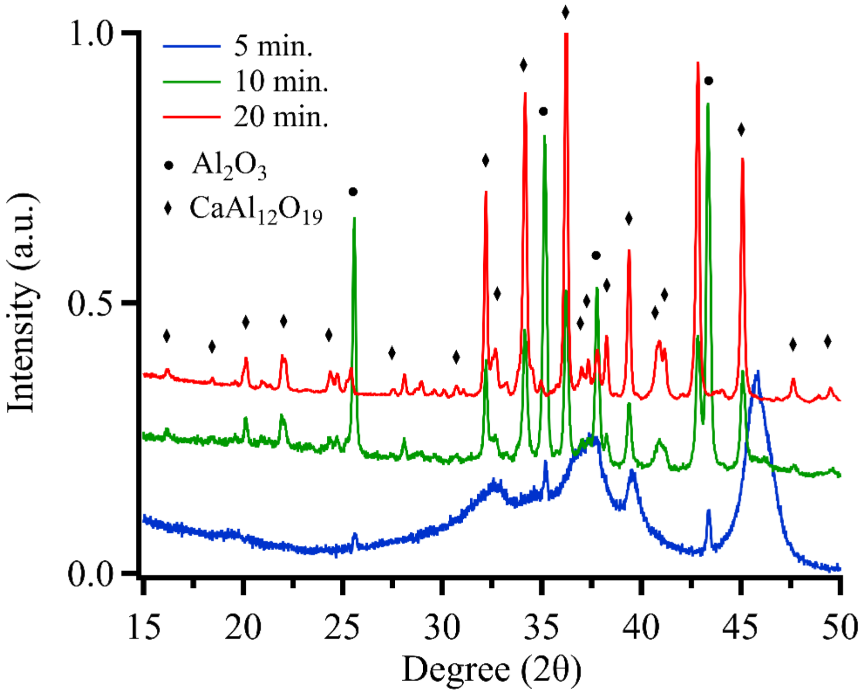

Figure S10. Powder-XRD patterns of the NPs obtained at different particle growth times, annealed at 1150 °C for 3 h.

References

1. Winter, G., et al., DIALS: implementation and evaluation of a new integration package. Acta Crystallographica Section D, 2018. **74**(2): p. 85-97.

Paper II: Luminescence spectroscopy of $CaAl_{12}O_{19}$:Eu^{3+} and $SrAl_{12}O_{19}$:Eu^{3+} nanoparticles

In this paper, excitation and emission spectra of Eu^{3+} in $CaAl_{12}O_{19}$ and $SrAl_{12}O_{19}$ have been studied in detail. The emission of Eu^{3+} on the high symmetry Sr site without charge compensation has been observed and identified using crystal field calculations. Additional emission lines are observed and are assigned to Eu^{3+} associated to charge compensating defects. Our studies showed that at least three different types of charge compensation processes are taking place for the Eu^{3+} ion in both $CaAl_{12}O_{19}$ and $SrAl_{12}O_{19}$ NPs. Moreover, emission bands from the higher excitation states ($^5D_{1-3}$) of the Eu^{3+} ion was observed at 298 K, which has rarely been observed in particular for in metal oxide hosts.

This paper was submitted to J. Luminescence.

Luminescence spectroscopy of $CaAl_{12}O_{19}:Eu^{3+}$ and $SrAl_{12}O_{19}:Eu^{3+}$ nanoparticles

Jafar Afshani [a], Teresa Delgado [*a,b], Gheorghe Paveliuc [a], Hans Hagemann [*a]

[a] Département de Chimie Physique, Université de Genève, Quai Ernest-Ansermet 30, Genève 1211, Switzerland.

[b] Chimie ParisTech-CNRS, IRCP (PSL), 11 Rue P. et M. Curie, 75005, Paris, France

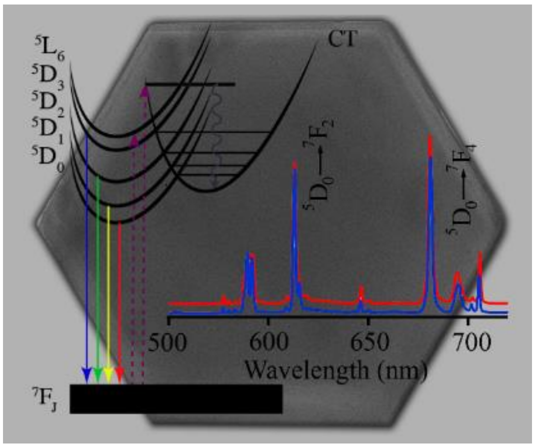

Abstract

Development of red-emitting phosphors have gained enormous interest in recent year, due to their great potential for biological applications as well as display panels and solid-state lighting. For potential biological applications, size controlled nano-particles (NPs) are important. Trivalent europium has been commonly doped into different inorganic structures to obtain red phosphors. Among these inorganic materials, due to their wide transparency windows and high stabilities, Ca/SrO-Al_2O_3 crystals have proven to be excellent hosts for rare-earth metal-ions including europium, as luminescent activators. $CaAl_{12}O_{19}$ (CA_6) and $SrAl_{12}O_{19}$ (SA_6) with band gaps larger than 7 eV, both crystallize in a common high symmetry (D_{3h}) and the Ca^{2+}/Sr^{2+} (M^{2+}) experience similar local environment. 200 nm-sized nanocrystals of CA_6 and SA_6 have been prepared. Luminescent properties of Eu^{3+}, which substitutes for M^{2+} in these crystals, was studied at 298 and 5 K. Unaccustomed for Eu^{3+}, the strongest emission was observed to originate from the $^5D_0 \rightarrow {}^7F_4$ transition. Furthermore, emissions from the higher excited states ($^5D_{1-3}$) of the f-configuration of Eu^{3+} were also observed in these nanoparticle hosts at room temperature. In addition to the bands assigned to Eu^{3+} on the high symmetry D_{3h} site by CF calculations, additional bands assigned to lower symmetry charge compensated sites have been identified.

Keywords: Calcium aluminate, strontium aluminate, Eu^{3+} luminescence, nanoparticles, charge compensation.

Introduction

Calcium and strontium aluminates doped with rare earth ions find many applications ranging from lasers to persistent phosphor materials [1-5]. Various experiments have shown that the trivalent rare earth ions replace the divalent strontium ions in the crystal [6]. This requires that the additional positive charge must be compensated. In the case of $SrAl_2O_4$ (SA) and $Sr_4Al_{14}O_{25}$ (S_4A_7), there are voids in their crystal structures, which allow for interstitial charge compensation [1, 7]. This is not the case for SA_6. The latter compound has a compact crystal structure and crystallizes in a hexagonal structure with the space group $P6_3/mmc$ [8, 9]. There are two formula units per unit cell in this structure, which consists of five different crystallographic sites for Al^{3+} (three AlO_6 octahedra, one AlO_5 trigonal bipyramidal, and one AlO_4 tetrahedra), but only one crystallographic site for the M^{2+} ion. CA_6 is isostructural with SA_6. In these crystals, the M^{2+} ion coordinates to 12 oxygen atoms (Figure 1). The distance between the six in-plane oxygen atoms and the central Ca^{2+} ion is 0.278 nm, while the six out-of-plane oxygen atoms are located at 0.270 nm from the central atom [8]. These values for SA_6 are 0.278 nm and 0.274, respectively [9].

Trivalent europium is well-known for emitting strongly from the $^5D_0$ excited state to the $^7F_2$ state at an emission wavelength of about 615 nm [10]. Red-emitting nanoparticles may find applications in the study of biological systems, and it has been shown that strontium aluminates present low cytotoxicity [11]. The emission and excitation spectra of Eu^{3+} and Eu^{2+} in SA_6 have been presented previously [12]. In this work, we present in detail the luminescence properties of Eu^{3+} in SA_6 and CA_6 nanoparticles (NP) of about 200 nm size. We identify, using CF calculations, the emission bands corresponding to Eu^{3+} on the high symmetry Sr site, as well as additional bands for Eu^{3+} in lower symmetry environment. It appears further that the intensity of the $^5D_0 \rightarrow {}^7F_4$ transition around 680 nm is particularly strong in both CA_6 and SA_6, which makes them even more attractive for potential applications.

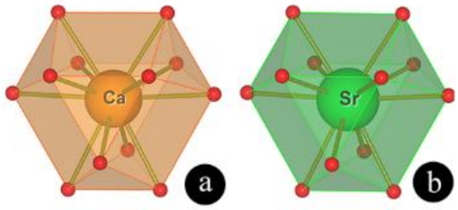

Figure 1. The local coordination geometry of Ca^{2+} (a) and Sr^{2+} (b) in $CaAl_{12}O_{19}$ and $SrAl_{12}O_{19}$ crystals, respectively.

Experimental

Materials and reagents

Strontium nitrate (99+% ACS reagent), aluminum nitrate nonahydrate (99+%), and urea (99.5%) were purchased from Acros Organics. Europium nitrate pentahydrate (99.9% trace metal basis) and polyvinylpyrrolidone (PVP) (M.W. 58000) were purchased from Sigma Aldrich and Fluka, respectively. Ethanol absolute (99.8%) was supplied by Fisher Scientific.

Instruments

A Teflon-lined stainless-steel autoclave was used for the preparation of the strontium aluminate precursor NPs. These NPs were annealed in a Carbolite tube furnace. A Panalytical X'pert Pro MPD (Cu Kα = 1.5406 Å) was used to collect the X-ray powder diffraction (XRD) data.

TEM images were taken with a Tecnai G2 sphere with 120 keV electrons focused on the sample. Samples were dispersed in ethanol, and few drops of this dispersion were added on a carbon coated copper grid (Formvar carbon film, 200 mesh).

A Horiba Jobin Yvon Fluorolog 3-22, equipped with a photo multiplier tube (PMT) detector was used to obtain the photoluminescence spectra. A closed-cycle Janis-Sumitomo SHI-4.5 cryostat equipped with a programmable temperature controller (Lakeshore Model 331) was used for the luminescence measurements at 5 K. Both excitation and emission slits for all luminescence measurements were set to 0.5 nm.

Synthesis of Ca/$SrAl_{12}O_{19}$:Eu^{3+} nanoparticles

The synthesis procedure will be presented in detail elsewhere [13]. Briefly, nitrate salts of calcium/strontium (1 mmol), aluminum (6 mmol), and europium (0.01 mmol) were dissolved in 8 ml distilled water along with 3 g of urea and 1.2 g of PVP. To this mixture 80 ml of EtOH was added and stirred to obtain a clear solution. The solution was heated in a Teflon-lined stainless-steel autoclave at 170 °C for 2 h. The autoclave was then cooled down to the room temperature and the product was centrifuged and washed with a H_2O/EtOH mixture. The precursor NPs were heated at a rate of 10 degree/minute and after remaining for 3 h at 1150 °C, they were cooled down to the room temperature at the same rate to obtain NPs of CA_6 and SA_6.

Results and discussion

Characterization

The powder-XRD patterns of both CA_6 and SA_6 NPs are presented in Figure 2. These patterns confirm that pure-phase $CaAl_{12}O_{19}$ and $SrAl_{12}O_{19}$ compounds were obtained by annealing their respective precursor NPs at 1150 °C as indicated in the phase diagram of the Ca/SrO-Al_2O_3 systems [1, 14, 15].

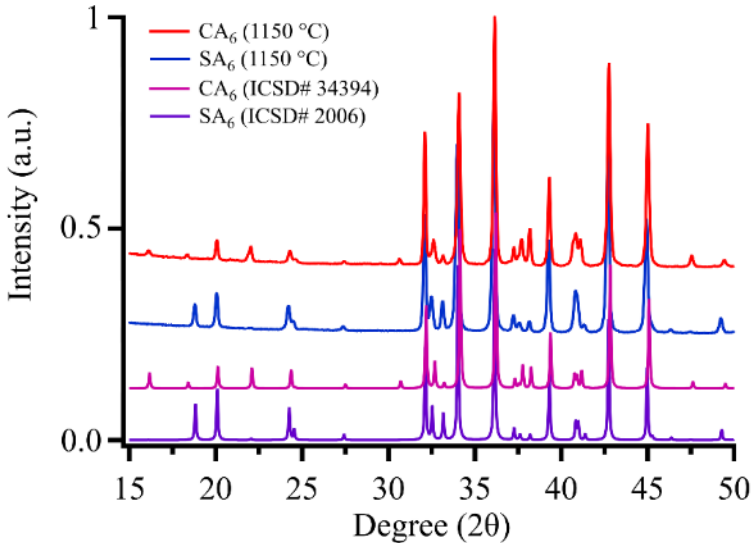

Figure 2. Powder-XRD patterns of the SA$_6$:Eu^{3+} and CA$_6$:Eu^{3+}, annealed at 1150 ˚C for 3 h.

The TEM images in Figure 3 show that spherical precursor NPs with a narrow size distribution in the range of 200-300 nm were obtained for both CA$_6$ and SA$_6$. Throughout the annealing process, both precursor NPs transformed into crystalline hexagonal NPs. Very little aggregation of the particles occurred during the annealing process and the grain size remained in the nano range.

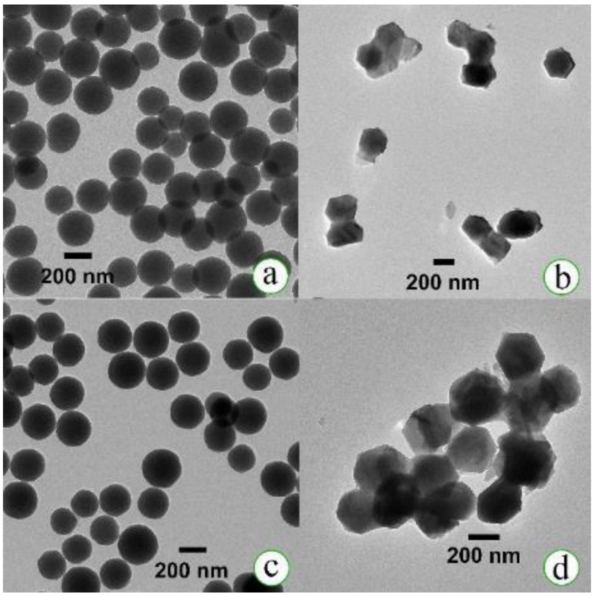

Figure 3. TEM images of CA$_6$ precursor NPs (a), CA$_6$ NPs annealed at 1150 °C (b), SA$_6$ precursor NPs (c), and SA$_6$ NPs annealed at 1150 °C (d).

Luminescence studies

Excitation spectra of both samples at 298 and 5 K

Figure 4 compares the excitation spectra of Eu^{3+} in the CA_6 and SA_6 host NPs at 298 K and 5 K. Both spectra are recorded at 613 nm. A broad excitation band is observed around 300 nm, which is assigned to the oxygen to europium charge transfer (CT). The oxygen to europium CT band in calcium/strontium aluminates normally occurs around 250 nm [7, 16]. The large red-shift in this case can be attributed to the relatively long Eu^{3+}-O^{2-} bond lengths in the $MAl_{12}O_{19}$ structure [17]. This band peaks at slightly higher energies for CA_6 and extends further to the lower energies compared with SA_6. The relatively higher energy of the CT band can be explained by slightly shorter average $Ca^{2+}(Eu^{3+})$-O^{2-} bond length in CA_6. The sharp bands, expanded in the inset of Figure 4, originate from the intra-configurational f-f transitions. These bands are assigned to the $^7F_0 \rightarrow {}^5L_6$ and $^7F_J \rightarrow {}^5D_{3-1}$ transitions. This excitation spectrum for $SA_6:Eu^{3+}$ agrees with a previous report for $SrAl_{12}O_{19}:Eu^{3+}$ [12]. The bands at 533 and 415 nm originate from the $^7F_1 \rightarrow {}^5D_1$ and the $^7F_1 \rightarrow {}^5D_3$ transitions. Additional weak bands in these spectra most probably have vibronic origin as their energies lie within the range of the Raman bands reported for the SrO-Al_2O_3 system before (Figure S1) [16].

At 5 K the CT band shifted to higher energies by about 4 nm for both phosphors and as expected, the intra-configurational f-f transitions bands appear more resolved. The $^7F_0 \rightarrow {}^5D_{1,2}$ bands are observed as sharp singlets at 5 K at 524 and 463.5 nm, respectively. The $^7F_0 \rightarrow {}^5L_6$ band is resolved into a doublet at 394.5 and 396.75 nm. Furthermore, the relative intensity of the $^7F_0 \rightarrow {}^5L_6$ band increased at 5 K, whereas the intensities of the $^7F_0 \rightarrow {}^5D_{1,2}$ decreased. The weak excitation bands observed at 298 K originating from the $^7F_1$ state vanished at 5 K similar to the vibronic sidebands due to insufficient thermal energy. A separate comparison between the excitation spectra at 5 and 298 K for each phosphor is presented in Figures S2 and S3.

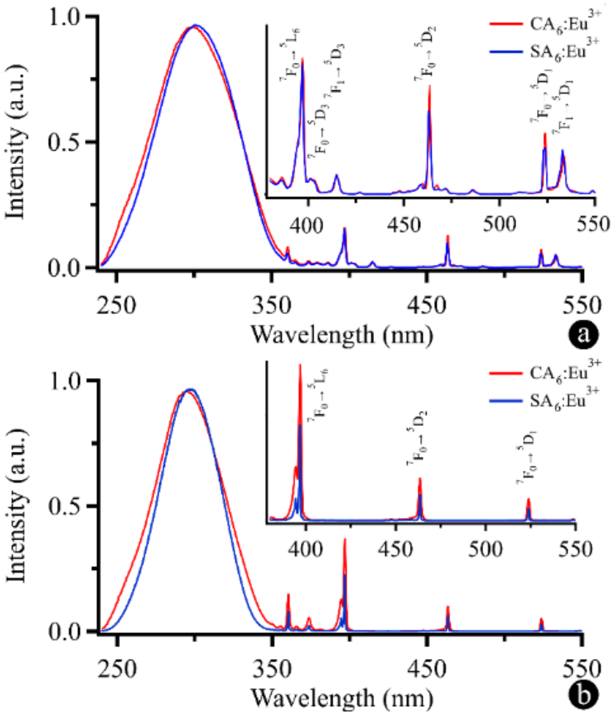

Figure 4. Excitation spectra of Eu^{3+} in CA_6 and SA_6 host NPs ($\lambda_{em.}$ = 613 nm) at 298 K (a) and at 5K (b).

Emission spectra of both samples at 298 and 5 K

The emission spectra of both phosphors at 297 and 5 K are presented in Figure 5a,b, respectively. The $CA_6:Eu^{3+}$ spectra are shifted upwards for better illustration purposes. The almost identical appearances of these two emission spectra as well as those of the excitation, reflects the similar local environment and symmetry of Eu^{3+} ion in these crystals. However, some bands in both excitation and emission spectra are slightly red-shifted (ca. 0.25 nm) for the $CA_6:Eu^{3+}$ relative to those of the $SA_6:Eu^{3+}$ NPs (Table 2). This agrees with the relatively higher chemical pressure felt by the Eu^{3+} substituting Ca^{2+} in the crystal structure [18]. For both NPs, all possible emission bands originating from the $^5D_0 \rightarrow ^7F_{1-6}$ could be identified in the range of 585-830 nm.

The magnetic-dipole (MD) induced $^5D_0 \rightarrow ^7F_1$ transition is found as a doublet at ≈ 590.5 nm for both phosphors with a small splitting of about 2.25 nm. There appears only one band for the $^5D_0 \rightarrow ^7F_2$ transition at 613.25 nm for both NPs with a small shoulder at 615.5 nm, hereafter described. The $^5D_0 \rightarrow ^7F_3$ transition appears as a triplet at 646 nm. Unlike almost all Eu^{3+} phosphors, where the $^5D_0 \rightarrow ^7F_2$ emission band occurs the strongest, these $CA_6:Eu^{3+}$ and $SA_6:Eu^{3+}$ NPs emit the strongest through the $^5D_0 \rightarrow ^7F_4$ transition at the deep-red region of the spectrum. This transition is split into four bands with the sharpest band at 681.5 nm. The $^5D_0 \rightarrow ^7F_{5,6}$ transitions are normally not reported in the literature since they fall in the range of the spectrum that is not covered efficiently by the commonly used detectors. Here, in these nanoparticles, the $^5D_0 \rightarrow ^7F_5$ band was obtained as a quartet at ≈ 750 nm with some shoulders and the lowest lying bands in energy were observed about 820 nm, which originate from the $^5D_0 \rightarrow ^7F_6$ transitions. The lifetimes of these $^5D_0 \rightarrow ^7F_J$ emissions were measured previously [12] and found to be 1.75 – 2.6 ms at room temperature, which are slightly longer compared with the SA host (0.7 µs – 1.6 ms) [7]. Table 2 compares the emission bands originating from the $^5D_0$ state for $CA_6:Eu^{3+}$ and $SA_6:Eu^{3+}$ NPs.

It is unaccustomed to observe Eu^{3+} emissions from the higher excited states as the excited electrons relax non-radiatively to the $^5D_0$ state, where then they emit light by relaxing to the ^7F_J ground state. Interestingly, $CA_6:Eu^{3+}$ and $SA_6:Eu^{3+}$ NPs both emit light from the $^5D_{1-3}$ levels in the blue, green, and yellow region of the spectrum, as well. This indicates that the ^5D_J states of the Eu^{3+} lie well below the bottom of the conduction bands of these NPs, due to their large band gaps (>7 eV for CA_6 [19] and 7.76 eV for SA_6 [20]). Although these emissions are rare for Eu^{3+} due to the fast phonon assisted relaxation [21] in particular in oxide systems, they can take place in inorganic structures. Nonetheless, even in inorganic structures, emission from the $^5D_3$ state has been scarcely witnessed, which occurred then normally at cryogenic temperatures [22, 23]. At room temperature, this emission was observed for a group of fluorides [21, 24]. Among metal oxide hosts emission from the $^5D_3$ excited state at room temperature was observed for $ZnY_4W_3O_{19}$.

In Figure 5, it is possible to compare the considerably lower intensity of the bands originating from the $^5D_{1-3}$ states in between 500-560 nm with those generated from the $^5D_0$ state. These emission bands are shown in more detail on the left-hand side of Figure 5, where different bands originating from the $^5D_{1-3} \rightarrow ^7F_{0-6}$ transitions are identified (the assignments on the spectra do not inclusively indicate all the emissions taking place).

Similar to the excitation spectra, the emission bands are better resolved at 5 K. This is more evident for the $^5D_0 \rightarrow ^7F_2$, where the shoulder observed at 615.5 nm at 298 K is resolved into a separate band. However, the relative intensities of all bands, as well as their splitting and positions remain nearly the same for both 298 K and 5 K. The bands originating from the higher excited states look identical for both spectra, as well. The emission spectra at 5 and 298 K for $CA_6:Eu^{3+}$ and $SA_6:Eu^{3+}$ are provided separately in Figures S4 and S5.

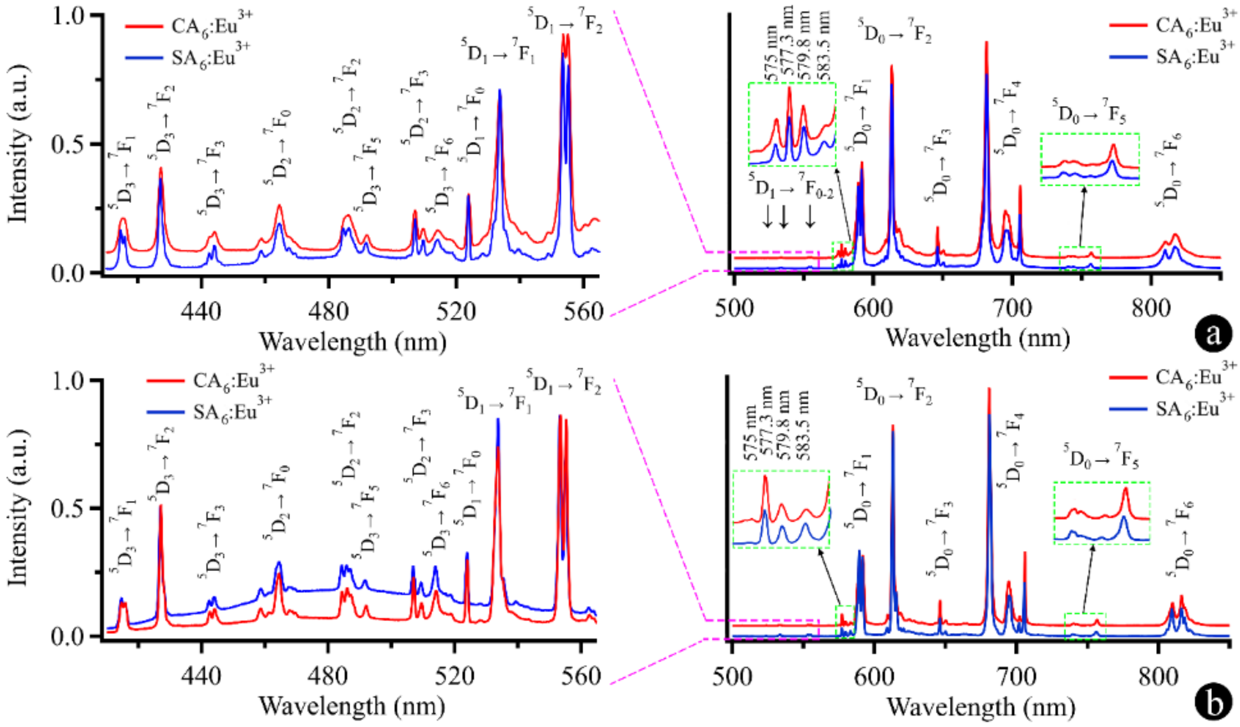

Figure 5. Emission spectra of $CA_6:Eu^{3+}$ and $SA_6:Eu^{3+}$ NPs at 298 K (a) and 5 K (b) ($\lambda_{exc.}$ = 300 nm for 500-850 nm and 397 nm for 410-565 nm).

Crystal field calculations

The analysis of the optical spectra of Pr^{3+}-doped SA_6 [25] has provided extrapolated CF parameters applicable for Eu^{3+}on the Sr^{2+} site in SA_6. Using these CF parameters, we have calculated the corresponding energy levels using the program of [26] which was adapted as in [27] to allow for CF parameters optimizations. Correspondingly, the values of the parameters used shifted somewhat (Table 1). Calculation of the energy levels allowed to assign the corresponding transitions observed in the spectra, as well as additional bands which will be discussed below. Figure 6 compares the positions of the calculated f-f transitions to those obtained experimentally. A full comparison of the energy levels between the experimentally obtained and the calculated values are presented in Table S1.

Table 1. Free ion parameters for Eu^{3+} and the calculated crystal field parameters in SA_6 structure. The parameters α, β, γ, and T^n were kept constant.

	Refs [10]^a, [25]^b	Present work
F^2(ff)	82786^a	87776.42
F^4(ff)	59401^a	58283.54
F^6(ff)	42644^a	43361.55
ξ_{4f}	1332^a	1326.78
B_{20}	-147^b	-125
B_{40}	571^b	653.88
B_{60}	-1195^b	-1815.75
B_{66}	-946^b	-1167.38
α(ff)	19.8^b	19.8
β(ff)	-617^b	-617
γ (ff)	1460^b	1460
T^2(ff)	370^b	370
T^3(ff)	40^b	40
T^4(ff)	40^b	40
T^6(ff)	-330^b	-330
T^7(ff)	380^b	380
T^8(ff)	370^b	370

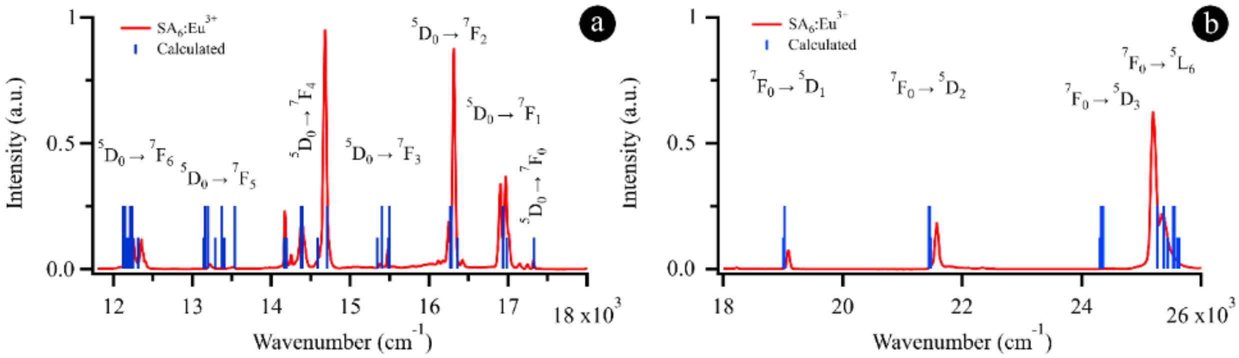

Figure 6. Observed emission (a) and excitation (b) spectrum of SA_6 at 300 nm and 613 nm, respectively at 5 K. Calculated positions of $^5D_0 \leftrightarrow {}^7F_J$ transition are indicated as vertical bars. Transitions towards degenerate ^7F_J states with E symmetry are indicated with the double height as compared to the non-degenerate states. Note: the calculated position of the $^5D_0 \rightarrow {}^7F_0$ transition is also shown, however this band is forbidden in D_{3h} symmetry.

Table 2. Wavelengths of the emission bands originating from the $^5D_0$ state in the CA_6 and SA_6 NPs at 5 K compared with the calculated ones.

Transition	$CA_6:Eu^{3+}$ (nm)	$SA_6:Eu^{3+}$	Calculated ($SA_6:Eu^{3+}$)
$^5D_0 \rightarrow {}^7F_1$	588.5 591.75	589.25 591.5	588.5 590.25
$^5D_0 \rightarrow {}^7F_2$	613.25	613.25	610.75 613.75 614.5
$^5D_0 \rightarrow {}^7F_3$	643.75 646.5 650.75	643.5 646.25 650.5	644.75 645 645.5 649 651.5
$^5D_0 \rightarrow {}^7F_4$	681.5 695.25 702.75 705.75	681.5 695.25 702.75 705.75	679.25 684.75 694.75 695.25 704.75 705.75
$^5D_0 \rightarrow {}^7F_5$	739.75 742.5 743.5 750 754.75 756.75	739.5 742.5 743.5 749.25 754.25 756.25	738.25 745.75 747.25 751.75 757.25 759.5 760.25
$^5D_0 \rightarrow {}^7F_6$	808 809.75 814.5 816 818.75 822 828.5	808 809.25 814 816 818.5 821.75 827.75	811.25 811.5 816.25 817 818.25 819.25 821.5 823.25 825

Emission under CT vs $^5L_6$ excitation bands: luminescence mechanism

It was already described that excitation to the $^5L_6$ state of the f configuration results in the emission from all the sublevel excited states ($^5D_{0\text{-}3}$). This indicates that although excited ^5D_J (J=1-4) can relax to the $^5D_0$ state non-radiatively, they emit also to the ^7F_J levels, directly. However, Figure 7 shows that under excitation to the CT band at 300 nm, the emission intensity from the $^5D_{2,3}$ states is strongly reduced (See Figure S6 for the $CA_6:Eu^{3+}$). This occurs at both 298 and 5 K and suggests that the excited electrons relax predominantly to the $^5D_0$ and to some extent to the $^5D_1$ states non-radiatively, while only small quantities of the excited electrons relax to the $^5D_{2,3}$ states due to the higher energy barriers illustrated in Figure 7.

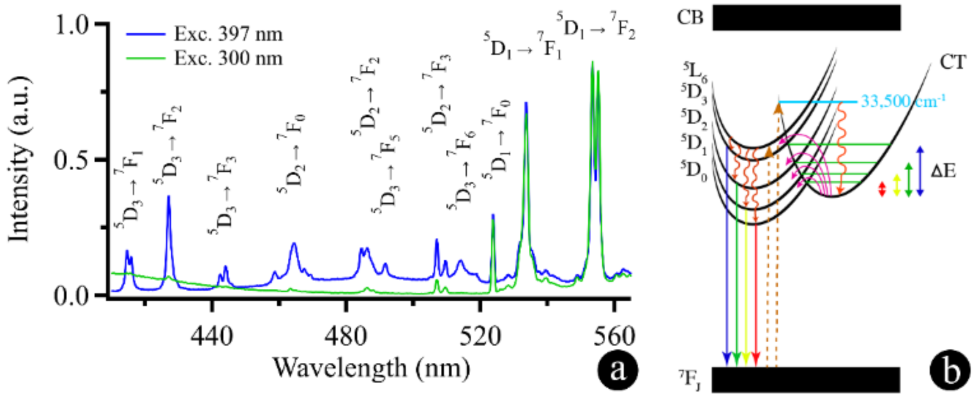

Figure 7. Comparison of the emission of $SA_6:Eu^{3+}$ from the $^5D_{1\text{-}3}$ states under excitation to the CT band (300 nm) vs excitation to the $^5L_6$ state (397 nm) at 298 K (a). Schematic illustration of non-radiative decay path from the excited $^5L_6$ and CT states towards the emitting $^5D_{0\text{-}3}$ states (see the text in section 3.2.4).

Local environment of Eu^{3+} ions by in-depth luminescence studies

In $MAl_{12}O_{19}$, the M atom is on a site with D_{3h} symmetry. The dopant Eu^{3+} ions are expected to replace M^{2+} in the crystal structure. As the valence of Eu^{3+} is different from the valence of M^{2+} ion, the charge must be compensated in the crystal, but not necessarily in the first coordination sphere.

The observed emission spectra of Eu^{3+} can be described in terms of the high site symmetry of M (D_{3h}). The $^5D_0 \rightarrow {}^7F_0$ transition is forbidden within the frame of the standard Judd-Ofelt theory, and is observed only when Eu^{3+} occupies one of the C_{nv}, C_n, or C_s symmetry as a result of the selection rule breakdown [10]. In the case of CA_6 and SA_6 both with the D_{3h} symmetry, this transition is not expected to be observed. Despite the symmetry predictions, relatively weak bands emerged in the range of 570-585 nm in the emission spectra of both NPs. This is where the $^5D_0 \rightarrow {}^7F_0$ transition is normally observed for Eu^{3+} [10]. In addition, the D_{3h} symmetry predicts only a doublet for the $^5D_0 \rightarrow {}^7F_1$ transition and a singlet band for the $^5D_0 \rightarrow {}^7F_2$ emission. Nonetheless, a shoulder was observed on both bands along with some wiggles. All these bands can be clearly recognized in the spectrum published for $SrAl_{12}O_{19}:Eu^{3+}$ before [12], as well. A comparison between the two emission spectra at 298 K and 5 K in Figures S4 and S5, in particular around the $^5D_0 \rightarrow {}^7F_2$ transition reveals a remarkable decrease in the intensities of some bands/wiggles or their disappearance at 5 K, suggesting the contribution of vibronic transitions. Intensity of the band at 575 nm, also decrease at 5 K, dramatically. However, the two shoulders observed on the $^5D_0 \rightarrow {}^7F_1$ and $^5D_0 \rightarrow {}^7F_2$ bands appeared even slightly stronger at 5 K, which rules out their vibronic origin or contribution.

The excitation spectra obtained at 575, 577, 580, and 583.5 nm in Figure 8a reveals a completely different environment for the Eu^{3+} emitting at 575 nm. In addition, for this Eu^{3+} the CT band was observed at 280 nm, whereas those corresponding to the rest of the emission bands appear in between 293-300 nm. Moreover, this CT band is about four times less intense compared to those in the other Eu^{3+} ions. In other words, the f-f transitions are stronger, which indicates a lower symmetry for the Eu^{3+} surrounding. These transitions presented in the inset of Figure 8a take place at higher energies with clearly distinguishable shapes for the Eu^{3+} emitting at 575 nm. These observations suggest a totally different environment and symmetry for this Eu^{3+} ion than the D_{3h} symmetry in the $SrAl_{12}O_{19}$ crystal lattice. On the other hand, the three spectra recorded at 577, 580, and 583.5 nm look very similar to the spectrum obtained for the Eu^{3+} in the SA_6 lattice ($\lambda_{em.}$ = 613 nm) with only minor differences, suggesting a similar local symmetry for them, as well. The very close energies of the CT band also suggest similar Eu^{3+}-O^{2-} distances.

The emission spectra (Figure 8b) obtained under excitation at these different wavelengths further confirms the previous observations. The spectrum at 575 nm differs dramatically from the rest. It shows a well-resolved triplet for the $^5D_0 \rightarrow {}^7F_1$ transition band as well as a huge splitting of at least 22 nm for the $^5D_0 \rightarrow {}^7F_2$ band, indicating that this Eu^{3+} ion is feeling a low-symmetry environment and a great crystal field effect. On the other hand, the three other spectra excited at 300, 577, and 580 nm look quite similar. The $^5D_0 \rightarrow {}^7F_1$ doublet with a shoulder at 588 nm is resolved into three separate bands in the spectrum excited at 577 nm. The $^5D_0 \rightarrow {}^7F_2$ band, however, is split into at least a triplet at 609, 613, and 615.5 nm for all the three spectra. The weak bands at 618 and 621 nm are not easy to assign to the Eu^{3+} in the SA_6 lattice, since they fall exactly under the two bands observed at the green trace. The evidence provided by these excitation and emission spectra in Figure 8 confirm the presence of four different Eu^{3+} ions in the CA_6 and SA_6 NPs. One of these ions that emits at 575 nm seems to feel a completely different environment, while the three others seem to be sitting at a slightly distorted D_{3h} site in the SA_6 and CA_6 crystal lattice. These results indicate at least 3 different types of CC processes taking place in the crystal structures of $CA_6:Eu^{3+}$ and $SA_6:Eu^{3+}$.

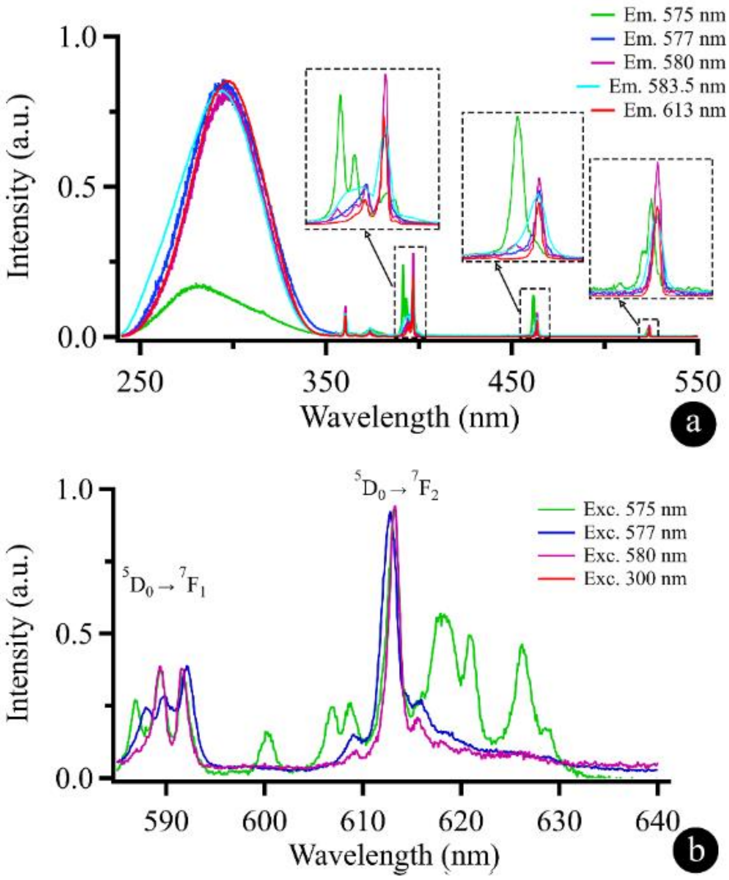

Figure 8. Excitation spectra of $SA_6:Eu^{3+}$ NPs at different emission wavelengths (a), and Emission spectra of $SA_6:Eu^{3+}$ NPs obtained by excitation at different wavelengths (b).

Conclusions

We have obtained photoluminescence spectra of Eu^{3+} in CA_6 and SA_6 NPs. For SA_6 phosphor, the observed emission bands were identified for the high symmetry Sr^{2+} site using CF calculations. The spectra obtained at both 298 and 5 K looked almost identical for CA_6 and SA_6. This similarity arises from the very similar local environments of Ca^{2+} and Sr^{2+} in the crystal structures of CA_6 and SA_6. A slight red-shift was observed for Eu^{3+} emission in CA_6 due to the chemical pressure induced as a result of replacing Ca^{2+} with the smaller ionic radii. Three different CC sites were detected in both compounds. Emissions from the $^5D_{1-3}$ were observed at 298 K for Eu^{3+} in both CA_6 and SA_6 phosphors. The excitation spectra revealed that the oxygen to europium CT band took place at 300 nm which is considerably lower compared to that of SA host (250 nm). Moreover, the most intense emission band was observed at deep-red region of the spectrum (680 nm) for both CA_6 and SA_6 NPs.

Acknowledgment

This work was supported by the Swiss National Science Foundation (projects 200020_182494, 200021_169033 and P400P2_191108/1).

References

1. H. Hagemann, J. Afshani, Chapter 321: Synthesis, luminescence and persistent luminescence of europium-doped strontium aluminates, Handbook on the Physics and Chemistry of Rare Earths, Elsevier, Vol 60 (2021) p.163-225, ISSN 0168-1273, https://doi.org/10.1016/bs.hpcre.2021.06.001.

2. R.E. Rojas-Hernandez, F. Rubio-Marcos, M.Á. Rodriguez, J.F. Fernandez, Long lasting phosphors: $SrAl_2O_4$:Eu,Dy as the most studied material, Renew. Sustain. Energy Rev., 81 (2018) 2759.

3. F. Reichert, D.-T. Marzahl, and G. Huber, Spectroscopic characterization and laser performance of Pr,Mg:$CaAl_{12}O_{19}$, J. Opt. Soc. Am. B, 2014. 31 (2): p. 349.

4. M. Fechner, F. Reichert, N.-O. Hansen, K. Petermann, G. Huber, Crystal growth, spectroscopy, and diode pumped laser performance of Pr, Mg:$SrAl_{12}O_{19}$, Appl. Phys. B, 102 (2011) 731.

5. J. Liu, Q. Song, D. Li, X. Xu, J. Xu, Growth and red-orange emission of Sm^{3+} doped $SrAl_{12}O_{19}$ single crystals, Opt. Mater., 101 (2020) 109754.

6. T. Nakamura, K. Kaiya, N. Takahashi, T. Matsuzawa, M. Ohta, C. Rowlands, G. Smith, P. Riedi, High frequency EPR investigations of gadolinium (III)-doped strontium aluminates, Phys. Chem. Chem. Phys., 3 (2001) 1721.

7. J. Bierwagen, T. Delgado, J. Afshani, S. Yoon, N. Gartmann, B. Walfortdand, H. Hagemann, Observation of multiple sites for trivalent Europium Ions in $SrAl_2O_4$, J. Lumin. 239 (2021) 118348.

8. A. Utsunomiya, K. Tanaka, H. Morikawa, F. Marumo, H. Kojima , Structure refinement of $CaO{\cdot}6Al_2O_3$. J. Solid State Chem., 75 (1988) 197.

9. A. J. Lindop, C. Matthews, D. W. Goodwin, The refined structure of $SrO.6Al_2O_3$, Acta Crystallographica Section B, 31 (1975) 2940.

10. K. Binnemans, Interpretation of europium (III) spectra. Coord. Chem. Rev., 295 (2015) 1.
11. J. B. Montes-Frausto, K. Juarez-Moreno, B. Can-Uc, G. A. Hirata-Flores, Synthesis and cytotoxic effects of $SrAl_2O_4$ persistent luminescence nanoparticles co-doped with Eu^{2+}/Dy^{3+} ions. Opt. Mater. Exp., 6 (2016) 1488.
12. S. Chawla, A. Yadav, Role of valence state of dopant (Eu^{2+}, Eu^{3+}) and growth environment in luminescence and morphology of $SrAl_{12}O_{19}$ nano-and microcrystals, Mater. Chemis. Phys., 122 (2010) 582.
13. J. Afshani, T. Delgado., C. Besnard, H. Hagemann, To be published.
14. F. Ganits, T.Y. Chemekova, Y.P. Udalov, The $SrO-Al_2O_3$ system, Zhurnal Neorganicheskoj Khimii, 24 (1979) 471.
15. D. Jerebtsov, and G. Mikhailov, Phase diagram of $CaO–Al_2O_3$ system, Ceram. Int., 27 (2001) 25.
16. S. Janáková, L. Salavcová, G. Renaudin, Y. Filinchuk, D. Boyer, P. Boutinaud, Preparation and structural investigations of sol–gel derived Eu^{3+}-doped $CaAl_2O_4$. J. Phys. Chem. Solid., 68 (2007) 1147.
17. H. E. Hoefdraad, The charge-transfer absorption band of Eu^{3+} in oxides. J. Solid State Chem., 15 (1975) 175.
18. V. D'Anna, L. M. Lawson Daku, H. Hagemann, F. Kubel, Ionic layered BaFCl and $Ba_{1−x}Sr_xFCl$ compounds: Physical-and chemical-pressure effects. Phys. Rev. B, 82 (2010) 024108.
19. R. G. Korpe, K. A. Koparkar, N. S. Bajaj, S. K. Omanwar. VUV investigation of blue emitting $MAl_{12}O_{19}$:Eu (M= Ca, Sr, Ba) phosphors synthesized by combustion method. in J. Phys.: Conference Series. 1644 (2020). IOP Publishing, DOI: 10.1088/1742-6596/1644/1/012056
20. D. Dutczak, T. Jüstel, C. Ronda, A. Meijerink, Eu^{2+} luminescence in strontium aluminates, Phys. Chem. Chem. Phys., 17 (2015) 15236.
21. Dejneka, M., E. Snitzer, and R. Riman, Blue, green and red fluorescence and energy transfer of Eu^{3+} in fluoride glasses. J. Lumin., 65 (1995) 227.
22. O. Moune, P. Porcher, P. Caro, A new analysis of the fluorescence spectrum of Eu^{3+} in A-type La_2O_3. J. Solid State Chem., 50 (1983) 41.
23. J. Hölsä, P. Porcher, Free ion and crystal field parameters for REOCl:Eu^{3+}. J. Chem. Phys., 75 (1981) 2108.
24. K. Biswas, A. D. Sontakke, K. Annapurna, Synthesis and structural probing of Eu^{3+} doped $BaYF_5$ nano-crystals in transparent oxyfluoride glass-ceramics. Int. J. Appl. Glass Sci., 3 (2012) 154.
25. B. Zandi, L.D. Merkle, J.B. Gruber, D.E. Wortman, C.A. Morrison, Optical spectra and analysis for Pr^{3+} in $SrAl_{12}O_{19}$, J. Appl. Phys., 81 (1997) 1047.
26. S. Edvardsson, D. Åberg, An atomic program for energy levels of equivalent electrons: lanthanides and actinides. Comput. Phys. Commun., 133 (2001) 396.
27. P. Pal, T. Penhouet, V. D'Anna, H. Hagemann, Effect of pressure on the free ion and crystal field parameters of Sm^{2+} in BaFBr and SrFBr hosts. J. Lumin., 134 (2013) 678.

Supplementary Information

Luminescence spectroscopy of $CaAl_{12}O_{19}:Eu^{3+}$ and $SrAl_{12}O_{19}:Eu^{3+}$ nanoparticles

Jafar Afshani [a], Teresa Delgado [*a,b], Gheorghe Paveliuc [a], Hans Hagemann [*a]

[a] Département de Chimie Physique, Université de Genève, Quai Ernest-Ansermet 30, Genève 1211, Switzerland.

[b] Chimie ParisTech-CNRS, IRCP (PSL), 11 Rue P. et M. Curie, 75005, Paris, France

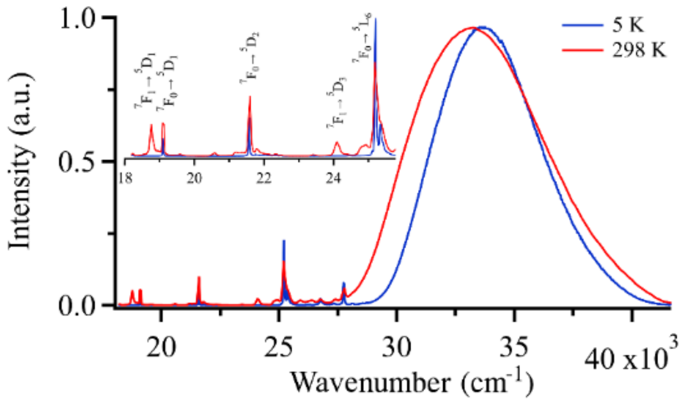

Figure S1. Excitation spectra of Eu^{3+} in SA_6 host NPs at 5 K vs 298 K ($\lambda_{em.}$ = 613 nm).

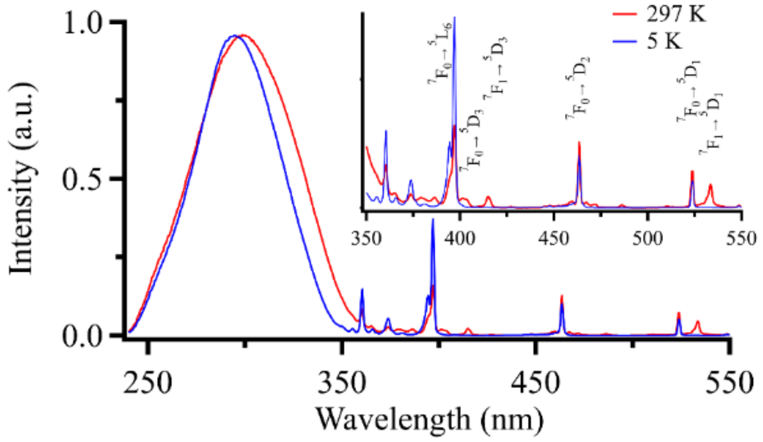

Figure S2. Excitation spectra of $CA_6:Eu^{3+}$ at 298 K vs 5 K ($\lambda_{em.}$ = 613 nm).

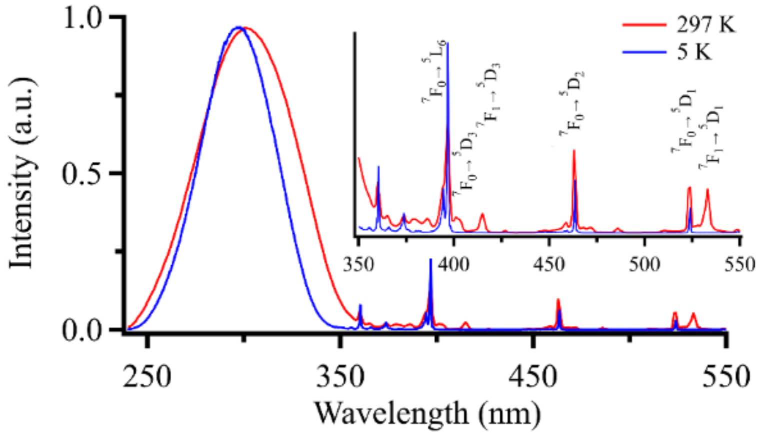

Figure S3. Excitation spectra of SA$_6$:Eu^{3+} at 298 K vs 5 K ($\lambda_{em.}$ = 613 nm).

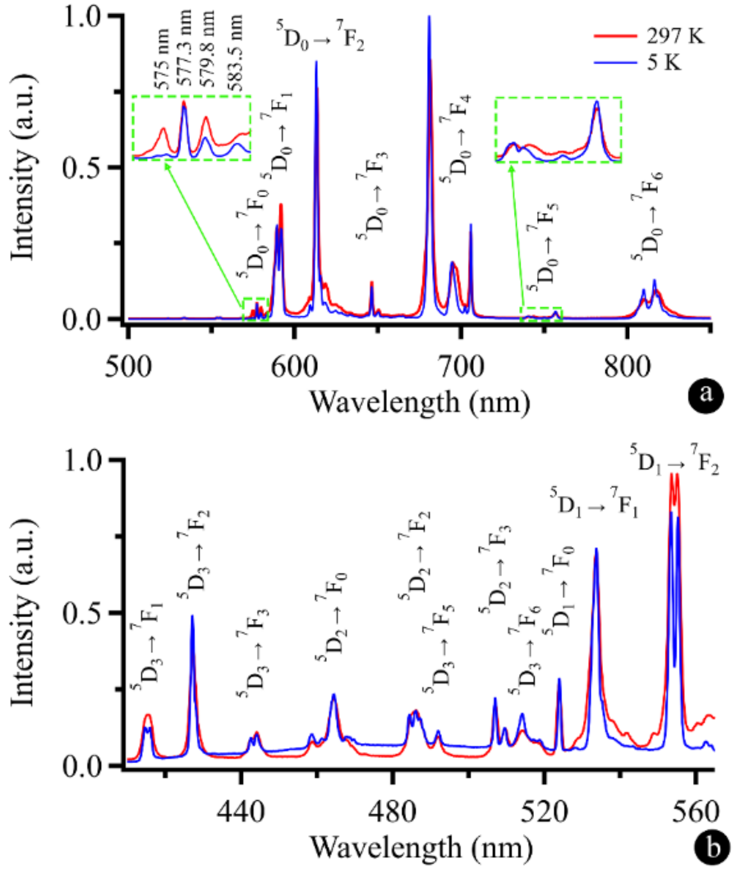

Fig S4. Emission spectra of CA$_6$:Eu^{3+} at 298 K vs 5 K [$\lambda_{exc.}$ = 300 nm (a) and 397 nm (b)].

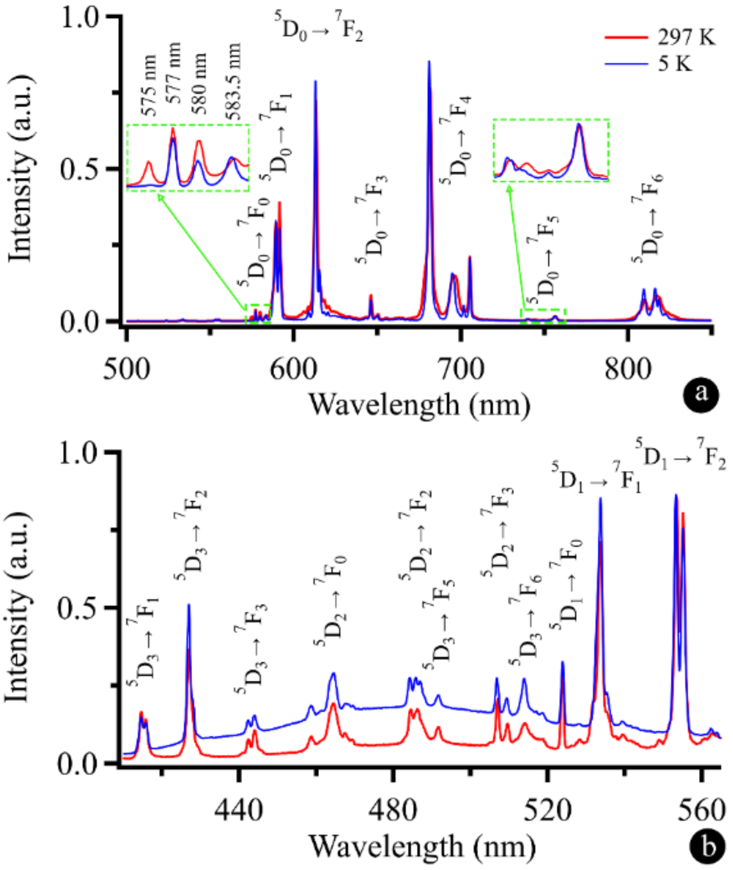

Fig S5. Emission spectra of SA$_6$:Eu^{3+} at 298 K vs 5 K [$\lambda_{exc.}$ = 300 nm (a) and 397 nm (b)].

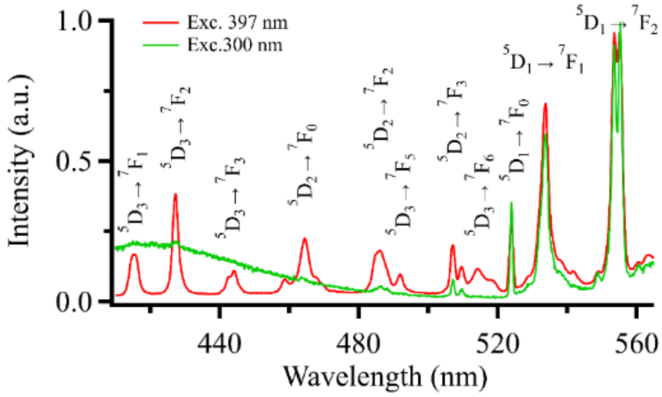

Fig S6. Comparison of the Emission of CA$_6$:Eu^{3+} from the $^5D_{1\text{-}3}$ states under excitation to the CT band (300 nm) and excitation to the $^5L_6$ state (397 nm) at 298 K.

Table S1. The experimental vs calculated energy levels of Eu^{3+} in CA_6 and SA_6 nanocrystals. The experimental error is about 15 cm/1 from the resolution of the luminescence experiments. The fifth column in the table presents the differences between the experimental and calculated values for SA_6 compound.

Energy levels	Exp. CA_6 (cm^{-1})	Exp. SA_6 (cm^{-1})	Cal. (cm^{-1})	Error (cm^{-1})
$^7F_0$	0	0	0	0
$^7F_1$	360	353	342.8	-10.2
$^7F_1$	431	417	393.2	-23.8
$^7F_1$	431	417	393.2	-23.8
$^7F_2$	1010	1010	961.4	-48.6
$^7F_2$	1077	1077	1044.5	-32.5
$^7F_2$	1077	1077	1044.5	-32.5
$^7F_2$	0	0	1063.0	
$^7F_2$	0	0	1063.0	
$^7F_3$	1850	1844	1824.6	-19.6
$^7F_3$	1850	1844	1824.6	-19.6
$^7F_3$	0	0	1832.4	
$^7F_3$	0	0	1842.0	
$^7F_3$	1951	1945	1926.1	-18.9
$^7F_3$	1951	1945	1926.1	-18.9
$^7F_3$	0	0	1986.0	
$^7F_4$	2634	2639	2615.0	-24
$^7F_4$	2634	2639	2615.0	-24
$^7F_4$	0	0	2729.8	
$^7F_4$	2930	2929	2942.2	13.2
$^7F_4$	2930	2929	2942.2	13.2
$^7F_4$	0	0	2953.3	
$^7F_4$	0	0	2953.3	
$^7F_4$	3084	3073	3143.2	70.2
$^7F_4$	3159	3149	3165.3	16.3
$^7F_5$	3805	3801	3788.9	-12.1
$^7F_5$	3810	3801	3788.9	-12.1
$^7F_5$	3851	3851	3925.4	74
$^7F_5$	3874	3874	3952.2	78.2
$^7F_5$	3874	3874	3952.2	78.2
$^7F_5$	3990	3977	4034.8	57.8
$^7F_5$	4068	4065	4131.2	66.2
$^7F_5$	4068	4065	4131.2	66.2
$^7F_5$	4110	4100	4168.4	68.4
$^7F_5$	4110	4100	4168.4	68.4
$^7F_5$	4127	4114	4183.7	69.7
$^7F_6$	4947	4947	5008.6	61.6
$^7F_6$	4974	4966	5012.4	46.4
$^7F_6$	5038	5038	5084.9	46.9
$^7F_6$	5072	5072	5094.2	22.2
$^7F_6$	5072	5072	5094.2	22.2
$^7F_6$	0	0	5113.4	
$^7F_6$	0	0	5113.4	
$^7F_6$	5106	5106	5127.7	21.7
$^7F_6$	5162	5155	5163.6	8.6
$^7F_6$	5173	5176	5187.9	11.9
$^7F_6$	5173	5176	5187.9	11.9
$^7F_6$	5250	5243	5212.4	-30.6
$^7F_6$	5250	5243	5212.4	-30.6

$^5D_0$	17323	17323	17335.1	12.1
$^5D_1$ $^5D_1$ $^5D_1$	19084 0 0	19088 0 0	19006.8 19024.7 19024.7	-81.2
$^5D_2$ $^5D_2$	21575 21575 0 0 0	21575 21575 0 0 0	21445.4 21445.4 21462.2 21462.2 21469.4	-129.6 -129.6
$^5D_3$			24305.1 24323.2 24332.3 24332.3 24346.5 24356.5 24356.5	
$^5L_6$	25189 25189 25349	25189 25189 25349	25271.5 25271.5 25370.8 25370.8 25377.0 25443.8 25535.2 25535.2 25553.3 25553.3 25603.4 25608.0 25634.5	82.5 82.5 21.8

Paper III : Peculiar emission of Eu^{3+} ion in calcium and strontium aluminates

This paper discusses the peculiar luminescence of Eu^{3+} ion identified in the amorphous phase strontium and calcium aluminate NPs. Investigating the luminescence of the Eu^{3+} ion during the amorphous to crystal phase transformation, revealed an unusual intense band at 566 nm in the spectrum of the Eu^{3+} in the amorphous phase. This band corresponded to a considerably low-lying oxygen to europium charge transfer (CT) band at 340 nm. The band at 566 nm is the highest energy ever observed for the $^5D_0 \rightarrow {}^7F_0$ transition of Eu^{3+}. We also identified a second peculiar emission in the amorphous phase at 571 nm with a corresponding CT band at 310 nm. This emission was reproduced even in different synthesis condition. In the calcium aluminate NPs the peculiar intense band appeared at 568 nm. The corresponding f-f transition appeared at relatively higher energies than the regular Eu^{3+} f-f transitions.

This paper is being further developed to understand the origin of these peculiar luminescence behavior of Eu^{3+}. We believe, this study can provide further information about the origin of previously reported the so-called “anomalous emission” of Eu^{3+}, as well as a deeper insight into the traps associated with the LPPs.

This paper is still under development.

Peculiar emission of Eu^{3+} in calcium and strontium aluminate nanoparticles

Jafar Afshani [a], Teresa Delgado [a,b], Hans Hagemann [*a]

[a] Département de Chimie Physique, Université de Genève, Quai Ernest-Ansermet 30, Genève 1211, Switzerland.

[b] Chimie ParisTech-CNRS, IRCP (PSL), 11 Rue P. et M. Curie, 75005, Paris, France

Abstract

The oxygen to Eu^{3+} charge transfer (CT) excitation band of amorphous strontium aluminate nanoparticles is observed at the remarkable low energy of about 33000 cm^{-1} (300 nm) at the emission wavelength of 613 nm ($^5D_0$-$^7F_2$ transition of Eu^{3+}). In these nanoparticles, a new strong emission band at 566 nm assigned to the $^5D_0$-$^7F_0$ emission of Eu^{3+} is observed. The corresponding excitation spectrum reveals a considerably red-shifted CT band around 340 nm (29400 cm^{-1}). These features are assigned to a peculiar Eu^{3+} species subject to significant mixing of CT and $4f^6$ states. A second peculiar emission with another low-lying corresponding CT band (32000 cm^{-1}) was further identified upon increasing the Eu^{3+} concentration. The energies of these CT bands showed an inverse relation with the energies of their corresponding intra-configuration f-f transitions. These new types of Eu^{3+} species in strontium aluminates could potentially be involved in the OSL quenching of traps postulated in the persistent phosphor $SrAl_2O_4$ and $CaAl_2O_4$.

Keywords: Anomalous emission, Eu^{3+} luminescence, Eu-O charge transfer, strontium aluminate, calcium aluminate.

Introduction

Strontium aluminates doped with rare earth ions are the subject of increasing research, which point out their great potential for many different applications [1]. In the course of our work on the synthesis of strontium aluminate nanoparticles with a precise size and shape control, we have used systematically Eu^{3+}-doped samples to document, in addition to X-ray diffraction, structural changes taking place during annealing at high temperature. We have thus obtained and characterized Eu^{3+} doped crystalline $SrAl_{12}O_{19}$ nanoparticles [2].

Eu^{3+} is known for its red luminescence originating from the $^5D_0$ excited state to the ^7F_J (J = 0 - 6) ground configuration [3]. However, only the usually most intense $^5D_0 \rightarrow {}^7F_2$ transition is responsible for this red luminescence, whereas the rest are normally very weak. Nevertheless, the intra-configurational f-f transitions of Eu^{3+} are sensitive to the local symmetry and coordination of the Eu^{3+} ion. For instance, although the $^5D_0 \rightarrow {}^7F_0$ transition is forbidden by the Jude-Ofelt theory, it can be observed in compounds where the Eu^{3+} ion occupies a C_s, C_n, or C_{nv} symmetry [3]. The intensity of the magnetic dipole $^5D_0 \rightarrow {}^7F_1$ transition is to a large extent independent of the Eu^{3+} environment [4], whereas the $^5D_0 \rightarrow {}^7F_2$ transition is called a "hyper-sensitive" transition due to its dramatic changes in different Eu^{3+} environments [5, 6]. In some compounds, the $^5D_0 \rightarrow {}^7F_4$ transition was observed to be dominant [2]. These features, in addition to the non-degeneracy of the $^5D_0 \rightarrow {}^7F_0$ transition, the lack of overlap between the emission bands of Eu^{3+} ion, and the simplicity of their interpretation have, indeed made the trivalent europium a great spectroscopic tool for studying structural properties of different solids including crystals, glasses, and solid solutions.

Long persistent phosphors (LPPs) are solid compounds consisting of an inorganic host and one or more luminescent activators [7]. As their name implies, these materials can keep luminescing for a long time (in some cases hours and days) after ceasing the irradiation source. Their long luminescence is associated with defects inside the crystalline host. The nature of these defects, which are commonly referred to as "traps" remains still under debate. $SrAl_2O_4$ and $Sr_4Al_{14}O_{25}$ co-doped with Eu^{2+} and Dy^{3+} are the best performing LPPs in the green and blue emission range, respectively. In this sense, $SrAl_2O_4$ has been studied extensively [8] and many studies have also been conducted on $Sr_4Al_{14}O_{25}$ [9-11].

In this work, we study systematically the evolution of the spectra of Eu^{3+} during different steps of the strontium and calcium aluminate nanoparticles synthesis and show evidence for a new Eu^{3+} species, which appears reproducibly, not only in amorphous strontium aluminates, but in amorphous calcium aluminates as well.

Experimental

Materials

Strontium nitrate and calcium nitrate (99+% ACS reagent), aluminum nitrate nonahydrate (99+%), and urea (99.5%) were purchased from Acros Organics. Europium nitrate pentahydrate (99.9% trace metal basis) and polyvinylpyrrolidone (PVP) (M.W. 58000) were purchased from Sigma Aldrich and Fluka, respectively. Absolute ethanol (99.8%) was supplied by Fisher Scientific.

Instruments

A Teflon-lined stainless-steel autoclave was used for the solvothermal synthesis of the strontium and calcium aluminate precursor nanoparticles (NPs). The annealing process was performed in a Carbolite tube furnace. The X-ray powder diffraction (XRD) data were collected on a PANalytical X'pert Pro MPD (Cu Kα = 1.5406 Å).

A Horiba Jobin Yvon Fluorolog 3-22, equipped with a photo multiplier tube (PMT) detector was used to obtain the photoluminescence spectra. A closed-cycle Janis-Sumitomo SHI-4.5 cryostat equipped with a programmable temperature controller (Lakeshore Model 331) was used for the luminescence measurements at 5 K. Both excitation and emission slits for all luminescence measurements were set to 0.5 nm.

Synthesis of strontium aluminate nanoparticles doped with Eu^{3+}

A solvothermal reaction was used to obtain the precursor NPs [12]. 0.212 g $Sr(NO_3)_2$ (1mmol), 0.750 g $Al(NO_3)_3$ (2mmol) and 0.01 g $Eu(NO_3)_3$ (3 molar percent with respect to Sr) salts along with 0.8 g urea were dissolved in 2 ml of distilled water. In the next step, 0.8 g PVP were added as a capping agent to the solution which was later mixed with 20 ml of EtOH. The solution was left at 150 °C for 2 h in a Teflon reactor confined in an autoclave. After cooling the reactor down to room temperature, the product was centrifuged and washed with EtOH. About 0.1 g of a white powder was obtained which was dried in air.

The obtained powder was ground to reduce the surface contact between the nanoparticles and minimize their aggregation at annealing temperatures. After heating the powder at 150 °C for 1 h to remove the physisorbed water and other volatiles, the powder was calcined at 600 °C for 5 h to remove the organic linkers and surfactants off the nanoparticles. The furnace was cooled down to room temperature and the calcined product was divided into two portions. These portions were annealed at 1100 °C (10 minutes) and 1150 °C (3 h), respectively.

The present synthesis method has been optimized and the synthesis mechanism as well as a thorough characterization of the prepared NPs is presented elsewhere [13].

Result and discussion

Characterization

Powder XRD analysis of the $SrAl_xO_y:Eu^{3+}$ nanoparticles annealed at two different temperatures are presented in Figure 1. The nanoparticles annealed at 1100 °C show weak lines which are assigned to the $SrAl_2O_4$ phase superimposed on a broad background. This indicates that the sample is mainly amorphous. Annealing these particles at 1150 °C for 3 h improved the crystallinity, and the $SrAl_2O_4$ phase transformed into $SrAl_{12}O_{19}$ phase. Nevertheless, the remaining broad background in the pattern suggests that there is still an amorphous phase present in the sample. It must be noted that the Sr:Al ratio of 1:12 of the crystalline strontium aluminate in the final product is much lower than the 1:2 ratio of the metal salts used in the reaction batch. The TEM images of the precursor and the annealed NPs are presented in Figure S1.

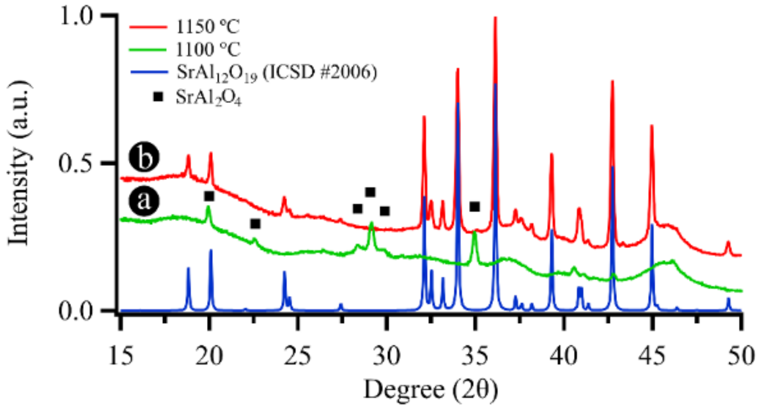

Figure 1. Powder XRD pattern for strontium aluminate nanoparticles annealed at a) 1100 °C for 10 minutes and b) 1150 °C for 3 h.

Luminescence studies

Figure 2 presents the luminescence of Eu^{3+}-doped strontium aluminate NPs calcined at 600 °C as well as those of the annealed ones at 1100 and 1150 °C. A typical emission spectrum of Eu^{3+} was obtained for all three samples under excitation at 393 nm, where Eu^{3+} is known to absorb strongly. The characteristic Eu^{3+} emission bands are all observed at 578, 590, 613, 655, and 700 nm. These bands originate from the intra-configurational $^5D_0\rightarrow{}^7F_{0-4}$ transitions, respectively. The $^5D_0\rightarrow{}^7F_2$ transition normally generates the most intense band in the Eu^{3+} spectra [3] as it is observed here under excitation at 393 nm. Surprisingly, under 340 nm excitation, an unusually intense band was observed at 566 nm (17670 cm^{-1}) for the sample annealed at 1100 °C. This band is absent in the spectra obtained for the samples annealed at 600 and 1150 °C. This intense band lies at a much higher energy (17670 cm^{-1}) than the typical $^5D_0\rightarrow{}^7F_0$ transition (≈17300 cm^{-1} [3]) of Eu^{3+} ion, even compared to the so-called anomalous emission of Eu^{3+} (≈17500 cm^{-1} [14]). Furthermore, another new emission band was observed at 641 nm for the sample annealed at 1100 °C under excitation at 340 nm. This band is located about 12 nm higher in energy than the $^5D_0\rightarrow{}^7F_3$ transition obtained under 393 nm excitation.

For the sample annealed at 1150 °C, the doublet band at 589 and 591 nm and a sharp singlet band at 613 nm observed under 340 nm excitation correspond to the $^5D_0\rightarrow{}^7F_1$ and $^5D_0\rightarrow{}^7F_2$ emissions of Eu^{3+} in the $SrAl_{12}O_{19}$ crystalline phase, respectively [2]. The emission spectrum excited at 393 nm corresponds thus to the Eu^{3+} ions in the amorphous phase.

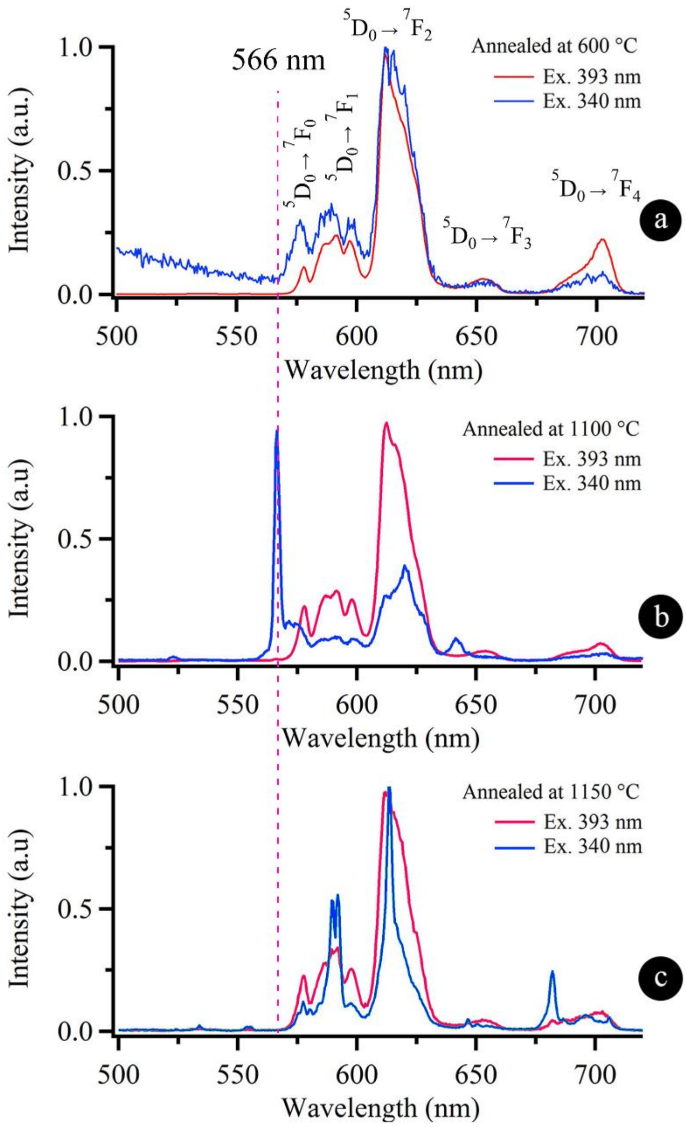

Figure 2. Emission spectra of the strontium aluminate nanoparticles annealed at a) 600 °C, b) 1100 °C, and c) 1150 °C.

The excitation spectra of the NPs annealed at 1100 °C and 1150 °C observed at 613 nm (Figure 3), show a typical oxygen to Eu^{3+} charge transfer (CT) band peaking at around 250 nm in the case of the sample annealed at 1100 °C (a) [15]. For Eu^{3+} in $SrAl_2O_4$, this band is observed around 265 nm at 5 K (see Figure S2) [15]. The sharp bands at 530, 464, 413, and 393 nm are assigned to the intra-configurational $^7F_0 \rightarrow {}^5D_{1-3}$ and $^7F_0 \rightarrow {}^5L_6$ transitions, respectively. The CT band at 300 nm observed in the case of the sample annealed at 1150 °C (b) also agrees with the previous report for Eu^{3+} ion in the $SrAl_{12}O_{19}$ crystal [16]. The spectrum monitored at 566 nm (Fig 3a), revealed a CT band at an unusual low energy of about 29400 cm^{-1}. The sharp emission bands in the spectrum lying at slightly higher energies relative to the above-mentioned $^7F_0 \rightarrow {}^5D_{1-3}$ transitions, suggests that this CT band, and hence the intense emission band at 566 nm correspond to a Eu^{3+} ion experiencing a totally different environment in the NPs.

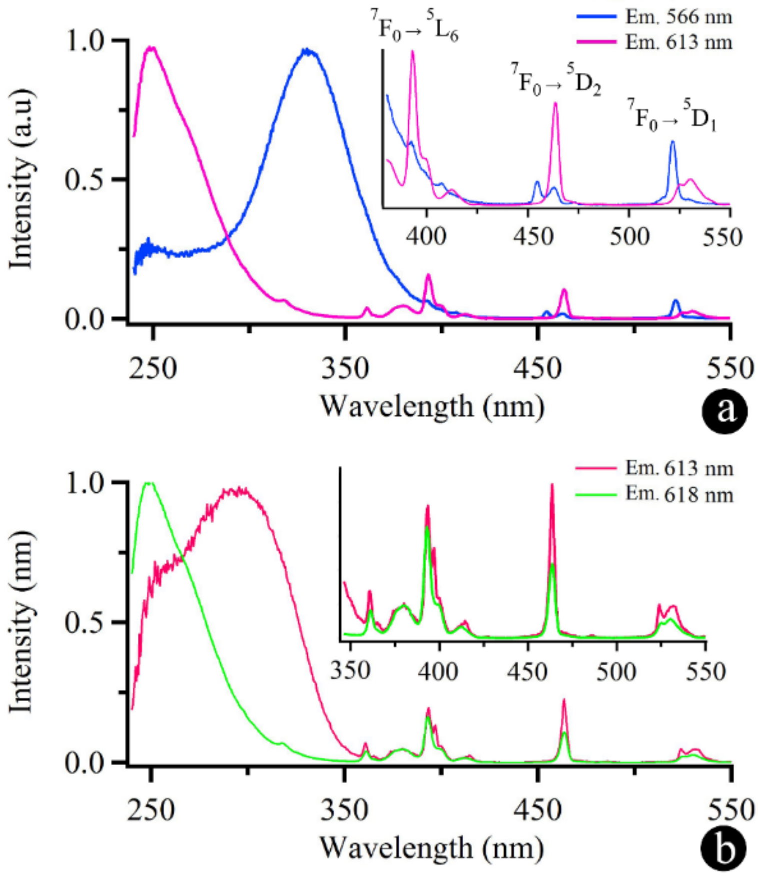

Figure 3. Excitation spectra of the nanoparticles annealed at a) 1100 °C observed for the emissions at 566 nm and 613 nm and b) 1150 °C for the emissions at 613 nm and 618 nm.

To further examine these observations, Eu^{3+}-doped strontium aluminate as well as calcium aluminate (CA:Eu^{3+}) NPs with a relatively higher ratio of $Sr(Ca)^{2+}$:Al^{3+} were prepared. To obtain this higher ratio, the reaction mixture was diluted by a factor of three and the total PVP:metal-ions ratio was reduced by a factor of two. These particles were annealed at different temperatures in between 900 and 1100 °C. The powder-XRD data show the formation of $CaAl_2O_4$ and $SrAl_2O_4$ phases at 900 °C (Figure 4). At 1000 °C both these phases grow bigger and at 1100 °C, $CaAl_2O_4$/ $CaAl_4O_7$ and $SrAl_2O_4$/ $Sr_4Al_{14}O_{25}$ mixed-phase compounds are obtained. The diffraction patterns show that the crystallinity of both compounds enhances by increasing the annealing temperature. Nonetheless, in all samples amorphous phases exist.

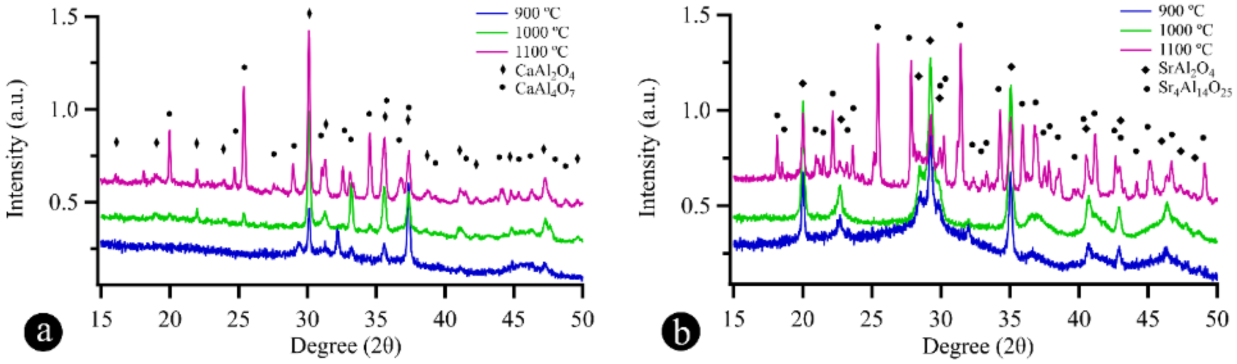

Figure 4. Powder-XRD diffraction patterns of a) CA:Eu^{3+}(2%) and b) SA Eu^{3+}(2%) NPs annealed at different temperatures for 1.5 h.

Excitation and emission spectra of the calcium and strontium aluminate NPs samples doped with Eu^{3+}(2%) annealed at different temperature are presented in Figure 5. These spectra reveal that these peculiar Eu^{3+} species are also obtained under different synthesis conditions as well as different Sr^{2+}:Al^{3+} ratios. The low-lying oxygen to europium CT band can be observed in the excitation spectra of both calcium aluminate and strontium aluminate, monitored at 566 nm (Figure 5a,c). However, these bands appear at 325 nm, which is 15 nm higher in energy compared to the spectrum presented in Figure 3. The regular oxygen to europium CT band is evident in both figures as a shoulder. For the CA:Eu^{3+} NPs, the ratio of the low-lying CT band relative to the regular CT, increases as a function of the annealing temperature from 900 to 1100 °C. On the other hand, for the SA:Eu^{3+} NPs, this ratio increases with increasing the annealing temperature from 900 to 1000 °C, and then decreases following increasing the annealing temperature to 1100 °C.

The singlet intense band is observed for CA:Eu^{3+} at 568 nm, while it appears once again, at 566 nm for the SA:Eu^{3+} NPs. This shows that, the nature of the neighboring cation has an impact on the energy of this transition of the Eu^{3+} ion. The intensity of this band follows exactly the same trend as described previously for its corresponding CT band for each one of the two compounds. This further confirms that, the unusual intense band at 568 nm is closely associated the low-lying CT band. Moreover, an additional unexpected band emerged at 637 nm in the emission spectrum of CA:Eu^{3+}, which is too high in energy to belong to a classic $^5D_0 \rightarrow {}^7F_3$ transition. Its energy is on the other hand, too low to originate from a typical $^5D_0 \rightarrow {}^7F_2$ transition. Similar to the CT band, the intensity of this band follows the intensity of the singlet intense band at 568 nm. This band appears at 641 nm for the SA:Eu^{3+} NPs. It is possible to presume that, this band would appear at relatively higher energies for the later NPs, considering the larger blue-shift of the intense $^5D_0 \rightarrow {}^7F_0$ transition, as well as those of the f-f transitions in the excitation spectra of the SA:Eu^{3+} NPs. Therefore, these bands at 637 and 641 nm for the CA:Eu^{3+} and SA:Eu^{3+} NPs, respectively, probably originate from the $^5D_0 \rightarrow {}^7F_2$ transition with a huge CF splitting.

For the SA:Eu^{3+} annealed at 1100 °C, another unusual intense band emerges at 652 nm, where the $^5D_0 \rightarrow {}^7F_3$ normally takes place. Similar to the $^5D_0 \rightarrow {}^7F_0$, this transition is forbidden within the framework of the Jude Ofelt-theory. Hence, only in exceptional cases [17] it appears to some extent intense. An intense $^5D_0 \rightarrow {}^7F_3$, is usually associated with the J-mixing [18]. However, unlike the band at 641 nm and the CT band, the intensity of this transition does not follow the intensity of the anomalous $^5D_0 \rightarrow {}^7F_0$.

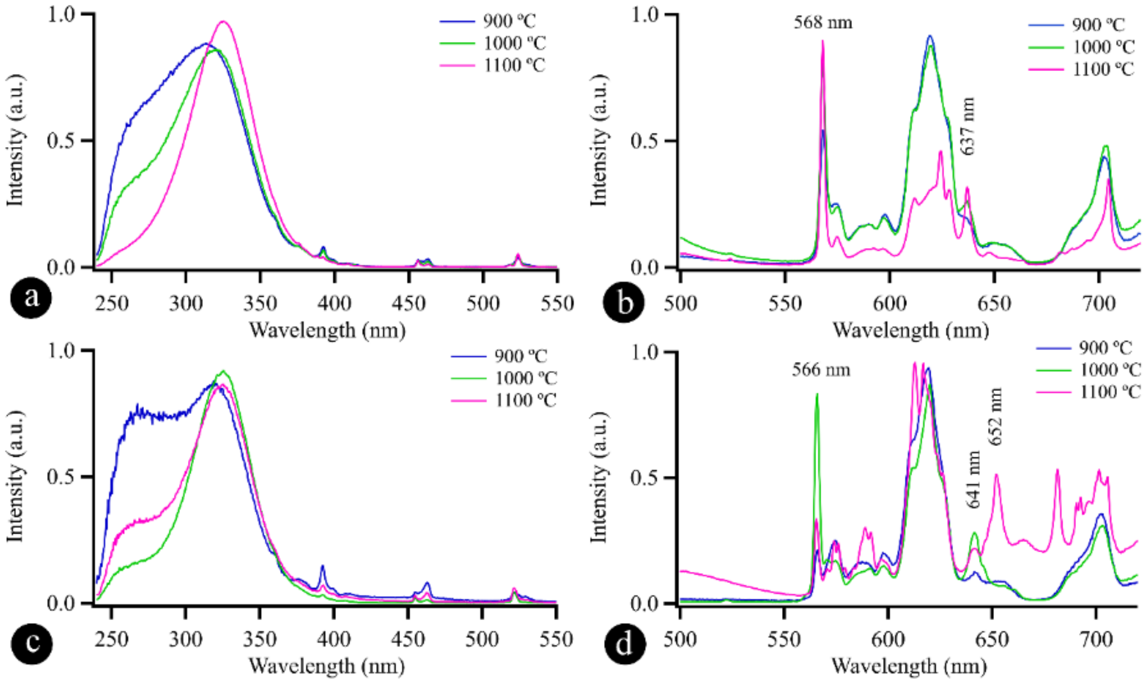

Figure 5. Excitation spectra of a) CA:Eu^{3+}(2%) and c) SA Eu^{3+}(2%) NPs observed at 568 and 566 nm, respectively. Emission spectra of b) CA:Eu^{3+}(2%) and d) SA Eu^{3+}(2%) NPs excited at 340 nm.

Eu^{3+} doped strontium aluminate NPs with higher nominal Eu^{3+} concentration (5%) were prepared to investigate the effect of concentration on the peculiar luminescence of the NPs. The emission spectrum excited at 340 nm revealed an additional relatively intense band at 571 nm (Figure 6). The corresponding CT band at 310 nm (Figure 7) suggested the presence of a second specific species.

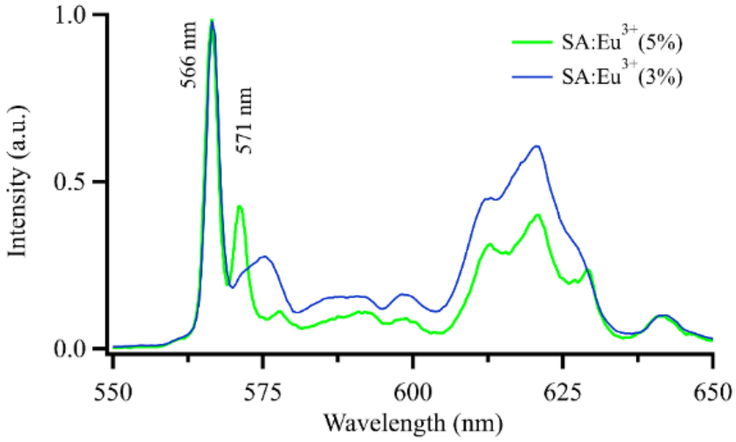

Figure 6. Room temperature emission spectra of the strontium aluminate nanoparticles doped with 3% and 5% Eu^{3+} (Both excited at 347 nm). Both compounds were annealed at 1100 °C for 10 minutes.

The excitation spectra obtained at 5 and 298 K are shown in Figure 7 for the SA:Eu^{3+}(5%) NPs. In both temperatures, the spectra were monitored at the three different emissions identified before. At 298 K, the CT bands corresponding to the 613, 571 and 566 nm emission wavelengths were observed at 250, 300 and 340 nm, respectively. At 5 K, the positions of these bands remained almost the same except for a 10 nm blue-shift for the spectrum observed at 571 nm. The intra-configurational f-f transitions, on the other hand, grow much stronger at 5 K in the spectra observed at 566 and 571 nm. A trend is observed between the energies of the CT bands and the energies of the f-f transitions. As the CT shifts to the lower energy, the $^7F_0 \rightarrow {}^5D_{1-3}$ bands shift towards the higher energies. This shift is in particular obvious for the $^7F_0 \rightarrow {}^5D_2$ transition which appears at 464 to 458.5 and 454.5 nm for the spectra monitored at 613, 571, and 566 nm, respectively. This probably rises from the higher magnitude of the mixing between the CT band with the $^5D_{0-3}$ excited states, as the CT band shifts to the lower energies.

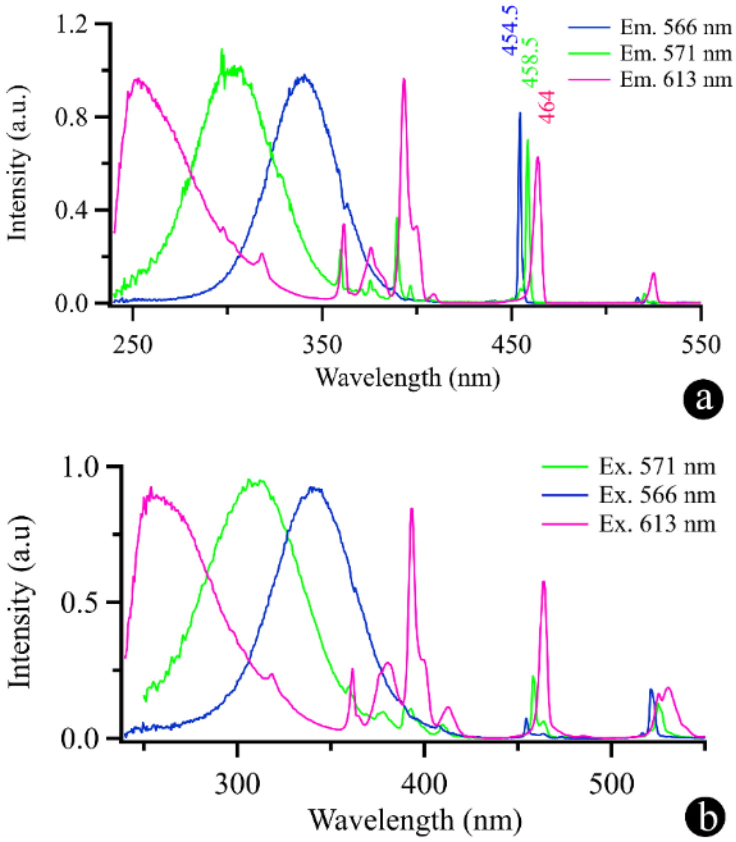

Figure 7. Excitation spectra of the SA:Eu^{3+}(5%) at different emission wavelengths at a) 5K and b) 298 K.

At 5 K, three entirely different emission spectra were obtained under excitation to the different $^7F_0 \rightarrow {}^5D_2$ transitions observed (Figure 8). A small band can be observed at 523 nm when exciting at 454.5 nm. This band originates from the $^5D_1 \rightarrow {}^7F_0$ transition. It is absent in the spectrum obtained at 458 nm. This can be due to the concentration quenching as it was already shown that the intensity of the band at 571 nm increasing by increasing the Eu^{3+} concentration. It can in turn suggest that, the green trace in the figure, originates from a site with neighboring Eu^{3+} ions, while the blue trace comes from a site with a single Eu^{3+} ion. This agrees with the previous $^7F_0 \rightarrow {}^5D_0$ transition observed for CA:Eu^{3+} (568 nm) at a different energy than that of the SA:Eu^{3+} (566 nm). This can be related to the electropositivity of the neighboring metal ion, since it can contribute to the delocalization of electrons of the bridging oxygen more onto the Eu^{3+} ion.

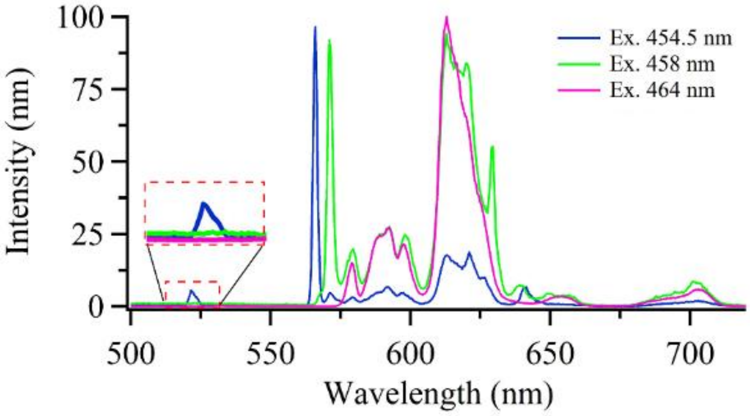

Figure 8. Emission spectra of SA:Eu^{3+}(5%) at different excitation wavelengths at 5 K.

Mechanism

Chen and Liu [14] introduced in 2005 the concept of anomalous Eu^{3+} spectra, which are characterized by a strong $^5D_0 - {}^7F_0$ emission band. This band has typically more than twice the intensity of the magnetic dipole allowed $^5D_0 - {}^7F_1$ emission band.

E. Zych et al. [19] observed two different emission spectra for Eu^{3+} in the Sr_2GeO_4 host. They reported a second CT band at 330 nm, in addition to the regular CT for Eu-O at 250 nm. The former CT band was attributed to the interstitial oxygen located in the first coordination sphere of the Eu^{3+} ion. This oxygen, supposedly binds only to the Eu^{3+} ion, facilitating the energy transfer compared to the bridging oxygen in the host framework.

Anomalously intense $^5D_0 \rightarrow {}^7F_0$ transition can appear in the so-called charge-unbalanced materials, where oxygen-compensating sites are likely to appear. Liu et al [20] reported an unusual emission for Dy^{3+} and a low lying CT band at around 300 nm for Eu^{3+} in $Mg_3F_3BO_3$ structure . Later, D. Van Der Voort and G. Blasse [21] prepared the same compound doped with Pr^{3+}, Gd^{3+}, Eu^{3+}, and Dy^{3+} ions, individually. In addition to witnessing the same anomalous spectra for Dy^{3+} and Eu^{3+}, they noticed unusual changes in the emission spectra of the two other ions, as well. The authors attributed the line observed at 614.5 nm to the hypersensitive $^4I_{15/2} \rightarrow {}^6H_{11/2}$ transition of Dy^{3+}. Their explanation included a thermal population, since the $^4I_{15/2}$ level lies above the $^4F_{9/2}$ level. D. Van proved this explanation wrong buy recording the emission spectrum at 4 K, where relative intensity of the peculiar emission remained almost unchanged.

For the Eu^{3+}-doped $Mg_3F_3BO_3$ compound [21], a sharp strong emission band was observed at 567.7 nm as well as a low-lying CT band at 300 nm. The authors assigned the CT band to the presence of a Eu-O center, where the oxygen atom is bound only to the europium and not to the boron.

According to the Judd-Ofelt theory, the f-f transitions of Eu^{3+} borrow the intensity from the intermediate CT state. This results in the mixing of the $4f^6$ excited states with the CT state with the opposite parity through interaction of odd CF or vibrational modes. It is believed that the CT states are closely related to the anomalous crystal field spectra. Therefore, CT-induced f-electron delocalization or covalency might significantly influence the energy levels of Eu^{3+} in solids [14]. This can be the reason why we see a shift of up to 12 nm between the typical an anomalous $^5D_0 \rightarrow {}^7F_0$ transitions.

Blass and Nieuwpoort [22] realized that the linear CF parameter, might significantly contribute to the strength of 0-0 and 0-2 transitions. Later, Wybourne [23] suggested a mechanism involving the spin-orbit interaction in the excited state configuration to include in the third-order ED contribution. By considering the intermediate CT state, the intensity of the 0-0 transition may be derived using the following semi-quantitative expression:

$$I(^5D_0 \rightarrow {}^7F_0) \ \alpha \ \frac{S_1^2}{\Delta_{CT}^4}$$

$$S_1 = \left(\frac{1}{3} \sum_{q=0,\pm 1} \left| A_{1q} \right|^2 \right)^{1/2}$$

where, Δ_{CT} is the peak position of the lowest CT band, S_1 is the scalar linear CF rotational invariant, and A_{1q} are the linear CF components, respectively. Thus, in the systems with small energy gap between the 4f and the CT states, strength of the $^5D_0 \rightarrow {}^7F_0$ transition can be influenced remarkably in the presence of even a small linear CF term in the CF Hamiltonian.

Conclusion

The present results show that in Sr-rich amorphous strontium aluminates, peculiar Eu^{3+} ions with probably a very strong europium-oxygen bond are formed. These species present a very low energy oxygen to Eu^{3+} charge transfer band. Considering the observation of detrapping by near UV light in the persistent phosphor $SrAl_2O_4:Eu^{2+}, Dy^{3+}$ [24], it is possible that this type of peculiar europium is at the origin of this detrapping in this type of LPPs. Despite changing the synthesis conditions and the Sr^{2+}/Al^{3+} ratio in the prepared NPs, the peculiar emission was observed. This emission was also detected in calcium aluminate NPs, where the intense $^5D_0 \rightarrow {}^7F_0$ transition appeared at a slightly lower energy. Finally, increasing the Eu^{3+} concentration gave rise to another, however, less intense peculiar emission. Moreover, the energies of the f-f transitions increased as the CT band shifted to lower energies.

Acknowledgment

This work was supported by the Swiss National Science Foundation (projects 200020_182494, 200021_169033 and P400P2_191108/1).

References

[1] H. Hagemann, J. Afshani, Chapter 321: Synthesis, luminescence and persistent luminescence of europium-doped strontium aluminates, Handbook on the Physics and Chemistry of Rare Earths, Elsevier, Vol 60 (2021) p.163-225, ISSN 0168-1273, https://doi.org/10.1016/bs.hpcre.2021.06.001.

[2] J. Afshani, T. Delgado, Gh. Paveliuc, H. Hagemann, Luminescence spectroscopy of $CaAl_{12}O_{19}:Eu^{3+}$ and $SrAl_{12}O_{19}:Eu^{3+}$ nanoparticles Journal of Luminescence, Submitted paper.

[3] K. Binnemans, Interpretation of europium (III) spectra, Coordination Chemistry Reviews, 295 (2015) 1-45.

[4] C. Görller-Walrand, K. Binnemans, Spectral intensities of ff transitions, Handbook on the physics and chemistry of rare earths, 25 (1998) 101-264.

[5] Q. Long, Y. Xia, Y. Huang, S. Liao, Y. Gao, J. Huang, J. Liang, J. Cai, Na^+ induced electric-dipole dominated transition ($^5D_0 \rightarrow {}^7F_2$) of Eu^{3+} emission in $AMgPO_4:Eu^{3+}$ (A= Li^+, Na^+, K^+) phosphors, Materials Letters, 145 (2015) 359-362.

[6] A. Kostyukov, V.N. Snytnikov, V.N. Snytnikov, A. Ishchenko, M. Rakhmanova, M. Molokeev, A. Krylov, A. Aleksandrovsky, Luminescence of monoclinic Y_2O_3:Eu nanophosphor produced via laser vaporization, Optical Materials, 104 (2020) 109843.

[7] J. Xu, S. Tanabe, Persistent luminescence instead of phosphorescence: History, mechanism, and perspective, Journal of Luminescence, 205 (2019) 581-620.

[8] R.E. Rojas-Hernandez, F. Rubio-Marcos, M.Á. Rodriguez, J.F. Fernandez, Long lasting phosphors: $SrAl_2O_4$:Eu,Dy as the most studied material, Renewable and Sustainable Energy Reviews, 81 (2018) 2759.

[9] M. Peng, Z. Pei, G. Hong, Q. Su, Study on the reduction of $Eu^{3+} \rightarrow Eu^{2+}$ in $Sr_4Al_{14}O_{25}$:Eu prepared in air atmosphere, Chemical Physics Letters, 371 (2003) 1-6.

[10] Z.-X. Yuan, C.-K. Chang, D.-L. Mao, W. Ying, Effect of composition on the luminescent properties of $Sr_4Al_{14}O_{25}:Eu^{2+},Dy^{3+}$ phosphors, Journal of Alloys and Compounds, 377 (2004) 268-271.

[11] M. Chithambo, Thermal assistance in the optically stimulated luminescence of superluminous $Sr_4Al_{14}O_{25}:Eu^{2+},Dy^{3+}$, Physica B: Condensed Matter, 603 (2021) 412722.

[12] H.G. Yang, G. Liu, S.Z. Qiao, C.H. Sun, Y.G. Jin, S.C. Smith, J. Zou, H.M. Cheng, G.Q. Lu, Solvothermal synthesis and photoreactivity of anatase TiO2 nanosheets with dominant {001} facets, Journal of the American Chemical Society, 131 (2009) 4078-4083.

[13] J. Afshani, T. Delgado, C. Besnard, Y. Sadian, H. Hagemann, Unpublished data, (2021).

[14] X. Chen, G. Liu, The standard and anomalous crystal-field spectra of Eu^{3+}, Journal of Solid State Chemistry, 178 (2005) 419-428.

[15] J. Bierwagen, T. Delgado, J. Afshani, S. Yoon, N. Gartmann, B. Walfort, H. Hagemann, Observation of multiple sites for trivalent europium ions in $SrAl_2O_4$, Journal of Luminescence, 239 (2021) 118348.

[16] S. Chawla, A. Yadav, Role of valence state of dopant (Eu^{2+}, Eu^{3+}) and growth environment in luminescence and morphology of SrAl12O19 nano-and microcrystals, Materials Chemistry and Physics, 122 (2010) 582-587.

[17] A.F. Kirby, F. Richardson, Detailed analysis of the optical absorption and emission spectra of europium (3+) in the trigonal (C_3) $Eu(DBM)_3.H_2O$ system, The Journal of Physical Chemistry, 87 (1983) 2544-2556.

[18] J. Lowther, Spectroscopic transition probabilities of rare earth ions, Journal of Physics C: Solid State Physics, 7 (1974) 4393.

[19] K. Fiaczyk, E. Zych, On peculiarities of Eu^{3+} and Eu^{2+} luminescence in Sr_2GeO_4 host, RSC Advances, 6 (2016) 91836-91845.

[20] X. Liu, Y. Zhang, Z. Wang, S. Lu, Luminescence and charge transfer bands of the Sm (3+) and Eu (3+) in $Mg_3BO_3F_3$, Journal of Luminescence, 40 (1988) 885-886.
[21] D. Van der Voort, G. Blasse, Anomalous rare-earth emission in magnesium fluoroborate, Journal of Physics and Chemistry of Solids, 52 (1991) 1149-1154.
[22] G. Blasse, A. Bril, W. Nieuwpoort, On the Eu^{3+} fluorescence in mixed metal oxides: Part I—The crystal structure sensitivity of thr intensity ratio of electric and magnetic dipole emission, Journal of Physics and Chemistry of Solids, 27 (1966) 1587-1592.
[23] B. Wybourne, Effective operators and spectroscopic properties, The Journal of Chemical Physics, 48 (1968) 2596-2611.
[24] D. Van der Heggen, J.J. Joos, P.F. Smet, Importance of evaluating the intensity dependency of the quantum efficiency: impact on LEDs and persistent phosphors, ACS Photonics, 5 (2018) 4529-4537.

Supplementary Information

Peculiar emission of Eu^{3+} in calcium and strontium aluminate nanoparticles

Jafar Afshani [a], Teresa Delgado [a,b], Hans Hagemann *[a]

[a] Département de Chimie Physique, Université de Genève, Quai Ernest-Ansermet 30, Genève 1211, Switzerland.

[b] Chimie ParisTech-CNRS, IRCP (PSL), 11 Rue P. et M. Curie, 75005, Paris, France

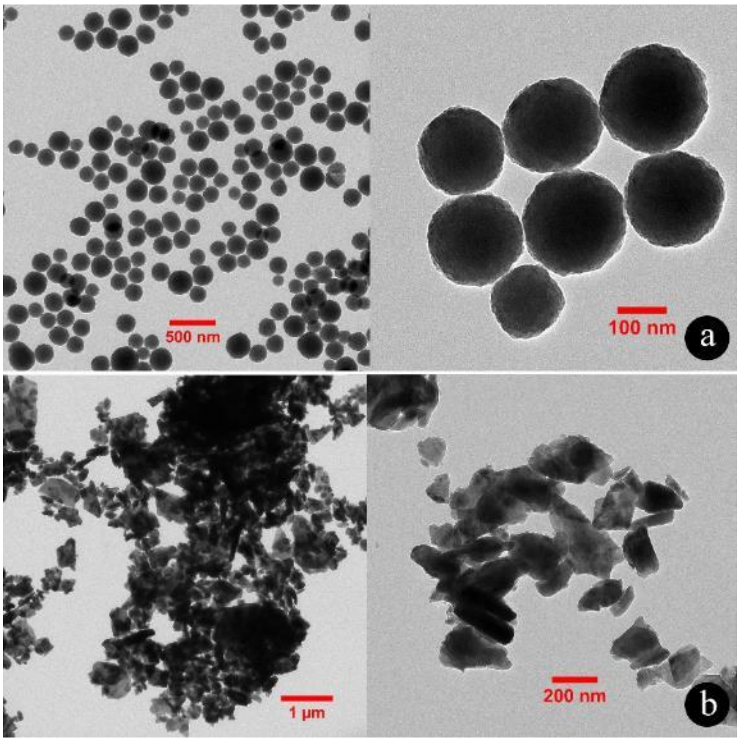

Figure S1. TEM images of SA:Eu^{3+} NPs a) precursor and b) annealed at 1150 °C.

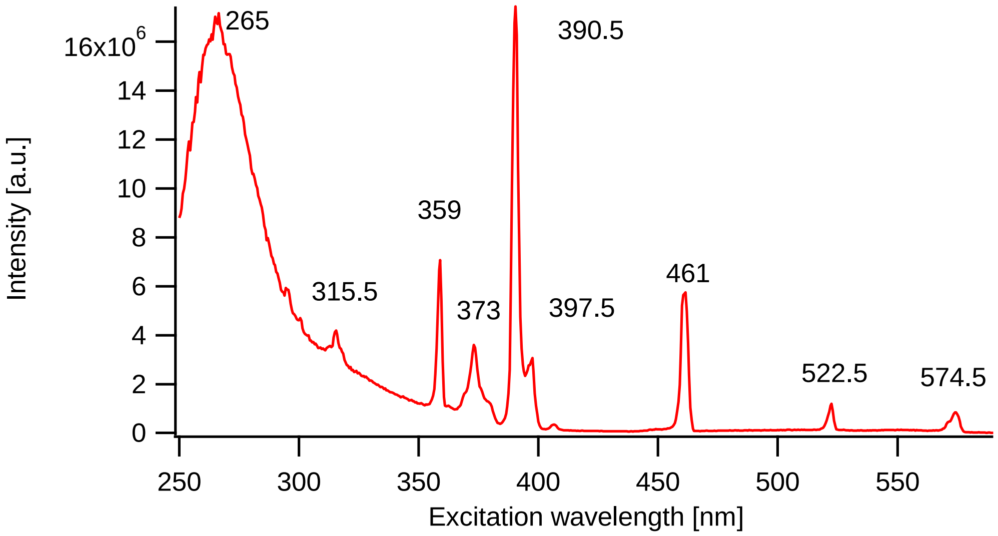

Figure S2: 5K excitation spectrum observed at 611 nm of crystalline $SrAl_2O_4$. Data taken from ref [16]:

Additional results from ongoing research

For systems like SrO-Al_2O_3 family with a complex phase diagram, it's not easy to obtain a pure crystalline phase since their synthesis involves different metal precursors. On the other hand, the afterglow properties of the long persistent phosphors (LPPs) such as $SrAl_2O_4$:Eu^{2+},Dy^{3+} is closely associated to the presence of the defects in their crystal structures. Understanding the crystallization process is prerequisite for designing and developing novel experimental strategies to gain control over the process and obtain pure-phase crystals. On the other hand, it can show the path to obtain either defect-free crystals or in contrast to introduce more defects into the lattice.

Crystallization phenomena are central to many processes in chemistry, material science, and biology. Beyond MO-Al_2O_3 systems, a wide variety of materials extending from inorganic to organic and biological crystals undergo an amorphous to crystalline transformation. Different techniques have been used for studying this process including nuclear magnetic resonance (NMR), transmission electron microscopy (TEM), and x-ray diffraction (XRD), mapping, and FT-IR and Raman spectroscopy. XRD is the main tool to study the crystallinity of nanoparticles. However, it can present only a global picture of compound and does not provide local and microscopic information. TEM, on the other hand, can be used for very small crystals and it can provide information about the local geometry and crystallite size in a single particle in real space. Electron diffraction can be used for the phase identification. TEM is indispensable for characterization of nanosized crystals, in particular when particle shape is the interest of the study.

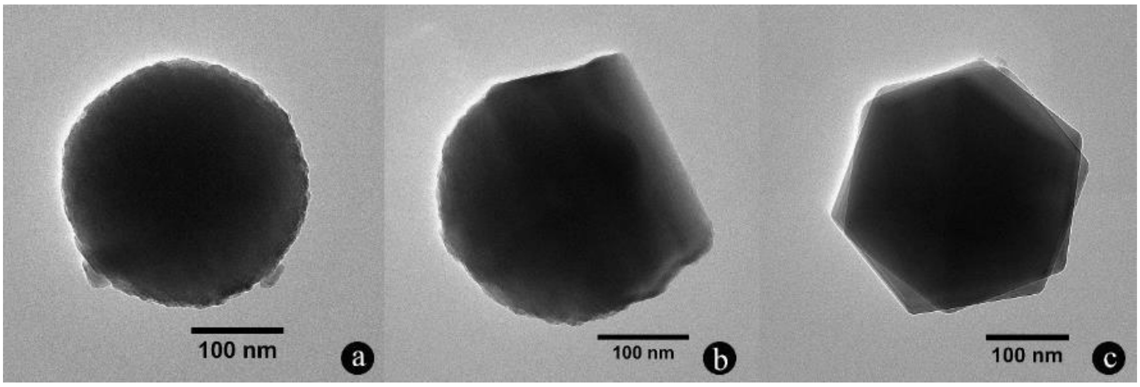

Figure 1. Shape transformation of amorphous spherical precursor SA_6:Eu^{3+} NPs to crystalline hexagonal NPs.

By optimization of the synthesis method presented in the “Paper I”, we successfully prepared $SrAl_2O_4:Eu^{2+},Dy^{3+}$ and $CaAl_2O_4:Eu^{2+}$ LPP NPs (Figure 2). We’re further optimizing the synthesis method to present a general method for the preparation of SrO-Al_2O_3 and CaO-Al_2O_3 compound with the desired $Sr(Ca)^{2+}:Al^{3+}$ ratio.

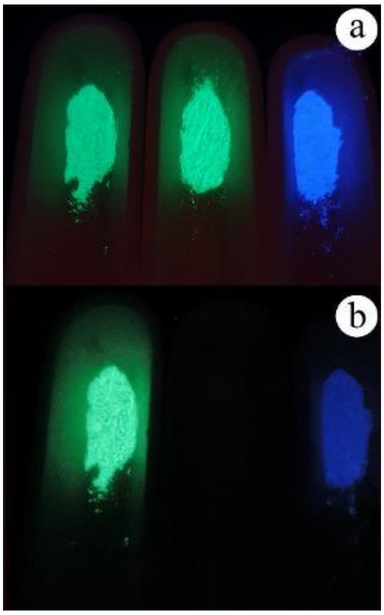

Figure 2. From left to right, $SrAl_2O_4:Eu^{2+},Dy^{3+}$ (Sample A145), $SrAl_2O_4:Eu^{2+}$ (Sample A148), $CaAl_2O_4:Eu^{2+}$ (Sample A149) NPs annealed at 1000 °C, under a) irradiation with a UV lamp, b) without irradiation.

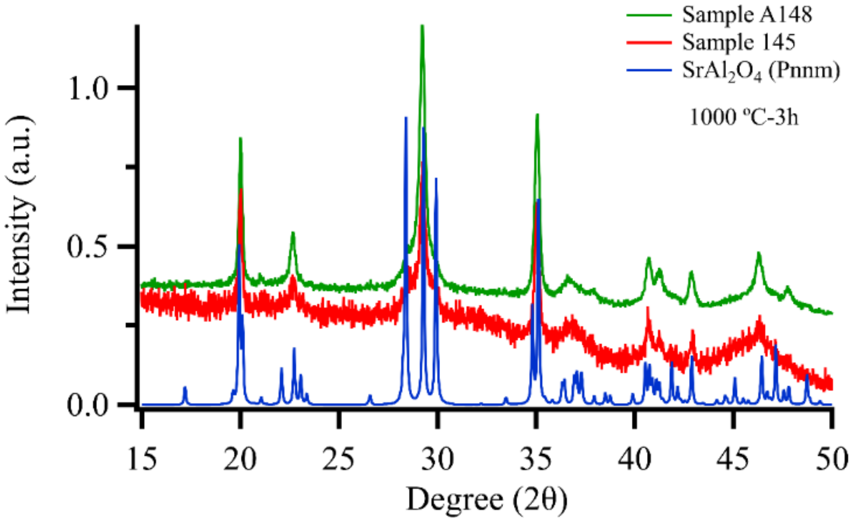

Figure 3. Powder-XRD diffraction patterns of Sample A145 ($SrAl_2O_4:Eu^{2+},Dy^{3+}$) and Sample A148 ($SrAl_2O_4:Eu^{2+},Dy^{3+}$) annealed at 1000 °C for 3 h under reducing atmosphere of carbon.

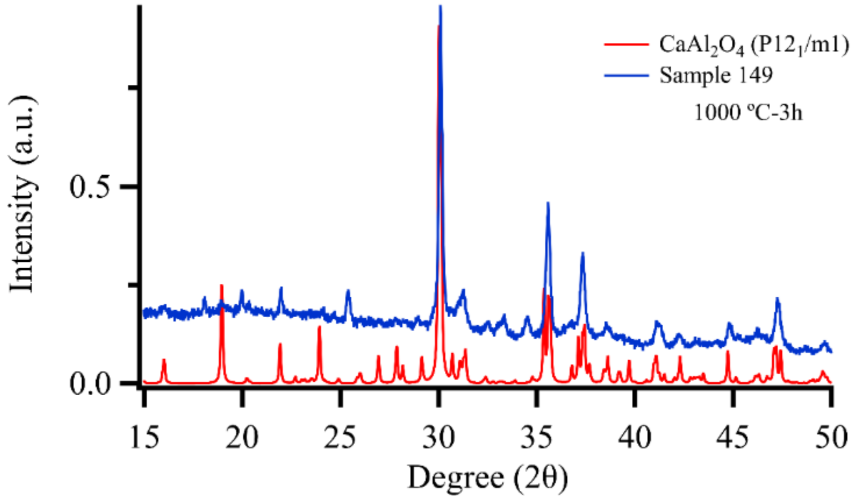

Figure 4. Powder-XRD diffraction patterns of Sample A149 ($CaAl_2O_4:Eu^{2+}$) and Sample A148 annealed at 1000 °C for 3 h under reducing atmosphere of carbon.

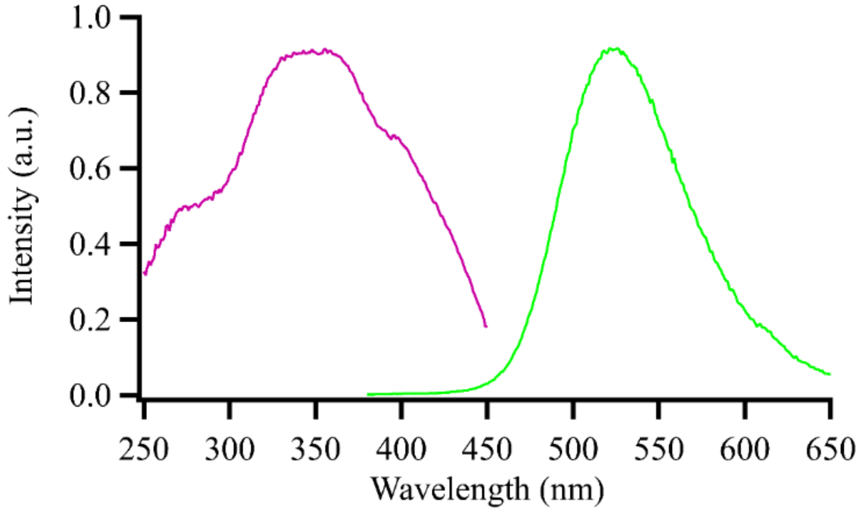

Figure 5. Excitation and emission spectra of $SrAl_2O_4:Eu^{2+},Dy^{3+}$ obtained at 525 and 360 nm, respectively.

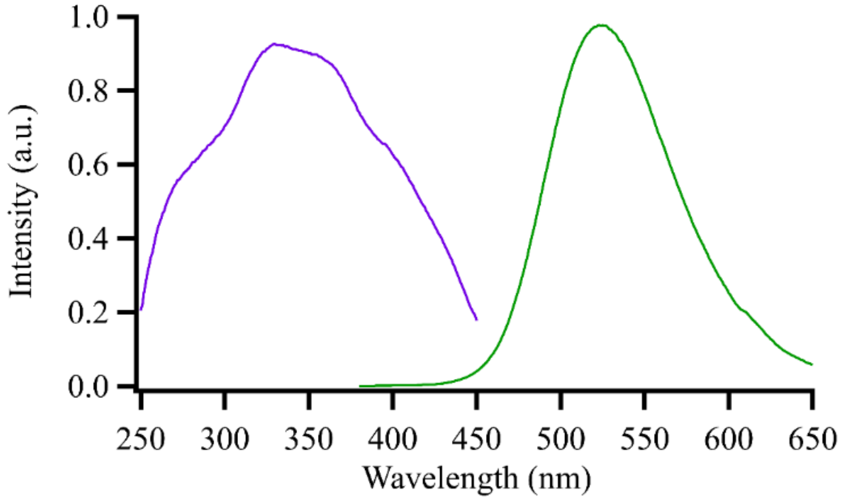

Figure 6. Excitation and emission spectra of $SrAl_2O_4:Eu^{2+}$ obtained at 525 and 360 nm, respectively.

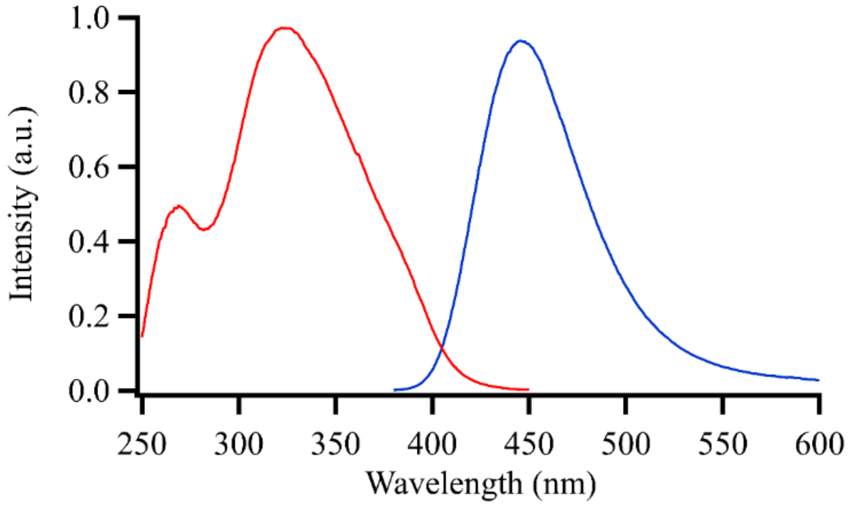

Figure 7. Excitation and emission spectra of $CaAl_2O_4:Eu^{2+}$ obtained at 470 and 360 nm, respectively.

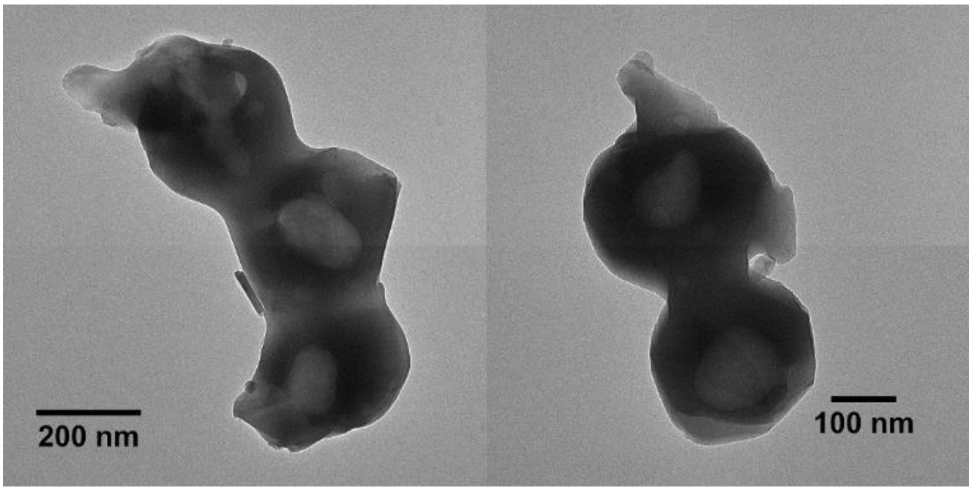

Figure 8. Hollow-structured crystalline NPs of $Sr_4Al_{14}O_{25}$:$Eu^{2+/3+}$.

Conclusions and outlook

In this thesis we presented a novel method for the preparation of $SrAl_{12}O_{19}$:Eu^{3+} NPs. A solvothermal method was used to prepare spherical $SrAl_{12}O_{19}$:Eu^{3+} precursor NPs with size distribution in between 200-300 nm. These precursor NPs underwent a shape transformation from the spheres to hexagonal platelets during the annealing process at 1150 °C to obtain crystalline NPs. This method worked perfectly for the preparation of $CaAl_{12}O_{19}$:Eu^{3+} NPs, as well. Our analysis of the precursor NP formation process showed a cooperation PVP+Al^{3+} gelation process. Unlike in the commonly used sol-gel methods, in our method micro-sized separate gels form. Similar to the microemulsion method where droplets act as micro-sized reactors, in the present method, micro-sized gels act as the reactors. The nucleation and growth processes take place inside these reactors. These gels are then spontaneously transformed into spherical precursor NPs of MO-Al_2O_3 (M=Ca, Sr) with homogeneous morphology and narrow size distribution. Indeed, the gel is consumed by the nuclei formed inside it during the growth step.

Doped with Eu^{3+} ion, these NPs showed deep-red luminescence. Unlike the majority of Eu^{3+}-based phosphors, in these NPs, the $^5D_0\rightarrow{}^7F_4$ transition at 680 nm was more intense than the $^5D_0\rightarrow{}^7F_2$ transition. In these NPs, in addition to the emissions from the $^5D_0$ excited state to the ^7F_J ground states, Eu^{3+} emits from the $^5D_{1\text{-}3}$ states at 298 K, as well. The emissions from the $^5D_{2,3}$ states almost quench under excitation to the charge transfer (CT) band. This indicates that there is an energy barrier to overcome in order to transfer electrons from the CT band to the ^5D_J states, and it grows larger as the energy of the ^5D_J state increases. Furthermore, detailed luminescence spectroscopy of these NPs, revealed the presence of at least three different CC processes taking place in their crystalline structure.

In the amorphous phase SrO-Al_2O_3, two different peculiar emissions were identified for the Eu^{3+} ion. An unusual intense band originating from the forbidden $^5D_0\rightarrow{}^7F_0$ transition was observed at an extremely high energy of about 17670 cm^{-1}. The corresponding CT band was, on the other hand, observed in a very low energy of 29400 cm^{-1}. These values were 17500 and 32200 cm^{-1} for the second peculiar emission, respectively, which emerged upon increasing the Eu^{3+} concentration. The peculiar emission was reproducible under different synthesis conditions. Changing the composition of the NPs from SrO-Al_2O_4 to CaO-Al_2O_4, shifted the peculiar $^5D_0\rightarrow{}^7F_0$ emission to slightly lower energies (about 17600 cm^{-1}). These results indicated that the energy of the $^5D_0\rightarrow{}^7F_0$ transition is influenced by the neighboring metal-ion to the peculiarly-emitting Eu^{3+} ion. This peculiar emission could be at the origin of the long persistent luminescence of MO-Al_2O_3 phosphors. On the other hand, since a very large crystal field (CF) effect is observed for this Eu^{3+}, it shows that the f orbitals of the rare-earth (RE) ions are not very untouchable. Understanding the origin of this peculiar luminescence of Eu^{3+} can pave the way for designing RE-based phosphors with novel luminescence properties.

The present synthesis method was shown to work well for the preparation of $MAl_{12}O_{19}$ precursor NPs. However, obtaining MO-Al_2O_3 NPs with relatively higher ratios of M^{2+} in the NPs (For instance, $SrAl_2O_4$) with this method, still remains challenging. This stems from the two-step precipitation of the metal-ions into the NPs in the present solvothermal reaction. Studying the mechanism of the reaction showed that, the nuclei were composed of only Al^{3+} metal-ions and the M^{2+} ions were precipitated onto the NPs during the growth process. This can result in an undesired secondary nucleation if the concentration of M^{2+} ions reach the supersaturation state. Secondary nucleation will then lead to the growth of particles with different compositions and morphologies (Figure 1). In the case of $MAl_{12}O_{19}$ NPs, the nominal concentration of M^{2+} is low enough to prevent reaching the super saturation state, if the reaction rate is slightly lowered by for instance by decreasing the H_2O ratio.

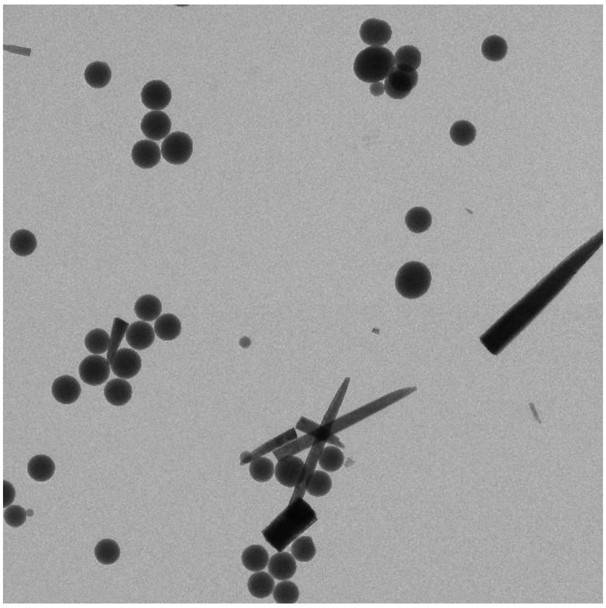

Figure 1. Growth of rod particles besides spherical NPs in the solvothermal reaction as a result of secondary nucleation.

It is possible to lower the reaction rate by decreasing either the reaction temperature or the amount of urea. However, at too low temperatures, the spherical NPs cannot be obtained (this depends on the amount of the PVP used). On the other hand, decreasing the ratio of urea results in smaller NPs as well as extended reaction times. These in addition to the delayed precipitation of the MCO_3 species onto the NPs, which expose the surfaces of the NPs to aggregation, result in Ostwald ripening. These are some of the challenges that must be overcome to generalize the present method for the preparation of $MO\text{-}Al_2O_3$ precursor NPs with the desired M^{2+}/Al^{3+} ratios.

Nevertheless, although preparation of the precursor NPs with the right ratios of M^{2+}/Al^{3+} is necessary for obtaining the desired crystalline phase, it is does not guarantee obtaining nanosized crystalline particles. Crystallization of the $MO\text{-}Al_2O_3$ compounds normally occur at very high temperatures (>1100 °C), which in many cases leads to their aggregation. We tried different methods to stop this aggregation. Dispersion of the precursor NPs in a H_2O/EtOH solution of PVP or other organics and evaporation of the solvent to reduce the contact surface of the NPs resulted in even more aggregation. Mixing and grinding the NPs with silica NPs also resulted in larger aggregation. Coating the NPs with silica and annealing them led to a solid-state reaction between the $SrO\text{-}Al_2O_3$ core and the silica shell producing $Sr_aAl_bSi_cO_d$ hollow spheres at 1000 °C (Figure 2). At 1100 °C crystalline $SrAl_2Si_2O_8$ was obtained (Figure 3). However, the NPs aggregated during the crystallization process. Therefore, development of new methods for the preservation of morphology and size distribution of NPs during the annealing process is still highly recommended.

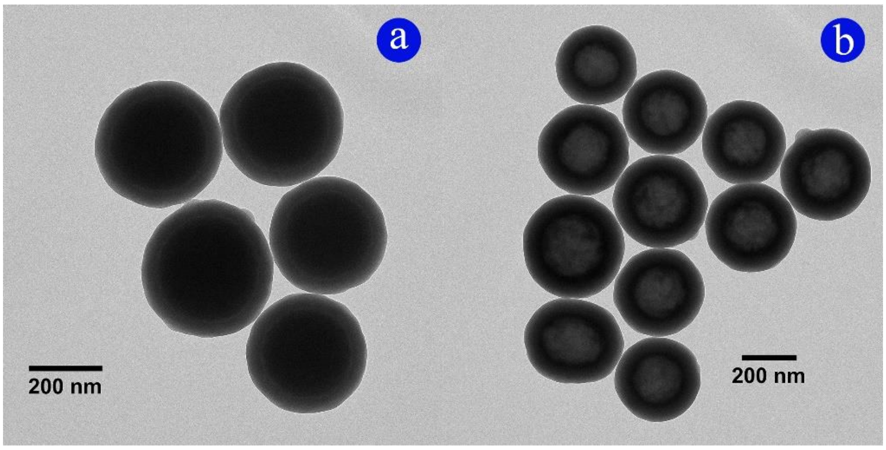

Figure 2. SrO-Al_2O_3@silica NPs a) before annealing and b) annealed at 1000 °C.

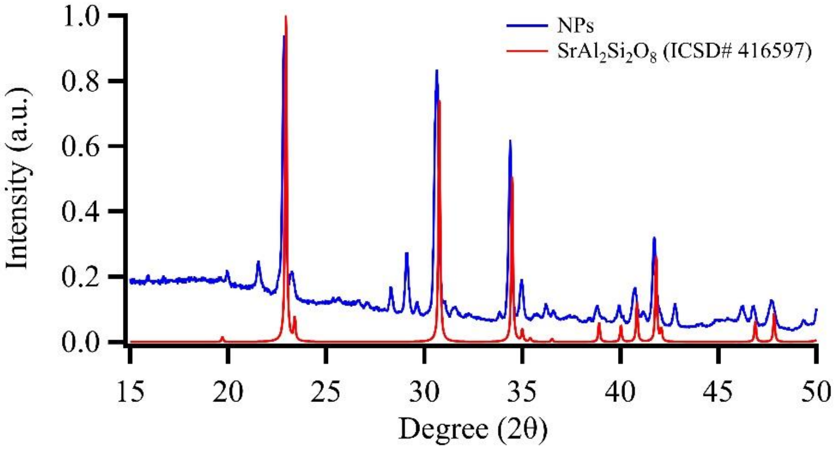

Figure 3. Powder-XRD diffraction pattern of SrO-Al_2O_3@Silica NPs annealed at 1100 °C for 2 h.

Currently, extensive research is focused on the red-emitting phosphors and in particular LPPs, since they are excellent candidates for bio-imaging applications. In addition to the Eu^{3+} doped NPs, we successfully prepared Mn^{4+}-doped crystalline NPs of $MAl_{12}O_{19}$, which emit in the deep-red region of the visible spectrum (Figure 4). Cr^{3+} is another red-emitting activator which can in principle be doped into these NPs. Therefore, detailed studies of other red-emitting dopants in the $MAl_{12}O_{19}$ NPs are recommended.

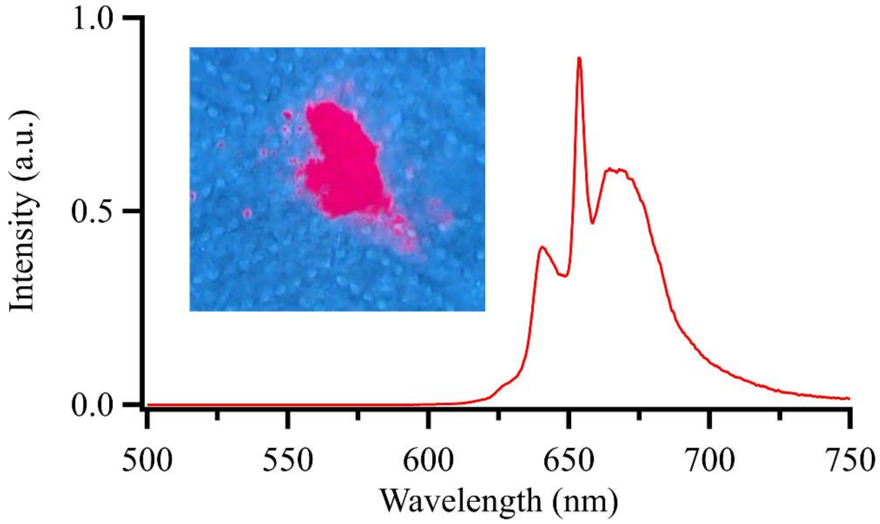

Figure 4. Emission spectrum of Mn^{4+}-doped $SrAl_{12}O_{19}$ NPs. Inset: $SrAl_{12}O_{19}:Mn^{4+}$ powder under 365 nm UV lamp.

With the homogeneous base NPs, it is possible to engineer them and for instance shift the green luminescence of $SrAl_2O_4:Eu^{3+},Dy^{3+}$ phosphor to the red or NIR region of the spectrum. This can be done by transferring energy from a core particle to a shell with a smaller bandgap, or through coupling with plasmonic materials. Furthermore, detailed study of the $SrO\text{-}Al_2O_3$ system in the amorphous phase and the transformation process to the crystalline phases can provide deeper insight into the afterglow mechanism of these materials. Janus particles of $SrO\text{-}Al_2O_3$ system can open new possibilities for obtaining novel luminescent properties, which normally would not be possible with the ordinary NPs. Moreover, decreasing the NP size down to below 20 nm, where the quantum confinement effect will come into play, can also result in novel optical properties.